R-743

STRAPDOWN SYSTEM PERFORMANCE OPTIMIZATION TEST EVALUATIONS (SPOT)

Final Report on Contract NAS 9-6823
Modification 11

by

Richard J. Blaha and Jerold P. Gilmore

February 1973

Volume I

CHARLES STARK DRAPER LABORATORY

MASSACHUSETTS INSTITUTE OF TECHNOLOGY

CAMBRIDGE, MASSACHUSETTS, 02139

R-743

Strapdown System Performance Optimization Test Evaluations (SPOT)

Final Report on Contract NAS 9-6823 Modification 11

by

Richard J. Blaha and Jerold P. Gilmore

VOLUME I

Charles Stark Draper Laboratory
Massachusetts Institute of Technology
Cambridge, Massachusetts
02139

Approved: Jerold P. Gilmore Date: 27 Feb 1973
J.P. GILMORE, DEPUTY ASSOCIATE DIRECTOR

Approved: Ralph R. Ragan /for Date: 27 Feb 73
N.E. SEARS, ASSOCIATE DIRECTOR

Approved: Ralph R. Ragan /for Date: 27 Feb 73
D.G. HOAG, DEPUTY DIRECTOR

Acknowledgment

The work presented in this report is sponsored by the NASA Manned Spacecraft Center of the National Aeronautics and Space Administration under Contract NAS9-6823 Modification 11 with the Massachusetts Institute of Technology. Special appreciation is expressed to the contract's technical monitor, Mr. Malcolm Jones, whose interest and ideas stimulated a thorough evaluation of strapdown performance in dynamic environments. Jerald Gilmore has technical responsibility for this contract and Dick Blaha designed and coordinated the program from the system design phase through to the test and analysis phase.

The assistance of many persons in the Charles Stark Draper Laboratory was required to implement the inertial system test facility including a real-time data processing capability. Specific attention to these people and their contribution is well deserving and timely in this acknowledgment.

Bob Booth for the guidance and interest provided throughout the program's duration and for his land navigation contribution (Section 5.3 of this report).

Dick McKern for his ideas relating to the dynamics of strapdown performance.

John Oehrle for his elegant implementation of the real-time compensation attitude, and navigation algorithms.

Jim Keenan, Dave Dove and Ken Vincent for their calibration, and analysis algorithms.

Dave Torrealba for the least square accelerometer modeling evaluation and Howard Musoff for his clever system attitude and least square models.

Dave Swanson and Richard Sheridan for their formulation of the calibration procedures.

Dave Brown for a reliable computer facility, and Duncan Sprague for the interpolator design.

Stephen Helfant and Linda Willy for the detailed attention given to data analysis and presentation.

Julie Feldman, John Sinkiewicz and George Bukow for the inertial instrument support.

Charles Lory for his creative ideas concerning pulse bursting, flood hangoff, and attitude storage.

Marty Snow and William Trosky for their fabrication and system test support.

Bill Eng and Dave Farrar for the graphic support of this report and Bernadette Erikson, Ellen Hurley, Lynne Sherman, Robin Schneider, Sharon Crawford and Linda Andrews for the preparation of the computer inputs and final compilation of the manuscript.

This report was prepared under DSR Project 55-29435 sponsored by the Manned Spacecraft Center of the National Aeronautics and Space Administration through contract NAS 9-6823.

Abstract

A three axis inertial system is packaged in an Apollo gimbal fixture for fine grain evaluation of strapdown system performance in dynamic environments. These evaluations have provided information to assess the effectiveness of real-time compensation techniques and to study system performance tradeoffs to factors such as quantization and iteration rate. The strapdown performance and tradeoff studies conducted in this program include:

1. Compensation models and techniques for the inertial instrument first-order error terms were developed and compensation effectivity was demonstrated in four basic environments; single and multi-axis slew, and single and multi-axis oscillatory.

2. The theoretical coning bandwidth for the first-order quaternion algorithm expansion was verified. The pseudo coning bandwidth was measured and identified to be a combined function of the attitude algorithm's coning bandwidth and the OA coupling compensation algorithm's bandwidth.

3. Gyro loop quantization was identified to affect proportionally the system attitude uncertainty.

4. Land navigation evaluations identified the requirement for accurate initialization alignment in order to pursue fine grain navigation evaluations.

VOLUME I

Table of Contents

LIST OF ILLUSTRATIONS

VOLUME II

TABLE OF CONTENTS

1.0 Introduction

Characteristic of strapdown inertial guidance systems is the measurement of specific force and angular rate inputs in the vehicle coordinate frame. Hence, the gyroscopes and accelerometers encounter the full dynamic environment imposed by the controlled vehicle's maneuvers and motions. To maintain an inertial reference frame, algorithms are implemented in a digital computer to process the gyro and accelerometer data. The data inputs as sensed by the inertial instruments include errors as a result of the instrument's physical characteristics. These errors result from factors such as scale factor linearity and inertia response, the mechanization of the torque-to-balance loops (quantization effects), and the bandwidth of the algorithms. The dynamic errors can be compensated provided that an error model can be defined for implementation in a general purpose mini-computer.

The objective of the program described in this report was to effect a fine grain test evaluation of a strapdown system in a dynamic environment to assess the effectivity of instrument error compensation techniques and system performance response to different algorithm iteration rates and quantization effects. To achieve this program objective a test facility was developed that enabled the introduction of a broad spectrum of multiple axis slew and oscillatory inputs to an experimental three axis gyro and accelerometer strapdown test package. The package was operated in real time with a general purpose mini-computer that included extensive compensation and strapdown algorithm software. Using this capability and corresponding software models a wide band performance evaluation of the torque-to-balance strapdown mechanization was effected. The resultant test and trade-off performance findings presented in the body of this report provides a fuller appreciation of the strapdown error propagation characteristics and identifies the opportunities for further strapdown system refinements and advanced software development.

The program objective has been fulfilled through the accomplishment of the following specific tasks as stipulated in the contract work statement [1] : 1) the assembly of a three axis inertial component strapdown unit consisting of three size 18 Inertial Rate Integrating Gyroscopes (18 IRIG), and three size 16 Permanent Magnet Pulsed Integrating Pendulums (16 PM PIP) and packaged within an Apollo Block I gimbal system (IMU#5). The gimbal system was modified to accept slew, oscillatory and other angular functional dynamic inputs via control of the gimbal torque motors to the instrument package, 2) the development of a test facility to

support the strapdown unit testing consisting of the electronics necessary for test operations, a Block I IMU modified to accept the package in place of the stable member, an Apollo rotary test station for accurate positioning of the IMU fixture with respect to gravity and earth rate inputs, and a computer for on-line real-time operation with the strapdown inertial unit, 3) the development of suitable software necessary for dynamic testing including calibration, and real-time instrument compensation algorithms and, 4) the development and conduct of a test program sufficient to evaluate strapdown system performance and the effectiveness of compensation in a dynamic environment.

In fulfillment of the above tasks, the program's accomplishments included: 1) the implementation of a test facility consisting of the dynamic gimbal test fixture, the three axis strapdown package with its supporting electronics (torque-to-balance loops, etc.) interfaced with the H316 mini-computer and the automatic test control electronics, 2) the development of analytic error models and software compensation routines that included: compensation for gyro errors such as gyro scale factor linearity, misalignment, Output Axis coupling, anisoinertia, Spin-Reference Axis cross-coupling, major anisoelasticity, bias and g-sensitive drift terms, and accelerometer scale factor, misalignment and bias. In addition higher order accelerometer models were evaluated using a least square technique operating on multi-position accelerometer test data, 3) implementation of full parameter compensation algorithms at three iteration rates; 100,50, and 25 updates per second, 4) implementation of a third order quaternion expansion algorithm (without the cross product term) and an inertial referenced land navigator at three iterative rates; 100,50, and 25 iterations per second, 5) calibration software for automatic static and dynamic parameter calibration, gimbal alignment certification and average float hangoff measurement, 6) the implementation of software for system diagnostic testing, data management, transfer, storage and analysis., 7) initiation of a broad base test program to evaluate:

a. Static and dynamic parameter calibration
b. Pseudo coning
c. SRA cross coupling and anisoinertia
d. Scale factor linearity
e. Pulse bursting
f. Coning
g. Quantization tradeoff
h. Algorithm iteration rate
i. Land navigation performance with tradeoff studies

This report describes in Section 2 the test facility and Section 3 discusses the inertial instruments and the appropriate error models. Section 4 discusses calibration, compensation and navigation software. Section 5 presents the test results including calibration statistics, bandwidth, quantization, compensation studies and navigation results. Also presented and discussed are the results of the "least squares" accelerometer data evaluations. Volume II of this report contains the security classified accelerometer calibration data (confidential).

Page intentionally left blank

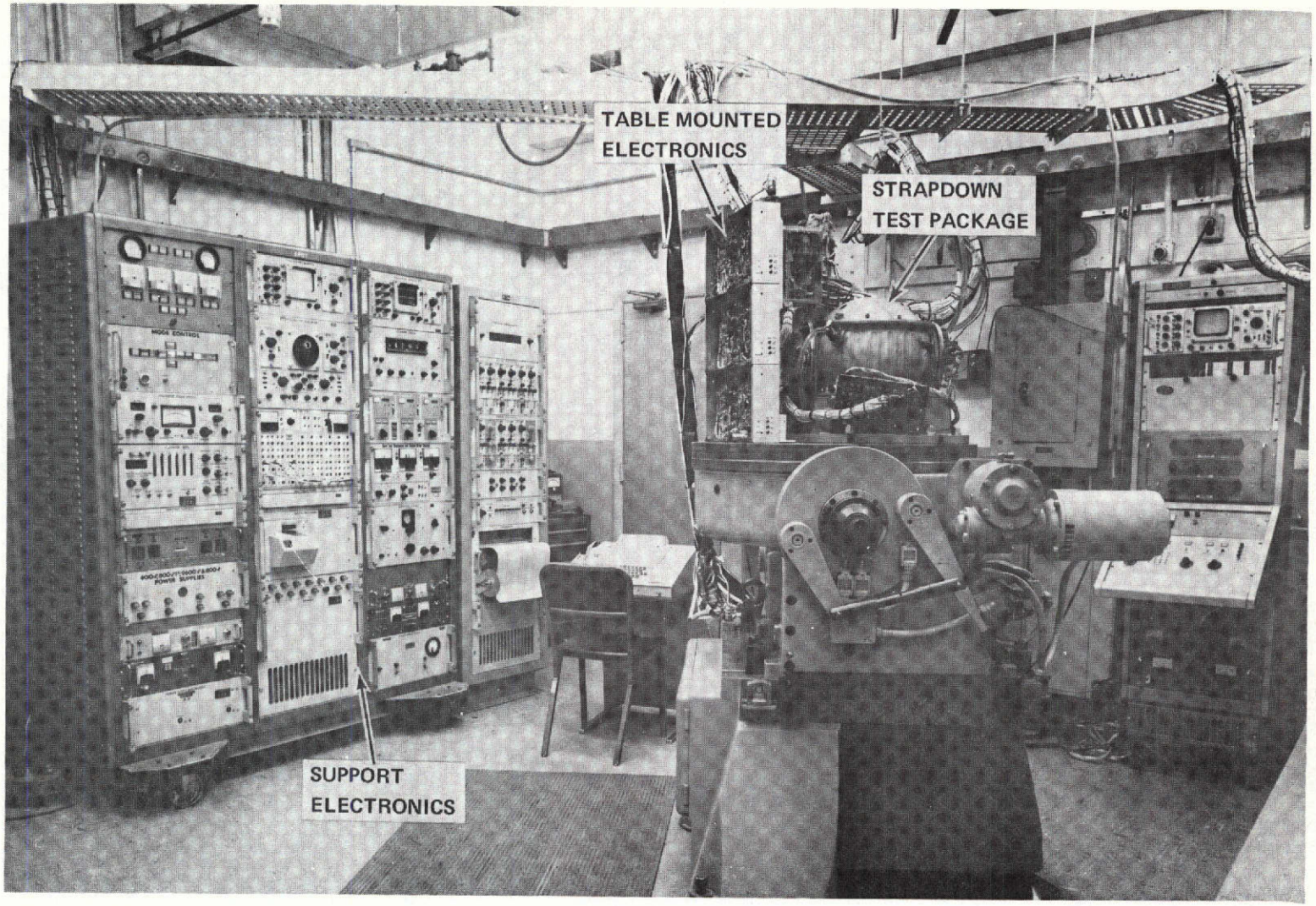

Fig. 2.1.2 SPOT TEST FACILITY.

2.2 Strapdown Instrument Test Package

The strapdown instrument test package is a three (3) axis inertial system mounted in a three (3) degree-of-freedom gimbal system. The gimbal system used is the prototype gimbal system for the Apollo Block II configuration. The strapdown test fixture capabilities and parameters are defined in Appendix A.

The inner member is an aluminum frame, fabricated as a part of the inertial subsystem Structure Mounted Attitude Reference Test Studies (SMARTS) Task II of contract NAS 9-6823[2]. The frame form factor is designed to replace the stable member of a prototype Apollo Block II gimbal configuration for the dynamic evaluations required in the current contract (modification 11 of contract NAS 9-6823).

Mounted on the aluminum frame are the gyros and accelerometers with their complement of pre-amplifiers and temperature controllers, a dual axis rate transducer (DART), two optical reference cubes, and frame mounted temperature sensors. (Figures 2.2.1 and 2.2.2.)

The gyro used in the strapdown package, the 18 IRIG Mod B is a single-degree-of-freedom integrating rate gyro specifically developed for the strapdown application. It has a permanent magnet torquer that is sized to be compatible with rates up to a radian per second. A description of the gyro is included in Section 3.2.

Each gyro is mounted in an adjustable alignment mounting assembly to allow freedom of adjustment of the gyro Input Axis about the Output Axis and Spin Reference Axes. Each gyro electronics complement includes individual temperature controllers and float suspension adjustment electronics. The signal generator (SG) pre-amplifier conditions the gyro output for reliable transmission through the gimbal slip rings to the pulse torque electronics. The pulse torque electronics are mounted on the rotary test table to minimize the distance from the gyro. Operationally, the pulse torque electronics provides a closed loop control of the gyro to maintain the gyro float at its null position. The gyro torque pulses ($\Delta\theta$) represent angular increments and are transmitted to the H316 mini-computer for data processing and analysis. In addition to the pulse torque electronics, the SG output is encoded into six(6) bits of digital data by the interpolator for float hangoff measurements and finer attitude quantization.

The accelerometer used in the strapdown package is the 16 PM PIP, a single-degree-of-freedom pendulous integrating specific force receiver. The accelerometer is designed to operate in a closed-loop torque-to-balance mode. A description of the accelerometer is included in Section 3.1.

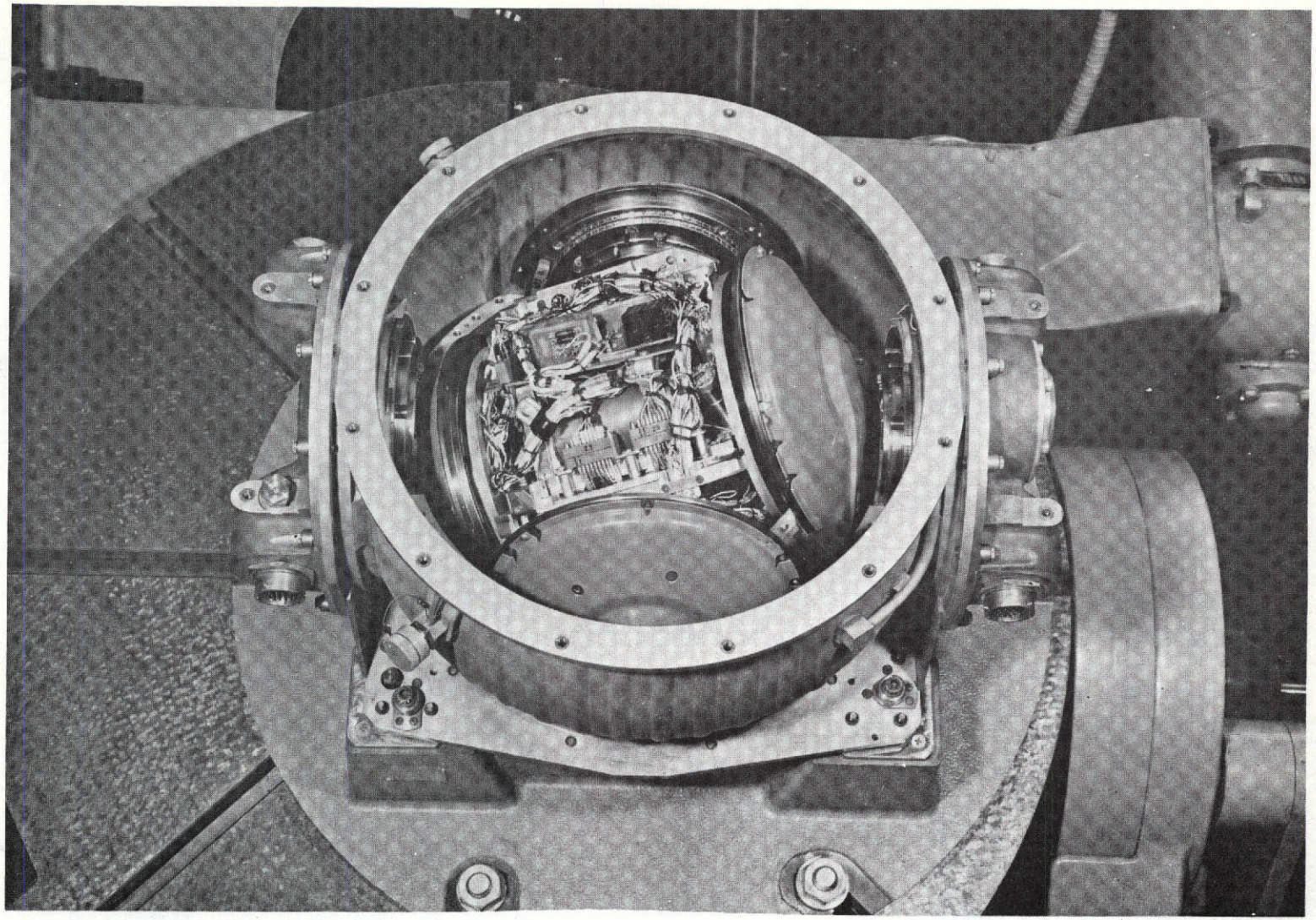

Fig. 2.2.1 STRAPDOWN TEST PACKAGE.

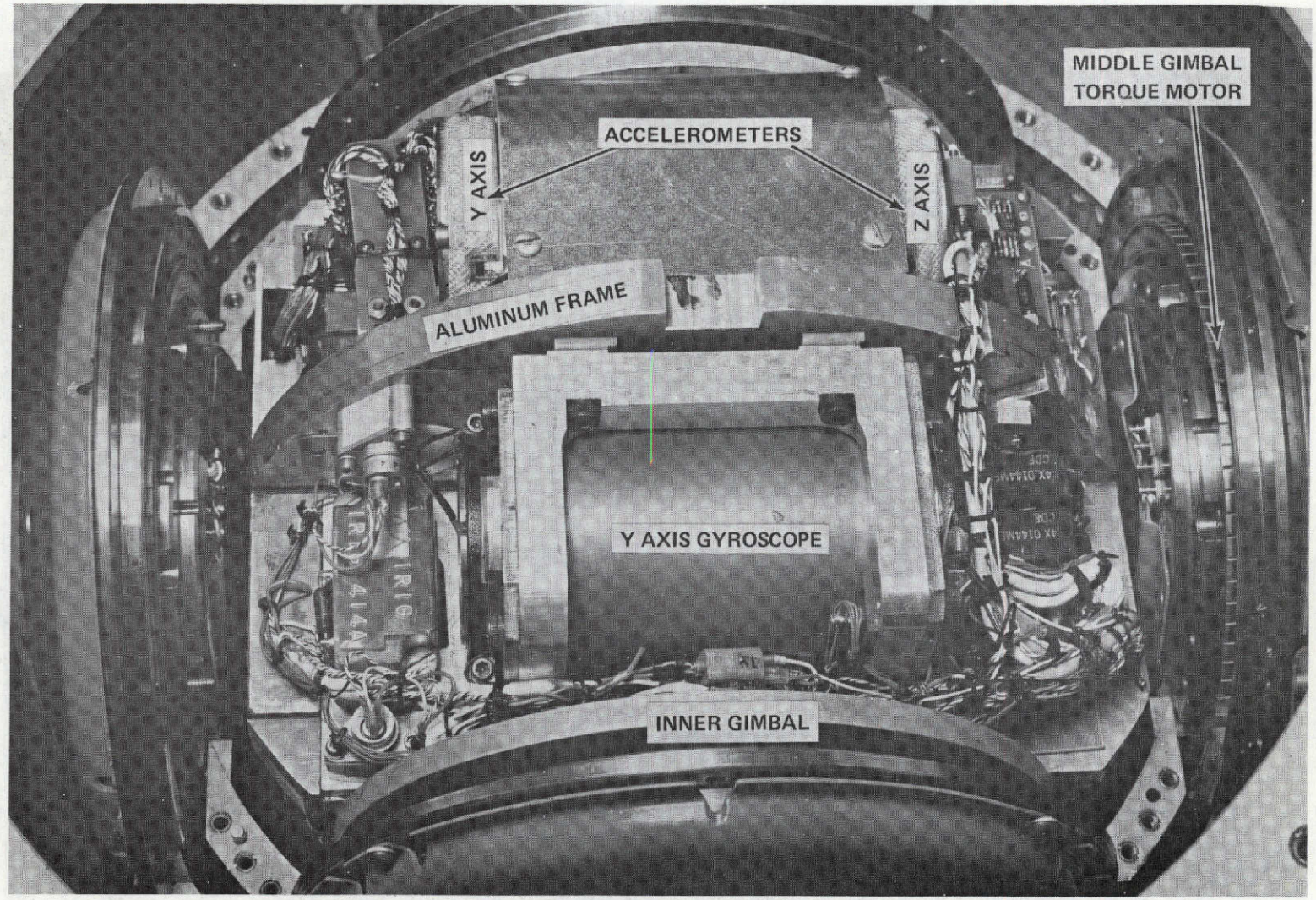

Fig. 2.2.2 GIMBAL INNER MEMBER.

Each accelerometer is supported on the aluminum frame by an alignment and mounting ring to enable freedom of adjustment of the accelerometer's Input Axis about the Output Axis and the Pendulous Reference Axis. In addition, the mounting ring contains the heater elements to maintain the accelerometer at operating temperatures. The mounting ring is separated from the aluminum frame with a 1/16 inch thick MYCALEX shim to provide thermal isolation from the aluminum frame.

A Mu metal shroud that usually encases the accelerometer body for magnetic field insulation was removed to allow clearance of the accelerometer through the aluminum frame mounting hole. Mu metal shielding was installed elsewhere on the inner frame to isolate the accelerometers from the gimbal torque motor magnetic fields.

The accelerometer electronics complement includes a proportional temperature controller and suspension adjustment hardware. A pre-amplifier conditions the accelerometer's signal generator (SG) output for transmission through the slip rings to the pulse torque-to-balance electronics. The torquing electronics pulse restraints the accelerometer float to its null position and furnishes incremental velocity data to the H316 computer.

A dual axis rate transducer (DART) is installed on the aluminum frame to inhibit the gimbal torque motor driving electronics in the event of a gimbal runaway. Under conditions of gimbal runaway it is possible that the wheel bearing rate capability of the 18IRIG MOD B gyro will be exceeded, and a catastrophic wheel-touchdown failure will occur. The DART instrument (a Northrop Nortronics component) is a subminiature rate sensor that uses a piezoelectric bimorph crystal element to detect torques within a fluid that rotates at 24,000 rpm. Gyroscope torque occurs from the interaction of the body fluid rotation with angular rates applied about two input axes. The output of the DART is a ac signal that is proportional in amplitude to the vectorial sum of the two input excitations. An electronic assembly monitors the DART output to provide noise filtering and signal sensing to inhibit the gimbal drive loops at excessive rates.

Two optical reference cubes were installed on the aluminum frame to align the strapdown body frame to an earth fixed reference frame. Optical sighting ports were machined in the middle and outer gimbal hats for alignment purposes. The optical cubes were useful for the initial package alignment and alignment stability measurements. Once the accelerometer alignment was established, the alignment to a reference frame was more efficiently determined from the accelerometer's output.

The strapdown thermal design uses separate proportional temperature controllers for each inertial instrument. Thermal control is maintained by temperature sensors that are wrapped around the inertial instruments case and heater coils attached to the mounting fixture. Heat transfer from the inertial instrument is directed through the aluminum frame to the outer case of the gimbal system. The outer case temperature is cooled to $42^{\circ}F$ by circulating glycol water through an integral coolant loop machined in the Apollo IMU case. Fans in the outer gimbal hat are included to reduce the thermal resistance between the strapdown system and the outer case.

The aluminum frame, on which the inertial instruments are mounted, incorporated integral coolant channels for heat exchange purposes and were used in the SMARTS test effort. In mounting the frame in a closed gimbal system, use of this coolant heat exchange feature was not possible. The reduced heat transfer characteristics of the gimbal system represented a design problem; however, rather than initiating a comprehensive thermal design, the gyro operating point was shifted upwards $10^{\circ}F$ to $140^{\circ}F$ and the accelerometer operating point was shifted downward $10^{\circ}F$ to $130^{\circ}F$. The strapdown thermal model is given in Appendix A, Figure A-2.

The higher gyro operating temperature reduces the gyro viscous fluid damping coefficient. Damping coefficient reductions, increase the float time constant and decrease the gyro transfer function between the angular input and the output float displacement. The float time constant increase, reduces the pulse bursting threshold and increases the float hangoff from its null position for a given Input Axis rate. These changes were accounted for in the software modeling and torque-loop design.

The accelerometer temperature reduction does not affect performance significantly. The accelerometer permanent magnetic design includes two shunting rings to minimize scale factor instabilities because of the magnet's temperature sensitivities. These rings were effective at the reduced operating temperature and the measured scale factor instabilities were bounded by a couple of ppm. At lower operating temperatures, the transfer gain between specific force inputs and output float displacement is reduced. However, this effect is corrected by an adjustment of the pulse torque threshold.

2.3 Pulse Torque Electronics

Both the gyroscopes and accelerometers operate with ternary pulse torque float restraining control loops. The function of the control loop is to apply torque commands to the gyro or accelerometer torquer to maintain the instrument output

axis at a null position. The loops are digital in nature; their outputs are pulses representing an angular increment ($\Delta\theta$) about the gyro Input Axis or equivalent velocity increments (ΔV) into the accelerometer. This incremental information is processed by the various compensation, attitude, and velocity algorithms to provide the package attitude with respect to an inertial coordinate frame.

Compensation circuits are included in the gyro loops to eliminate the "Pulse Bursting"[3,4] associated with the gyro time constant. A gyro signal generator (SG) output analog to digital convertor (interpolator) furnishes float position data for finer quantization and float hangoff measurements. The accelerometer loops do not have these ancillary electronics.

A simplified block diagram of the ternary pulse torque-to-balance control loop with the gyro pulse burst compensation and the gyro signal generator (SG) output interpolator is shown in Figure 2.3.1 (photograph Figure 2.3.2).

Because the gyro and accelerometer control loops are similar, only the gyro loop will be used to explain its method of operation. The control loop responds to an input from the signal generator (SG) output. The SG output is a 9600 hertz sinusoidal voltage that is proportional to the magnitude of the float angle displacement from null. The phase of the SG output is a direct function of the angular direction of rotation from the null position. A high narrow bandwidth preamplifier provides ample amplification and noise rejection for signal transmission through the gimbal slip rings. Further amplification is achieved in the pulse torque electronics buffer stage where the SG signal is phase shifted to assure maximum quadrature rejection with peak signal sampling.

Signal sampling is achieved with threshold level comparators. If the SG signal does not exceed the threshold level, no output is emitted and no torque command is generated. If the threshold level is exceeded, the interrogate logic determines the phase of the SG signal and generates the appropriate torque command. Torque commands, therefore, are applied in one of three states: positive, negative, or zero. This mode is identified as ternary.

A schematic, Figure 2.3.3, shows how the torque commands are generated in the pulse torque switching network.

For illustrative purposes, mechanical rather than the actual semiconductor switches are shown. The switch status is shown in the positive torque mode. Note that the torquing polarity is set by an H switch feeding current in the plus or minus

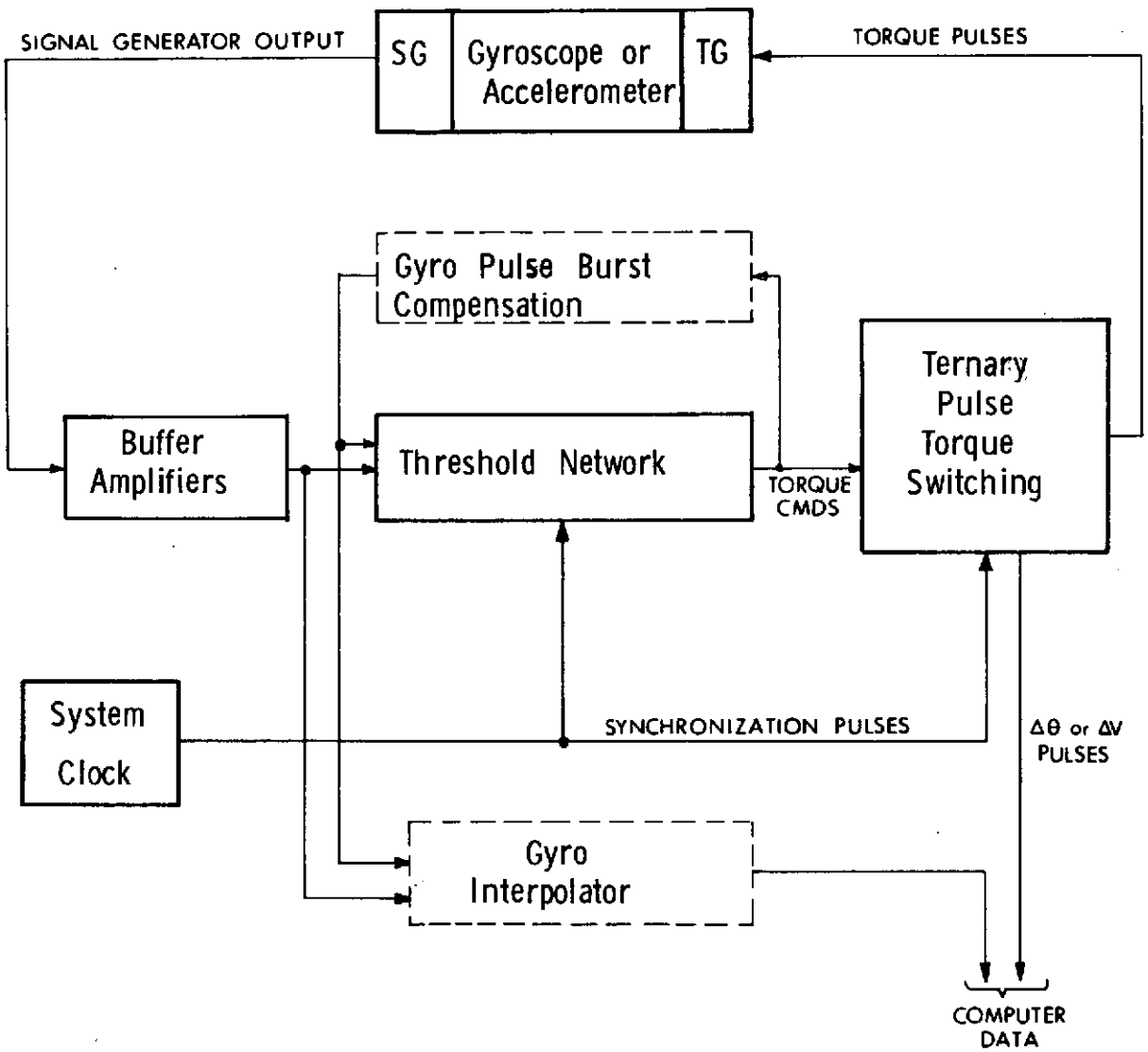

Fig. 2.3.1 Pulse Torque-to-Balance Control Loop.

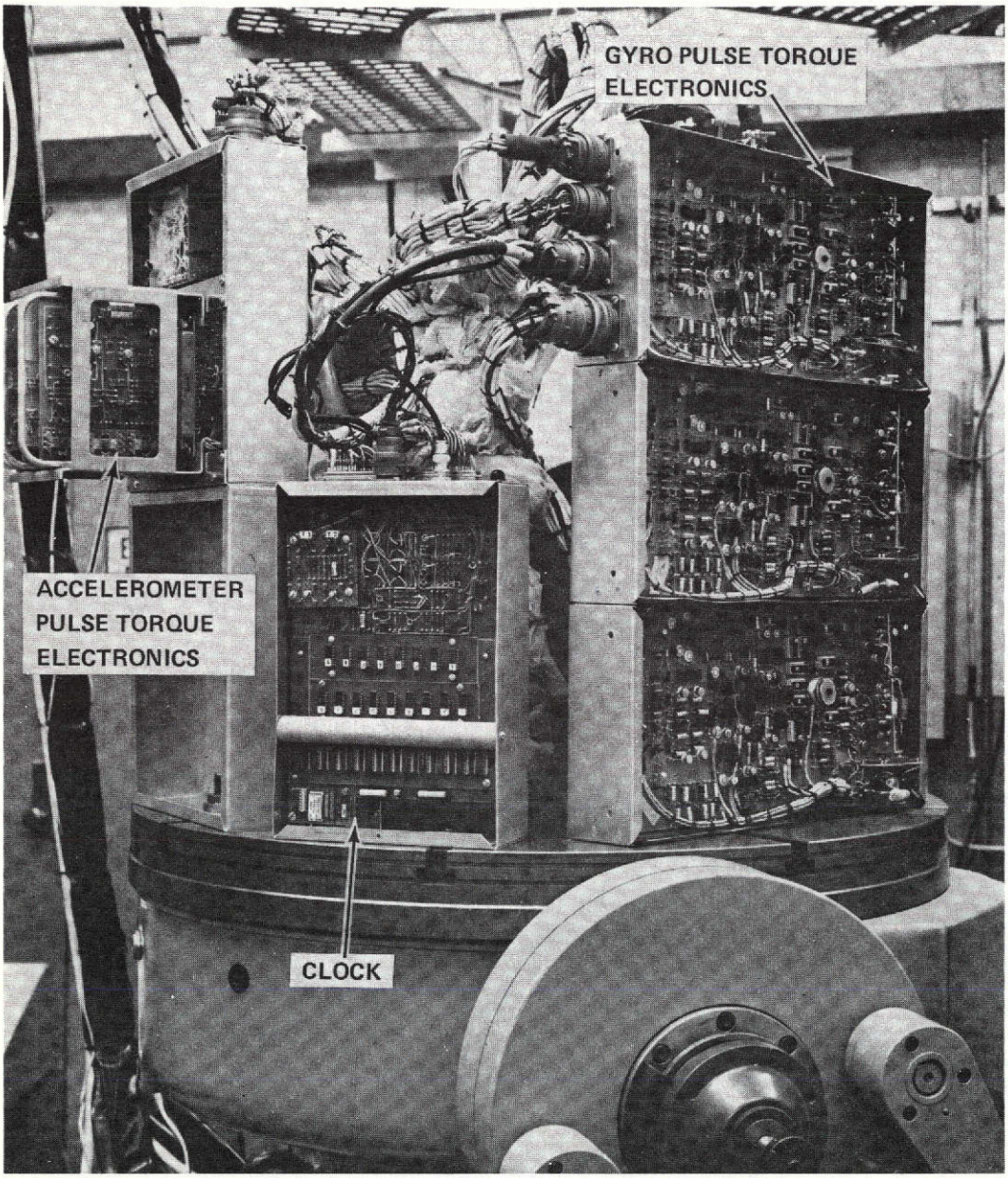

Fig. 2.3.2 TABLE MOUNTED ELECTRONICS.

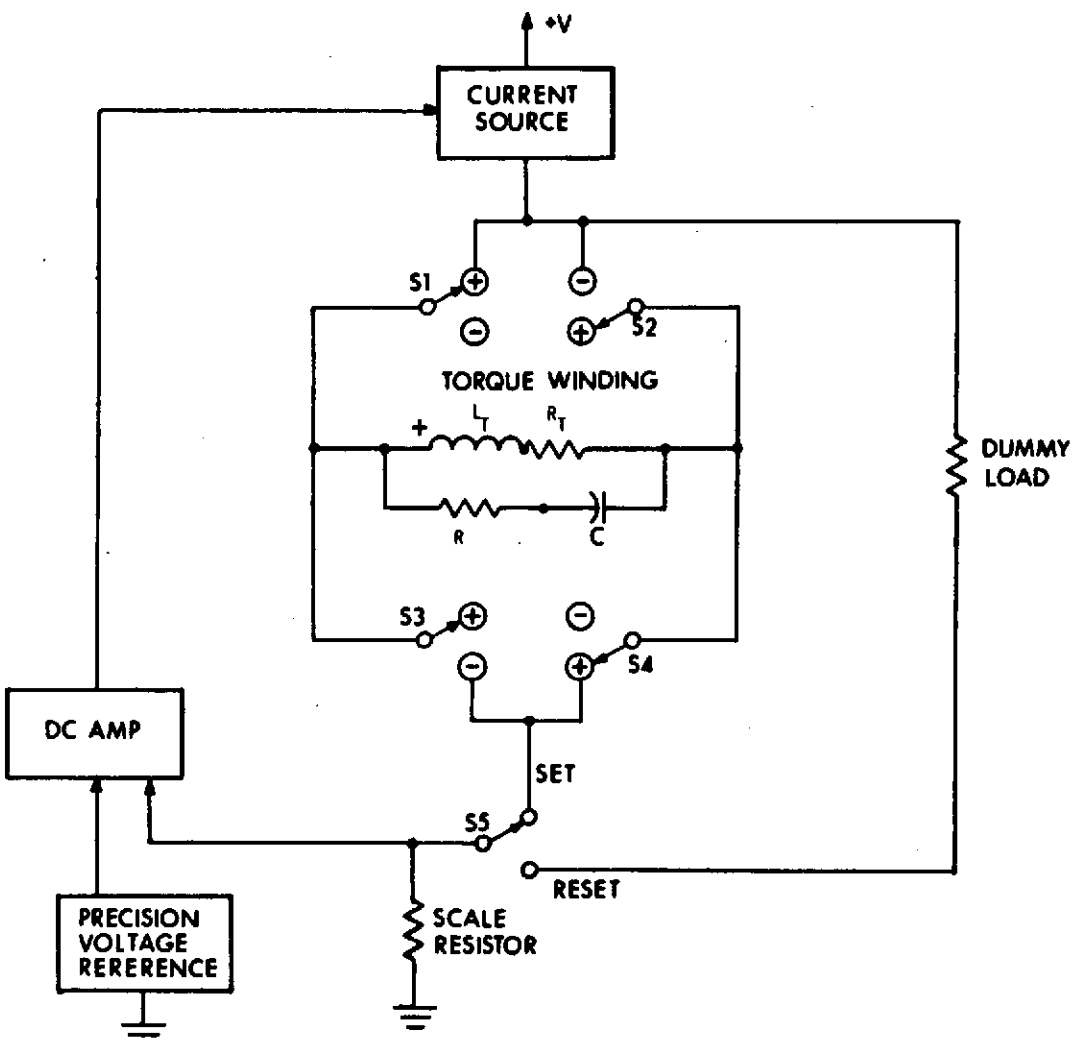

Fig. 2.3.3 Ternary Pulse Torque Switching.

direction of the winding. Switch S_5 operates so that current flows through either a dummy load or the torque winding.

The dummy load is a noninductively wound resistor approximately equal to the same resistance as the gyro torque winding mounted outside the torque electronics. The switch S_5 selects either command torquing (set position) or dummy load (reset position). Regardless of the torque-command state, the same current is fed into the scale-factor resistor. The voltage across this resistor is compared with a precision voltage reference at the input of a high-gain dc amplifier. The amplifier is part of a control loop that maintains a precise, direct current level. Note also that an RC network shunts the torque coil. It tunes the coil so that the load seen by the switches and current source is purely resistive.

The control of the set-reset switch S_5 in Figure 2.3.3 is clock synchronized to apply torque current as discrete pulses of fixed width. In each interrogation cycle, the clock issues interrogate, set and reset pulses defined in Figure 2.3.4. The time between the set and reset switching pulses is adjusted in 6.5μs increments.

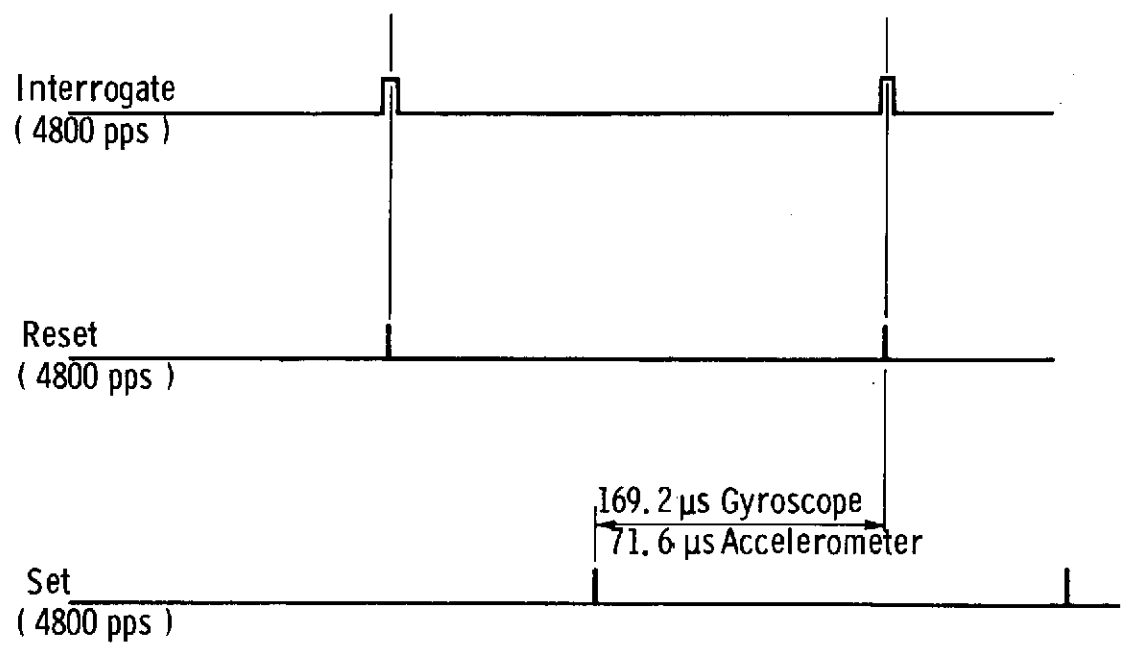

Fig. 2.3.4 Interrogate, Set and Reset Pulses.

The SG output is sampled at each interrogate cycle to determine if a positive, negative or no torque is required. If torque is required, S_5 is transferred to the set position by the set pulse and back to the reset position by the reset pulse.

Thus, at least a small fraction of each cycle is spent in the reset position. During this time of zero current in the H switch, the torque polarity can be reversed if required. If no torque is required, S_5 remains reset and the torque current is dissipated in the dummy load.

For this program, H switch protection logic was designed to prevent the simultaneous activation of switches S_1, S_2, S_3 and S_4. The torque command lines are monitored to assure that positive and negative torque commands do not occur together. If simultaneous detection is made, then the control loop is reverted to the torquing state of the previous interrogation cycle.

Operation in a binary loop mode may be achieved by suppressing the "no" torquing state. In this case only two torquing states are generated, positive and negative. If the torque threshold level is not exceeded, the previous interrogation cycle's torque command is repeated.

The basic torque-loop parameters used for the majority of tests are listed in Table 2.3.1.

In the first half of the SPOT program, the gyro loops operated with 70ma torquing current level and an 8 arc second loop quantization. The loop quantization was satisfactory for fine grain strapdown evaluation, however, the dynamic environment was rate limited to 0.2 radians/second. The dynamic environment range was later extended to 0.8 radian/second with a gyro loop rescaling by doubling both the torquing current and the torquing duty cycle. Hence, loop quantization was increased to approximately 40 arc seconds per pulse which resulted in a larger dynamic range.

The finer attitude quantization required for strapdown evaluation is achieved with an interpolator, scaled such that its least significant bit is equal to one-eighth of a gyro torque pulse (5 arc seconds). The interpolator provides attitude information stored by the float within the pulse torque quantization. This interpolator information is processed with the accumulated gyro torque pulses.

The interpolator is also used for float hangoff measurements. The selection of the mode of operation (attitude quantization or float hangoff measurement) is computer controlled through the activation of Field Effect Transistor (FET) switches. If the interpolator is to measure float hangoff, then the gyro SG output is sampled and converted to a digital representation. When the interpolator is used to quantize data for altitude algorithm processing, a signal component equivalent to the pulse

Table 2.3.1

Torque Loop Parameters

	GYROSCOPE	ACCELEROMETER
Interrogation	4800 PPS	4800 PPS
Duty Cycle	81.3%	35.1%
Torque Current	140 ma	73 ma
Quantization		
WITHOUT INTERPOLATOR DATA		
X Axis	35.6 $\widehat{\text{sec}}$/pulse	1 cm/sec/pulse
Y Axis	45.1 $\widehat{\text{sec}}$/pulse	1 cm/sec/pulse
X Axis	37.8 $\widehat{\text{sec}}$/pulse	1 cm/sec/pulse
WITH INTERPOLATOR DATA		
X Axis	4.5 $\widehat{\text{sec}}$/pulse	
Y Axis	5.6 $\widehat{\text{sec}}$/pulse	
Z Axis	4.7 $\widehat{\text{sec}}$/pulse	
LOOP RATE CAPABILITY		
X Axis	0.83 rad/sec	
Y Axis	1.06 rad/sec	
Z Axis	0.87 rad/sec	

burst compensation signal is subtracted from the gyro SG output prior to interpolator sampling. This signal processing is required because with pulse burst compensation, a larger float hangoff results with a corresponding larger attitude component in the gyro SG output. (See Section 3.2.) In addition, if a torque pulse is generated at the time of sampling, then the interpolator's output is preset to eliminate the redundant attitude information in the torquing pulse and the gyro float position. Figure 2.3.5 is the interpolator's block diagram.

The signal that is sampled by the interpolator is converted into a digital representation with a voltage ramp comparison convertor. Data transfer to the H316 computer is multiplexed over six (6) parallel lines into buffer registers. Data transfer is controlled completely from the H316.

2.3.1 Pulse Burst Compensation[3, 4]

A compensation network is incorporated in the torquing electronics to suppress pulse burst instabilities caused by inertia lags of the float response to torque commands. The compensation scheme used is the single pole analog circuit that anticipates the exponential movement of the float subsequent to the generation of a torquing pulse.

Figure 2.3.6 is the float response to a 80% duty cycle torque pulse. Note that during the first interrogation cycle only 26% of the total commanded float motion is achieved. This fact establishes a pulse bursting threshold defined by the Input Axis steady state rate that is 13% of the gyro full-on rate capability. Assume that at a particular sampling time that the float is just below the torquing threshold. No torquing pulses will be generated. At the next sampling period the float will be approximately 13% above the torquing threshold and a torquing pulse will be generated. The float sums the steady state input and the response to the torque pulse. If the steady state rate is slightly above 13%, a second torque pulse will also occur during the subsequent sampling period. Thus, two torque pulses have been generated in response to an input that warrants only one pulse. If the steady state rate is below 13%, pulse bursting will never occur.

2.4 Resolver to Digital Encoder

The resolver to digital encoder (RDE) converts the analog gimbal information into seventeen (17) bits of digital data. The RDE output is used as an attitude reference to compute system attitude errors. Seventeen bits are used to provide a 10 arc second accuracy with a tracking capability up to one radian per second. The RDE

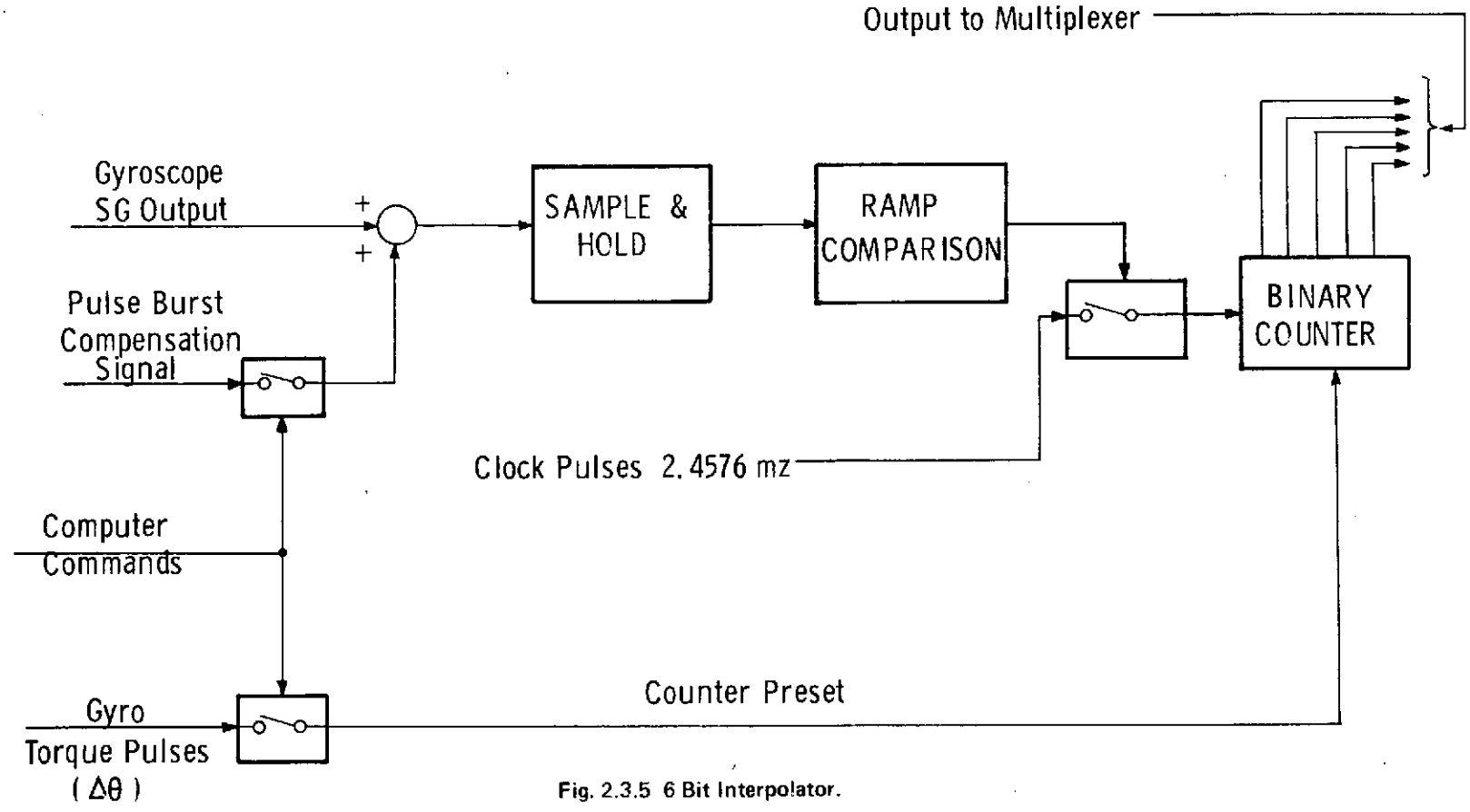

Fig. 2.3.5 6 Bit Interpolator.

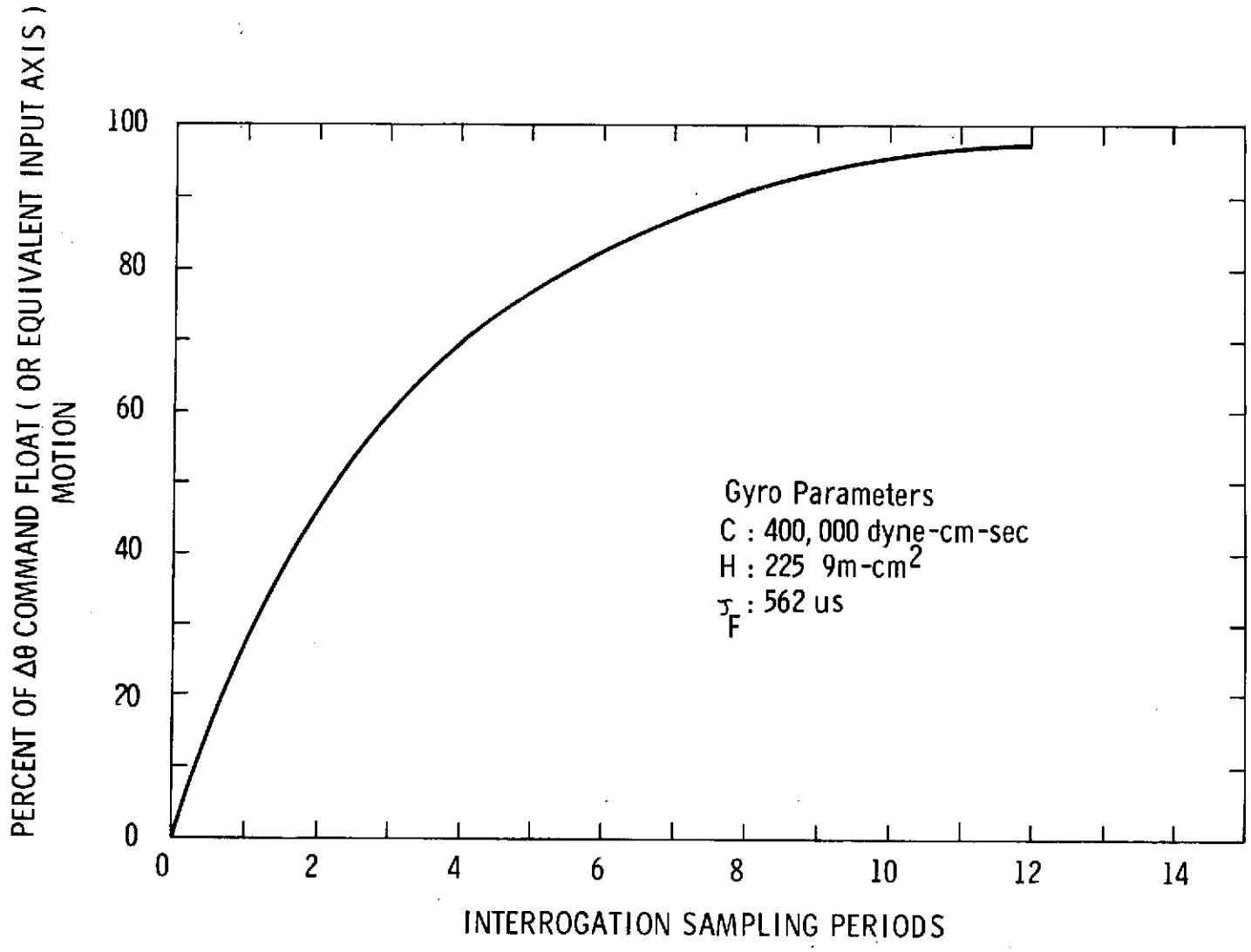

Fig. 2.3.6 Float Response to a 80% Duty Cycle Torque Pulse.

design is based on the Apollo Coupling Data Unit (CDU) angle encoding concept ($\sin(\theta-\psi)$). However, a sample and hold technique with higher bandwidth switching was used to achieve linear 60°/sec tracking without two speed switching as in the Apollo CDU. Field effect transistors (FET) replaced capacitor coupled transistor switches and monolithic operational amplifiers replaced discrete components. Both of these design changes increased the encoder's bandwidth.

Figure 2.4.1 is the functional diagram of the RDE. The RDE is a servo type of analog-to-digital convertor that transforms resolver signals into digital data. Digital conversion is completed in two steps. First the coarse section of the RDE operates in a closed looped system to solve the equation:

$$\text{Sin}\ (\theta-\psi) = \text{Sin}\,\theta\cos\psi - \cos\theta\,\text{Sin}\,\psi$$

Where

θ = gimbal angle

ψ = incremental value of attenuation that is required to null the input signal. ψ is dependent on the activation of specific combinations of FET switches in series with gain adjusting resistors. The exact combination of FET switch activation is determined by the RDE output.

The seven most significant bits are used to null the coarse system loop. Hence, a coarse null is first achieved within 2.8° of the actual gimbal position. Once a coarse null is achieved, the fine system is activated to establish a null within 0.0035° of the gimbal position. This is the second step of digital conversion. After a fine system null is achieved, the output data is sampled and processed at the H316 computer.

2.5 COMPUTATIONAL FACILITY

2.5.1 Introduction

The SPOT computational facility comprises three separate, but interconnected computer facilities: 1) a Honeywell H316 mini-computer is used for direct interface and computational support of the strapdown test system, 2) a Honeywell DDP516 computer facility is used for software development and data storage, and 3) an IBM 360/75 computer facility for the sophisticated data processing, analysis, and plotting. Figure 2.5.1 shows the major components of the SPOT computation facility and their interconnection. This section discusses the H316 computer; its interface to the strapdown system and utilization in conjunction with the DDP516 facility.

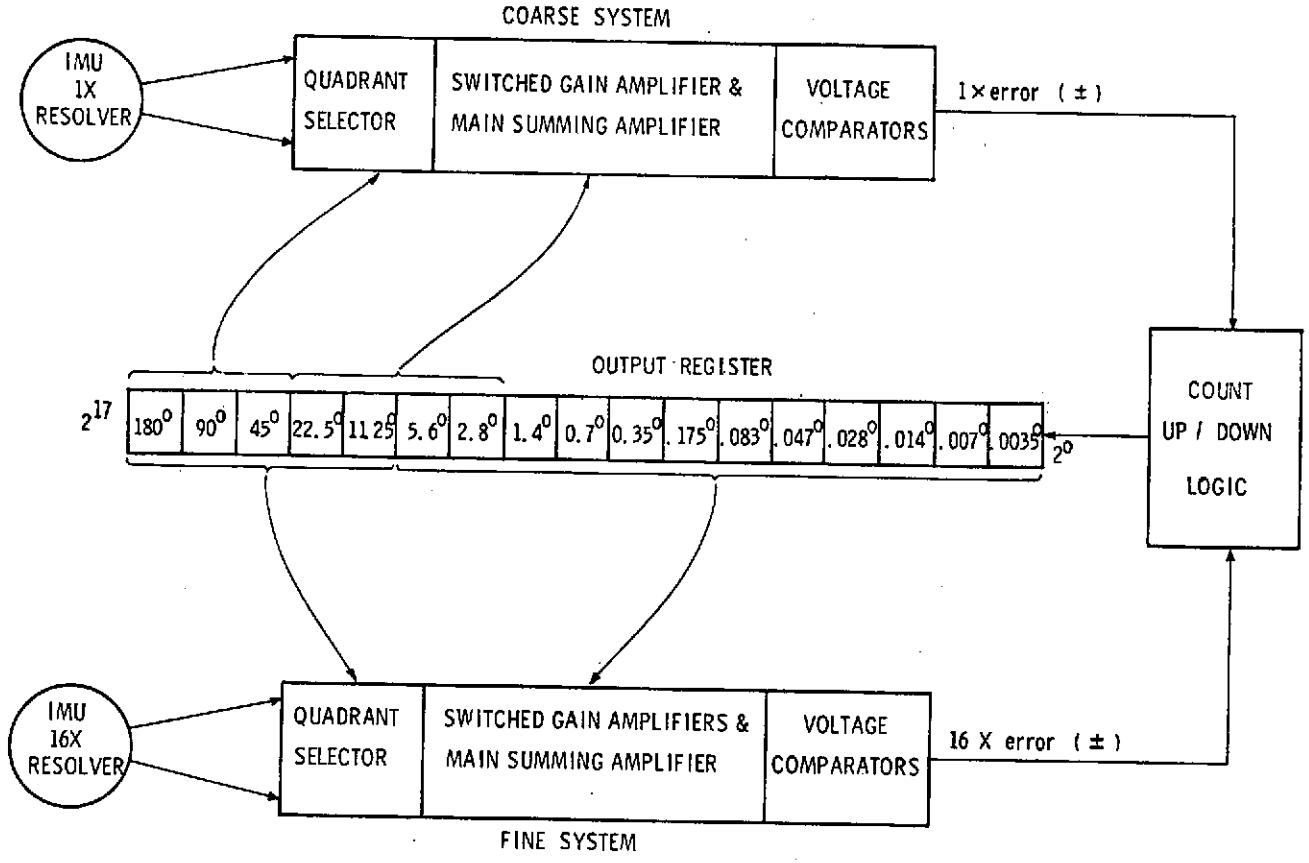

Fig. 2.4.1 Resolver to Digital Encoder.

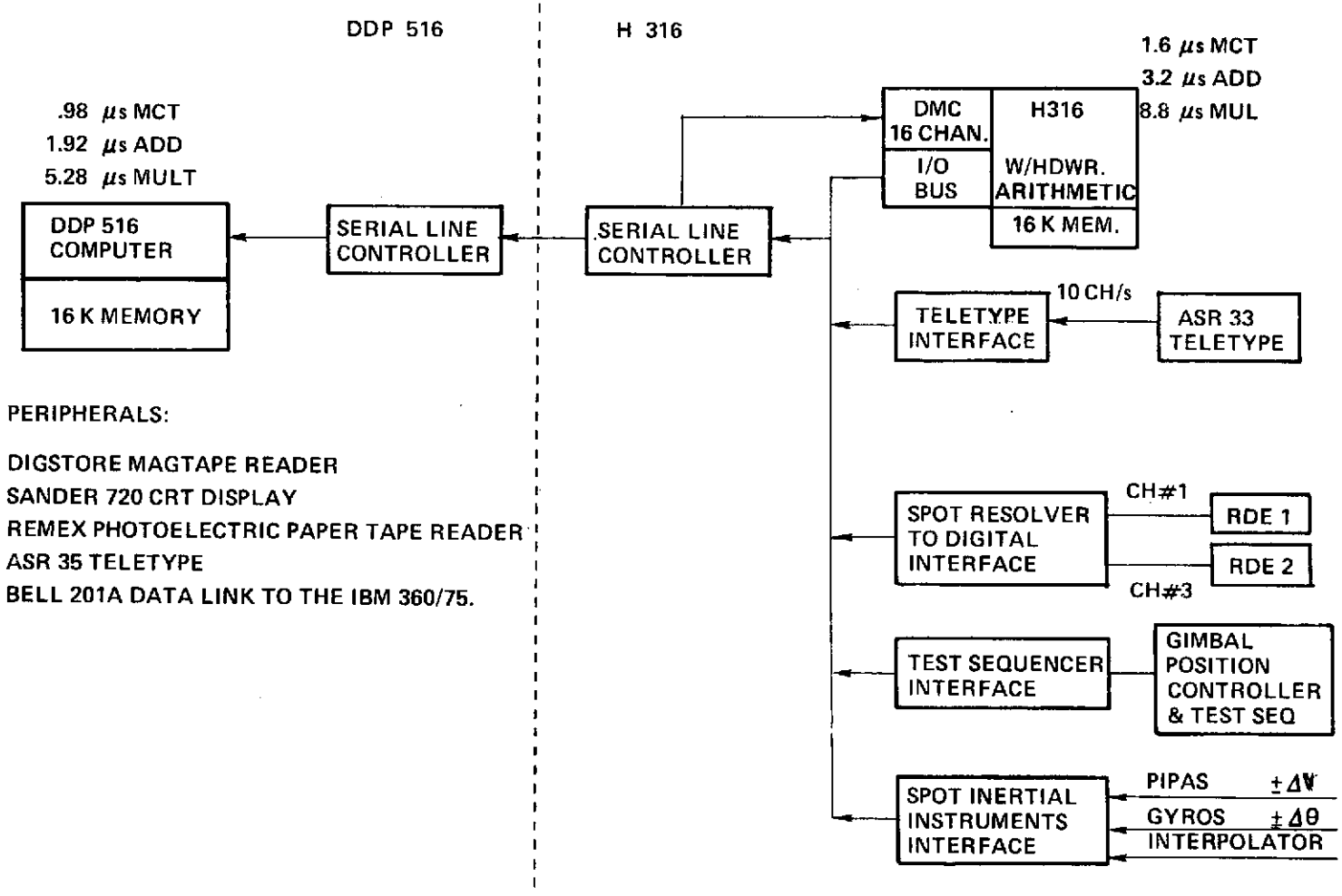

Fig. 2.5.1 Computational Facility.

The Honeywell H316 mini-computer is central to the SPOT test facility. It controls the automatic calibration programs which permit overnight instrument certification. Attitude and navigation algorithms enable the evaluation of the strapdown dynamic performance.

Although the H316 mini-computer is adequate with its memory cycle time of 1.6 μs and a 16K word memory for the development and execution of the SPOT programs, a serial link to the more powerful DDP516 facility was provided to facilitate software development and enable access to mass storage.

The DDP516 computer with its complement of peripheral equipment such as; disk storage, a CRT display, and a telephone data link, affords three distinct advantages to the SPOT facility:

1. The 7 million word disk memory provides sufficient storage for the full set of SPOT operating programs and test data. When an operational program is required at the H316, the selected program is transferred from the disk memory under program control through a serial data link between the computers.

   Test data is accumulated on the disk memory for later recall to perform parameter computation and analysis.

2. Efficient software development is possible at the DDP516 facility using the Sander's 720 CRT display, the mass storage, and a powerful set of editing and debugging software. Since the instruction sets of the two machines (316 and 516) are identical, it is advantageous to write and debug the full complement of SPOT software on the DDP516 facility.

3. A Bell 201A data set links the DDP516 to the IBM 360/75 which allows the transfer of formatted data to the 360/75 facility for computation, compilation, statistical analysis and plotting.

As illustrated in Figure 2.5.1, all of the peripheral equipment supporting the H316 mini-computer, including the serial data link, is connected by a single input-output (I/O) bus line. The sequence and control of the peripheral equipment is accomplished under program control with the combination of two methods: 1) Input/Output instructions, and 2) a single level interrupt system.

The Input/Output instruction is the language used to communicate with the peripheral equipment. The complete instruction repertoire is given in Appendix B.

The second method of program control is achieved by a single level of interrupt which allows any one of the pheripheral equipment to interrupt the computer's processor. With priority decisions, the single line is capable of handling multiple interrupts. It exercises this capability by interrogating devices (peripherals) one at a time under program control until it finds the source of the interrupt. This interrogation is generally done in order from the highest priority device to the lowest. Since interrupts can be inhibited by the processor while the higher priority device is serviced it is possible to share the single line among multiple device interfaces.

The hardware that interfaces the H316 mini-computer to the strapdown system and to the DDP516 computer was designed and implemented in five main sections; 1) the serial data link between the H316 and the DDP516, 2) the interface to the gyro and accelerometer pulse torque-to-balance loops, 3) the interface to the gyro SG interpolator, 4) the interface to the resolver-to-digital encoder, and 5) the interface necessary for computer controlled gimbal positioning. A discussion of these interface designs now follows.

2.5.2 Serial Data Link

The serial data link is a synchronous, hard wire data link between the H316 and the DDP516. The interface is identical, with minor modifications, to the Honeywell supplied synchronous line convertor. Characters are transferred to the data link interface from the computer I/O bus by bytes (8 bits each) in parallel where they are converted to a serial form and clocked out to a matching interface in the other computer. A series of synchronizing characters proceeds any transmission to identify the beginning of the information characters.

2.5.3 Pulse Torque Electronics Interface

The net total of gyro and accelerometer pulses are accumulated in six separate 8 bit up-down counters. The plus and minus $\Delta\theta$ or ΔV lines for each axis are separate but are combined as a single input to the up-down counter. The leading edge of the incoming pulse on either the plus or minus line determines the counting direction. The torque loops are mechanized such that pulses of both polarities will never occur simultaneously.

An "output control pulse" initiates the pulse accumulation through clearing and interface enabling functions. A preset timer register is enabled to count interrogation pulses and interrupt the computer in order to read accumulated torque

pulses when the register's count is full. With counter presets, the computer interrupt is generated at any integral number of interrogate pulses up to 255. Thus, the preset timer register is used to release the computer for other operations while the torque pulses are being accumulated.

2.5.4 Interpolator Interface

The six (6) bit interpolator quantizes the gyro signal generator (SG) output into 64 levels over a range of eight pulse torque thresholds. The interpolator-computer interface is a single set of six parallel lines. The input lines to the computer are buffered with a six (6) bit accumulator to isolate the transmission lines from the address bus. Data transfer is initiatized with a test instruction to determine that the interpolator is ready with valid information. An "output control" pulse then selects which of the three interpolator outputs (X, Y, or Z axis) is to transmit. The interpolator information is directly added to the accumulated gyro pulses. No clearing function is required because the interpolator is reset at every interrrogation cycle.

2.5.5 Resolver to Digital Encoder (RDE)

The 17 bit analog to digital converter quantizes the gimbal angular information into 10 arc seconds increments. The RDE-computer interface consists of two sets of 17 parallel lines with gating circuits at the computer to input data into the computer register. Data transfer is initiated with a test instruction to check for synchronism between the RDE interrogation signal and the 800 pps timing signal. This check establishes the beginning of the RDE conversion cycle. After waiting 5 interrogation cycles (1040 microseconds) to assure complete RDE analog to digital conversion, an input instruction is used to gate the RDE output into the computer's register. An inhibit line is also available to assure that data transfer is not accomplished before the analog-to-digital conversion is completed. Because the 17 bits exceeds the capacity of the computer's 16 bit accumulators, the data is read in two parts. The two low order bits are read first, followed by the 15 high order bits to form a double precision word. An RDE zero control pulse is available to electronically reset the RDE to a zero orientation and to force the completion of a conversion cycle.

2.5.6 Test Sequencer Interface

The test sequencer enables automatic gimbal system positioning for computer controlled inertial instrument calibration. The interface between the test sequencer

circuitry and the computer includes four groups of data lines: 1) six data lines are used to transmit gimbal positioning commands, 2) a control pulse line is used to sequence the inner, middle, and outer gimbal position commands over the same data lines, 3) a position ready pulse line is used to flag the computer when the desired test position has been achieved, 4) an end of test pulse line is used by the computer when data acquisition cycle is completed and a new sequence cycle is to begin. The end of test pulse clears all circuits to accept new information.

2.6 Support Electronics-Automatic Test Facility

The electronic equipment required to support, monitor, and excite the strapdown test system was integrated into the SPOT test facility to include the typical complement of dc and ac supplies and monitoring equipment, as well as a unique capability for computer controlled testing.

The ac supplies include the gyro wheel supply, the ducosyn suspension supply and the resolver excitation supply which were adapted from hardware used in prior programs. The monitoring equipment includes the oscilloscopes for gyro wheel current and SG output visual monitoring, inertial instrument temperature monitors with hot and cold alarms, and a seven channel strip chart recorder for continuous thermal surveillance.

An automatic test capability was developed to increase the utilization to the test facility and to enable the accumulation of calibration data for statistical and stability evaluations. The automatic test capability was implemented with a modified Apollo gimbal position control electronics assembly (GPC) and "test sequencer" electronics interface with the H316 computer. Figure 2.6.1 shows the one axis mechanization of the test sequencer electronics and its interface to the GPC, H316 computer, and gimbal system.

The "test sequencer" accepts incoming computer commands and converts them into activating signals to select one of two operating modes in the GPC: 1) a coarse mode, and 2) a fine mode. The "coarse mode" energizes the gimbal torque motors to rotate at a constant speed of 0.066 radian per second. This is the mode used to change the strapdown system orientation. As the gimbals are rotated, the resolver null positions are counted in a binary counter. When the counter reads the desired preset count, the GPC is switched to the "fine mode" to electronically lock the gimbal system to a resolver null position. Note that the amount of gimbal rotation is determined by counter presets that are selected prior to rotation. When all three gimbals are in the "fine mode" the desired test orientation has been achieved

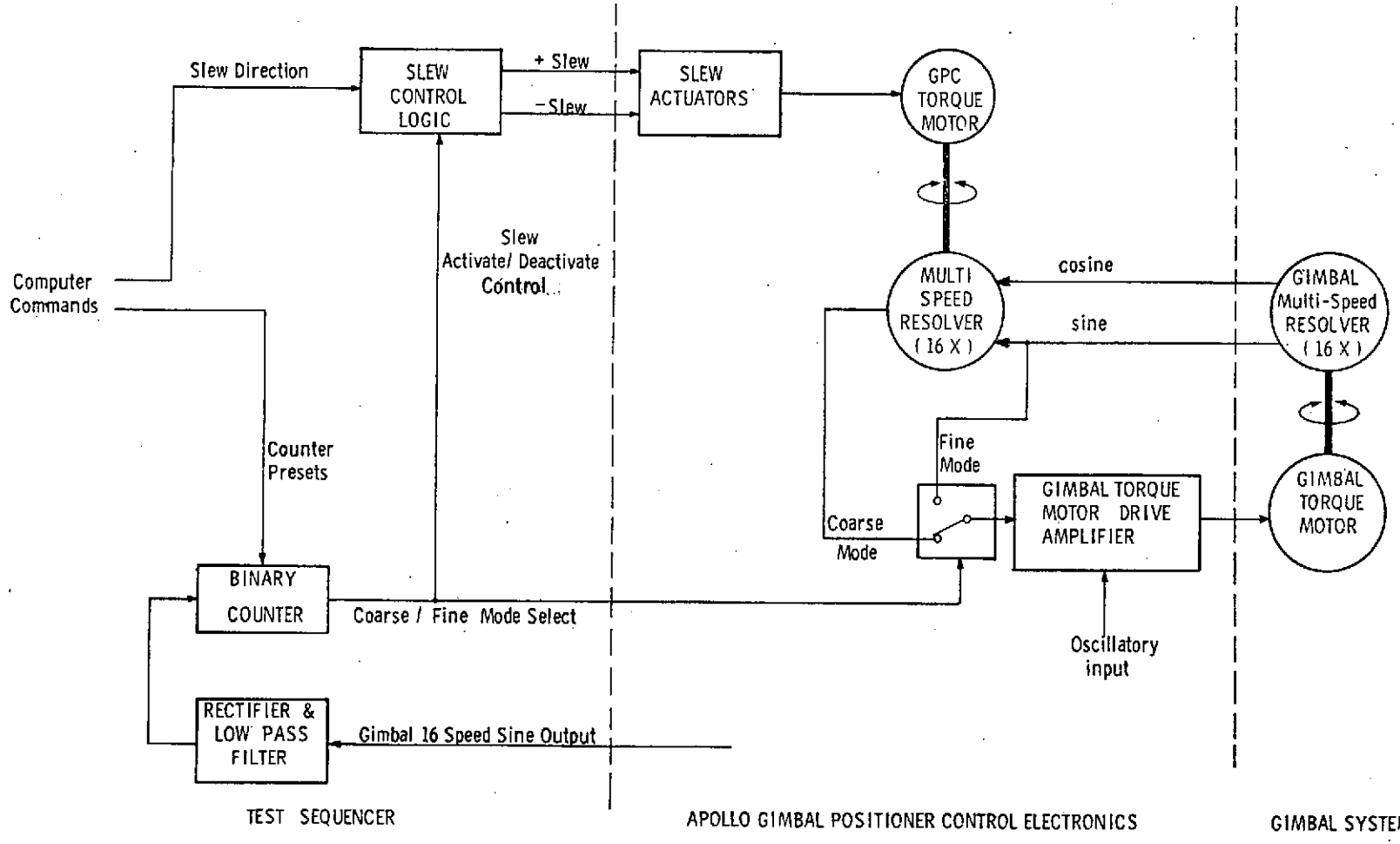

Fig. 2.6.1 Automatic Test Control.

and a command is transmitted to the computer to activate the data acquisition programs.

Automatic dynamic calibration is achieved with the outer gimbal programmed for continuous rotation and the inner and middle gimbals programmed for orientation changes. The outer gimbal rotation is accomplished by locking the last stage of the binary counter in the reset state. In the reset state, the gimbal position control loop is switched into the coarse mode and slewing is maintained at 0.066 radians per seconds.

Slewing speeds other than 0.066 radians per second are possible, but not in the automatic mode. A second torque motor with a multi-speed resolver is connected to the gimbal resolver. Controlled speeds up to one radian per second are available.

Gimbal oscillatory excitations are produced by driving the gimbal torque drive amplifier from a low frequency commercial oscillator. The gimbal position control loop is switched to the fine mode for oscillatory tests.

To prevent gyro wheel damage (high speed touch down) resulting from excessive gimbal rates, three rate protection schemes were incorporated to prevent gimbal runaway.

1) The primary rate protection scheme is the gimbal dump circuits that inhibit the torque motor drive electronics when the back emf (of the gimbal torque motors) exceeds a given threshold.
2) The secondary rate protection device is a frame mounted dual axis rate transducer (DART), a device that generates a voltage level equivalent to the vectorial sum of rates about two orthogonal axes. Electronic circuits deactivate the gimbal drive loops when the DART output exceeds a prescribed threshold level.
3) When the GPC is in the "fine mode", gimbal movement in excess of 3^{o} is prevented by inhibiting the drive electronics.

3.0 Inertial Instruments and Compensation Parameters

3.1 16 Permanent-Magnet-Pulsed-Integrating Pendulous Accelerometer (16PM PIP)

3.1.1 Physical Description

The 16 PM PIP is a single-degree-of-freedom integrating specific force receiver. Figure 3.1.1 is a mechanical line schematic and Table 3.1.1 presents a survey of operational and control parameters. The PIP consists of a cylindrical body (float) that is suspended within a cylindrical case by a dense, highly viscous fluid. The fluid also provides rotational motion damping. In addition to the fluid buoyant support, the float is supported and centered radially and axially by a microsyn (variable reluctance transducer) at each end of the case.

The float has freedom of rotation about its longitudinal axis (Output Axis) and the float mass that is offset from the Output Axis provides specific force sensitivity along an Input Axis. Thus, specific force inputs rotate the float. The float rotation is sensed by the signal generator (SG), a linear angle-to-voltage generator located at one end of the instrument case. When the SG output voltage reaches a given threshold value, a discriminator detects the polarity of the SG signal and generates a torque command that switches a controlled current pulse of fixed amplitude and duration into the torque generator winding. The torque generator (TG) is a linear current-torque transducer, located at the opposite end of the case. The polarity of torquing is set to oppose the sensed input torque.

3.1.2 Principle of Operation

The float acts as a torque-summing member and the torques acting on the float (neglecting uncertainty torques) can be expressed as:

$$I_{OA}\frac{d^2\theta}{dt} + C\frac{d\theta}{dt} + ml\,a_{in} \pm M_{(tg)} = 0 \qquad (3.1.1)$$

$I_{OA}\frac{d^2\theta}{dt}$ = the torque due to inertia of the float

I_{OA} = moment of inertia of the float about OA

θ = angle of rotation of the float about OA

$C\ \frac{d\theta}{dt}$ = the viscous damping torque about OA

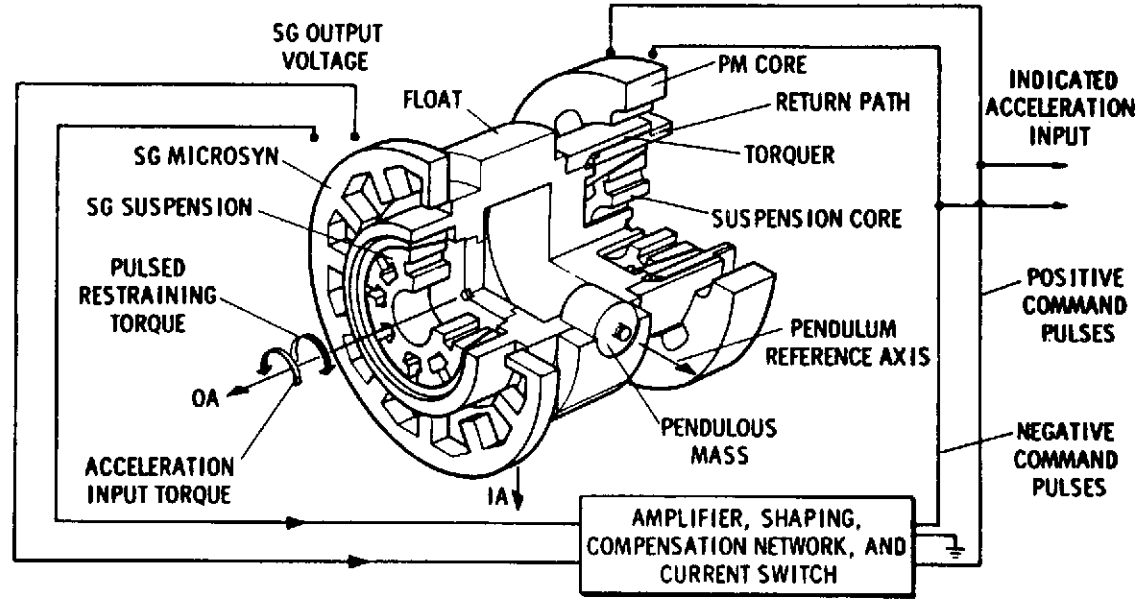

Fig. 3.1.1 Line Schematic of the 16 PM PIP.

TABLE 3.1.1

16 PM PIP PARAMETER SURVEY

	Nominal Value	Symbol
Pendulosity	1 gm-cm	ml(p)
Output Axis Moment of Inertia	24 gm-cm/sec^2	I_{OA}
Damping Coefficient	14×10^4 dyn-cm/rad-sec	C
Float Time Constant	170 μsec	t_f
Pendulous Ref. Axis Moment of Inertia	35 $\frac{\text{gm-cm}}{\text{sec}^2}$	I_{pra}
Anisoinertia Coefficient	1 $\frac{\text{cm/sec}^2}{\text{radian/sec}^2}$	$\frac{I_{IA}-I_{pra}}{ml}$
Torquer Sensitivity	265 $\frac{\text{dyne-cm}}{\text{ma}}$	S_{TG}
Torquer Time Constant	27 μsec	t
Torquer Temp. Sensitivity	<10 ppm/$^\circ$C	
Signal Generator Sensitivity	20 mv/mr	S_{SG}
Suspension Reaction Torque	< 0.2 dyne-cm	
Elastic Restraint	< 0.01 dyne-cm/mr	
Operating Temperature	130°F	
Excitation SG & Suspension	4V, 9600-cps, 100 milliamps/ end housing	

C	=	damping coefficient
mla_{in}	=	input acceleration torque
ml	=	pendulosity of float
a_{in}	=	component of acceleration input along IA
$M_{(tg)}$	=	restraining torque provided by the torque generator for a fixed current amplitude

Integrating:

$$I_{OA} \frac{d\theta}{dt} + C\theta = ml\,\Delta V_{in} + \int_o^t \pm M_{(tg)}\,dt \qquad (3.1.2)$$

where ΔV_{in} = change in velocity along IA.

The terms on the left-hand side of equation (3.1.2) represent the dynamic storage of the instrument. These terms can be assumed constant in a steady state input condition because the control-loop maintains the float at the null position. Thus, the torquer output (M_{tg}) balances the specific-force input in steady state conditions and the indicated change in velocity is expressed as:

$$\Delta V_{in} = \frac{1}{ml} \int_o^t \pm M_{tg}\,dt \qquad (3.1.3)$$

M_{tg} is a time invariant torque pulse. When sized by the pendulosity of the float (ml) each torque represents an increment of velocity (ΔV) measurement where ΔV is the scale factor of the instrument. The indicated velocity input (V_{IND}) is determined by accumulating the positive (N^+) and negative (N^-) torque pulses for a given test period (t_t) and multiplying the result by the scale factor (ΔV).

Thus

$$V_{IND} = \Delta V \sum_{n=1}^{t_t/t_c} (N^+_{(n)} - N^-_{(n)}) \qquad (3.1.4)$$

where

$$\Delta V = \frac{M_{tg} t_s}{ml}$$; t_s is the torque pulse duration

t_c is the period of the interrogation cycle

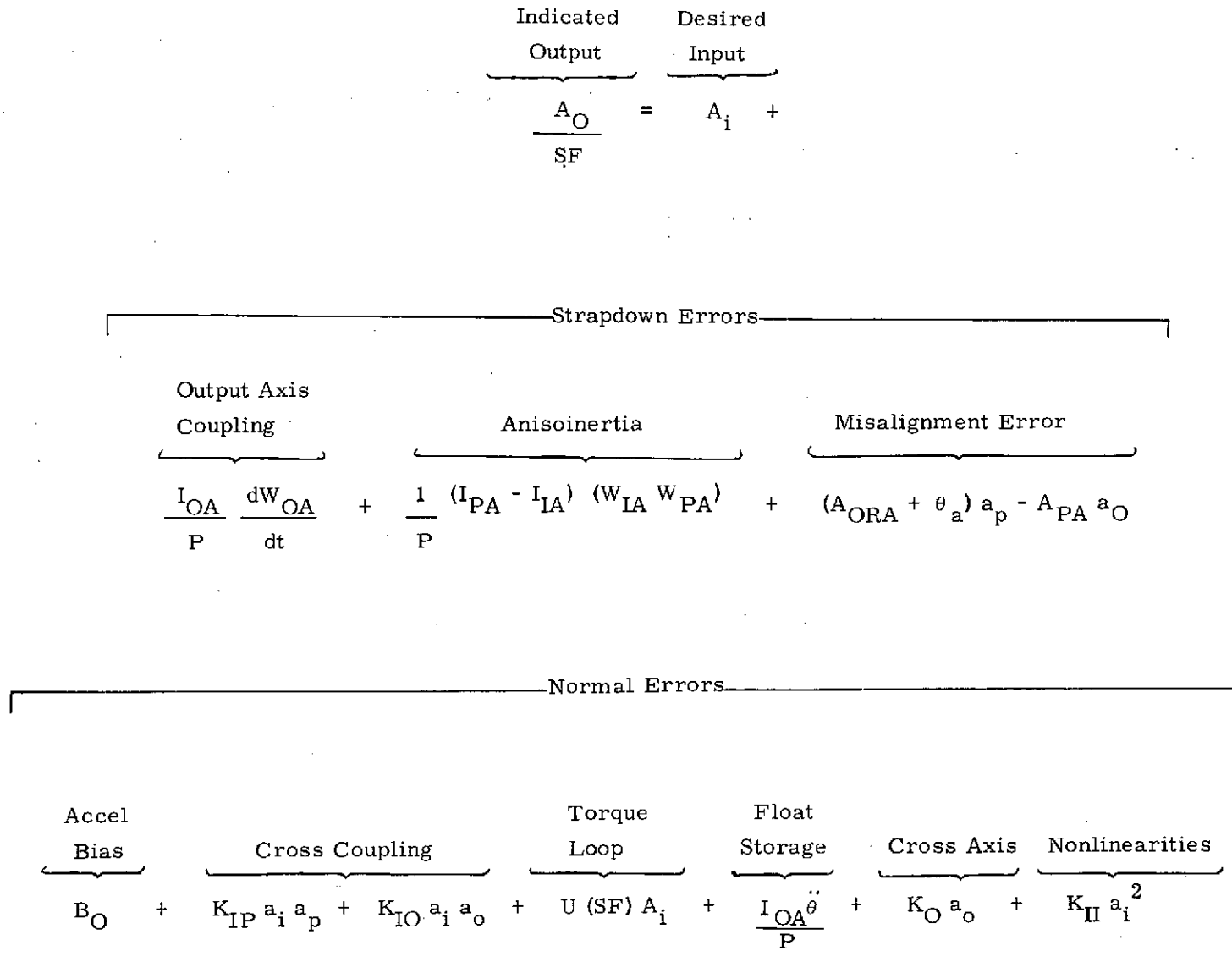

FIGURE 3.1.2 ACCELEROMETER DYNAMIC MODEL

The indicated velocity is the time integral of the average indicated accelerometer over the update interval. This quantity includes the acceleration sensed along the Input Axis and the addition of various error sources characteristic of the accelerometer. The full accelerometer model describing the response of a pulsed integrating pendulous accelerometer in dynamic environments is given in Figure 3.1.2 with the various error parameters described in Appendix C. Errors such as sculling which are generated in linear vibration environments, are not included because the gimbal test bed environmental inputs are restricted to oscillatory and angular rotations.

3.1.3 Accelerometer Model

Table 3.1.2 lists and estimates the magnitudes of the first order, second order and dynamic accelerometer error terms.

Although the first order error terms (bias and misalignment angles) have a limited effect on attitude errors, their effect on navigation performance is significant. Therefore, the first order terms are included in the calibration and compensation models.

The second order error terms have a negligible effect on attitude and navigation performance. These terms are evaluated using least square and fourier modeling techniques with multi-position accelerometer data inputs (See Section 5.4).

The dynamic terms, if excited with the environments defined, have a significance that is equivalent to the first order terms. These dynamic terms were not modeled because with the original gyro pulse torque scaling, the testing environment was reduced by a factor of four and the error magnitudes were negligible. The application of higher dynamic environments merit evaluation of dynamic accelerometer modeling techniques.

3.2 18 Integrating Inertial Gyro Mod B (18 Mod B)

3.2.1 Physical Description

The 18 IRIG Mod B gyro is a single-degree-of-freedom gyroscope that was developed at the MIT CS Draper Laboratory. The basic features of the 18 IRIG Mod B gyro are its reduced size, gas bearing wheel package and permanent magnet torquer. The 18 IRIG Mod B design is specifically designed for strapdown environment applications. The torquer, for example, is compatible with input rates up to one radian per second. Similarly, the magnetic suspension design is capable of withstanding radial side loading for rates in excess of one radian per second.

TABLE 3.1.2 ACCELEROMETER ERROR PARAMETERS

ERROR PARAMETER	INFORMATION SOURCE	ERROR MAGNITUDE	EQUIVALENT SYSTEM ERROR
First Order Error Sources			
Bias (B_o)	Accelerometer Calibration Data	0.3 cm/sec^2	A 0.3 cm/sec^2 bias error affects the gyro compensation of acceleration sensitive drift components (0.003 meru for a 10 meru/g gyro or 300 ppm). 0.3 cm/sec^2 is also 300 ppm of one g.
Misalignment Angles (A_{ORA}, A_{PA})	Accelerometer Calibration Data	0.25 mr	A 0.25 mr accelerometer misalignment miscompensates a 10 meru/g gyro and results in a 0.06 meru error (6000 ppm)
Second Order Error Sources			
Scale Factor Non-Linearity (K_{II})	Centrifuge Test Data	4 ug/g^2	At one g the error is 4 ppm of g
Cross Coupling (K_{IP}, K_{IO})	Multi-Position Accelerometer Test Evaluation (Fourier and Least Square Analyses)	30 ug/g^2	30 ppm of one g
Cross Axis (K_O)	Estimated from suspension stiffness and accelerometer geometry	1 ug/g	1 ppm of one g
Dynamic Error Sources			
OA Coupling	Calculated for: a) 0 to 1 radian angular acceleration	a) 20 cm/sec per rad/sec, however self cancelling during de-acceleration	Assuming that the acceleration from 0 to 1 radian/second is accomplished in 5 seconds, the indicated acceleration error is 4 cm/sec^2 or 4000 ppm of one g
	b) $\hat{W}$ = 0.3 rad/sec is the maximum gimbal oscillatory velocity	b) float motion is below pulse torquing threshold	0
Anisoinertia	Calculated for $W_{IA} = W_{PA} = 1$ rad/sec $I_{PA} - I_{IA} = 1$ gm=cm^2	1 cm/sec^2	1000 ppm of one g

The 18 IRIG Mod B gyro (Figure 3.2.1) has a gas-bearing wheel that rotates at 24,000 rpm and develops an angular momentum of 150,000 gram-centimeters^2/second. The wheel is driven by a 4 pole, 800 hertz, 2 phase synchronous hystersis motor. The wheel bearing consists of a stabilized journal pressurized by outboard thrust plates. The wheel and motor structures are mounted in a hermetically sealed cylindrical float and is pressurized with one atmosphere of neon gas. The float is surrounded by a high density damping fluid for fluid buoyant support and rotational motion damping. In addition to the fluid buoyant support, a 8 pole magnetic microsyn suspension is available at both ends of the case for support and centering of the float within the gyro case.

At one end of the case is a signal generator (a 12 pole multiple-E-connected microsyn) whose output magnitude is proportional to the angular position of the float about the Output Axis. At the other end of the case is the permanent-magnet torque generator consisting of an Alinico V permanent magnet with 8 poles, an armco iron return path and 8 torquing coils each having 144 turns.

Table 3.2.1 presents a survey of operational and control parameters for the 18 IRIG Mod B gyro.

3.2.2 Principles of Operation

The equation of motion for an ideal single-degree-of-freedom gyro is given by

$$I_{OA}\,\ddot{A}_{OA} + C\,\dot{A}_{OA} + KA_{OA} = H\,W_{IA} + M_{tg} + U_T \qquad (3.2.1)$$

where

- I_{OA} = moment of inertia of the float about its output axis (gm-cm^2)
- A_{OA} = float-to-case angle about the output axis (rad)
- C = float damping coefficient about output axis (dyne-cm/rad/sec)
- K = elastic spring constant about the output axis (dyne-cm/rad)
- H = wheel angular momentum (gm-cm^2/sec)
- W_{IA} = angular rate of the case about the input axis (rad/sec)
- M_{tg} = commanded torque of the torque generator (dyne-cm)
- U_T = uncertainty torque acting on the gyro float about the output axis (dyne-cm)

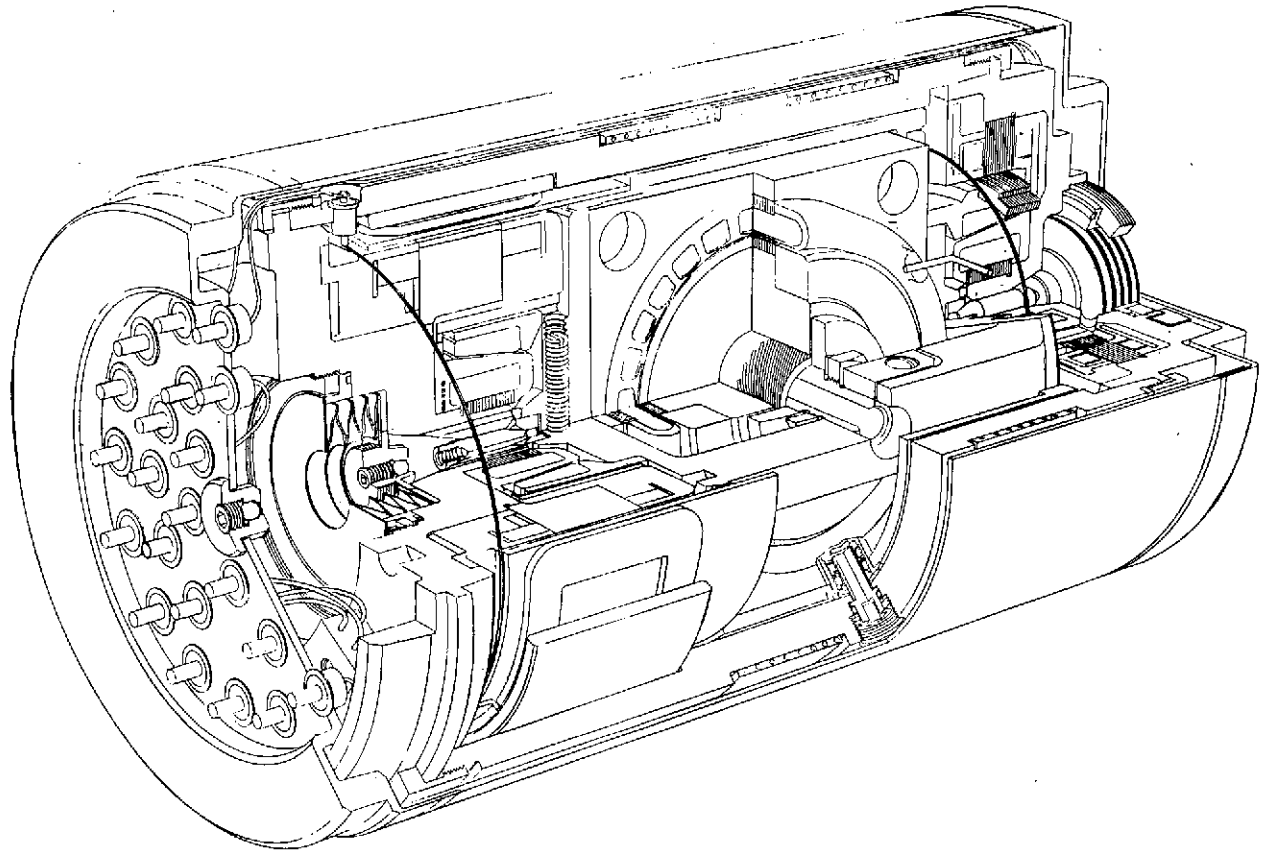

FIGURE 3. 2. 1 18 IRIG MOD B CUTAWAY VIEW

TABLE 3.2.1

18 IRIG MOD B NOMINAL PARAMETERS

AND OPERATIONAL FEATURES

Gyro Constants	Units		Symbol
Angular Momentum	0.151×10^6	$\frac{gm\text{-}cm^2}{sec}$	H
Output Axis Damping Coefficient	~400,000*	dyne-cm-sec	C_{OA}
Output Axis Inertia	225	$gm\text{-}cm^2$	I_{OA}
Float Time Constant	~550*	μsec	$t_f = \frac{I_{OA}}{C_{OA}}$
Transfer Function	7.6*	$\frac{millivolts}{milliradian}$	$(\frac{H}{C_{OA}} S_{SG})$
Torquer Time Constant	55	μsec	$t_{tg} = \frac{L}{R}$
Anisoinertia Coefficient	1×10^{-4}	$rad/(rad/sec)^2$	$\frac{I_{SA} - I_{IA}}{H}$

* Parameters given are for a 140°F floatation temperature. At the nominal floatation temperature (130°F), C_{OA} = 502,000 dyme-cm-sec, t_f = 450 μsec, and the transfer function = 6.

For the condition of no torque commands ($M_{tg} = 0$), a constant-input rate will cause a constant torque about the gyro-float Output Axis. The resultant Output Axis float rotation corresponding to the torque is expressed as:

$$A_{OA} = \frac{H}{C} \int W_{IA}\, dt \qquad (3.2.2)$$

Since the float output angle, A_{OA}, is proportional to the integral of input angular rate, W_{IA}, the gyro is called an integrating gyro. When the gyro is being pulse-torqued, the scale factor is defined as the angular motion about the gyro Input Axis that yields the same Output Axis rotation as one torque pulse.

The scale factor is expressed in Equation 3.2.3, under steady state conditions ($M_{tg} = HW_{IA}$) where M_{tg} is a time invariant torquing level and t_s is the duration of torquing.

$$SF = \frac{M_{tg}\, t_s}{H} \qquad (3.2.3)$$

The scale factor is used to determine the input axis angular displacement (A_{IA}) by scaling the accumulated positive (N^+) and negative (N^-) torque pulses.

$$A_{IA} = \frac{t_s}{H} \sum_{n=1}^{t_t/t_c} \left(M_{tg}^{+} \; N^{+}(n) - M_{tg}^{-} \; N^{-}(n) \right) \qquad (3.2.4)$$

where M_{tg}^{+} - commanded torque (dyne-cm) for positive torque pulses
M_{tg}^{-} - commanded torque (dyne-cm) for negative torque pulses
t_c - interrogation period (208 microseconds)
t_t - test period

3.2.3 Gyro Model

The full gyro model describing the response of a pulsed integrating gyro in dynamic environments is given in Figure 3.2.2 with the normal errors (gyro drift) described in Appendix D.

The strapdown error sources are further discussed in this chapter and are excited when the gyro operates in dynamic environments. One group of the dynamic error sources is geometrical in nature such as coning and would be observed even in an ideal gyro instrument. Coning errors are inherently compensated in the system attitude algorithm based on knowledge of the dynamic inputs. Coning is discussed in greater detail in Section 4.2.5.

$$\underbrace{\text{Output Axis Float Dynamic Torques}}_{I_{OA}\ddot{A}_{OA} + C_{OA}\dot{A}_{OA}} = \underbrace{\text{Desired Torque}}_{H_S W_{IRA}} +$$

Normal Errors

$$\underbrace{\text{Torques due to acceleration squared sensitivity}}_{(K_{SS} - K_{II})\ a_{SRA}\ a_{IRA}} + \underbrace{\text{Torques due to acceleration sensitivities}}_{(ADIA)\ a_{IRA} + (ADSRA)\ a_{SRA} + (ADOA)\ a_{ORA}} + \underbrace{\text{Acceleration insensitive Torques}}_{NBD}$$

Strap Down Errors

$$\underbrace{\text{Commanded Torque}}_{SF \times I_{TG}} - \underbrace{\text{Output Axis Coupling Torque}}_{I_{OA} W_{ORA}} - \underbrace{\text{Cross-coupling Torque}}_{H_s W_{SRA} A_{OA}} + \underbrace{\text{Anisoinertia Torque}}_{(I_{SA} - I_{IA})\ W_{IRA} W_{SRA}} + \underbrace{\text{SF linearity Coefficient}}_{K_2\ W_{IRA}} - \underbrace{\text{Misalignment}}_{\nu_{OA} W_{SRA} + \nu_{SRA} W_{ORA}}$$

FIGURE 3.2.2 GYRO DYNAMIC MODEL

The second group of strapdown errors result from the physical gyro or torque loop departing in performance from the ideal instrument. These error sources include: anisoinertia, scale factor linearity, SRA cross coupling and OA coupling. If properly calibrated, the dynamic error sources are adequately compensated in the algorithms. (See Section 4.2.2). The instrument dynamic errors are discussed below with a concluding section devoted to gyro attitude storage and attitude quantization.

3.2.3a Anisoinertia

The anisoinertia error term arises from the difference in the inertia about the float Spin and Input Axes. The applicable gyro response equation is:

$$I_{OA}\,\ddot{A}_{OA} + C_{OA}\,\dot{A}_{OA} = (I_{SA} - I_{IA})\,W_{IRA}\,W_{SRA} \qquad (3.2.5)$$

Only simultaneous inputs about the Input Reference Axis (IRA) and the Spin Reference Axis (SRA) can exercise the anisoinertia error. For constant rotational rates applied simultaneously about the IRA and SRA (W_I and W_S respectively), starting at t=0, the steady state drift rate (W_D) is found to be:

$$W_D = \left(\frac{(I_{SA}(f) - I_{IA})}{H}\right) W_I\,W_S$$

$I_{SA}(f)$ = Float inertia about the Spin Axis (a frequency dependent function) (3.2.6)

I_{IA} = Float inertia about the Input Axis

The multi-axes oscillatory environment is defined by two excitations that have the same frequency, but different amplitudes and have some relative phase (ϕ).

$$A_{SRA} = a\sin\omega t \qquad W_{SRA} = a\omega\cos\omega t$$
$$A_{IRA} = c\sin(\omega t+\phi) \qquad W_{IRA} = c\omega\cos(\omega t+\phi) \qquad (3.2.7)$$

The steady state drift rate in an oscillatory environment is determined to be:[5]

$$W_D = \left(\frac{I_{SA}(f) - I_{IA}}{2H}\right) a\,c\omega^2 \underbrace{(\cos(2\omega t+\phi+\psi)}_{\text{sinusoid}} + \underbrace{\cos\phi)}_{\substack{\text{non-zero}\\ \text{time average}}} \qquad (3.2.8)$$

where $\psi = \tan^{-1}(2\pi\tau)$ and $(\tau\omega^2) << 1$

The steady state drift rate comprises a sinusoidal component with twice the input frequency and a constant, non-zero time average component expressed as:

$$W_D = \left(\frac{I_{SA}(f) - I_{IA}}{2H} \right) \; a\, c\omega^2 \; \cos\phi \qquad (3.2.9)$$

Hence, a kinematic rectification of the oscillatory input occurs and the resultant error is dependent on the relative phase between the two inputs and is maximum at an in phase condition (ϕ = "0").

The inertia of the float spin axis is expressed as a function of frequency ($I_{SA}(f)$) to account for the decoupling of the wheel element from the input excitation when the oscillatory input exceeds the wheel hunt frequency. The wheel hunt frequency (generally in the range 2 to 5 hertz) is defined by the natural frequency of oscillation which is determined by the inertia of the wheel element and the stiffness of the wheel motor. As the input frequency increases through the wheel hunt region the inertia difference ($I_{SA}(f) - I_{IA}$) is estimated to change from 21 gm-cm^2 at low frequencies to -40 gm-cm^2 above wheel hunt for the 18 IRIG Mod B gyro design. In the current program, only the low frequency anisoinertia coefficient is modeled in the compensation algorithm. The incorporation of a frequency dependent coefficient requires the spectral analysis of the environment from the gyro pulse outputs, a task beyond the scope of the current program but worthy of future investigations if environments above the wheel hunt frequency are anticipated. Based on Saturn V and XB-70 flight data, [5] the random angular environment associated with a shuttle vehicle at a navigation base is essentially limited to below 1 hertz. Therefore meaningful errors associated with changes in inertia with frequency is not expected to be encountered for that environment.

The effective anisoinertia error generated in the gimbal system for various test inputs is illustrated in Table 3.2.2.

TABLE 3.2.2 ANISOINERTIA ERROR MAGNITUDES

frequency (hertz)	$\frac{I_{SA}(f)-I_{IA}}{H}$ (μradian per radian/second)	a (radian)	c (radian)	Drift Error (meru)	Drift Error (^{o}/hr)
.5	140	0.024	0.022	5	0.08
1	140	0.024	0.022	20	0.3
5	-267	0.0057	0.011	-113	-1.7
10	-267	0.0015	0.004	- 43	-0.65
25	-267	0.0002	0.0006	- 5	-0.08

3.2.3b Scale Factor Linearity

Characteristic of permanent magnetic torquer gyros is the torquing response variation with respect to rate. Intensive tests conducted in other programs [7] have verified the rate dependent variation and have attempted to analyze its sources. Part of the variation is attributed to the torquer itself and part to the torquing loop mechanization. All loop mechanizations tested (ternary, binary, and analog) have exhibited a rate dependent scale factor.

The scale factor linearity calibration curves for gyros 427A, 422B, are shown in Figures 3.2.3 and 3.2.4. The ordinate scale is plotted relative to the scale factor magnitude calibrated at +0.066 radians per second about the Input Axis. The linearity curves are the best fit lines drawn between data from two sequential calibrations. In general, the scale factor spread between test runs is 10 ppm. The difference in the average scale factor for a positive rate about the gyro Input Axis (IA) from the negative rate about IA is the result of a pulse torque-to-balance loop unbalance and/or an instrument SG to TG misalignment. The 427A and 422B gyro linearity functions (Figures 3.2.3 and 3.2.4) are characteristic of resistively tuned gyro torquer coils. At high rates, the curve is concave upward because of two factors: 1) a TG-SG misalignment, and 2) power effects due to torquer heating.

Figure 3.2.5 shows the scale factor linearity curve for gyro MB4. Note that the scale factor spread over the full dynamic range is less than gyros 427A and 422B, but its variation is not linear. The MB 4 gyro linearity curve is typical when torquer coils are purposely mistuned to reduce the linearity spread but with the cost of achieving a non-linearity scale factor function. The test data given in Section 5.2.6 demonstrates that a gyro linear scale factor function (as displayed in Figures 3.2.3 and 3.2.4) can be adequately compensated (within 7 ppm) in the real time data processing algorithms and therefore torquer mistuning techniques are not necessary.

3.2.3c SRA Cross Coupling Errors

SRA cross coupling errors result from the Input Axis being offset from its reference direction because of float rotations about the Output Axis (OA). If rotational rates are applied simultaneously about the Input and Spin Reference Axes (SRA), errors will result by the amount of rate detected by the gyro Input Axis along the SRA. In oscillatory environments the float rotation about the OA is a sinusoidal function. Hence, if the oscillatory excitations about the Input and Spin Reference Axes are in phase then kinematic rectification will occur and a steady state drift error will result.

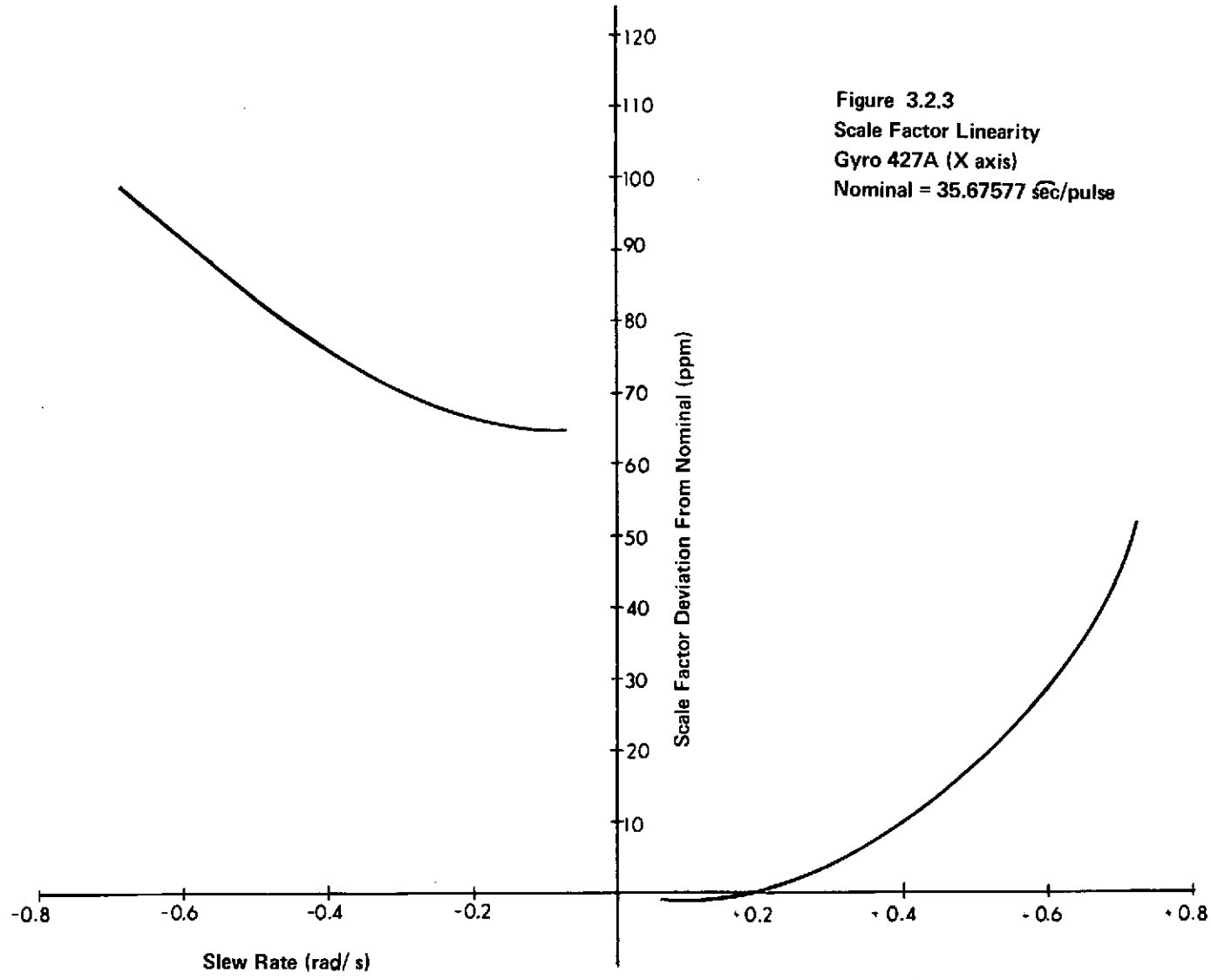

Figure 3.2.3
Scale Factor Linearity
Gyro 427A (X axis)
Nominal = 35.67577 sec/pulse

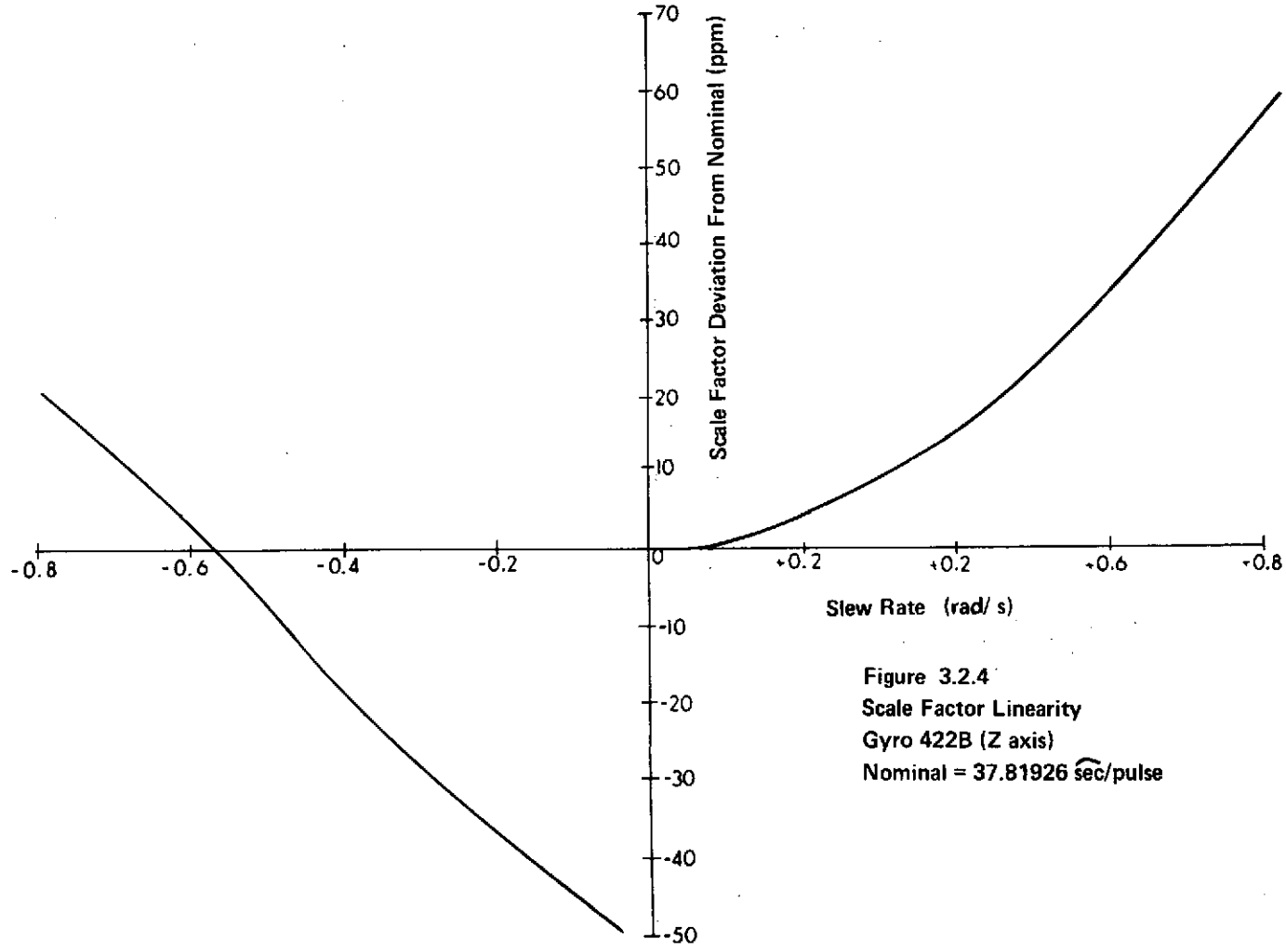

Figure 3.2.4
Scale Factor Linearity
Gyro 422B (Z axis)
Nominal = 37.81926 $\widehat{\text{sec}}$/pulse

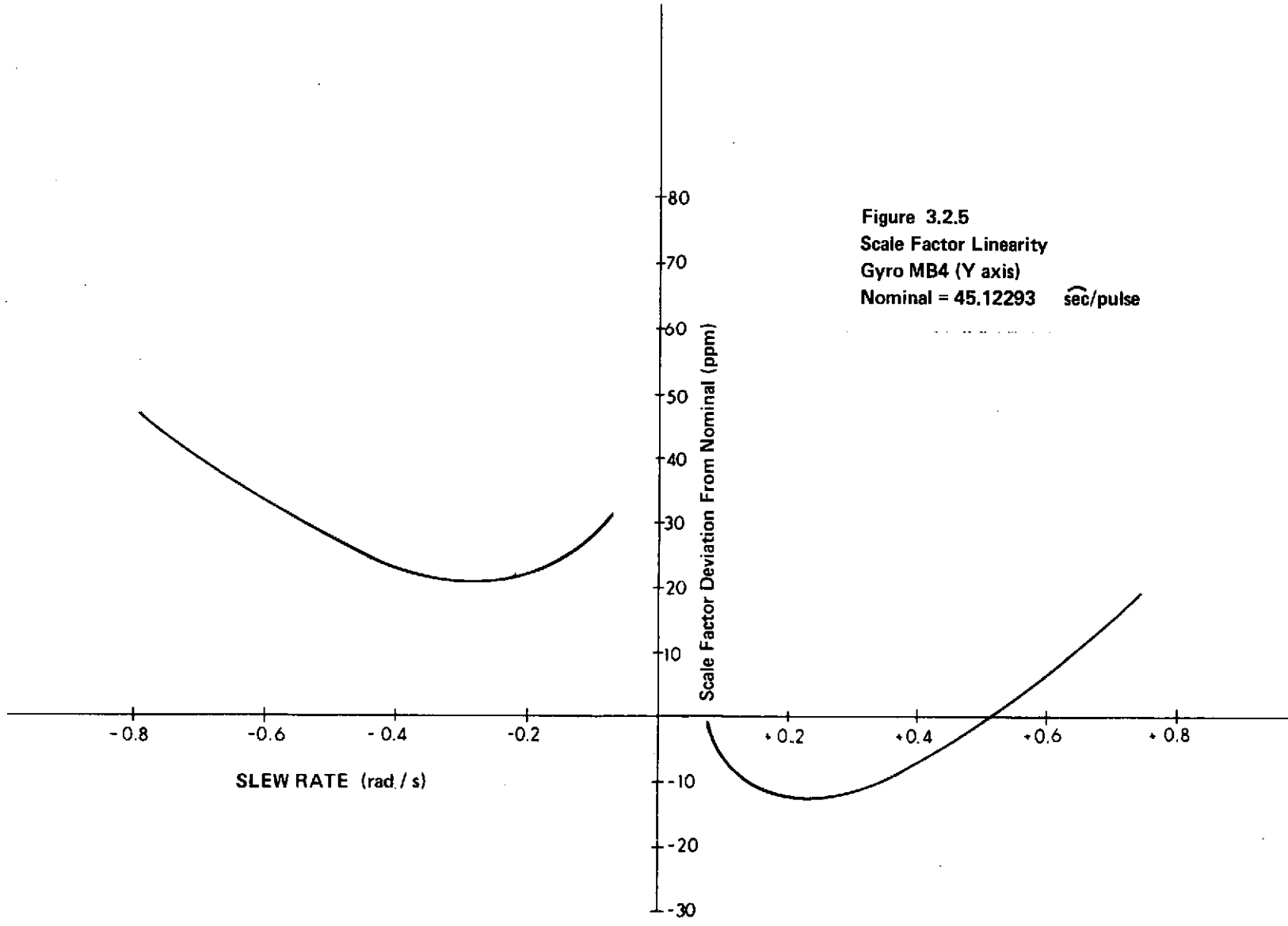

Figure 3.2.5
Scale Factor Linearity
Gyro MB4 (Y axis)
Nominal = 45.12293 $\widehat{\text{sec}}$/pulse

Compensation of SRA cross coupling errors depends on the accurate description of the float rotation by a function describing the average float hangoff in response to input axis rates. After the hangoff function has been defined, the amount of cross axis error can be estimated and the appropriate corrections made.

An analytical study by Lory [8] has defined the linear relationship between the average float rotational offset (float hangoff) and the average Input Axis rate. For the ternary-torque loop with pulse burst compensation, the relationship is expressed as:

$$\langle\theta\rangle = \overbrace{(d - 1/2)\ \mathrm{sgn}\,(v)}^{\text{low rate offset}} + \overbrace{v\,(1 + \textstyle\sum \tau_K)}^{\text{rate dependent factor}} \qquad (3.2.10)$$

where:

$\langle\theta\rangle$	is the average float rotational offset
v	is the average input angular rate sized to the full-on gyro loop rate capabilities
$\sum\tau_K$	is the sum of the gyro time constants (torquer and float) sized to the interrogation period
d	is the torquing threshold defined by the float rotation from null required to generate a torque pulse
sgn(v)	+1 for v positive 0 for v zero -1 for v negative

The assumptions of the above model includes a constant input angular rate and that the pulse burst compensation network gain is set to equal the sum of the gyro time constants.

Without pulse burst compensation, the float hangoff function is expressed as:

$$\langle\theta\rangle = \underbrace{(d-1/2)\ \mathrm{sgn}\,(v)}_{\text{low rate offset}} + \underbrace{v}_{\text{rate dependent factor}} \qquad (3.2.11)$$

The float hangoff functions are shown in Figure 3.2.6.

Note that a torque rebalance loop implemented with pulse burst compensation increases the average float hangoff for a given input rate. The float hangoff increase is dependent on the sum of the gyro time constants. The average float hangoff functions for gyro 427A, MB 4, and 422B are shown in Figures 3.2.7, 3.2.8, and 3.2.9 respectively.

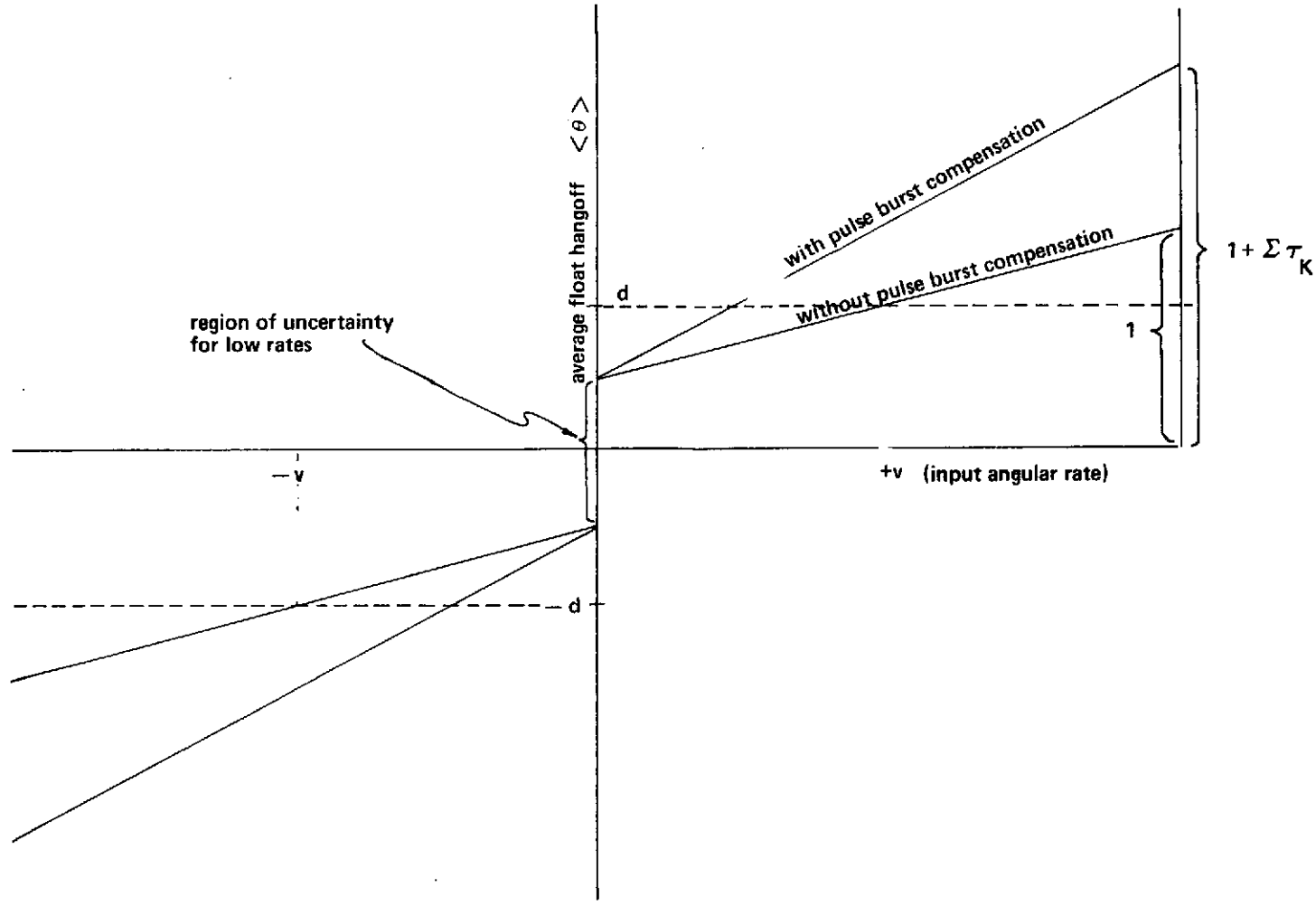

Fig. 3.2.6 Float Hangoff Functions.

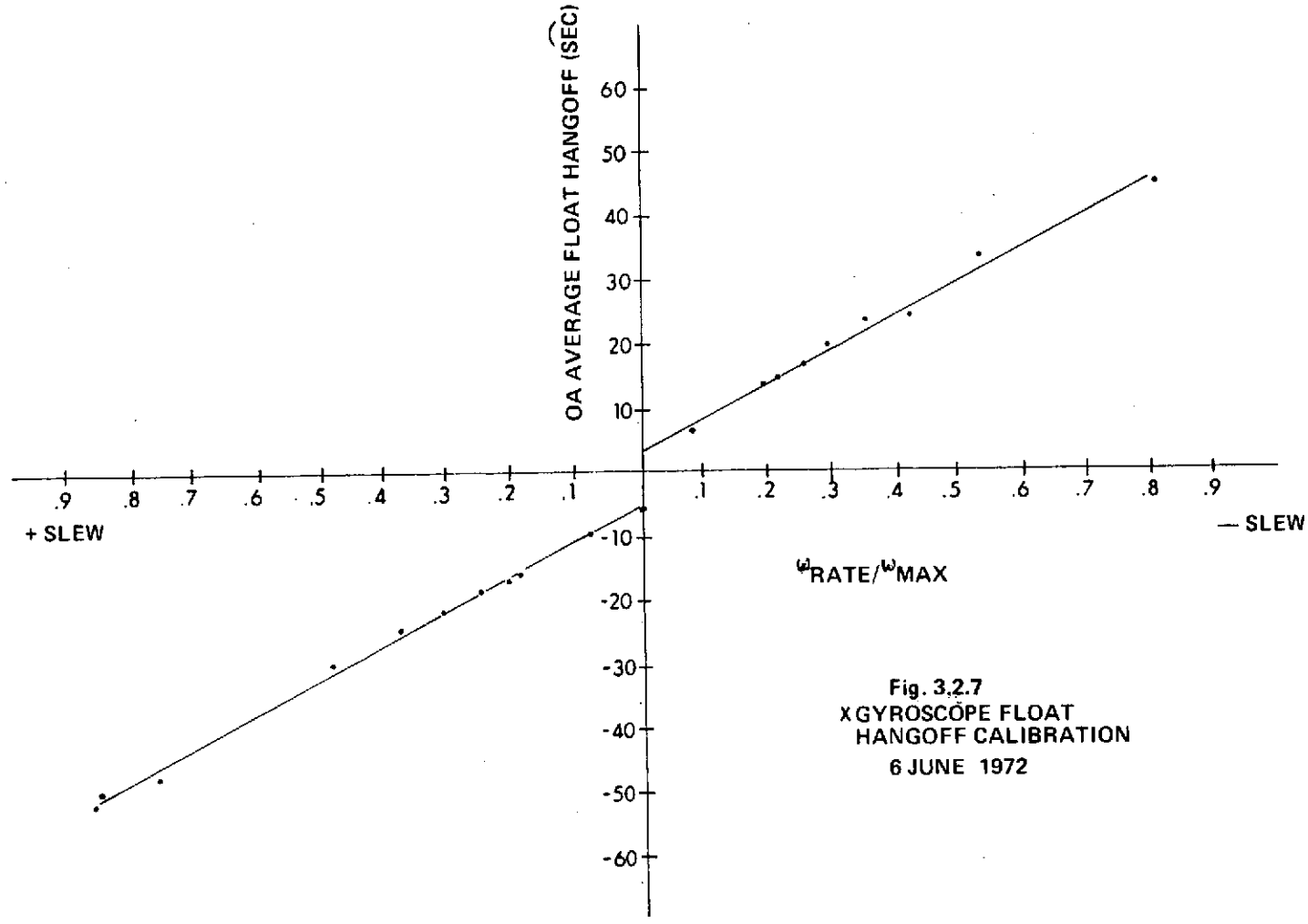

Fig. 3.2.7
X GYROSCOPE FLOAT
HANGOFF CALIBRATION
6 JUNE 1972

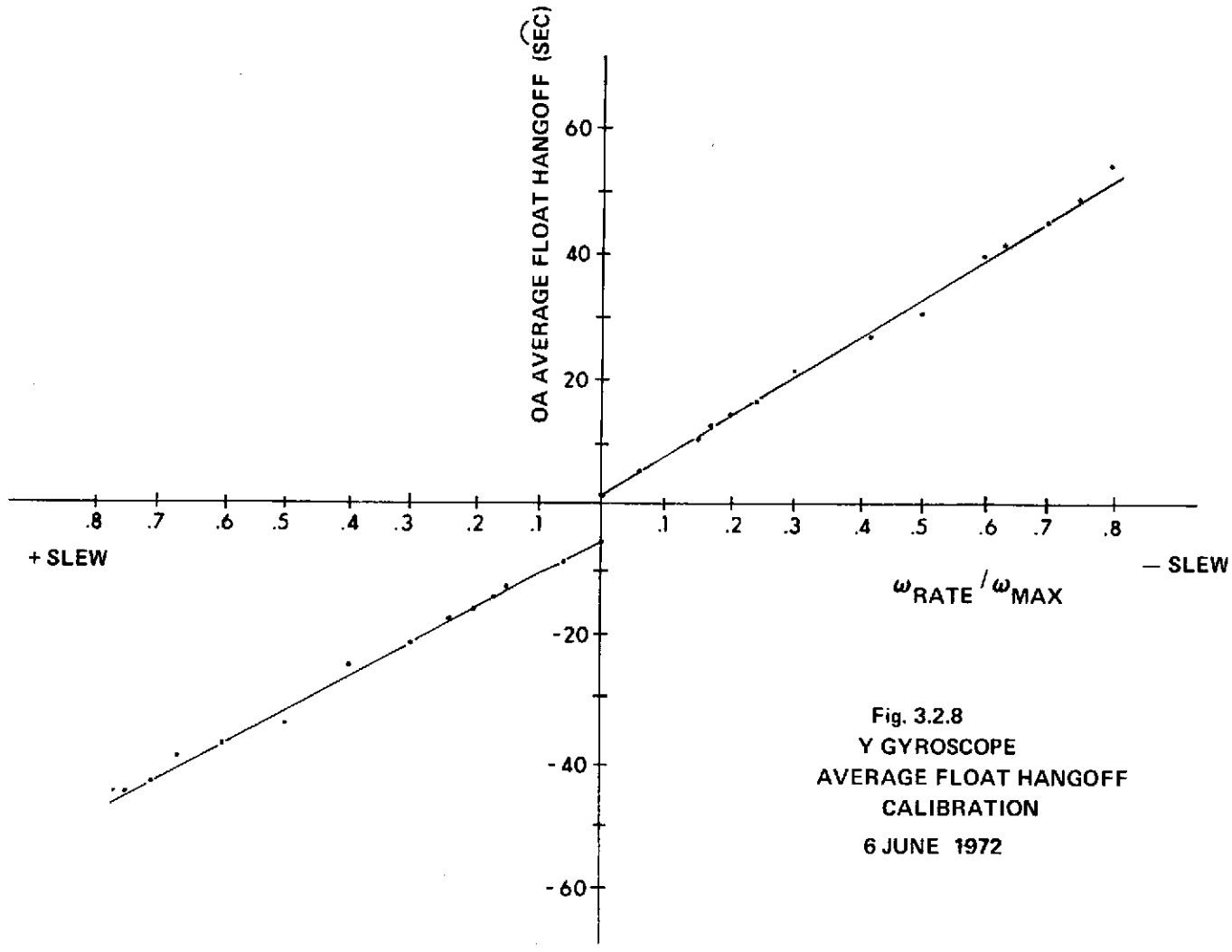

Fig. 3.2.8
Y GYROSCOPE
AVERAGE FLOAT HANGOFF
CALIBRATION
6 JUNE 1972

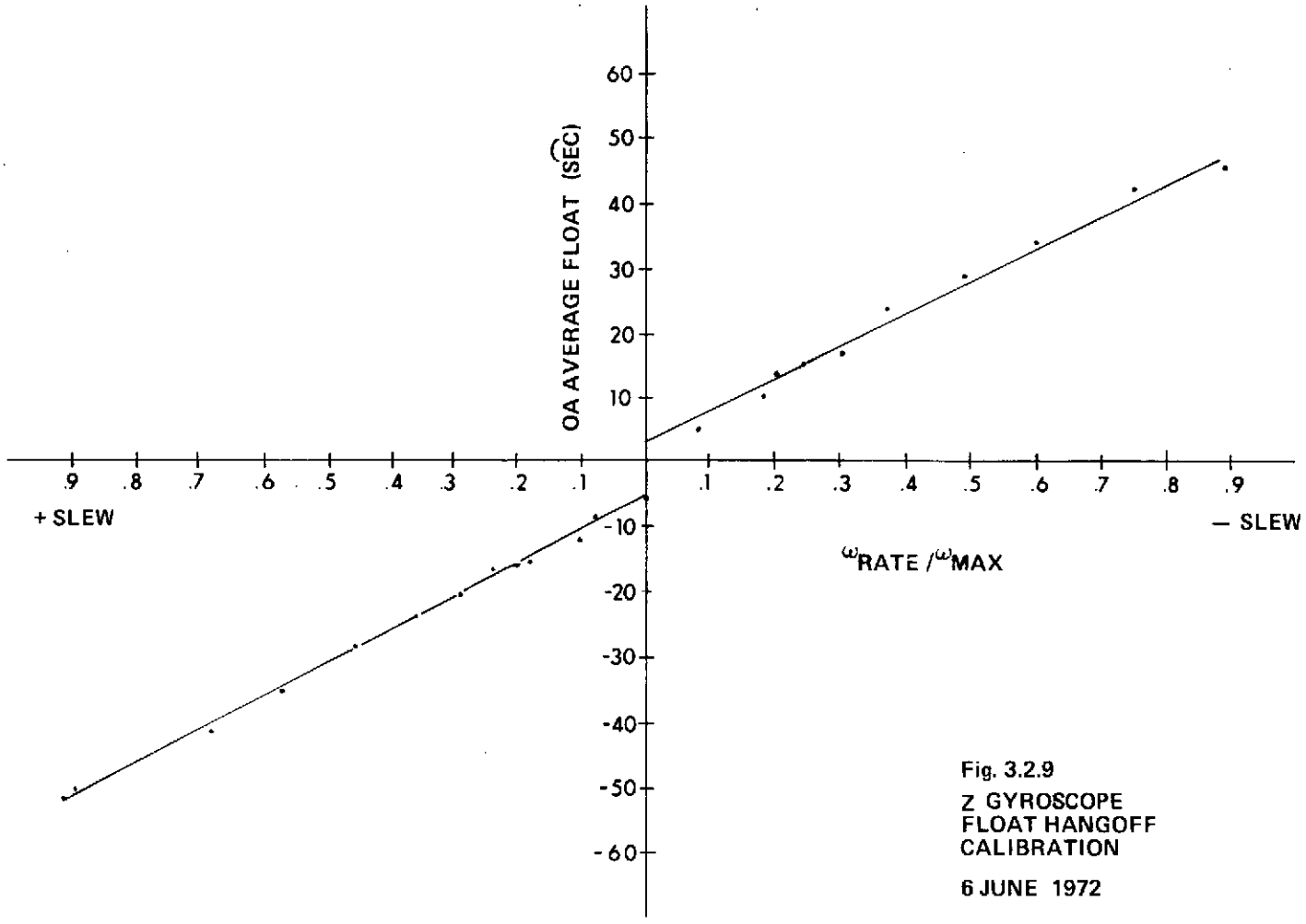

Fig. 3.2.9
Z GYROSCOPE
FLOAT HANGOFF
CALIBRATION

6 JUNE 1972

As shown in the figures, with the pulse burst compensation gain and loop threshold correctly set, the float hangoff approximately equals half the torquing threshold plus a rate dependent hangoff term that increases with rate. The slope is related to the sum of the gyro torquer and float time constants (from Equation 3.2.10). It should be noted that in the low rate region (for example when no torque pulses are generated during an interaction interval) the exact float hangoff is undefined in the region of uncertainty (See Figure 3.2.6). From these float hangoff calibration curves, one estimates the gyro float time constants to be 560, 570, and 540 microseconds for gyros 427A, MB 4 and 422B respectively. These time constants are greater than the typical 18 IRIG Mod B time constant (450 microseconds), however, this is the expected result of operating the gyros at higher temperatures.

The linear float hangoff function is the model that was used for SRA cross coupling error compensation. Rate estimates are derived from the gyro pulse count in an algorithm iteration interval and are used to determine the operating point corresponding to the hangoff curve. However, when no torque output pulses occur in an iteration interval, rate estimates can not be made and in such a case, float position uncertainty can be in error by a maximum of 1.5 torquing thresholds (1.5d). This error is attributed to the fact that the exact float position is somewhere in the dead zone region defined by the torquing thresholds. Because the torquing threshold has not been exceeded, accurate knowledge is unavailable as to the exact float position.

To account for SRA coupling errors that might arise when the float is in the torque dead zone region, the interpolator is used to read float position mid point in the iteration interval when no torque pulses occurred during a computer iteration interval. For this reading, interpolator furnishes float position directly by quantizing the gyro signal generator (SG) output. The compensation model therefore also included direct use of hangoff measurement in addition to the linear model. Use of the direct float read out for SRA coupling compensation is not possible over the full rate range because of dynamic limitations and the need for an "average" hangoff over the entire iteration interval. With high dynamic inputs, the mid point reading of the interpolator does not necessarily represent average float hangoff.

In the constant rotational environment, with inputs applied simultaneously about the input (W_{IRA}) and spin reference axes (W_{SRA}) the uncompensated SRA cross coupling drift is expressed as:

$$\text{Drift Error} = \left(d - \frac{1}{2}\right) W_{SRA} - \left(1 + \sum \tau_K\right) W_{SRA}\ W_{IRA}$$

For example if (d-1/2) = 20 microradians and $(1 + \sum \tau_K)$ = 257 microradians per radian/second, a one radian per second rotational rate could generate a drift error equal to 3250 meru (49°/hr) if no compensation were used.

In the oscillatory environment, with the magnitude of input axis oscillation (c) much larger than the spin reference axis (a) oscillation, the SRA cross coupling drift due to rectification is expressed as:

$$\text{Drift Error} = \frac{2}{\pi} a\omega \left(d - \frac{1}{2}\right) - \left(1 + \sum \tau_K\right) \frac{ac\omega^2}{2}$$

Where:

$$W_{IRA} = c \sin\omega t$$

$$W_{SRA} = a \sin\omega t$$

The effective rectification generated in the gimbal system for various test inputs is given in Table 3.2.3.

TABLE 3.2.3 RECTIFICATION MAGNITUDES

frequency (hertz)	a (radians)	c (radians)	Drift (MERU)	Error (°/hour)
.5	0.024	0.022	+2.9	0.04
1	0.024	0.022	-12.6	0.19
5	0.0057	0.011	-48.6	0.73
10	0.0015	0.004	+2.2	0.03
25	0.0002	0.0006	+11.	0.17

3.2.3d OA Coupling

OA coupling error is a function of the float inertia response. OA coupling errors are exhibited in two ways depending on the nature of the environment. The first way is a lagging effect when the gyro is excited by a transient input. Figure 3.2.10 shows the effect on attitude error propagation during the acceleration and deacceleration phase of a ten revolution slew test at 0.15 radians/second (9.8°/sec). OA coupling errors are manifested as steps in attitude errors which nearly averages to zero in a complete acceleration-deacceleration cycle. With OA coupling compensation effected, as in Figure 3.2.11, the steps of attitude error are virtually eliminated.

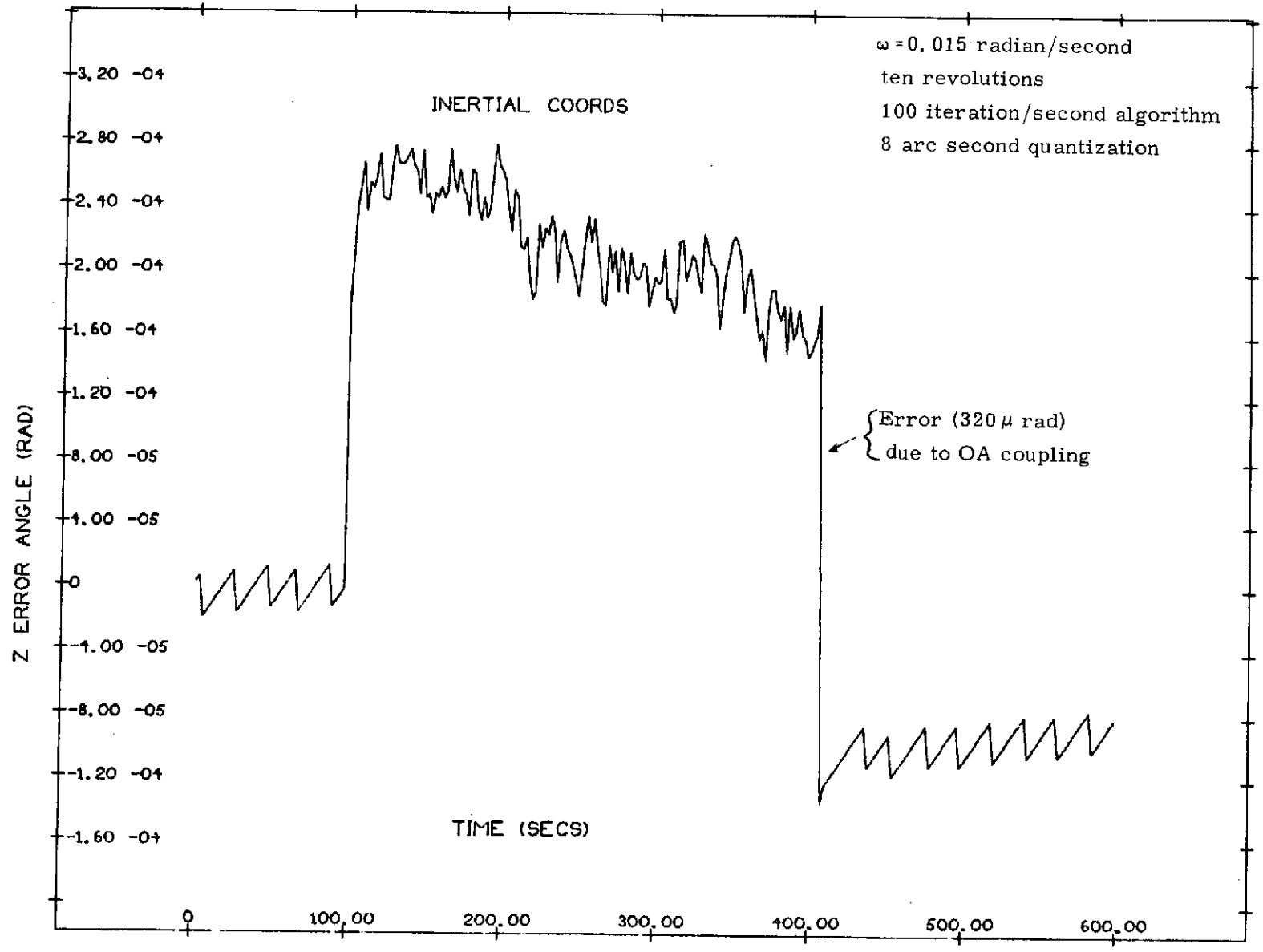

FIGURE 3.2.10 - OA COUPLING ERROR PROPAGATION IN A SLEW ENVIRONMENT

FRAME Ø15

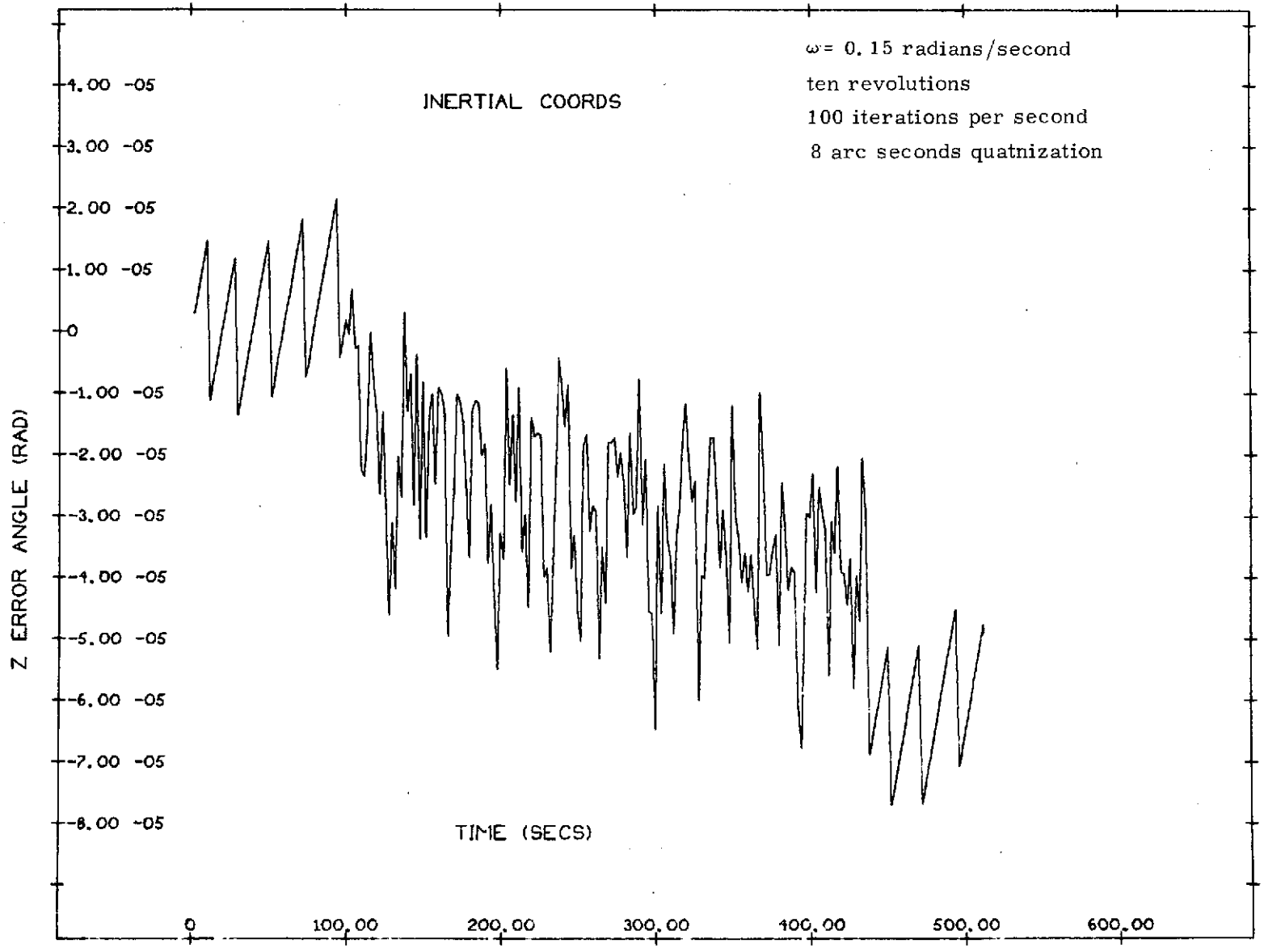

FIGURE 3.2.11 - SLEW ENVIRONMENT ERROR PROPAGATION (OA Coupling Effects Compensated)

FRAME 009

The second way OA coupling errors are exhibited is in the oscillatory environment. When an oscillatory input is impressed about a gyro's Output Axis because of its inertia, the float will lag the excitation and extra torque pulses will be required to maintain the float's null position. If the oscillatory excitation about the Output Axis is:

$$\omega_O = a \sin\omega t \tag{3.2.12}$$

then the OA coupling error oscillation is:

$$\text{OA coupling error} = I/H\ \dot{\omega}_O = I/H\ a\omega \cos\omega t \tag{3.2.13}$$

where I is the float output axis inertia and H is the gyro wheel angular momentum.

The correct compensation model is to estimate the rate change magnitude about the Output Axis, then to scale the estimate by the ratio I/H. The resultant quantity is subtracted from the input gyro torque pulse count. OA coupling errors which are not compensated in an oscillatory environment appear as a second sinusoidal input by the attitude algorithm. Because of its 90^o phase displacement with the input oscillation, the attitude algorithm assumes a coning input and corrects by adding a drift component on the third axis. This drift component is an error and is termed "pseudo coning drift." Pseudo coning compensation evaluations are discussed further in Section 5.2.2.b.

3.2.4 Attitude Storage

Attitude storage results from the lagging response of the SDF gyro float to an input stimulus. Figure 3.2.12 is the SDF floated gyro model, normalized for unity gain. Figure 3.2.12 also gives a comparison of float response between an ideal integrator and the typical gyro.

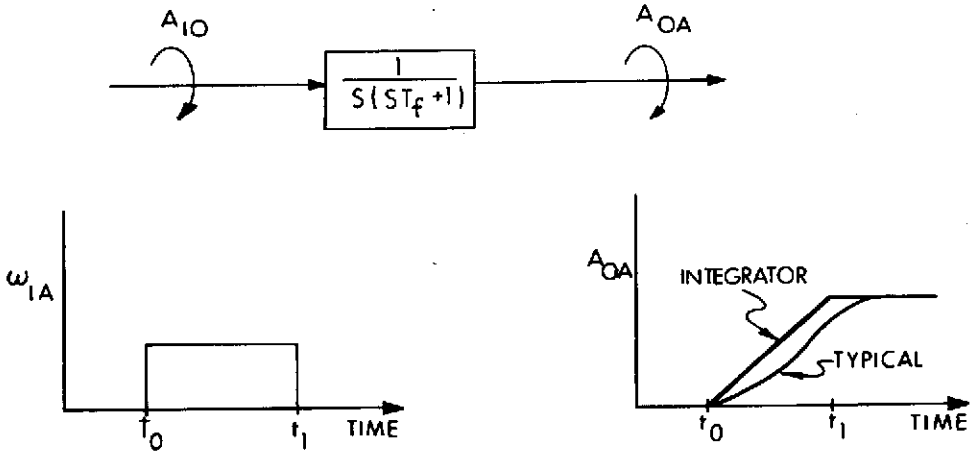

Figure 3.2.12 Gyro Pulse Response

Float storage is defined as the difference between the ideal integrator and the gyro's responses and therefore represents the change in attitude that is sensed by the gyro, but not yet translated into float motion.

Typically, the gyro float position is pulse restrained to a null position with electronics applying torque pulses whenever the float exceeds a given threshold. The torque commands are applied through an almost identical gyro model with the result that in a given time interval the energy that is stored from torquing nearly cancels the energy stored due to the applied input rate.

Figure 3.2.13 is the gyro model expanded to include the effect of torquing:

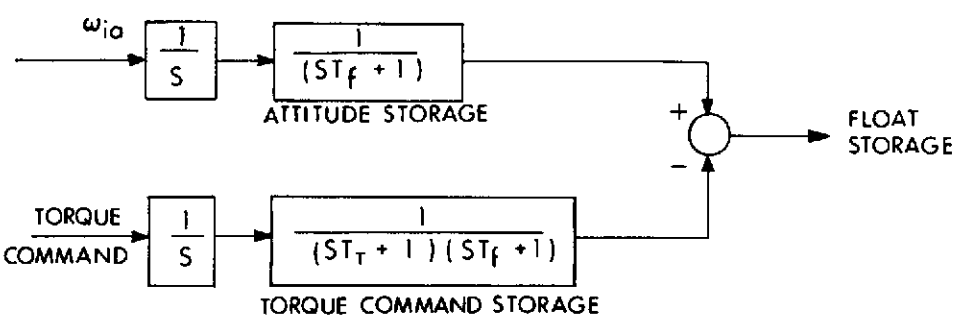

Figure 3.2.13 Gyro model with torquing

The torquing model includes in addition to the float time constant (T_f), the torquer time constant (T_t). Thus, float storage is modified by torque command storage when stimulated by both a rate input and a torquer input and the resultant float lag becomes a function only of the torquer time constant (T_t).

Storage as a function of input axis rate is illustrated in Figure 3.2.14. Also shown are the float hangoff functions defined in Section 3.2.3c. The important observation from Figure 3.2.14 is that float storage is a linear function of input rate but not equal to the magnitude of the float hangoff.

3.2.5 Fine Attitude Quantization with Hybrid Operations (i.e. Torque Loop Plus Interpolation)

Without the interpolator electronics the system quantization is determined by the gyro's torque loop quantization (for example, 40 arc seconds). Because there is gyro float storage, a small quantity of attitude is stored within the gyro. This stored attitude data is represented by the residual change in the float movement that is not detected by the torque loop.

Without pulse burst compensation in effect, the interpolator measures the required residual float movement by digitizing the signal generator (SG) output. In this mode of operation the interpolator information is added to the accumulated torque pulses for a finer quantization that is defined by the interpolator's bit size.

However, when pulse burst compensation is in effect, the loop dynamics are modified and consequently the float movement no longer represents the true gyro response. With pulse burst compensation, a signal is added to the signal generator (SG) output which predicts where the float should be based on the occurrence of torquing. By predicting the float movement, the magnitude of storage error is modified. Therefore, the pulse burst compensation signal must be subtracted from the SG output such that the resultant signal represents the true float position under conditions of no pulse burst compensation. The resultant signal is now in error by only the float storage which if necessary can also be corrected because of its linear relationship with respect to rate (See Figure 3.2.14).

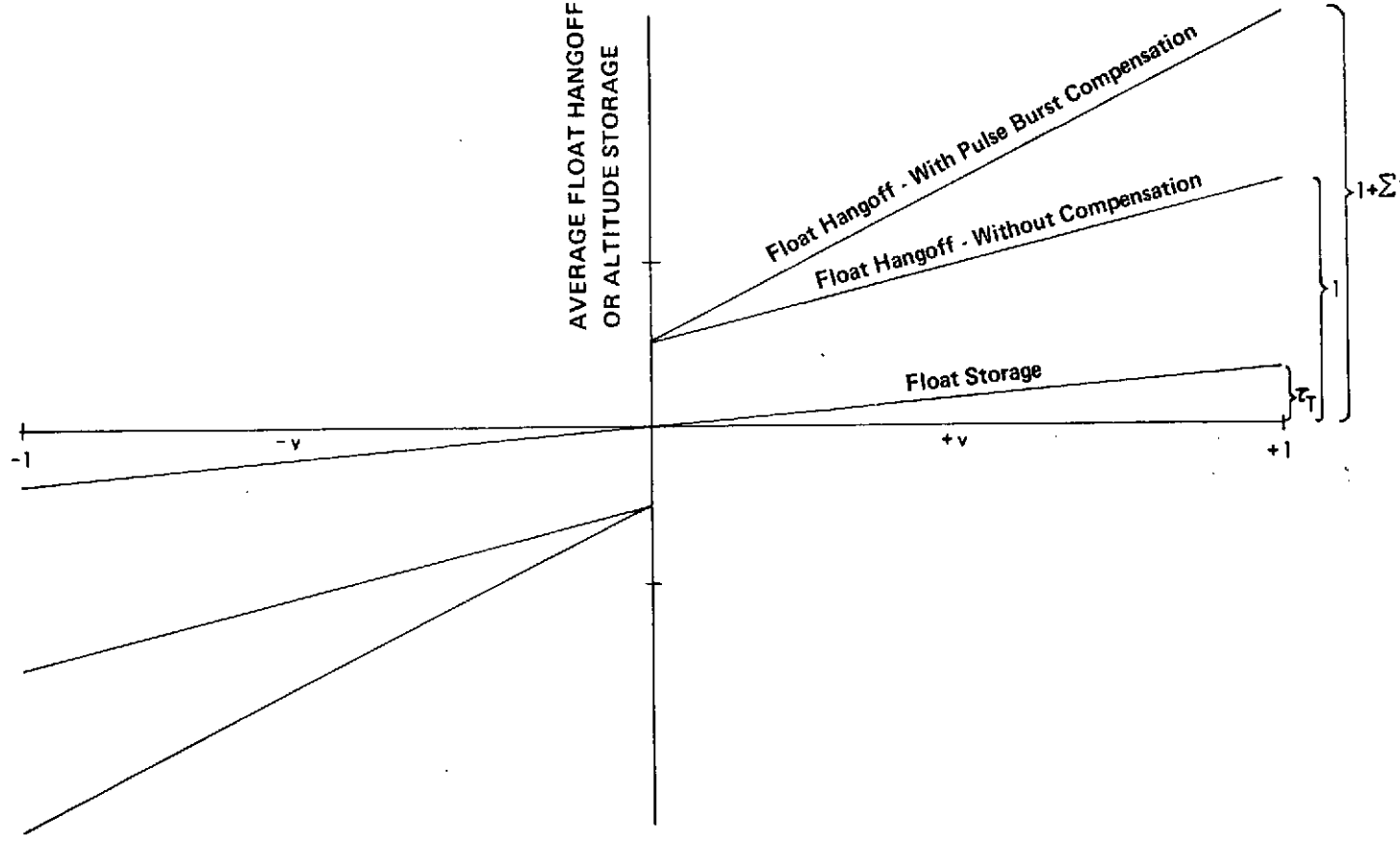

Fig. 3.2.14 Attitude Storage and Float Hangoff Functions.

4.0 Software Development

4.1 Introduction

A dedicated H316 mini-computer is used to support the strapdown inertial system and to provide comprehensive data processing capabilities that include automatic inertial instrument calibration, system attitude maintenance capabilities and land navigation. In addition, the software design facilitates the evaluation of system tradeoffs and provides for efficient data processing and management. A considerable software development effort is necessary to achieve the above test capability. The software developed to support the program's requirements is discussed in this text in five subsections: 1) calibration software, 2) compensation, attitude and velocity algorithms, 3) attitude error analysis software, 4) land navigation algorithms, and 5) H316 mini-computer and IBM 360/75 remote terminal software.

4.2 Calibration Software

The calibration software enables the automatic calibration of the inertial instrument parameters. Two sets of software were written - one set to calibrate the gyro drift components and the accelerometer parameters such as; scale factor, bias, and alignment, (so called static calibration) and the second set to calibrate gyro scale factor, misalignment angles, and anisoinertia (so called dynamic calibration).

Calibration is achieved in two parts. Data outputs from the inertial instruments are first accumulated and stored in the H316 computer. This operation is accomplished under control of the data acquisition software. Final data reduction and display in engineering units is done in the DDP516 under control of the data transfer software that is stored in the disc file. The inertial instrument parameters calculated are shown in Table 4.2.1.

4.2.1 Data Acquisition Software

The data acquisition program performs four basic functions: 1) automatic calibration control, 2) data accumulation , 3) data format conversion and storage, and 4) data transfer control.

The static calibration data acquisition software sequences the strapdown system through twelve calibration positions (see Appendix P). Gyro and accelerometer pulses are accumulated for a ten minute test period and then stored in the H316 buffer.

TABLE 4.2.1 INERTIAL INSTRUMENT PARAMETER CALIBRATION

STATIC CALIBRATION

	Parameter	Calibration Unit
Gyro	Bias (NBD)	meru*
	Acceleration Sensitive Drift (ADOA, ADIA, and ADSRA)	meru/g
	Major Compliance ($K_{SS} - K_{II}$)	meru/g^2
Accelerometer	Positive and Negative Scale Factor (SF^+, SF^-)	cm/sec/pulse
	Misalignment of the Input Axis about the Output Axis (SO) and about the Pendulous Reference Axis (SP)	radians
	Accelerometer Bias (B_o)	cm/sec^2

DYNAMIC CALIBRATION

	Parameter	Calibration Unit
Gyro	Positive and Negative Scale Factor (SF^+, SF^-)	radian/pulse
	Misalignment of the Input Axis about the Output Axis (GO) and the Spin Reference Axis (GS)	radian
	Anisoinertia Coefficient	radians/radian/second

* Meru is equivalent to one thousandth of the earth's rotational rate or 0.015^o/HR.

The dynamic calibration data acquisition program drives the outer gimbal either positively or negatively in six test positions determined by the inner and middle gimbal orientations (see Appendix R). Gyro torque pulses are accumulated for a given test duration determined by the rotational rate and the number of complete revolutions selected for calibration. The resolver to digital encoder monitors the angular rotation of the outer gimbal to identify the starting and ending points of the data acquisition cycle. As backup to the resolver encoder, additional software was written to determine the test duration from the automatic test control electronics that emits a position ready pulse for every 360^{o} of gimbal rotation.

The calibration sequence is initialized by the operator aligning the system with all gimbals at zero degrees, and providing as an input to the computer the test record identifiers and special test sequence requests. For dynamic calibrations, the number of revolutions per test is also selected. Once initialized, the calibration sequence is completely automated and under computer control.

The data acquisition software is controlled with a main executive program which calls the appropriate subroutines required for specific system operation. The first operation executed is the development of actuating signals that command the gimbal's rotation to the desired calibration position. Gimbal orientation is possible in sixteen different positions that correspond to the sixteen multi-speed resolver null positions. The executive program determines, from a stored table, the gimbal orientation of the next calibration position. Actuating signals are developed from this information and gimbal rotation is activated. When the desired test orientation is achieved, a position ready pulse is generated to switch the gimbal positioning loops to a high gain servo mode about the multi-speed resolver signal and to notify the executive controller that the data acquisition cycle can begin.

The executive program now transfers control to the data acquisition subroutine that accumulates the torque pulses (gyro and accelerometer), and clock timing pulses. Both positive and negative torque pulses are accumulated for each of the six inertial instruments with the use of twelve memory locations. Two locations are assigned to each instrument to accumulate positive and negative torque pulses seperately.

Time is accumulated with a main counting loop, implemented to accumulate time seperately for each of the six inertial instruments. When the first gyro or accelerometer pulse is sensed for each instrument, a time counter is read into a "starting time" buffer for that instrument. The time counter continues to be incremented every interrogate cycle thereafter. At the end of test, the time of the last pulse for each instrument is stored into a "end time" buffer to determine the

test duration within an interrogation cycle (208 micro-seconds). This procedure synchronizes the time of test individually for each inertial instrument to the occurrence of the initial and final torque pulses.

Dynamic calibration also synchronizes the outer gimbal rotation to the occurrence of the initial and final torque pulses. Because the resolver encoder's sampling rate is 800pps, a linear interpolation is made based on the gimbal test rate to estimate the rotational angle at the time of the initial and final torque pulses.

When the data acquisition cycle is completed, the executive calls a Fortran subroutine to convert the raw data into a double precision floating point format for initial display on the teletype and storage in the H316 buffer memory for subsequent data reduction. The inspection of the raw data on the teletype verifies the reasonability of data prior to transfer to the DDP516. The data format includes the different pulse count totals, time, and gimbal angles.

The data acquisition and control program requires approximately 25% of the H316 - 16K word memory capacity. Each test position requires 160 words and a memory capacity for 52 sets have been assigned. This is sufficient for four complete automatic static and dynamic calibrations before a data transfer to the disc via the DDP516 is required.

When the 160 word set is stored in the H316 buffer, the DDP516 is interrogated for its readiness to accept data. Data is transferred to the DDP516 only if the appropriate programs are resident in the DDP516 core. If the required DDP516 programming has been established, program control is returned to the data acquisition executive for continuation of the calibration sequence. Data that is not transferred to the DDP516 is stored in the H316 until the limit of 52 sets is reached at which time the calibration cycle halts for a data transfer.

4.2.2 Data Transfer Software

Data transfer to the DDP516 is accomplished with an interaction of the data acquisition software with the data transfer software that is resident in the DDP516 core. A serial data link which connects the two computers is used for data transmission. A series of synchronizing pulses are transmitted to identify the start of data characters. One complete 160 word data set is transmitted into the DDP516 core with a checksum verifier. The checksum assures transmission reliability. If transmission is correct, the data set is permanently stored in the disk file.

Disk filing is accomplished using four subroutines that interface with the DDP516 Disk Operating System (DOS). The same four subroutines maintain the active data file (DATAKK) which includes three major components: 1) the 160 word calibration data sets, 2) the system alignment angles that are used as inputs to the calibration compution programs, and 3) the results of parameter computation.

Each DATAKK data set is assigned a serial number with a back pointer to the previously stored data set. Disk storage occurs after the serial number is read into the DDP516 core. The DATAKK index is then updated and the DOS system closed. The serial number is transmitted over to the H316 for teletype display and cues the H316 to transmit the next data set. The data "transfer and storage sequence" continues until the H316 buffer is empty, at which time control is returned to the data acquisition executive for resumption of the calibration cycle.

When the DDP516 determines that a complete set of calibration data (twelve test positions) has been transferred from the H316, Fortran subroutines are called to compute the calibration parameters using the equations given in appendixes P and R. The results are printed on the DDP516 teletype, and stored on the disk file. After the computed parameters are stored, the DDP516 returns control to the H316 for additional data transfer, if its buffer is not yet empty. Therefore, the H316 operating with the DDP516 provides a continuous calibration capability. The H316 operating by itself is memory limited to four static or dynamic calibrations.

4.3 Compensation, Attitude, and Velocity Algorithms

4.3.1 Introduction

The strapdown system performance is dependent on the efficient real time data processing of the gyro and accelerometer outputs into attitude and velocity updates. Figure 4.3.1 shows the data processing algorithms that include the compensation algorithms, the attitude algorithm, and the velocity algorithm.

4.3.2 Compensation Algorithms

The gyro compensation algorithm corrects the body referenced angular pulses to account for errors attributed to bias, drift and dynamic error sources. The corrected angular increments are the input to a quaternion expansion algorithm to derive system attitude information.

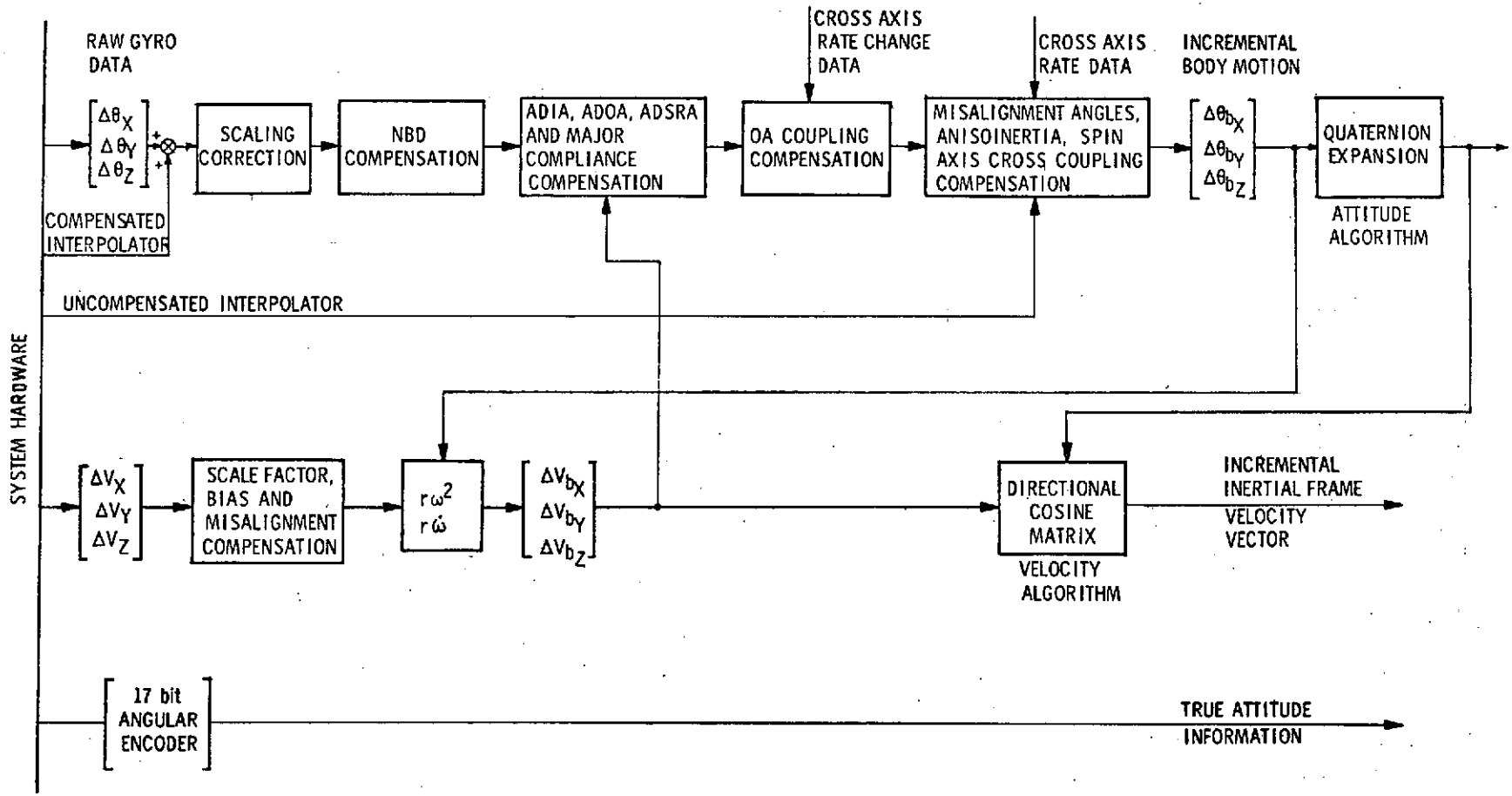

Fig. 4.3.1 -SPOT Algorithms.

The accelerometer compensation algorithm corrects body reference velocity increments to account for accelerometer bias and alignment. A directional cosine matrix transforms the velocity increments into the inertial frame.

The corrected accelerometer pulses are used to compensate the gyro's acceleration sensitive drift components. This procedure allows the accurate compensation of g field sensitive error sources without requiring indirect estimates of the gravity vector. Similarly, rate estimates derived from corrected gyro torque pulse data compensates the accelerometer's centripetal acceleration component and the gyro's OA coupling, anisoinertia, and scale factor components.

An important adjunct to the compensation algorithm is the load making program. This program inputs and scales all compensation parameters into appropriate formats for storage in specified memory locations. The data in its specified locations is "on call" to the compensation algorithms.

The compensation algorithms are implemented at three iteration rates: 100, 50 and 25 iterations per second. This is achieved by changing the compensation iteration interval which is controlled by the preset interrupt counter. At 100 iterations per second the counter interrupts every 48 interrogation cycles (0.01 second) and at 50 iterations per second the interrupt is every 96 cycles. The gyro and accelerometer read routines are changed to halve the pulse scaling to account for the doubling in the iteration interval. This was the most direct and efficient method, requiring no modification to the load making program.

An alternative method is to maintain the read routines constant, and change the compensation parameter scaling. This scheme was evaluated and found to require an increase in software and operator assistance. Other modifications necessary to allow operation at the different algorithm iteration rates pertain to the attitude and velocity algorithms to account for the revised pulse scaling.

The gyro and accelerometer compensation iteration intervals are equal but are staggered to allow the gyro derived attitude data to be available at the middle of the accelerometer update interval.

4.3.2.a Gyro Compensation Algorithm

The gyro compensation model is defined in Figure 4.3.2.

The detailed compensation equations and sequence are given in Appendix E. This discussion provides a descriptive review of the processing flow illustrated in

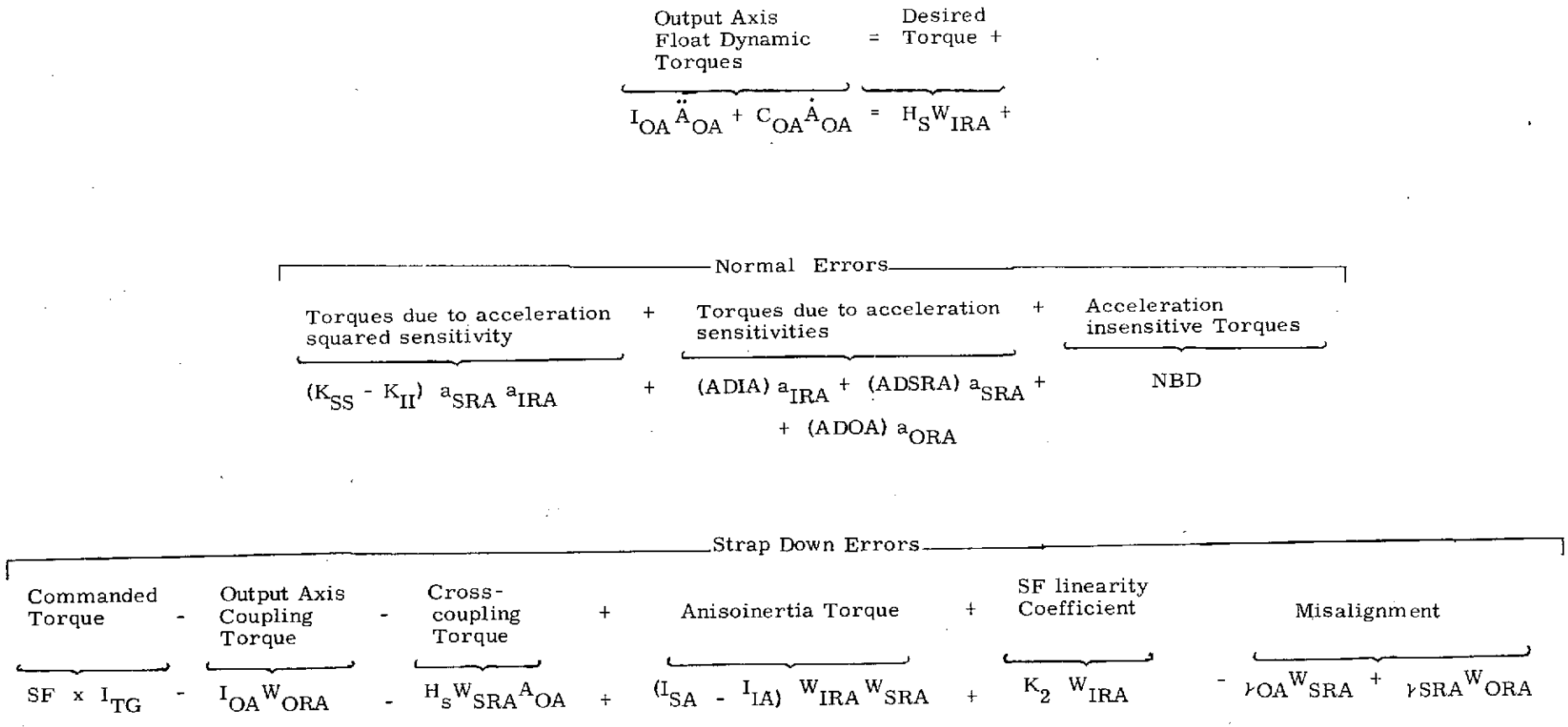

FIGURE 4.3.2 GYRO COMPENSATION MODEL

Figure 4.3.1. Before the gyro pulse outputs are corrected for the various gyro error parameters, finer attitude quantization information from the gyro interpolator is added to the accumulated gyro pulses. Because pulse burst compensation is in effect, the compensated interpolator output is used (See Section 3.2.4). The quantization increment furnished by the interpolator is varied by the use of a masking instruction which selects one of four quantization magnitudes. For example, with the interpolator information completely masked, the algorithm quantization is 40 arc seconds per pulse, while with none of the six interpolator bits masked, the quantization is 5 arc seconds. Intermediate quantization levels of 10 and 20 arc seconds are achieved by masking the least or the next to least significant interpolator bits respectively.

The raw attitude data is scaled by the gyro scale factor to determine the input axis angular displacement. Pulse scaling is accomplished in two steps. First, the accumulated pulses are sized to a nominal scale factor determined for computational efficiency to be an even power of two. The nominal scale factors selected for the X, Y, and Z axis gyro are 45×2^{-18}, 57×2^{-18}, and 48×2^{-18} radian per pulse respectively. The different nominal scale factors are required because of the variations in configuration of the 18IRIG Mod B gyros used. The second step of gyro pulse scaling is to correct for the deviation of the true scale factor from the nominal value. The scale factor compensation model includes two terms; a low rate scale factor component and a rate dependent component. The low rate scale factor is determined from baseline test data and is stored in a memory location determined by the load making program. The rate dependent factor is a linear function of the input axis rate which is based on real time rate estimates by the gyro input pulse count (reference Section 3.2.3b).

The acceleration insentive drift component (NBD) is compensated by adding incremental corrections to the gyro pulse count. The magnitude of the correction increment is derived from the NBD magnitude and from the compensation iteration time.

The acceleration sensitive drift components are corrected with body referenced acceleration estimates from the accelerometer outputs. Based on the accelerometer output, the magnitude of the drift component to be compensated, and the iteration time duration, incremental corrections are applied to the gyro pulse count.

Output axis (OA) coupling drift errors (reference Section 3.2.3d) result from a lagging float motion in response to rate changes about the output axis (inertia torque). Hence, extra torque pulses result when the gyro case is accelerated.

These pulses operate to maintain the float at the signal generator (SG) null position. OA coupling error compensation is accomplished by using OA angular acceleration estimates derived from a second gyro whose Input Axis is collinear with the Output Axis of the gyro requiring compensation. Correction is applied to the pulse count by weighting the OA rate change estimates by the gyro parameter ratio I/H (Moment of inertia about OA/wheel angular momentum).

Spin Reference Axis (SRA) cross coupling drift errors (reference Section 3.2.3c) derive from float OA rotations. Those rotations (float hangoff) cause the Input Axis to sense an angular rate composed of the rate about the Input Reference Axis plus a component of the rate imposed about the Spin Reference Axis. To compensate SRA cross coupling errors, it is necessary to determine the float OA angular displacement and the imposed SRA rate. A two-step method is implemented to determine float hangoff. The point-slope model derived in Section 3.2.3c, Equation 3.1.10, is used with rate estimates from the gyro. When no rate estimates are available (for example, no torque pulse during an iteration interval), the uncompensated interpolator output is used to establish the float hangoff magnitude and polarity.

Anisoinertia drift (reference Section 3.2.3a) is generated when simultaneous IA and SRA angular rates cause drift due to the float dynamics corresponding to the differences in SA and IA float inertias. Anisoinertia error compensation is based on estimating the IA and SRA rates and scaling the rate product by a coefficient that is a function of the inertia difference. The coefficient used is a constant low frequency coefficient that does not account for inertia shifts along the SA resulting from wheel rotor decoupling effects above the wheel hunt frequency. The implementation of the more complex rate dependent coefficient requires the spectrum analysis of the rate estimates, a task worthy of further investigation. In actual flight environments, however, the typical random frequency spectrum is below the wheel hunt range (2-4 hz) and therefore the simple model approach appears to be adequate.

Gyro misalignment angles cause attitude errors by sensing angular rates from orientations other the Input Reference Axis. The misalignment angle about the Spin Reference Axis is a fixed quantity that is dependent on gyro mounting alignments. The Output Axis misalignment, however, includes in addition to the fixed quantity, dynamic alignment terms that represent the effects of hangoff due to the applied input rate. The fixed misalignment errors are corrected by subtracting the estimated rate error resulting from misalignments from the gyro pulse count. Dynamic error terms such as Anisoinertia and SRA cross coupling have processing similarities to

the Output Axis misalignment term (i.e., multiplication by the Spin Reference Axis rate estimate) and therefore the composite of these errors is treated in the same processing block in Figure 4.3.1.

4.3.2.b Accelerometer Compensation Algorithm

The accelerometer compensation model used in this program included only the following terms:

indicated output | input | accelerometer bias | misalignment errors

$$\frac{A_o}{SF} = A_I + B_o + (\gamma_{ORA})\, a_{PRA} - (\gamma_{PA})\, a_{ORA} + \underbrace{R\omega^2 + R\dot{\omega}}_{\text{centripetal and tangential acceleration}}$$

Figure 4.3.3 - Accelerometer Compensation Model

The detailed compensation equations and their sequence is given in Appendix F. As noted in Section 3.1.3 other accelerometer dynamic terms such as anisoinertia and OA coupling were not compensated for in this program. They can introduce significant although transient type errors (as tabulated in Table 3.1.2). It was intended to investigate modeling compensation for these terms. However, the program emphasis was directed to gyro dynamic modeling and time did not permit their implementations.

This discussion provides a descriptive review of the processing flow. The accelerometer pulses are first scaled by the accelerometer's scale factors to determine the magnitude of the velocity increment. Two scale factor values are used to distinguish differences between positive and negative acceleration inputs.

Accelerometer bias is corrected by adding increments to the pulse count. The increment magnitude is based on the bias magnitude and duration of the compensation interval.

The accelerometer misalignment angles are both fixed quantities dependent on the mounting alignment. Misalignment errors are corrected by subtracting the estimated acceleration errors from the input accelerometer pulse count.

Centripetal acceleration ($r\omega^2$) and tangential acceleration ($r\dot{\omega}$) normalization is required because of the dispersed location of the accelerometer mass elements.

Ideally, the mass elements of the three accelerometers in an inertial system should be located at a single point such that all acceleration can be sensed in three dimensions at a single point. This situation is obviously impossible to attain. The errors caused by the angular rotation of each separate accelerometer mass element with respect to an arbitrary reference point is represented by a centripetal error and by a tangential rotation acceleration error (see Appendix G).

If a convenient system reference location is chosen, compensation for angular rate errors from any instrument can be accomplished. The rotational error sources are computed from the different instrument positions, and by the use of the sensed body angular rate and change in rate over the compensation interval. For this program, the X accelerometer mass element is the point of reference.

4.3.3 Attitude Algorithm

The attitude algorithm is a transformation algorithm that provides a mathematical recurrent form to transform data from one frame of reference to another. The type of attitude algorithm implemented in this program is the four parameter quaternion transformation.[9]

The basic quaternion algorithm is of the form

$$\bar{q}(t + \Delta t) = \bar{q}(t)\ \bar{x}(t, \Delta t) \tag{4.3.1}$$

Quaternion $\bar{q}(t)$ is the attitude quaternion at time t, and $\bar{q}(t+\Delta t)$ is the attitude quaternion at $t+\Delta t$. Thus, quaternion $\bar{q}(t)$ propagates over a time interval Δt to quaternion $\bar{q}(t+\Delta t)$ as a function of the update quaternion $x(t, \Delta t)$. The update quaternion represents incremental attitude information updated by the gyro loops. The exact third order quaternion expansion is given as

$$\bar{x}(t, \Delta t) = 1 + \frac{\bar{\theta}}{2} - \frac{1}{2}\left[\frac{\bar{\theta}}{2} \cdot \frac{\bar{\theta}}{2}\right] - \frac{1}{6}\left[\frac{\bar{\theta}}{2} \cdot \frac{\bar{\theta}}{2}\right]\frac{\bar{\theta}}{2} - \frac{1}{6}\left[\frac{\bar{\theta}^*}{2} \times \frac{\bar{\theta}}{2}\right] \tag{4.3.2}$$

$\bar{\theta}$ is the current attitude update from the gyro loops and $\bar{\theta}^*$ is the set of angular increments over the past sampling interval.

The third order algorithm expansion implemented in this program includes two main subroutines: the first subroutine updates the quaternion of rotation to perform the third order attitude algorithm.[10] The equation representing the algorithm is expressed as:

$$\begin{aligned}
\rho_x' &= \lambda S\alpha_x + R\rho_x + S\,(\rho_y\alpha_z - \rho_z\alpha_y) \\
\rho_y' &= \lambda S\alpha_y + R\rho_y + S\,(\rho_z\alpha_x - \rho_x\alpha_z) \\
\rho_z' &= \lambda S\alpha_z + R\rho_z + S\,(\rho_z\alpha_y - \rho_y\alpha_x)
\end{aligned} \tag{4.3.3}$$

where S and R are functions of the gyro angular increments $\Delta\theta$:

$$\bar{\alpha} = \frac{\Delta\bar{\theta}}{2}$$

$$S = \left(1 - \frac{1}{24}(\Delta\bar{\theta}\cdot\Delta\bar{\theta})\right)$$

$$R = \left(1 - \frac{1}{8}(\Delta\bar{\theta}\cdot\Delta\bar{\theta})\right)$$

This algorithm implementation is a third order quaternion expansion without the cross product term $\left[\frac{1}{6}\left(\frac{\bar{\theta}^*}{2}\times\frac{\bar{\theta}}{2}\right)\right]$. The cross product term approximates the angular velocity change between each axis from one iteration to the next. The modified algorithm does not affect the third order performance in the constant slew environment. In the coning environment, however, the modified algorithm will function with the bandwidth characteristics of a first order algorithm.

Each quaternion component, λ, ρ_x, ρ_y, and ρ_z, is formed from three 16 bit signed computer words with the resulting capacity up to a 45 bit signed word. Thirty-seven (37) significant bits were selected for the 100 iteration per second algorithm. One bit uncertainty during an iteration interval corresponds to a 0.01 meru uncertainty. The 50 and 25 iteration per second algorithms were implemented with 36 and 35 bits of significance respectively because the input gyro pulse scaling was halved with update time reduction.

The second subroutine of the attitude algorithm corrects the quaternion to maintain the unity constraint. It imposes the constraint that:

$$\lambda^2 + \rho_x^2 + \rho_y^2 + \rho_z^2 = 1 \tag{4.3.4}$$

by approximating the following equations:

$$\lambda' = \lambda d$$

$$\rho_x' = \rho_x d$$

$$\rho_y' = \rho_y d \qquad (4.3.5)$$

$$\rho_z' = \rho_z d$$

where

$$d = \frac{1}{\sqrt{\lambda^2 + \rho_x^2 + \rho_y^2 + \rho_z^2}}$$

4.3.4 Velocity Algorithm

The velocity algorithm constructs a cosine matrix from the quaternion which transforms a vector in the body frame to the inertial frame. The cosine matrix is expressed in terms of the quaternion element as:

$$C_B^I = \begin{vmatrix} 1-2(\rho_y^2 + \rho_z^2) & 2(\rho_x\rho_y - \lambda\rho_z) & 2(\rho_x\rho_z + \lambda\rho_y) \\ 2(\rho_x\rho_y + \lambda\rho_z) & 1-2(\rho_x^2 + \rho_z^2) & 2(\rho_y\rho_z - \lambda\rho_x) \\ 2(\rho_x\rho_z - \lambda\rho_y) & 2(\rho_y\rho_z + \lambda\rho_x) & 1-2(\rho_x^2 + \rho_y^2) \end{vmatrix}$$

and

$$\bar{V}^I = C_B^I \bar{V}^B$$

Figure 4.3.4 Velocity Algorithm

The directional cosine matrix elements are derived each update with 30 bits of significance. Hence, each element is accurate to 1 part in a billion.

4.3.5 Algorithm Evaluation

The three axis strapdown test system developed in this program permits the evaluation of the algorithm's performance characteristics in various environments. By selecting the test environment, specific error sources are isolated and therefore can be evaluated.

As background information, this section reviews prior simulation and analysis studies that define inherent algorithm performance characteristics. The areas of study include: 1) attitude algorithm small angle error studies, 2) pseudo coning drift evaluations, 3) coning environment studies, 4) algorithm slewing errors, and 5) algorithm round-off errors.

4.3.5.a Attitude Algorithm Small Angle Studies

A study by H. Musoff[11] evaluates the relationship between algorithm performance and small angle deviations that include alignment errors and gyro drift. The analysis uses system quaternion differential equations to determine that an earth rate compensated algorithm propagates attitude errors in the inertial frame as ramping sinusoids. The sinusoidal periodicity is a direct function of earth rate and therefore has a 24 hour period. The ramp slope and the peak to peak sinusoidal amplitude are linear combinations of the system alignment angles and gyro drift (see Appendix H).

Figures 4.3.5, 4.3.6, and 4.3.7 are the attitude errors in the inertial frame for a 63 hour test period with the system fixed to an east, down and north orientation (X, Y and Z axes respectively). The measured attitude errors match the theorectical results in two ways: 1) the attitude errors propagate as sinusoids, and ramps are observed only on the two axes with significant earth rate components (down and north) and, 2) the sinusoidal periodicity is 24 hours.

Since the attitude drift magnitudes are linear combinations of the system alignment errors and gyro drift, a solution was attempted to determine the error parameters from the measured drift error. An explicit solution was not possible because of insufficient number of independent equations. Instead, the data was analyzed with a comparison to SIRU system test in which a 0.5° alignment error was impressed about the vertical and east axes. The comparison, in terms of peak to peak sinusoidal magnitude, is given below:

TABLE 4.3.1 SPOT-SIRU COMPARISON
PEAK TO PEAK SINUSOID MAGNITUDE

	SIRU SYSTEM (0.5° Alignment Offset)	SPOT SYSTEM
VERTICAL AXIS	20.0 m radians	1.6 m radians
NORTH AXIS	18.0 m radians	1.6 m radians
EAST AXIS	24.0 m radians	2.0 m radians

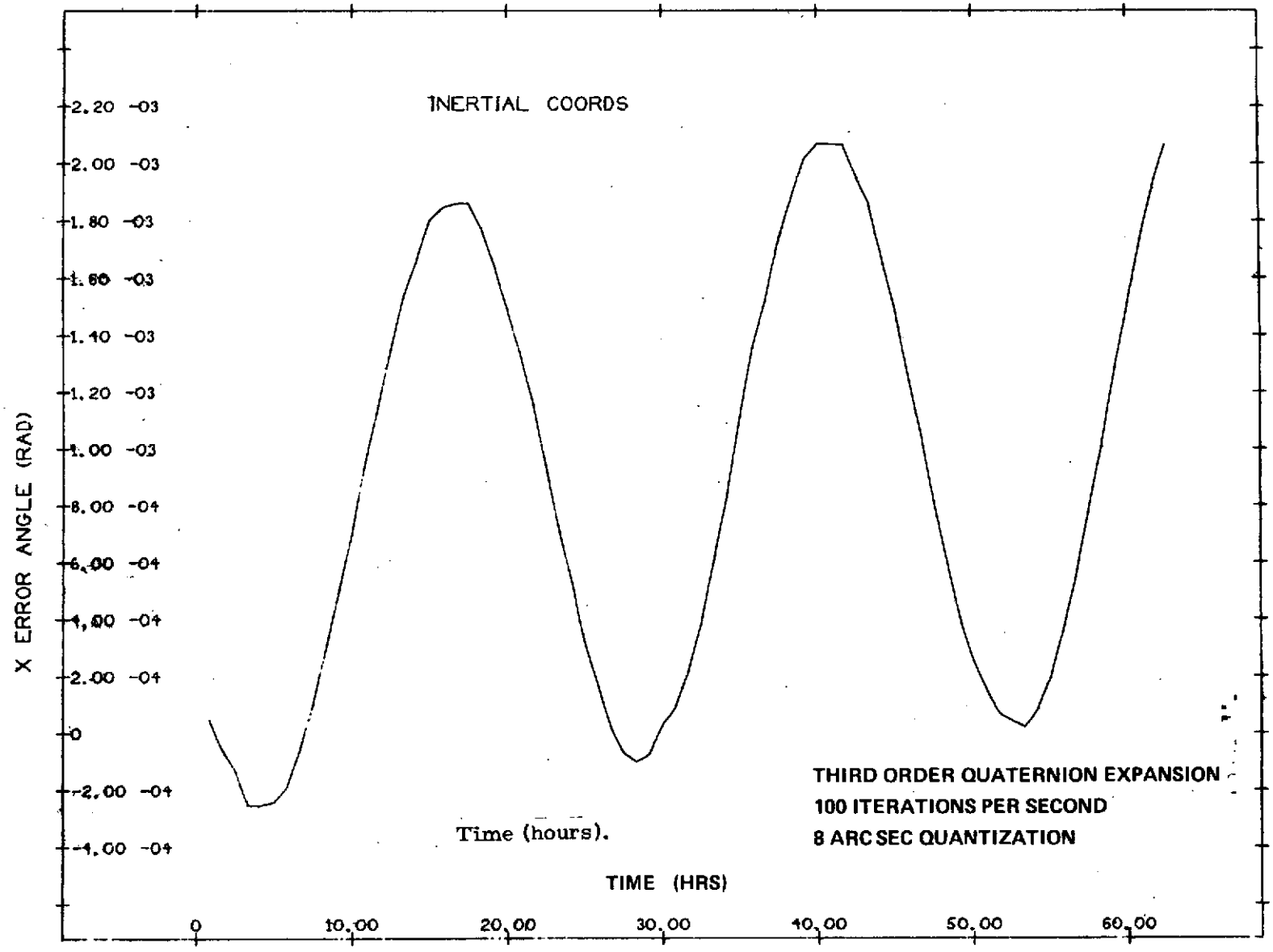

Fig. 4.3.5 East Axis Attitude Error

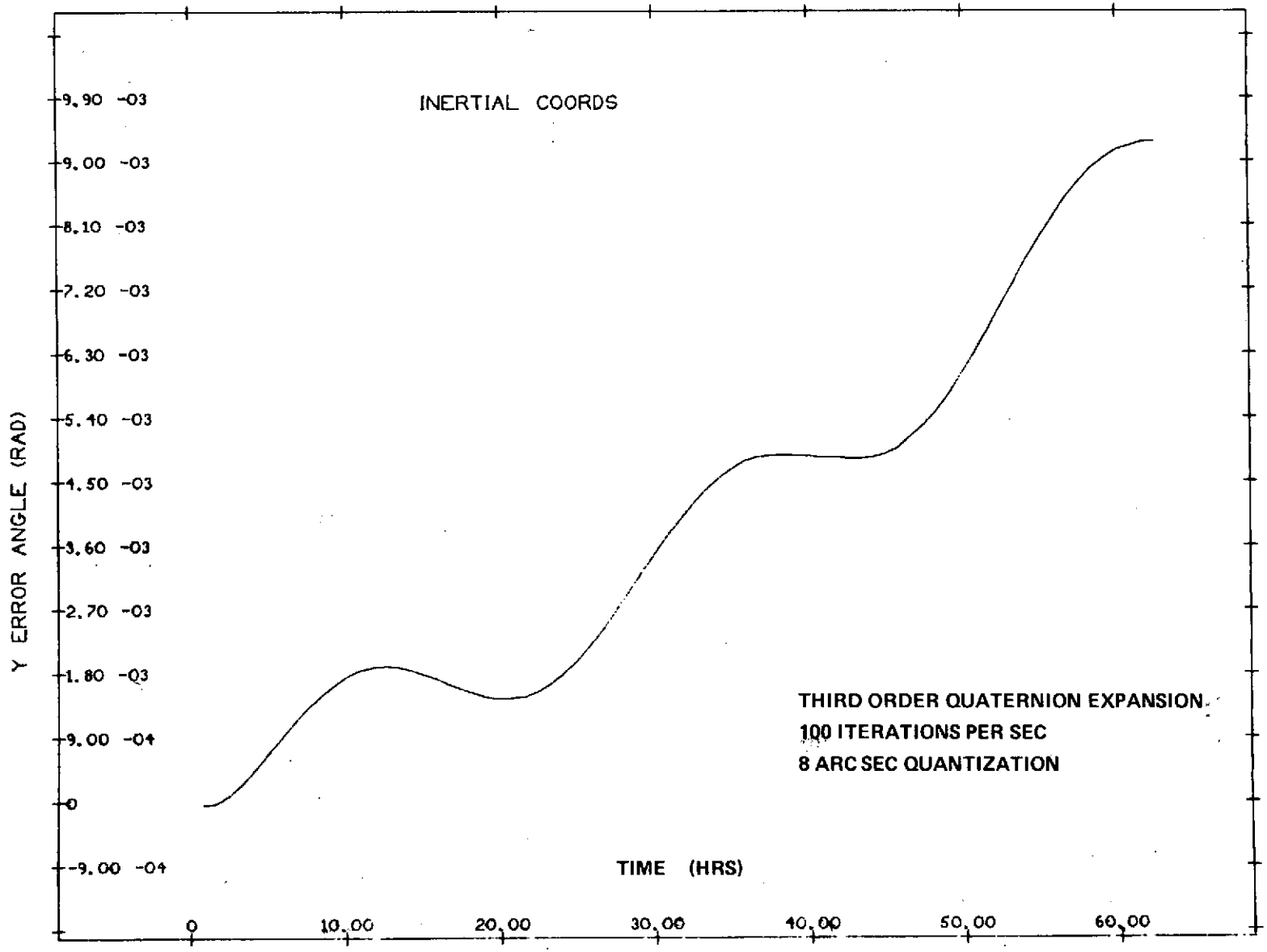

Fig. 4.3.6 Vertical Axis Attitude Error.

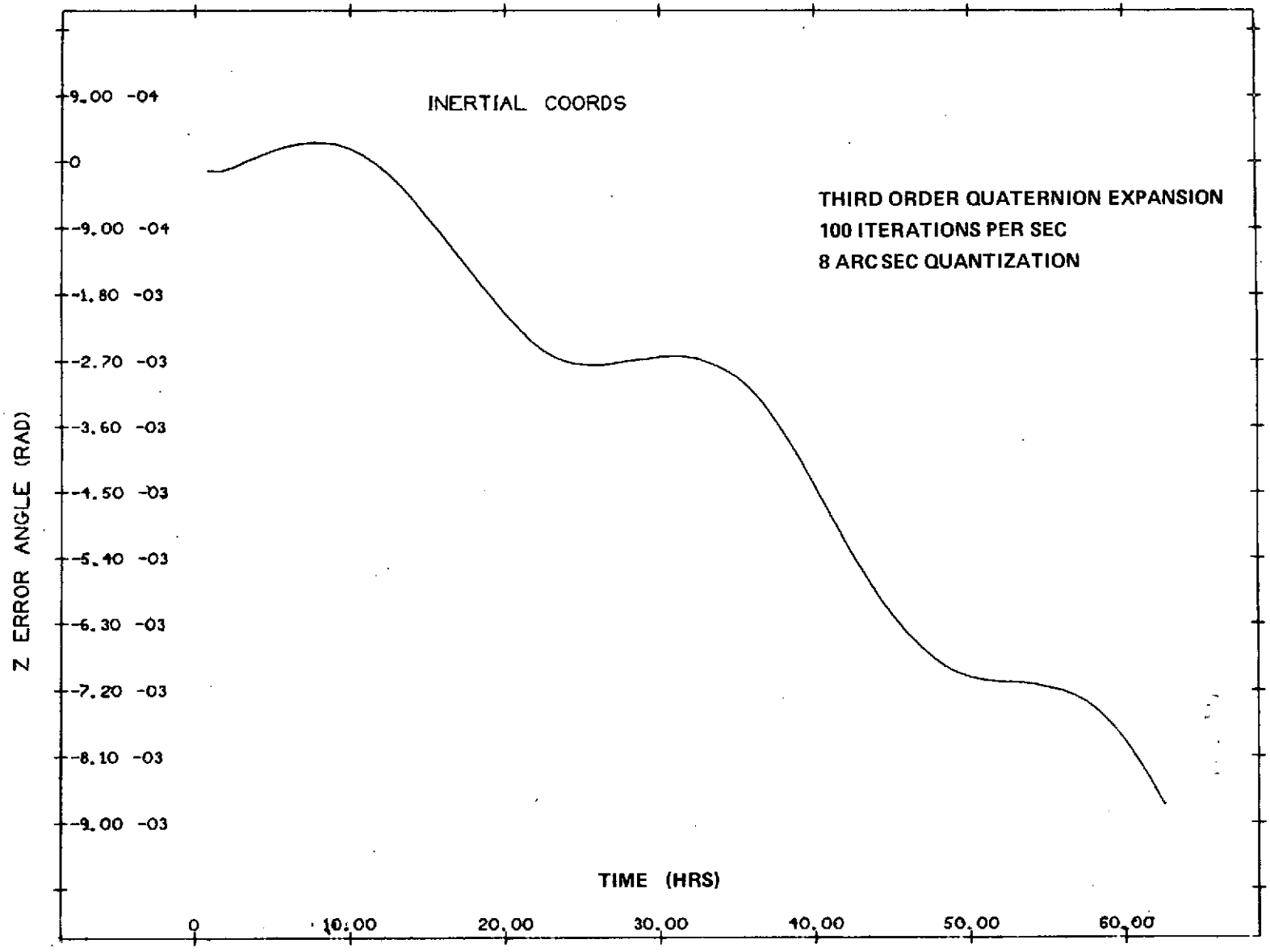

Fig. 4.3.7 North Axis Attitude Error.

The ten to one ratio between the SIRU and SPOT sinusoidal amplitudes implies that the SPOT alignment error is no greater than 0.05^{o}. This alignment calculation however neglected the gyro drifts residuals and assumed a linear relationship between the alignment errors and the peak to peak siniousidal magnitude. Thus, the actual alignment error is considerably less than 0.05^{o}.

4.3.5.b Pseudo Coning Drift Evaluations

Pseudo coning drift results if OA coupling errors are not compensated. As an example, in a single axis oscillatory environment without OA coupling compensation, the attitude algorithm is excited on two axes. The first axis is the normal input oscillation sensed by the gyroscope whose input axis is along the axis of oscillation. The second axis results from OA coupling errors. The OA coupling error is a function of the float inertia response and is proportional to the derivative of the input oscillatory motion. Thus;

$$\text{input oscillation excitation} = a \sin\omega t$$

$$\text{OA coupling error} = I/H\, a\omega \cos\omega t$$

where

a is the peak oscillatory amplitude (4.3.6)

ω is the oscillatory frequency

I is the float inertia about OA

H is the angular momentum

If OA coupling errors are not compensated, the attitude algorithm operates on both inputs, assuming them to be true oscillatory inputs that are displaced by 90^{o} and corrects for a non-existent kinematic coning drift on the third axis. The resulting effect is the generation of an attitude drift error that is exactly equal to:

$$\text{pseudo coning drift} = \frac{I a^2 \omega^2}{2H} \qquad (4.3.7)$$

The pseudo coning drift test evaluations that are described in Section 5.2 were conducted using gimbal oscillatory excitations over a range of 0.5 to 25 hertz. (The closed loop response for the outer and inner gimbals for the above test spectrum is illustrated in Appendix A, Figure A.1). The effective pseudo coning error generated in the gimbal test system for various test inputs is illustrated in Table 4.3.2.

TABLE 4.3.2 PSEUDO CONING ERROR MAGNITUDES

Oscillatory frequency (hertz)	Outer gimbal amplitude (radians)	Pseudo Coning Drift meru	^{o}/HR
0.5	0.024	77	1.15
1.0	0.024	308	4.62
3.0	0.011	605	9.08
5.0	0.0057	434	6.66
10.0	0.0015	120	1.8
25.0	0.0002	11	0.17

Coning Evaluations

True coning, unlike pseudo coning, is a kinematic drift that occurs in the single-degree-of-freedom gyro mechanization in a multi-axis oscillatory environment. Coning is evaluated with two phase displaced oscillations with identical frequency applied to two of the three orthogonal axis, and thereby causing the third axis to trace a cone at an angular rate equal to the rotation frequency and with an amplitude proportional to the product of the input excitation. The third axis senses a rate equal to:

$$\text{Drift Rate} = \frac{a\, b \sin\phi}{2}\, \omega \qquad (4.3.8)$$

where

a and b are the peak oscillatory amplitudes

ϕ is the phase displacement between the oscillatory inputs

ω is the oscillatory frequency

Coning drift is corrected by sensing the sinusoidal inputs and their relative phase, and subtracting from the third axis the appropriate drift magnitude. Attitude algorithm coning performance is therefore related to its bandwidth.

Figure 4.3.8 shows the performance of three algorithm orders in the coning environment.[9] Coning error (defined by the ratio of algorithm output drift magnitude

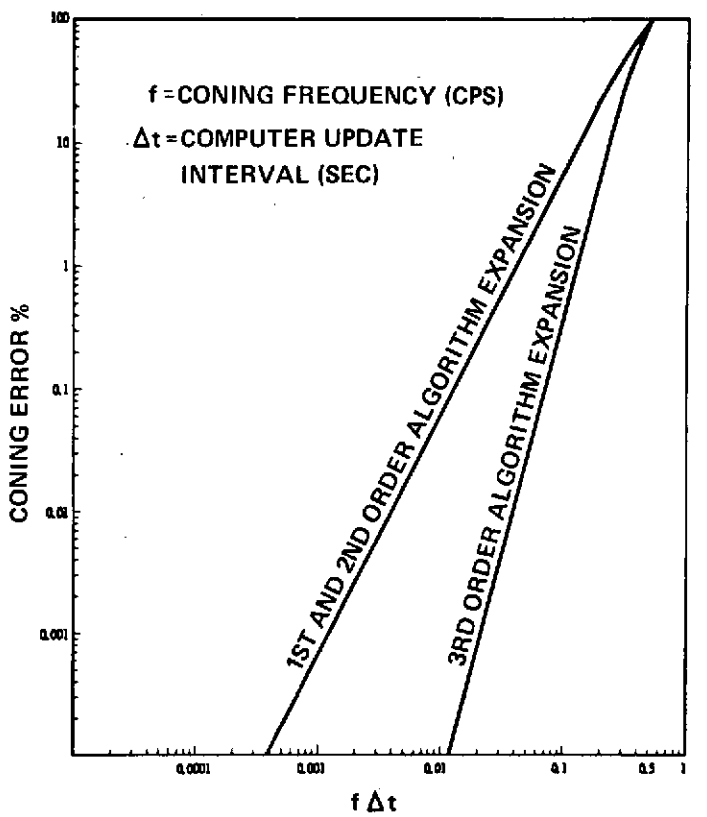

Fig. 4.3.8 Normalized Coning Response.

to the coning drift input) is plotted as a function of the oscillatory frequency (f) multiplied by the computer update interval (Δt).

With regard to the use of the Figure 4.3.8, one can determine the coning error in a specific strapdown computational mechanization for a known coning environment in the following manner. Assume a first order algorithm operating at 100 iterations per second. Then for 1 Hz coning input frequency the $f\Delta t$ point on the abscissa of Figure 4.3.8 corresponds to 0.01. The percentage coning error that would propagate would then, from the curve correspond to approximately 1% on the ordinate for the first order curve. The resultant coning drift rate would then correspond to 1% of the solution to Equation 4.3.8 for the specific cone angles and frequency.

The algorithm performance curves in Figure 4.3.8 are derived using small angle approximations (coning amplitude is less than 5^{o}), and with zero algorithm quantization. With quantization, time lags are introduced into the attitude information and SRA cross coupling errors become more significant. Coning performance is also influenced by quantization. At low frequencies, coning performance tends to degrade due to quantization however, at higher frequencies the quantization effects are masked by the effects of the finite iteration interval and the performance closely follows the curve shown in 4.3.8.

Note, that the first - and second- order algorithms performance are identical. These results agree with computer simulations by Otten [12], and illustrate the similarity of their algorithm bandwidth characteristics. The significant improvement observed by the third order algorithm is related to the use of both past and present incremental gyro outputs. The point $f \Delta t = 0.5$, represents the theoretical limit in the ability of any algorithm to recognize any coning input. That is, at least two samples for each cycle of a sinusoidal input are required for adequate input recognition.

The algorithm performance characteristics generated in Figure 4.3.8, assume a symmetrical coning input. The same results also apply to non-symmetrical inputs, as was imposed by the gimbal test system, since the coning error term is a squared trigonometric function.

The effective coning environment based on gimbal oscillatory data and the expected first-order algorithm performance is given in Table 4.3.3.

TABLE 4.3.3 CONING ENVIRONMENT

Frequency (hertz)	Amplitude (radians) Inner Gimbal	Outer Gimbal	Coning Input meru	°/HR	Coning Error for a 100 update/second algorithm (%)
0.5	0.022	0.024	11,930	179	0.012%
1.0	0.022	0.024	23,720	356	0.05%
5.0	0.011	0.0057	13,600	204	1.4%
10.0	0.004	0.0015	2,800	42	6.0%
25.0	0.0006	0.0002	110	1.6	25.0%

4.3.5.c Algorithm Slewing Errors

For a constant-slew rate the rotational angle error for various orders of algorithm expansion is given in Table 4.3.4 where θ is the total angle traveled over the update interval.

TABLE 4.3.4 ALGORITHM SLEWING ERRORS

Algorithm Order	Three Axis Slewing Error	Unit Length Degradation Error
1	$\frac{\theta^3}{12}$	$\frac{\theta^2}{4}$
2	$\frac{\theta^3}{24}$	$\frac{\theta^4}{64}$
3	$\frac{\theta^5}{480}$	$\frac{\theta^4}{192}(1 - \frac{\theta^2}{12})$

A trade-off exists in selecting the iteration interval with respect to slew rate because the errors are dependent on the angle accumulation per update. For high slew inputs, a relatively fast iteration rate is required to minimize the generated error. Figure 4.3.9 illustrates these trade-offs.

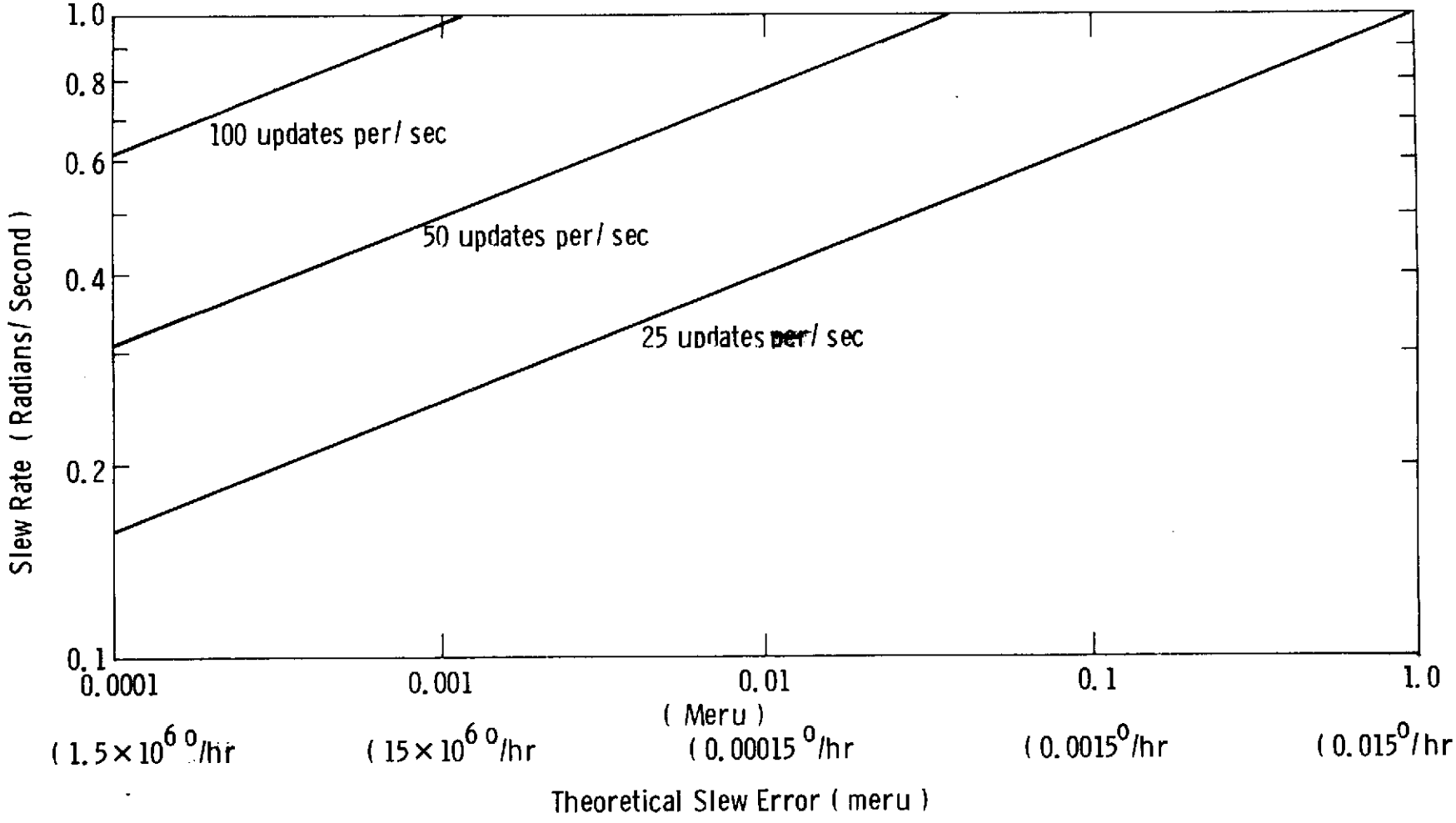

Fig. 4.3.9 Slew Error Tradeoffs.

The slewing errors are negligible with a third order algorithm. At 25 iterations per second in a one radian per second environment the slewing error is less than 1.0 meru (0.015° 1 HR).

4.3.5.d Algorithm Round-off Errors

Computer round-off errors result from the finite word length used in implementing the algorithms. In this system, the 100 iterations per second algorithm uses 37 bits per word, and the 50 and 25 updates per second algorithms use 36 and 35 bits respectively.

Computer simulations [14] have established that round-off errors propagate as sinusoidal functions. Hence, in the long term, the error averages to zero. The frequency of propagation is equal to the quaternion frequency which is half the mechanical slewing frequency of the instrument package. The error magnitude is a function of the arithmetic operations required in each iteration. Therefore, its magnitude is independent of the mechanical slew rate, and is a function of both the algorithm expansion order and computer word length. The peak round-off error increases with algorithm complexity and therefore the error will differ for the same algorithm order depending on the computational efficiency of the particular program coding and the number of operations. Hence, the third order algorithm without the cross product term has less round-off errors. The peak magnitude for a complete third order algorithm (including cross-product term) is given in Table 4.3.5.

TABLE 4.3.5 PEAK ROUND-OFF ERRORS

Algorithm Implementation	Single Axis Slew Environment	Three Axis Slew Environment
100 updates/second	0.1 meru (0.0015°/HR)	1.0 meru (0.015°/HR)
50 updates/second	0.3 meru (0.0045°/HR)	1.2 meru (0.018°/HR)
25 updates/second	0.4 meru (0.006°/HR)	1.4 meru (0.021°/HR)

These errors are not considered significant because of the averaging effect.

4.4 Error Quaternion

The fine grain evaluations of the real time compensation and attitude algorithms requires the comparison of the quaternion generated from the attitude algorithm to

a perfect quaternion based on attitude data furnished from the resolver encoders and system alignment calibration data.

The perfect quaternion is defined as a unit quaternion that transforms an arbitrary vector in the body frame (B) to an earth fixed navigation frame (N) that coincides with the rotary table axes of east, down and north.

$$\text{Perfect quaternion} = (\bar{q}_B^N)_p$$

Such that

$$\overline{V}_N = (\bar{q}_B^N)_p \; \overline{V}_B \; (\bar{q}_B^N)_p^* \tag{4.4.1}$$

The perfect quaternion is developed entirely from the angular rotations that isolate the strapdown body frame from the navigation frame. These isolating rotations include: the gimbal orientation, resolver alignment errors, gimbal nonorthogonalities and table leveling errors.

The quaternion that is computed from the attitude algorithm output is also a unit quaternion relating the body frame to the navigation frame, but with a different formation.

$$\text{Computed quaternion} = (\bar{q}_B^N)_c \tag{4.4.2}$$

where:

$$(\bar{q}_B^N)_c = (\bar{q}_I^N)\,(\bar{q}_{B0}^I)\,(\bar{q}_B^{B0})$$

$\bar{q}_B^{B0}$ a unit quaternion equal to the output of the attitude algorithm. It relates a vector in the body frame at any time to the body frame at t = 0. Thus at t = 0, $\bar{q}_B^{B0} = (1, 0, 0, 0)$

$\bar{q}_{B0}^I$ a unit quaternion that relates the body frame at t = 0, to an inertial frame of reference. It is a time independent transformation since the inertial frame never moves and the body frame at t = 0 is also fixed.

$\bar{q}_I^N$ a unit quaternion which depends only on the earth's rotation

$$\bar{q}_I^N = \cos \text{wiet}/2 + (\bar{j}\,\frac{\text{wiev}}{\text{wie}} - \bar{k}\,\frac{\text{wieh}}{\text{wie}})\sin \text{wiet}/2 \tag{4.4.3}$$

wieh - horizontal earth rate component

wiev - vertical earth rate component

$$wie = \sqrt{wiev^2 + wieh^2}$$

The error quaternions are formed by comparing the perfect and computed quaternion as follows:

error quaternion in the body frame

$$\bar{q}_{eB} = (\bar{q}_B^N)_p^* (\bar{q}_B^N)_c \tag{4.4.4}$$

error quaternion in the inertial frame

$$\bar{q}_{eI} = (\bar{q}_B^N)_p (\bar{q}_B^N)_c^* \tag{4.4.5}$$

Derivations of the error quaternions are given in Appendix I and J. In the body frame the error quaternion represents the transformation between two body frames: the actual body frame and the computed body frame. This means that the error quaternion in the body frame is the difference between where the body actually is, and where the algorithm indicates it is. Likewise the error quaternion in the inertial frame represents the transformation between the true inertial frame and the computed inertial frame.

To demonstrate the significance of the above error quaternions, an analysis is included in Appendix K which illustrates the effects of alignment errors, gyro scale factor errors, and gyro drift on attitude error propagation in a slew environment.

A IBM 360/75 program is implemented to compute and plot error quaternions in the body and inertial frames. The software is written to accept the system quaternion and angular encoder information from either magnetic tapes or via the Bell 201A data set link. Program flexibility is incorporated to bypass select data points, provide data smoothing and to select the range of the ordinate scale.

4.5 Land Navigation Software

An inertially stabilized land navigator [15,16] is implemented for real time processing in the H316 computer. The block diagram of the navigation algorithm is given in Figure 4.5.1 and the difference equations in Appendix L. The navigation algorithm operates at one iteration per second with information inputs provided by the strapdown system and associated compensation algorithms.

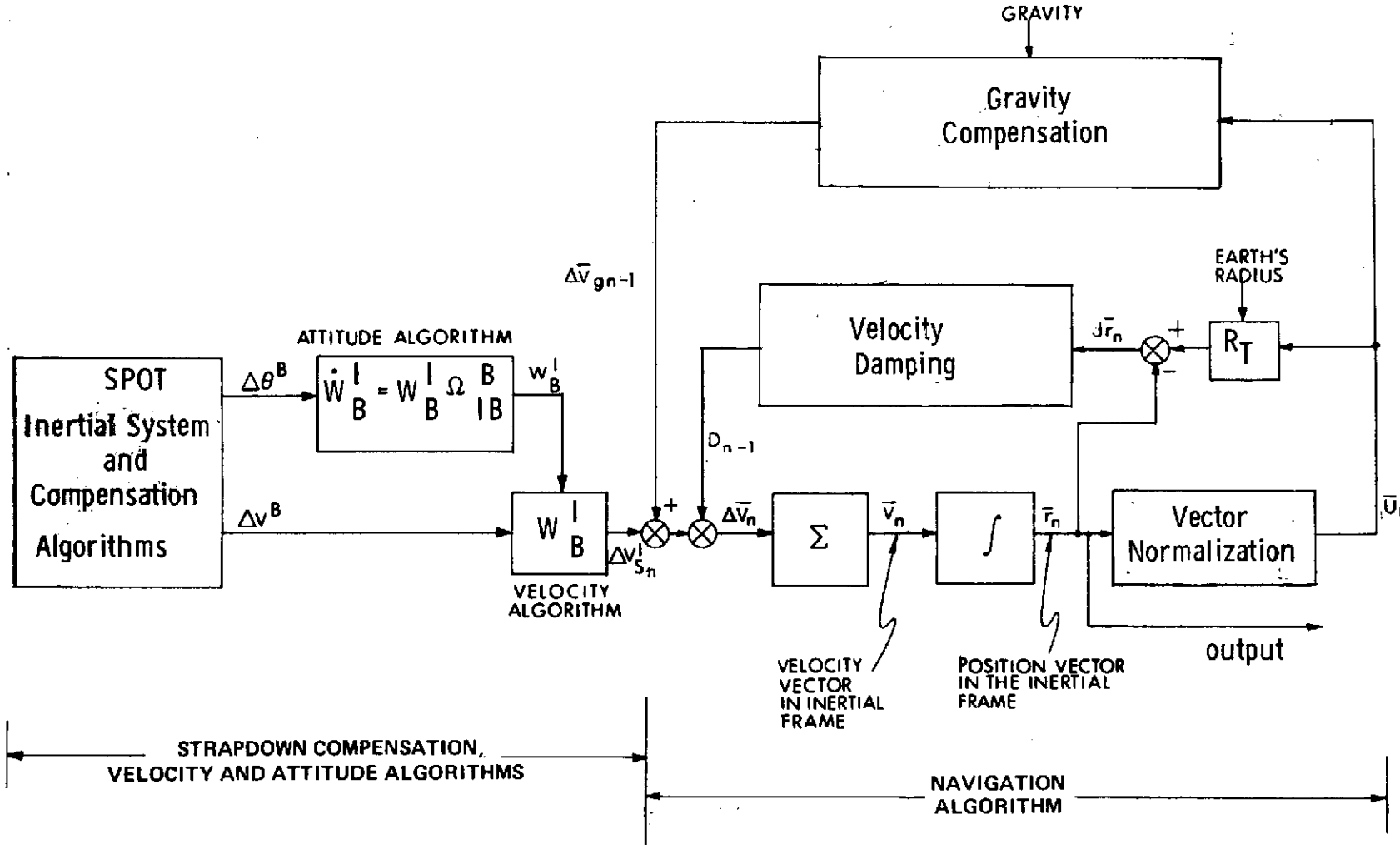

Fig. 4.5.1 Inertial Reference Navigator.

The inertially stablized land navigator computes the velocity and position vectors in the inertial coordinate frame. Forty-five (45) bits of accuracy are used.

A local vertical navigator was also considered for implementation, however, greater programming complexities were expected because of Coriolis force compensation requirements. The advantage of the local vertical navigator is that latitude and longitude parameters are derived in the navigation frame and therefore conversion computations are not required. For this reason the local vertical navigator provides a better interface for analysis and display purposes.

The inertially stablized navigator by performing computations in the inertial frame that is earth centered and non-rotating and therefore does not require coriolis computation. Hence, its algorithm is less complex to implement. The position vector in this implementation (shown in Figure 4.5.2) is earth centered and describes location (P) on the earth's surface. Note that the Z component is along the polar axis, and the X and Y components are orientated in the equatorial plane with Y axis east. From this vector latitude and longitude parameters are then derived. For ease of use, the latitude and longitude parameters are computed remotely using the IBM 360/75 computer via the magnetic tape interface. Appendix L describes the analysis algorithm.

4.6 Diagnostic and IBM 360/75 Remote Terminal Programs

In addition to the calibration and compensation software diagnostic and analysis software are required for hardware and software verification, and for parameter computations.

The verification of the complex algorithms required the writing of various diagnostic programs in the H316 language. These programs verified the integrity of the algorithm's instruction; their sequence and interface with the system's hardware.

The IBM 360/75 computer and its remote terminal facility provides quick turnaround capabilities that proved indispensable to system calibration and analysis software development.

The H316 diagnostic and IBM 360/75 remote terminal programs are listed, with a brief description, in appendix (M).

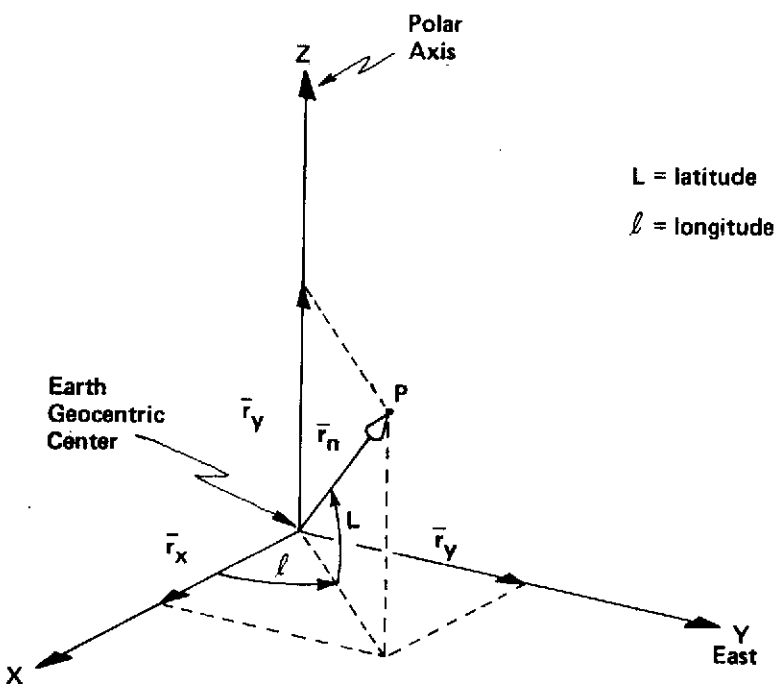

Position Vector $\bar{r}_n = \bar{r}_x + \bar{r}_y + \bar{r}_z$

Fig. 4.5.2 Navigation Position Vector.

5.0 Evaluation Results

5.1 Calibration Results

5.1.1 Introduction

Inertial instrument calibration is necessary for the fine grain evaluation of strapdown system performance. Without accurate calibration data, the isolation of algorithm quantization and bandwidth errors from the inertial instrument error sources is not possible. Periodic calibration is therefore required to establish the current instrument calibration. The automatic test facility permitted instrument certification nightly. In addition, the large amounts of system calibration data provided meaningful statistical insights into the short and long-term data characteristics.

This section discusses the calibration procedures and results. First discussed is the gimbal alignment calibration results that determines the strapdown package orientation with respect to an earth fixed reference frame. The gimbal calibration results demonstrate gimbal alignment shifts with system temperature cycling and that a linear correlation exists between accelerometer calibration data and the gimbal's alignment. These results are important in that they allowed the routine verification of gimbal alignment with accelerometer data.

Static calibration results are next discussed in terms of their short and long term statistics. Statistical evaluations of gyro calibration data demonstrated less than one meru (0.015°/HR) drift stabilities between instrument calibrations. This conforms to the program's requirement. Evaluation of the gyro data over a sixteen month period has established a level of performance across several system cooldowns and wheel start - stop sequences. The accelerometer data is presented in Volume II.

Dynamic calibration discussions include gyro scale factor and alignment calibration, anisoinertia calibration, and verification of accelerometer centripetal acceleration effects.

5.1.2 Gimbal Calibration

For this test program, since the gimbal system is the test bed, the determination of the orientation of the inner gimbal package with respect to an earth fixed reference frame is extremely important. Thus, characteristic gimbal orientation errors associated with leveling errors, gimbal non-orthogonalities and resolver

misalignments were calibrated. The calibrations were then used in a transformation matrix to define the inner package attitude.

The gimbal alignment errors are defined in Appendix N and Figure 5.1.1 is the direction cosine matrix, using small angle approximations, that determines the strapdown package orientation (X_{ref}, Y_{ref}, and Z_{ref}) in terms of an earth fixed frame (X_e, Y_e, and Z_e. The earth fixed frame coincides to the test table triad of east, down, and north.

The gimbal calibration, a technique similar to Apollo gimbal calibration procedures, uses accelerometer nulls to calibrate the alignment errors. The attitude difference between the accelerometer's horizontally orientated Input Axis and the test table's horizontal axis defines a specific sum of gimbal alignment errors and accelerometer alignment and bias. Twenty-four (24) unique calibration positions are used with a simultaneous equation solution to isolate the required alignment magnitude. The calibration uncertainty, a function of accelerometer and test table positioning uncertainties, is seven (7) arc seconds (0.034 milliradians). Appendix N lists the calibration positions and calibration equations. The calibration computations are performed on the IBM 360/75 remote terminal facility.

Gimbal calibration data was periodically obtained during the course of the program. Review of the data illustrates a gimbal alignment stability within the calibration uncertainties (0.034 milliradians) for benign test periods that included no gimbal disassemblies and temperature cycling. Three system cooldowns to room temperature (70^{o}F) were experienced during the observation period, reasons included building air conditioner maintenance, power outages and gyro wheel start problems. During one of these overnight cooldowns (9 August 1971), the gimbal alignment shifted greater than the measurement uncertainty. Specifically, the inner and middle gimbal resolver alignments (ϵ_{IGR} and ϵ_{MGR}) shifted 0.18 milliradians and the inner gimbal non-orthogonality (ϵ_{IGA}) shifted 0.098 milliradians. This occurrence demonstrated that even in a well designed gimbal system (Apollo 1 technology), structural expansion and contraction from temperature cycling can cause gimbal alignment shifts to require recalibration.

The gimbal alignment shift was also observed in the accelerometer calibration data. For benign test periods, the standard deviation of the accelerometer Input Axis alignment is generally 0.02 milliradians. Note that this magnitude is similar to the gimbal uncertainty. Over the 9 August 1971 cooldown, the accelerometer alignment shifted 0.15 milliradians which is equivalent in magnitude to the gimbal alignment shift. Hence, the gimbal alignment shift was detected in the accelerometer

$$\begin{bmatrix} X_{Ref} \\ Y_{Ref} \\ Z_{Ref} \end{bmatrix} = \underbrace{\begin{bmatrix} 1 & 0 & 0 \\ 0 & -1 & 0 \\ 0 & 0 & -1 \end{bmatrix}}_{\substack{\text{INNER MEMBER IS MOUNTED } 180^0 \\ \text{ABOUT THE X AXIS}}} \underbrace{\begin{bmatrix} \cos(\theta_{IG} + \epsilon_{IGR}) & 0 & \sin(\theta_{IG} + \epsilon_{IGR}) \\ 0 & 1 & 0 \\ -\sin(\theta_{IG} + \epsilon_{IGR}) & 0 & \cos(\theta_{IG} + \epsilon_{IGR}) \end{bmatrix}}_{\substack{\text{INNER GIMBAL ORIENTATION } (\theta_{IG}) \text{ AND} \\ \text{RESOLVER MISALIGNMENT ANGLE } (\epsilon_{IGR})}} \underbrace{\begin{bmatrix} 1 & 0 & 0 \\ 0 & 1 & \epsilon_{IGA} \\ 0 & -\epsilon_{IGA} & 1 \end{bmatrix}}_{\substack{\text{INNER GIMBAL} \\ \text{NON-ORTHOGONALITY } (\epsilon_{IGA})}} \times$$

$$\times \underbrace{\begin{bmatrix} \cos(\theta_{MG} + \epsilon_{MGR}) & \sin(\theta_{MG} + \epsilon_{MGR}) & 0 \\ -\sin(\theta_{MG} + \epsilon_{MGR}) & \cos(\theta_{MG} + \epsilon_{MGR}) & 0 \\ 0 & 0 & 1 \end{bmatrix}}_{\substack{\text{MIDDLE GIMBAL ORIENTATION } (\theta_{MG}) \text{ AND} \\ \text{RESOLVER MISALIGNMENT ANGLE } (\epsilon_{MGR})}} \underbrace{\begin{bmatrix} 1 & 0 & -\epsilon_{MGA} \\ 0 & 1 & 0 \\ \epsilon_{MGA} & 0 & 1 \end{bmatrix}}_{\substack{\text{MIDDLE GIMBAL} \\ \text{NON-ORTHOGONALITY } (\epsilon_{MGA})}} \times$$

$$\times \underbrace{\begin{bmatrix} 1 & 0 & 0 \\ 0 & \cos(\theta_{OG} + \epsilon_{OGR}) & \sin(\theta_{OG} + \epsilon_{OGR}) \\ 0 & -\sin(\theta_{OG} + \epsilon_{OGR}) & \cos(\theta_{OG} + \epsilon_{OGR}) \end{bmatrix}}_{\substack{\text{OUTER GIMBAL ORIENTATION } (\theta_{OG}) \text{ AND} \\ \text{RESOLVER MISALIGNMENT ANGLE } (\epsilon_{OGR})}} \underbrace{\begin{bmatrix} 1 & \epsilon_{fz} - \epsilon_{TR} & \epsilon_{fy} \\ \epsilon_{TR} - \epsilon_{fz} & 1 & \epsilon_{TT} + \epsilon_{fx} \\ -\epsilon_{fy} & -(\epsilon_{TT} + \epsilon_{fx}) & 1 \end{bmatrix}}_{\substack{\text{GIMBAL FIXTURE MISALIGNMENT } (\epsilon_{fx}, \epsilon_{fy}, \epsilon_{fz}) \\ \text{AND TABLE LEVELING ERRORS } (\epsilon_{TT}, \epsilon_{TR})}} \begin{bmatrix} X_E \\ Y_E \\ Z_E \end{bmatrix}$$

FIGURE 5.1.1 - GIMBAL DIRECTION COSINE MATRIX CHAIN

calibration data. Restoration to the baseline accelerometer alignment measured prior to the cooldown was achieved when the gimbal system was re-calibrated.

The interdependency between gimbal and accelerometer alignment data demonstrates the usefulness of the accelerometer data to monitor the gimbal calibration status. Rather than calibrating the gimbal alignment on a periodic basis, a task that requires considerable time, calibration is necessary only when the accelerometer data indicates that it is warranted. Of additional interest is the possibility that the accelerometer alignment data can be used in an adaptive process to correct gimbal alignment anomalies. Thus, a system alignment maintenance capability based on accelerometer inputs may exist and therefore warrants future study of possible implementation.

5.1.3 Static Calibration

A twelve position procedure is used to calibrate the gyro drift components and the accelerometer's scale factor, null bias and alignment angles. In each of the twelve positions, gyro $\Delta\theta$ pulses and accelerometer ΔV pulses are accumulated for a ten minute test period. Six of the twelve position are cardinal test positions with each triad axis orientated, up and down, along a vertical axis. The six remaining test positions orientate the triad at an offset angle of 45° from the vertical for major compliance (anisoelasticity) calibration. The test positions are given in Appendix P with the pertinent calibration equations.

The gyro calibration model is a five parameter model (see Appendix D) comprising the non-acceleration sensitive drift component (NBD), and the three acceleration sensitive drifts: ADIA, ADOA, and ADSRA, and major compliance ($K_{SS} - K_{II}$).

$$\overbrace{SFX\ I_{TG}}^{\text{Commanded Torque}} = \overbrace{H_S \omega_{IRA}}^{\text{Input Axis Rate}} + \overbrace{NBD}^{\text{Acceleration in Sensitive Torque}} + \overbrace{(ADIA)a_I + (ADOA)a_O + (ADSRA)a_S}^{\text{Acceleration Sensitive Torques}}$$

$$+ \overbrace{(K_{SS} - K_{II})a_S a_I}^{\text{Acceleration Square Torque}} + \overbrace{A_{ORA} f(\omega_{Ie}) + A_{SRA} f(\omega_{Ie})}^{\text{Misalignment Angles}} \qquad (5.1.1)$$

Gyro Calibration Model

four overnight calibrations (designated as one-third day), 2) one calibration per day for three consecutive days, and 3) one calibration per day for three weeks. The standard deviations are computed for each group; using 27 one-third day samples, 9 three day samples and 3 three week samples. Figure 5.1.2 is the histogram showing the average standard deviation for each period.

The one-third day stability is generally 0.5 meru (0.0075°/HR) or better and the three day stability is 1.0 meru (0.015°/HR). This performance level is adequate for the maintenance of calibration intergity for the fine grain strapdown evaluations.

Gyro 415 has the best overall stability, however, the results are inconclusive with regard to rating the performance of the 410 series, 18IRIG Mod B gyro. The gyros selected for test may not represent the typical performance level of their respective gyro family. In addition, system level tests introduce various unknown parameters that are impossible to separate from the gyro performance. These parameters include: gimbal alignment uncertainty, positional (orientation in the IMU) sensitivities, and differences in the pulse torque electronics and power supplies, interface and noise levels.

Most of the statistics increase with the test interval. This increase may be caused by the randomness of data, changes across environmental variations, and/or a ramping drift with time (gyro MB-4 ADSRA has a ramp component of 10 meru/g per month).

Note that ADOA and major compliance are generally not time dependent.

The long term gyro drift performance (NBD, ADSRA, and ADIA) are plotted in Appendix Q for gyros MB-2*, MB-4, and 415. The test period encompasses a sixteen month period, April 1971 to July 1972, and therefore measures gyro performance across five system cooldowns and six wheel stop-start sequences that are described also in Appendix Q.

The long term drift data illustrates known generic physical design performance problems of the early 18IRIG Mod B gyro family used in this test program. One such problem is ADIA and ADSRA shifts across cooldowns. For example, MB-2, measured a 20 meru/g change (0.30°/HR) across the 9 August 71 cooldown. This cooldown sensitivity has been attributed to structural instabilities caused by

* The MB gyro population was fabricated by Bendix.

Gyro scale factor and the two gyro alignment angles are also included in the calibration model, however, their values are entered as known quantities from dynamic calibration data. Hence, an iterative process is necessary for gyro calibration between the static and dynamic procedures.

With each accelerometer sensitive drift component calibrated, a gyro bias drift value is obtained; NBDI, NBDO, and NBDS respectively for the Input Axis, Output Axis, and Spin Reference Axis orientated vertically. It has been observed that differences exist between the three bias drift magnitudes, for example, NBDI≠NBDO≠NBDS. This difference is caused by positional sensitivities as affected by measurement uncertainties and thermal gradients. Clearly, because the phenomenon is observed in both gimbal and strapdown systems, additional study of fine grain system calibration procedures is warranted. For compensation purposes, the average of the three values (NBDI, NBDO, NBDS) is used and for gyro MB-2 this has been determined to be the least square value.

The accelerometer model (see Appendix C) comprises a single null bias, two alignment angles, and separate scale factors for positive and negative acceleration inputs.

Indicated Output		Input Axis Acceleration		Accelerometer Bias		Misalignment Errors	
$\frac{A_O}{SF^+ \text{ or } SF^-}$	=	A_i	+	B_O	+	$A_{ORA}a_P - A_{PA}a_O$	(5.1.2)

Accelerometer Calibration Model

The acceleration parameter calibration is based on a four position calibration procedure. Section 5.4 presents the results of studying higher order accelerometer models with data inputs from up to 48 test positions. The similar five parameter accelerometer model, however, proved satisfactory with accelerometer compensation results verified within the uncertainty of the null bias. The accelerometer calibration results are presented and discussed in Volume II of this report.

The automatic test facility is used to sequence the strapdown package through the twelve positions required for inertial instrument calibration. Overnight calibration (four complete calibration cycles in a ten (10) hour period) were run periodically during the test period. During the four month period (19 May 1971 to 16 September 1971) 180 sets of calibration data were compiled for each inertial instrument. This data population was divided into three groups: 1) three of the

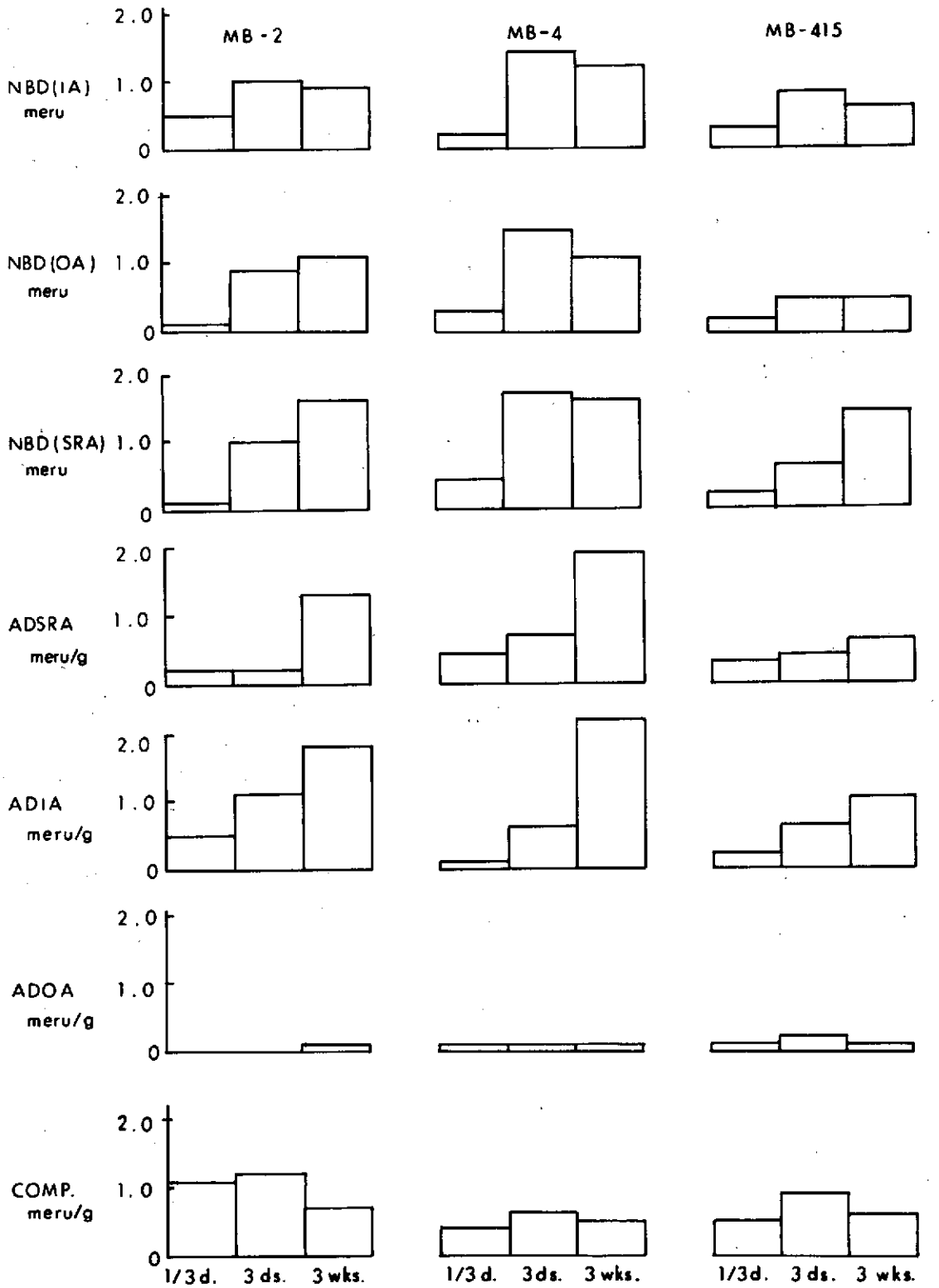

Figure 5.1.2 Calibration Standard Deviations - 180 Data Points Per Gyro
(19 May 1971 to 16 September 1971)

dissimilar materials used, for example, the torquer coil support (beryllium-oxide-ceramic) and the float (beryllium), and material mismatches in the wheel assembly. Significant improvements are anticipated with the 18IRIG Mod D gyro which is designed with a PM torquer and an integral beryllium oxide coil support that is the sleeve for the entire beryllium oxide float body. It also has an integral wheel gimbal assembly and the balance adjustment screws have been eliminated.

A second generic problem is the exponential change of ADSRA over a long period of time. Gyro MB-4 ADSRA shifted 80 meru/g over a sixteen month period with a two month time constant. Such shifts can be attributed to the floatation fluid filling empty cavities and thereby shifting the center of gravity over a period of time [14]. The 18IRIG Mod D gyro has been designed with many improvements including the elimination of adhesive joints between dissimilar materials. Data on several instruments has verified that this drift change phenomenon has been eliminated.

5.1.4 Dynamic Calibration

5.1.4a Gyro Scale Factor and Alignment Calibration

A three position procedure is used to calibrate gyro scale factor and alignment angles. In each position, positive and negative constant rotational rates are impressed about a horizontal, east-west orientated axis. The calibration positions and equations are given in Appendix R.

Data accumulation is achieved within an exact revolution of the applied rate. Therefore, the contribution of the acceleration sensitive drift components averages to zero. The nonacceleration drift component is compensated from the accumulated torque pulses by an amount based on the drift magnitude and test duration. Second order effects such as anisoinertia are not considered in the scale factor calibration because of their insignificant effect (less than 0.05 ppm).

Gyro scale factor calibrations are achieved automatically at a rate of 0.066 radians per second. From the accumulated system test data, a six (6) hour standard deviation of 5.0 ppm and a two (2) month benign test period standard deviation of 12 ppm was demonstrated. The gyro alignment stability is established as 50 microradians (10 arc second), primarily a test resolution uncertainty resulting from the alignment uncertainties of the gimbal system.

5.1.4.b Anisoinertia Calibration

A three position calibration procedure is designed to calibrate the low frequency anisoinertia coefficient, defined by:

$$\text{Anisoinertia coefficient} = \frac{I_{SA} - I_{IA}}{H} \qquad (5.1.3)$$

I_{SA}, I_{IA} are the float inertias about the Spin Axis and Input Axis respectively. H is the wheel angular momentum.

The anisoinertia calibration procedure was based on orienting the inner and middle gimbals with a 45° offset so that the gyro Input Axis is 45° with respect to the horizontal. The outer gimbal axis is then rotated causing equal rates to be simultaneously impressed about the gyro Input Axis (IA) and Spin Reference Axis (SRA). In each test the gyro SA and IA bisector axis, (the axis of rotation) is along the east-west line. The calibration positions (7, 8 and 9) and calibration equations are given in Appendix R.

The accuracy of the anisoinertia calibration, however, was severely limited because of a high sensitivity to the gimbal alignment and pulse count uncertainties. Appendix S presents an analysis that defines the anisoinertia sensitivity to gyro scale factor errors, pulse count uncertainty and gimbal alignment errors. The sensitivity to gimbal alignment errors is inversely proportional to rotational speed. Because the rotational rate is limited to the full-on rate capability of the gyro loops, further improvement is not possible in the 45° offset calibration position unless the gyro input axis is oriented further from the axis of rotation. At this 45° angle, a 33% coefficient uncertainty was measured for every arc second of alignment uncertainty. With an offset of 67.5°, the measured sensitivity is 26% of coefficient change per arc second of gimbal alignment uncertainty. These uncertainty magnitudes severely limited the ability to calibrate anisoinertia in the gimbal test fixture.

Because the inertia difference ($I_{SA} - I_{IA}$) and the wheel angular momentum (H) parameters are constant parameters and are accurately measured during gyro fabrication, anisoinertia calibration was not considered critical in this program. Section 5.2.2 discusses the results of anisoinertia compensation using specification sheet values for gyro inertia and angular momentum.

5.1.4c Centripetal Acceleration Calibration

Centripetal acceleration calibration is conducted to demonstrate the centripetal acceleration phenomenon and to verify the spatial location of the accelerometers for accurate compensation.

Calibration is conducted by accumulating accelerometer (ΔV) pulses for four revolutions at selected rates from 0.066 to 1 radian per second. The accumulated pulses, weighted by the accelerometer scale factor, represents an indicated acceleration that includes null bias and centripetal acceleration. The null bias effects are removed and an indicated centripetal acceleration function is obtained, illustrated in Figures 5.1.3 and 5.1.4 for the Y and Z accelerometers respectively. The abscissa scale is rotational rate squared (ω^2), and therefore the linear slope is the distance between center of rotation to the accelerometer. The slope value agrees within 0.1 centimeter of mechanical drawing measurements. Hence, the centripetal acceleration compensation parameters are adequately determined from the mechanical drawings. The difference between the indicated acceleration at the positive and negative low rates is a function of testing and analysis uncertainties. Only three negative rotational rates were tested and without additional points, a more accurate determination of the calibration curve is not possible.

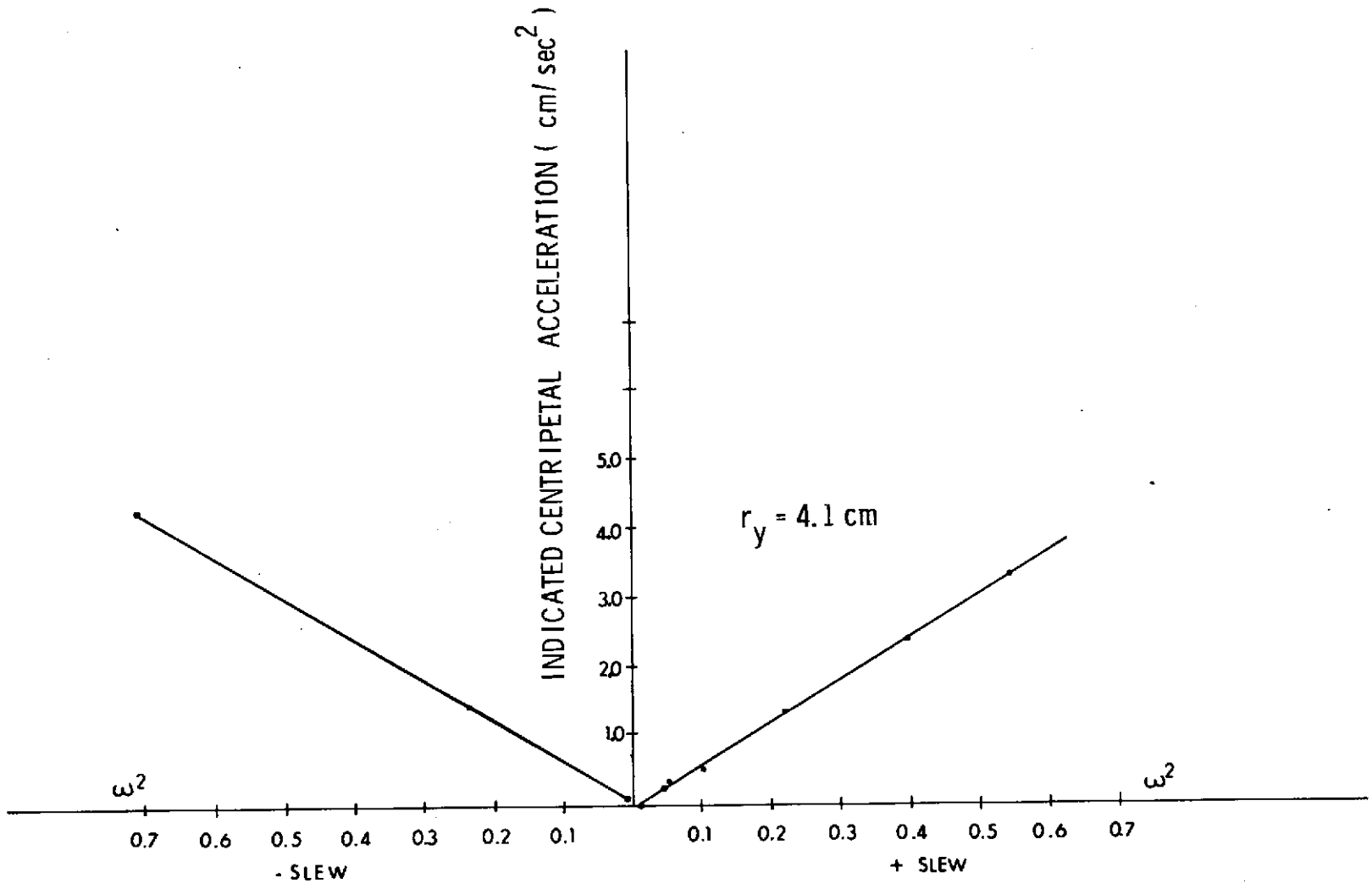

Figure 5.1.3 Centripetal Acceleration Calibration (Y Axis)

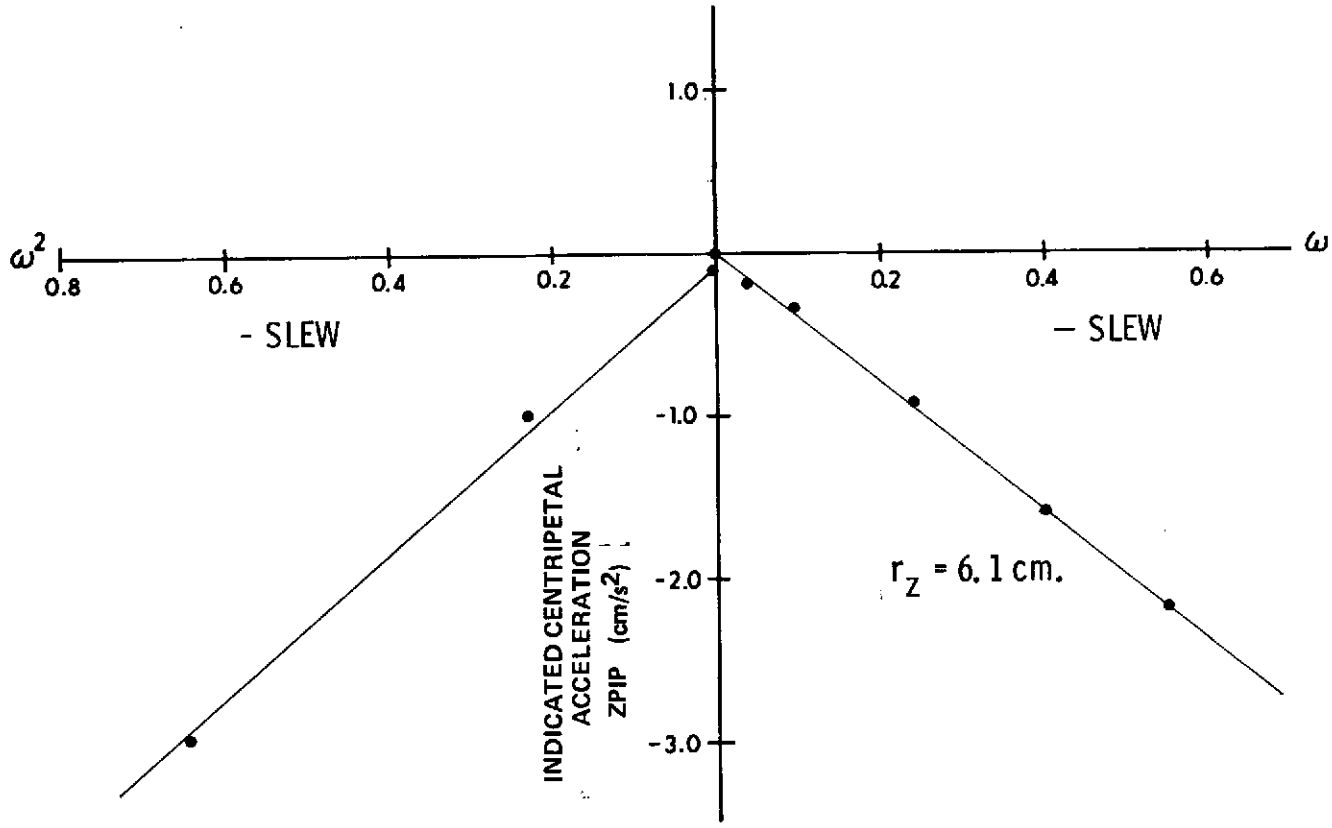

Fig. 5.1.4 Centripetal Acceleration Calibration. (Z AXIS)

5.2 Compensation Evaluation Results

5.2.1 Introduction

The main objective of this program is to evaluate the performance of an inertial strapdown system in dynamic environments. These evaluations centered on the verification of the real-time compensation models and techniques, discussed in Section 4.3.2, and on the understanding of strapdown performance limitations relating to system quantization and bandwidth.

Significant results are achieved in this program. The coning bandwidth has been measured and correlates well with theoretical results. Quantization effects in the coning environment were exhibited by an increase in the low frequency coning errors as a result of attitude lags.

The assimulation of the coning bandwidth data with OA coupling results allowed the determination of the inherent bandwidth of the OA compensation technique. The OA coupling compensation bandwidth is found to be a function of the sampling technique. From the analysis of the test results, it was observed that a more effective attenuation of OA error propagation is attainable when the OA compensation algorithm is operated at a higher iteration rate than the attitude algorithm.

Other results discussed in this text pertain to gyro scale factor linearity compensation (the results proved 7 ppm compensation effectiveness over the full dynamic range), and the compensation of anisoinertia and SRA cross coupling errors. Gyro quantization is found to proportionally affect the system attitude uncertainty.

The effective evaluation of strapdown error phenomenon requires the selection of a specific test environment to isolate the desired error parameter. Figure 5.2.1 depicts the SPOT gyro strapdown orientations with respect to a single axis slew (constant angular rate) test input. Tabulated in the Figure is a list of the error sources that are excited with respect to each body axis by a slew about the Z axis. The predominate error sources in this environment are the scale factor error of the gyro whose Input Axis is along the axis of rotation and the misalignments of the gyros whose IAs are perpendicular to the axis of rotation. Thus, the single axis slew environment is an effective test environment for evaluating scale factor compensation and scale factor linearity compensation. Analysis of the off-axis attitude error propagation allows one to size gyro alignment errors.

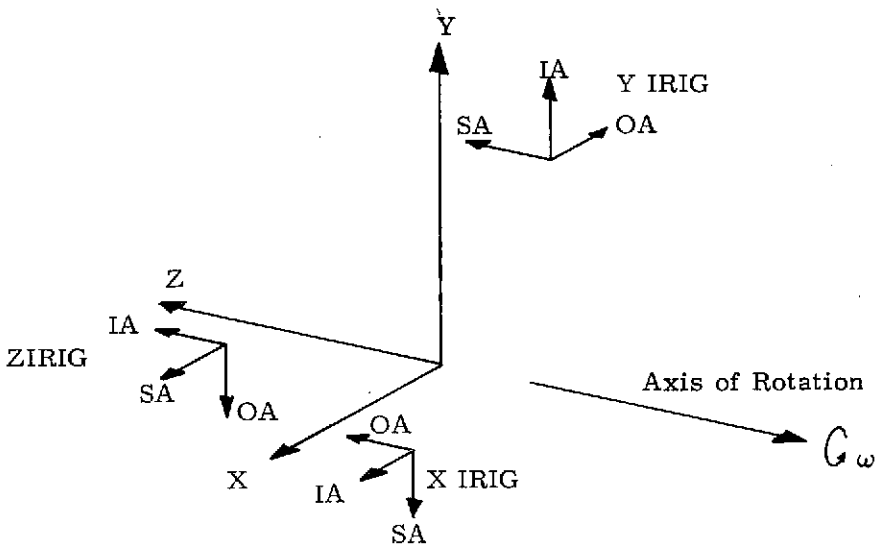

Error Sources

X axis	Y Axis	Z Axis
SA misalignment (XIRIG)	OA misalignment (YIRIG)	Scale factor compension error (ZIRIG)
OA coupling error during acceleration and deacceleration phases (XIRIG)		

Figure 5.2.1
Single axis slew environment (ω) about Axis Z

Figure 5.2.2 shows the gyro orientation with respect to simultaneous test rates applied about the X and Y axes. Note that the X axis error propagation includes contributions from scale factor, gyro alignment, anisoinertia and SRA cross coupling errors. To adequately evaluate anisoinertia and SRA cross coupling error compensation, scale factor and alignment error compensation must first be determined in the single axis slew environment.

Figure 5.2.3 depicts the single axis oscillatory test environment. The predominate error source is the pseudo coning drift which propagates about the Z axis. This test environment is used to evaluate the effectiveness of OA coupling compensation and for end-to-end strapdown bandwidth studies. Quanitzation tradeoffs are also evaluated in this environment.

Figure 5.2.4 illustrates the multi-axis oscillatory test environment in which error propagation is dependent on the relative phase of the oscillations. For example, in phase oscillations ($\epsilon=0^{o}$) generate anisoinertia and SRA cross coupling errors about the X axis while quadrature oscillations ($\epsilon=90^{o}$) would generate a coning error about the Z axis. Observe that OA coupling error compensation must first be determined in the single axis oscillatory environment. The multi-axis oscillatory environment is used to evaluate coning bandwidths and anisoinertia - SRA cross coupling error compensation.

5.2.2 Bandwidth Studies

5.2.2.a Coning

When two orthogonal axes are oscillated with a 90^{o} phase displacement, a coning environment is imposed to the strapdown system. The strapdown algorithm detects the oscillatory inputs, their magnitudes and relative phase, and generates a third axis drift to cancel the coning drift.

The attitude algorithm has a known effective bandwidth in responding to a coning input. This bandwidth was defined using computer simulations and is discussed in Section 4.3.5.c. The objective of coning testing in this program is to verify the simulation results and to evaluate the effects of gyro torque loop quantization.

Table 5.2.1 shows the oscillatory inputs applied, the estimated coning drift generated (based on equation 4.3.8), and the theoretical coning errors that are defined as the algorithm drift output to the coning drift input. Two algorithm orders (first and third) are evaluated at 100 iterations per second. Coning evaluation at 25 hertz

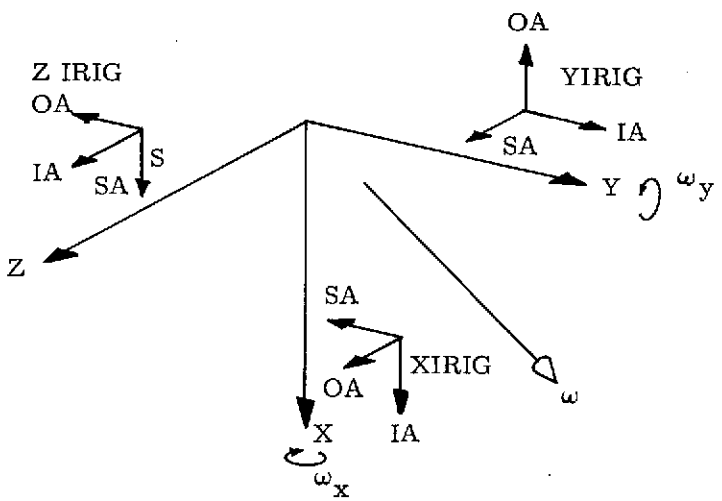

Error Sources

X Axis	Y Axis	Z Axis
negative scale factor compensation error	positive scale factor compensation error	
anisoinertia and SRA cross coupling errors	OA coupling during acceleration and deacceleration	OA coupling during acceleration and deacceleration
OA misalignment	SRA misalignment	OA, SRA misalignment

Figure 5.2.2
Multi-axis slew environment about X and Y axes

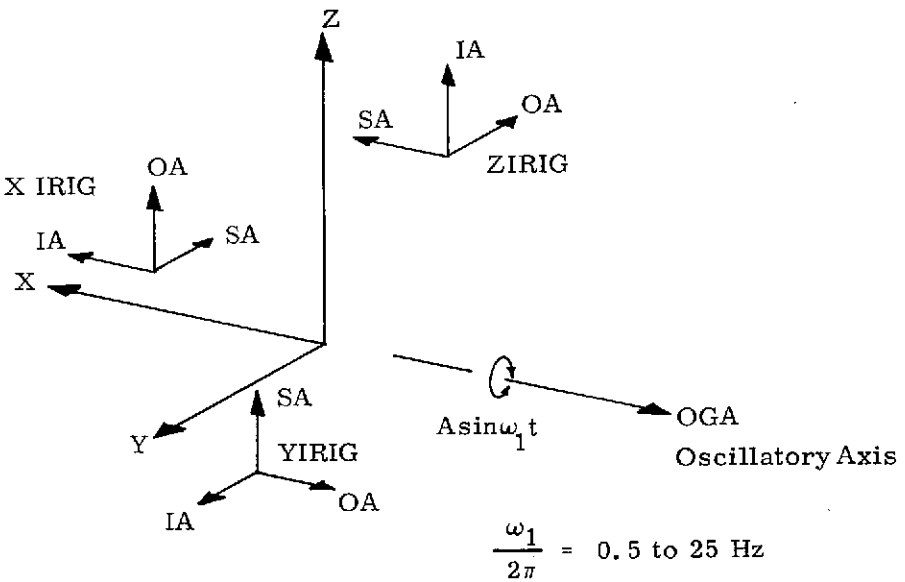

Error Sources

X Axis	Y Axis	Z Axis
Scale Factor compensation errors	OA coupling error	Pseudo coning error
	SA misalignment	OA misalignment

Figure 5.2.3

Single Axis Oscillatory Environment about the X Axis

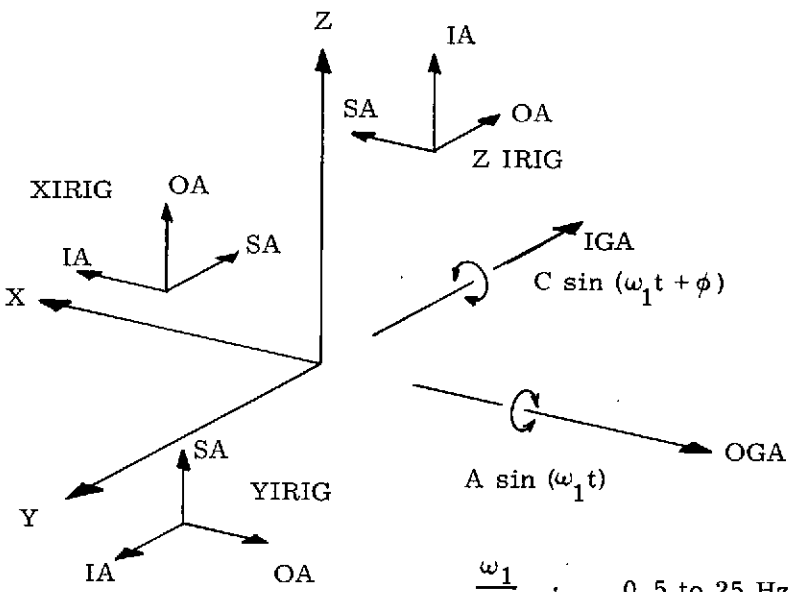

Error Sources

X Axis	Y Axis	Z Axis
Scale Factor compensation errors	Scale factor compensation errors	Coning (sin ϵ)
Pseudo coning due to Z IRIG coupling error		Pseudo coning due to Y IRIG coupling error
Anisoinertia (cos ϵ)		Cross axis coupling oscillations about OA causes Z input axis to rectify oscillatory motion about X

Figure 5.2.4

Multi-axis oscillatory environment about X and Y axes

was not conducted because the oscillatory magnitude equaled the gyro loop quantization. Under these conditions, large errors will exist in detecting the coning input.

TABLE 5.2.1 CONING ENVIRONMENT AND PERFORMANCE

Frequency (hertz)	Oscillatory Amplitude (radians) Inner Gimbal	Outer Gimbal	Coning Input Meru	°/hr	Theoretical Coning Error (%) First Order	Third Order
0.5	0.022	0.024	23,720	179	0.012	0.00001
1.5	0.022	0.024	11,720	356	0.05	0.00008
5.0	0.011	0.0057	13,600	204	1.4	0.02
10.0	0.004	0.0015	2,800	42	6.0	0.4

Figure 5.2.5 shows the coning input magnitude in meru (°/Hr) and the theoretical coning performance for the first and third order algorithms. Suppression of the coning drift input is achieved by both algorithms, although the third order algorithm is clearly superior. The major difference between the first and third order algorithm expansions is a cross product term that upgrades the system attitude data using angular rate change estimates between different axes. Because of an oversight in the initial software design, the cross product term was omitted from the third-order algorithm implementation. Thus, the coning performance achieved corresponded to the first-order bandwidth. It was intended to modify the software and conduct limited testing with the third order bandwidth. However, the failure of gyros MB-4, 427 precluded further testing. Verification was not considered essential, however, since the behavior is analytically definable and has been comprehensively simulated. In the constant rotational environment, the cross product term contributes nothing and the modified algorithm performs as a third-order algorithm.

Three variations of computational quaternion parameters were tested:

1) a 100 iterations per second algorithm with a 5 arc seconds quantization level,
2) a 100 iterations per second algorithm with a 40 arc seconds quantization level, and
3) a 50 iterations per second algorithm with a 5 arc seconds quantization level.

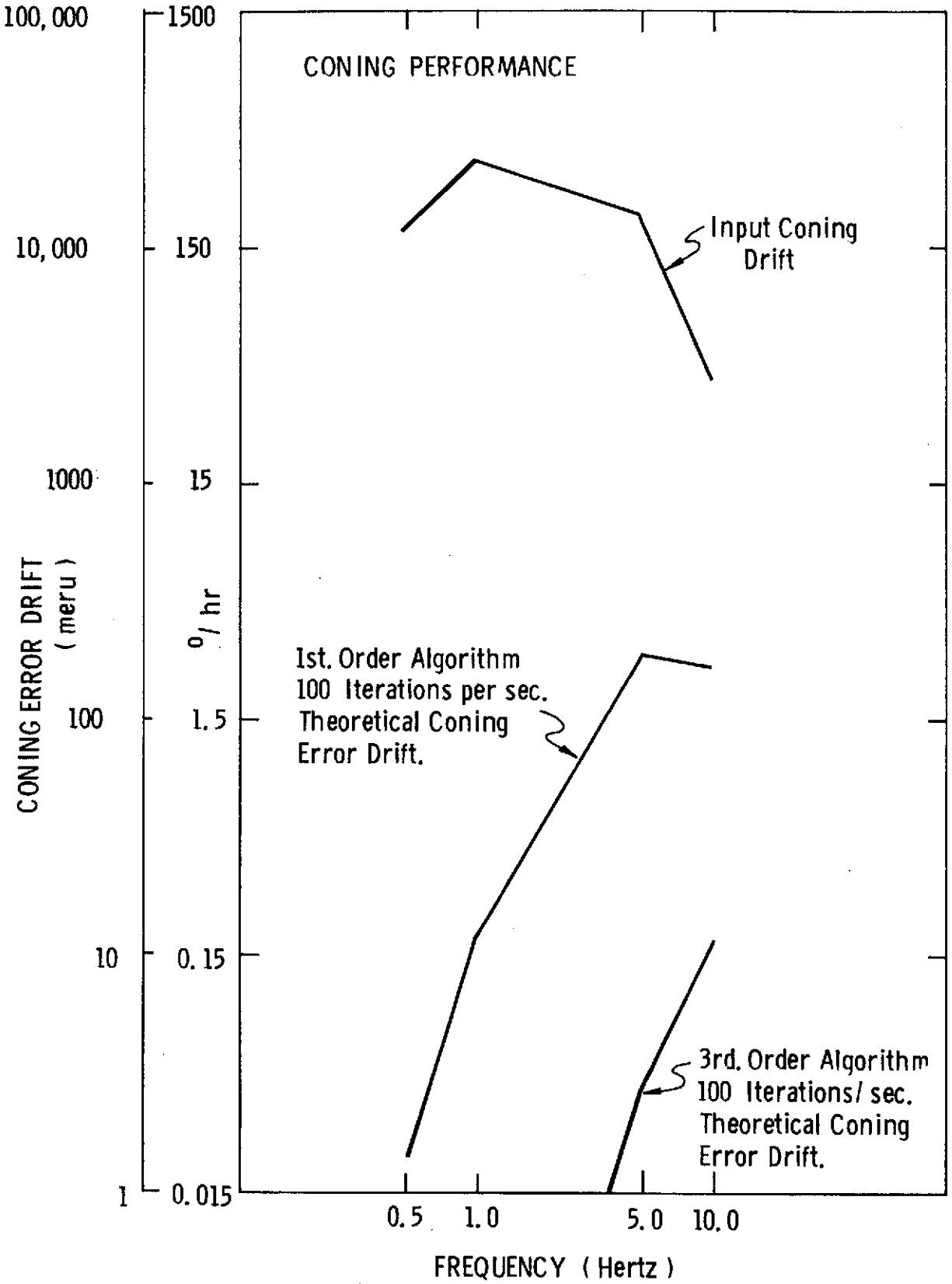

Figure 5.2.5 - CONING PERFORMANCE (THEORETICAL)

The results of operating these algorithms in coning environments from 0.5 to 10 hertz are presented in Figure 5.2.6, superimposed on the theoretical normalized curves given in Section 4.3.5.c. Normalization accounts for the fact that the abscissa plots the product of computer iteration time (Δt) and coning frequency (f). The ordinate scale is coning error in percent expressed as the algorithm drift output to the total coning drift input.*

Figure 5.2.6 also demonstrates the fact that a third order quaternion expansion without the cross product term performs with a first order algorithm bandwidth.

The deviation of performance from theoretical at low frequencies is a manifestation of gyro loop quantization effects. The theoretical curves assume a zero quantization and, therefore, because of attitude lags introduced by quantization larger coning errors are expected. Note that with larger quantization levels (for example, the 5 and 40 arc second quantization at 100 iterations per second) the low frequency error increases (from 0.3% to 0.85% at f Δt = 0.005). Quantization effects have no effect at higher frequencies because the quantization error is bounded over a finite interation interval, and the total error magnitude is significantly greater.

At higher frequencies (for example 10hertz), the deviation of the algorithm's performance from theoretical is the result of distortion effects as the coning frequency approaches the sampling frequency. This effect tends to reduce compensation effectiveness because of the reduced amplitude after sampling.

The 50 iterations per second algorithm performs closer to the theoretical expectation. One should not however assume that this is an optimal iteration rate. It is probable that testing uncertainties, e.g. phase adjustments have influenced the test results and to investigate this further would require a much more accurate test capability and technique.

---

* For a 100 iterations per second algorithm, Δt = 0.01. Thus the theoretical 10hertz coning error (Δt f = .1) is 6% for the first order algorithm and 0.4% for the third order algorithm.

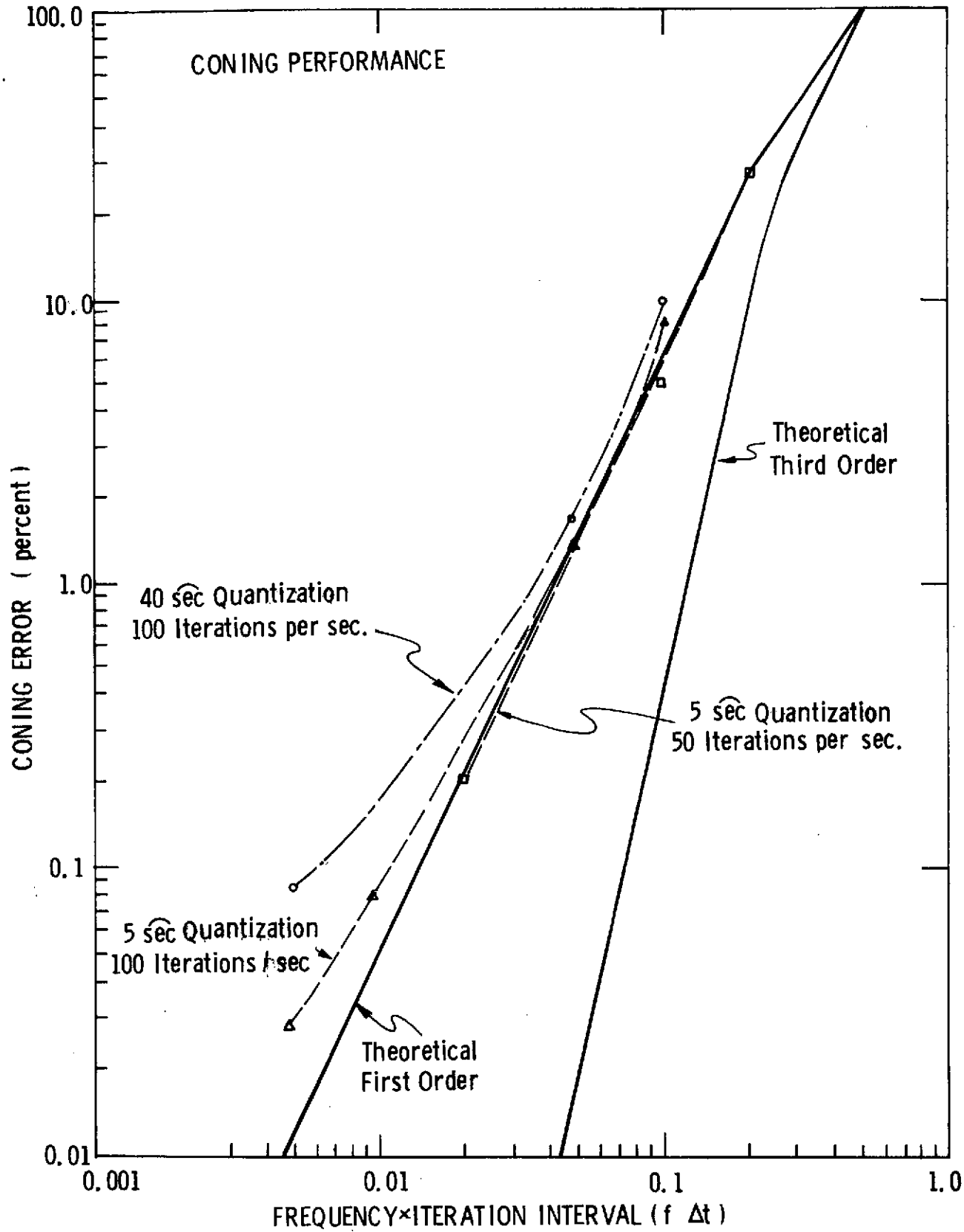

Figure 5.2.6 - CONING PERFORMANCE (MEASURED)

The theoretical coning bandwidth is illustrated in Figure 5.2.7 by displaying coning compensation effectiveness* (1-coning error) as a function of frequency for the first-order algorithms implemented in this program. From the Figure the coning bandwidth has a low pass band characteristic. For example, the 100 iterations per second algorithm starts to rolloff at 2 hertz with 95% compensation effectiveness observed at 8 hertz.

The test data obtained in this program has verified the basic low frequency coning bandwidth characteristics. The 50 iterations per second algorithm measured performance matched the theoretical bandwidth for the test spectrum 1 to 10 hertz. The measured 100 iterations per second algorithm bandwidth rolled off slightly faster than theoretical, within expected testing uncertainties. Gyro loop quantization effects predominate at low frequencies and therefore do not measurably affect the bandwidth characteristics.

Wider bandwidths are expected with the inclusion of the cross-product term in the quaternion mechanization. The cross product term third order bandwidth characteristics derived analytically are displayed in Figure 5.2.8. Note that the third order bandwidth is extended (approximately 99% compensation effectivity is achieved at three times as high a frequency), however, a sharper high frequency rolloff is evidenced. Future dynamic strapdown evaluations should be implemented with the cross product term to verify the third order bandwidth.

5.2.2.b Output Axis (OA) Coupling Compensation Bandwidth

OA coupling errors propagate from lagging float motion (inertia torque) when angular rate changes are applied about the Output Axis. As the float lags the case's oscillatory motion, additional torque pulses are generated to maintain the float at a null position. The added torque pulses describe an oscillatory motion (OA coupling error) that is proportional to the derivative of the input oscillatory motion. Thus, the gyro response to the single axis input oscillation is an output corresponding to two oscillations that are 90° phase displaced. With respect to the attitude algorithm these gyro outputs correspond to a coning environment even though the third axis is not coning. However, the attitude algorithm assumes coning exists and incorrectly

* Coning compensation effectiveness measures the amount of coning drift suppressed by the attitude algorithms.

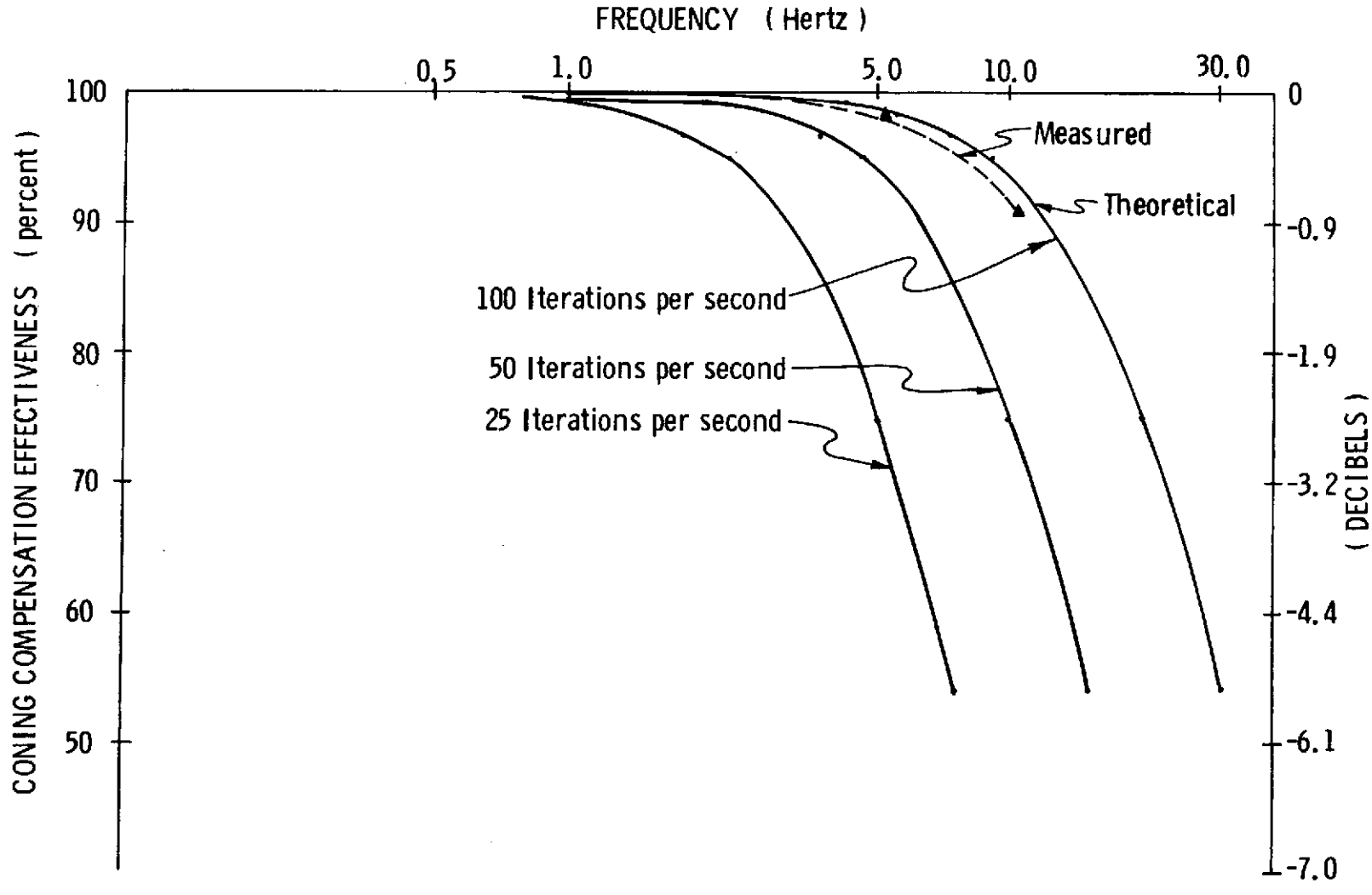

Figure 5.2.7 - CONING BANDWIDTH (FIRST ORDER ALGORITHM)

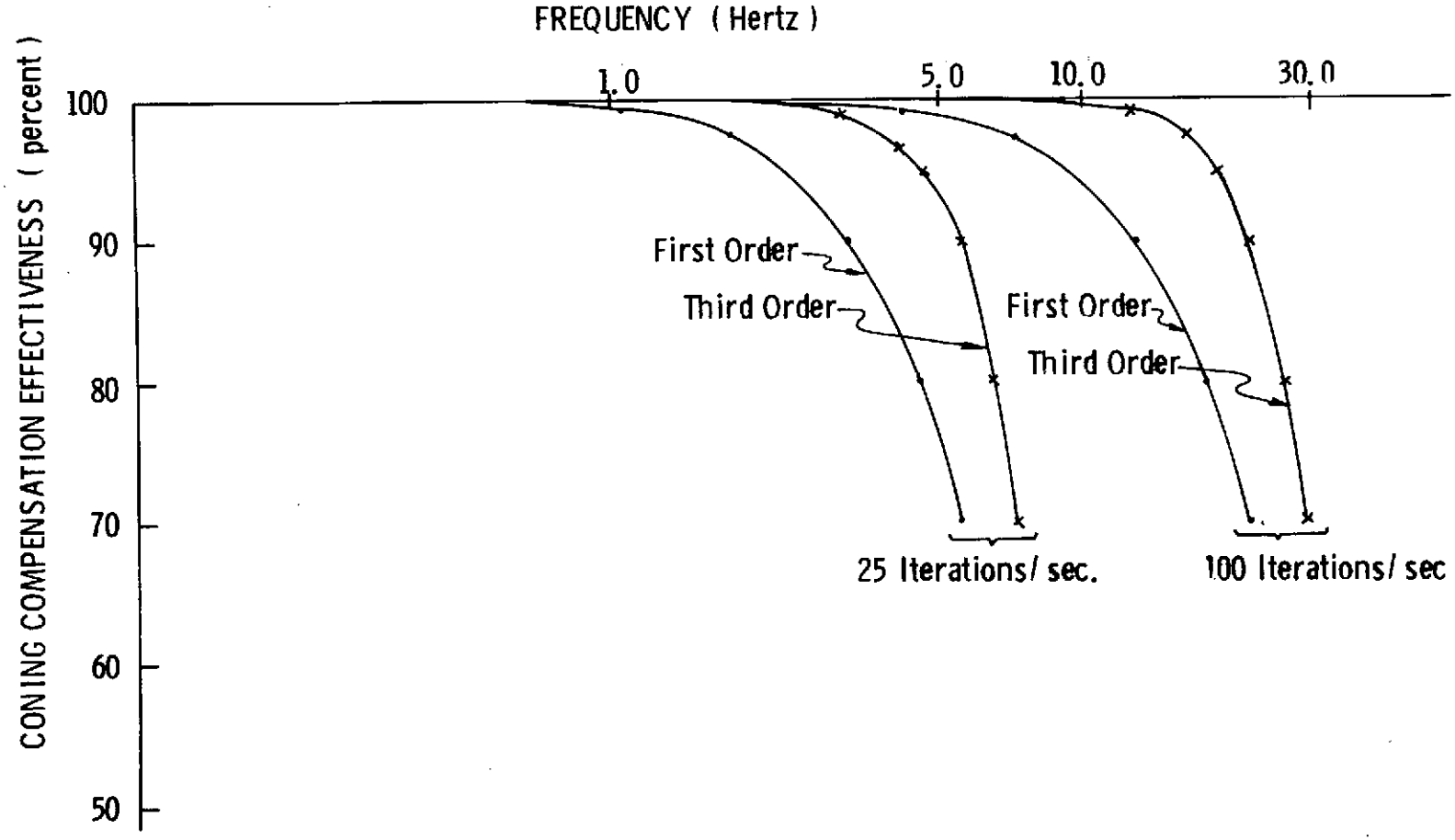

Figure 5.2.8 - CONING BANDWIDTH

applies an attitude drift correction to the third axis. This erroneous drift correction is termed "pseudo coning drift", and equals:

$$\text{pseudo coning drift} = \frac{a^2 \, I/H \, \omega^2}{2}$$

where:

a = peak amplitude of the oscillatory input

ω = oscillatory frequency I/H is the gyro parameter ratio: float inertia about OA/wheel angular momentum.

The evaluation of OA coupling compensation bandwidth is described in conjunction with Figure 5.2.9 . The test environment is shown in Figure 5.2.3.

Note that the attitude algorithm senses the input oscillations on the X axis and on the Y axis, uncompensated OA coupling errors. To compensate the OA coupling error, rate estimates are derived from a second gyro whose Input Axis is collinear with the input excitation ($a\sin\omega t$). From these rate estimates a rate change magnitude is determined and scaled by the gyro ratio, I/H, to estimate the OA coupling oscillation. The estimated oscillation is subtracted from the gyro whose output reflects the OA coupling oscillation. The difference represents the OA coupling error seen by the algorithm.

The character of the pseudo coning error propagation is directly related to the attitude algorithm's bandwidth defined in Section 5.2.2.a from the coning environment results. Coning bandwidth is low pass with the theoretical three (3) db point established as 22% of the algorithm's iteration rate and with an approximate 6/octave rolloff slope. If OA coupling errors are uncompensated and pass through to the attitude algorithm, they will propagate as a pseudo coning drift in the system attitude performance and will roll off with the coning bandwidth. Thus in the region in which coning correction degrades, uncompensated pseudo coning drift is attenuated.

Figure 5.2.10 shows the pseudo coning error drift measured with a 100 iteration per second algorithm and compares this data to the theoretical drift error calculated from oscillatory magnitudes given in Section 3.5.6 (Table 4.3.6) and using Equation 4.3.7 . The measured drift correlates to the theoretical drift within testing uncertainties (quantization, frequency, and oscillatory amplitude). Thus, the coning bandwidth is not a limiting factor for the 100 iteration per second algorithm for the test spectrum, 0.5 to 10 hertz.

Also shown in Figure 5.2.10 is the significant reduction in pseudo coning drift that was achieved with the same test inputs but with the OA coupling errors

OA COUPLING COMPENSATION MECHANIZATION

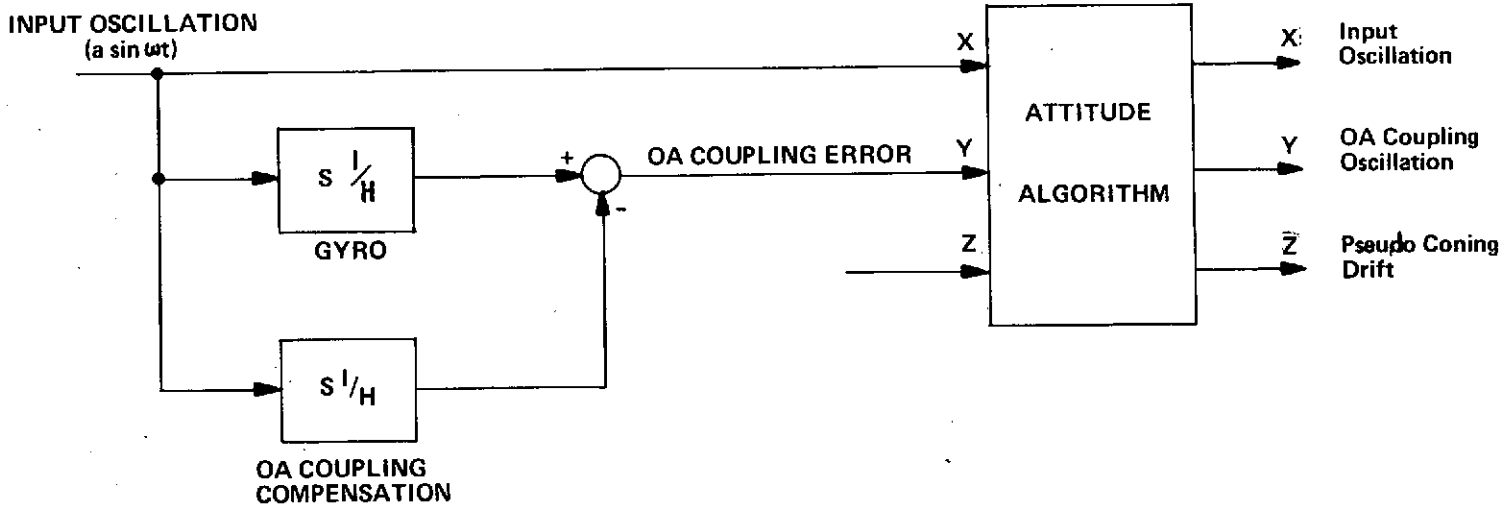

Figure 5.2.9 - OA COUPLING COMPENSATION MECHANIZATION

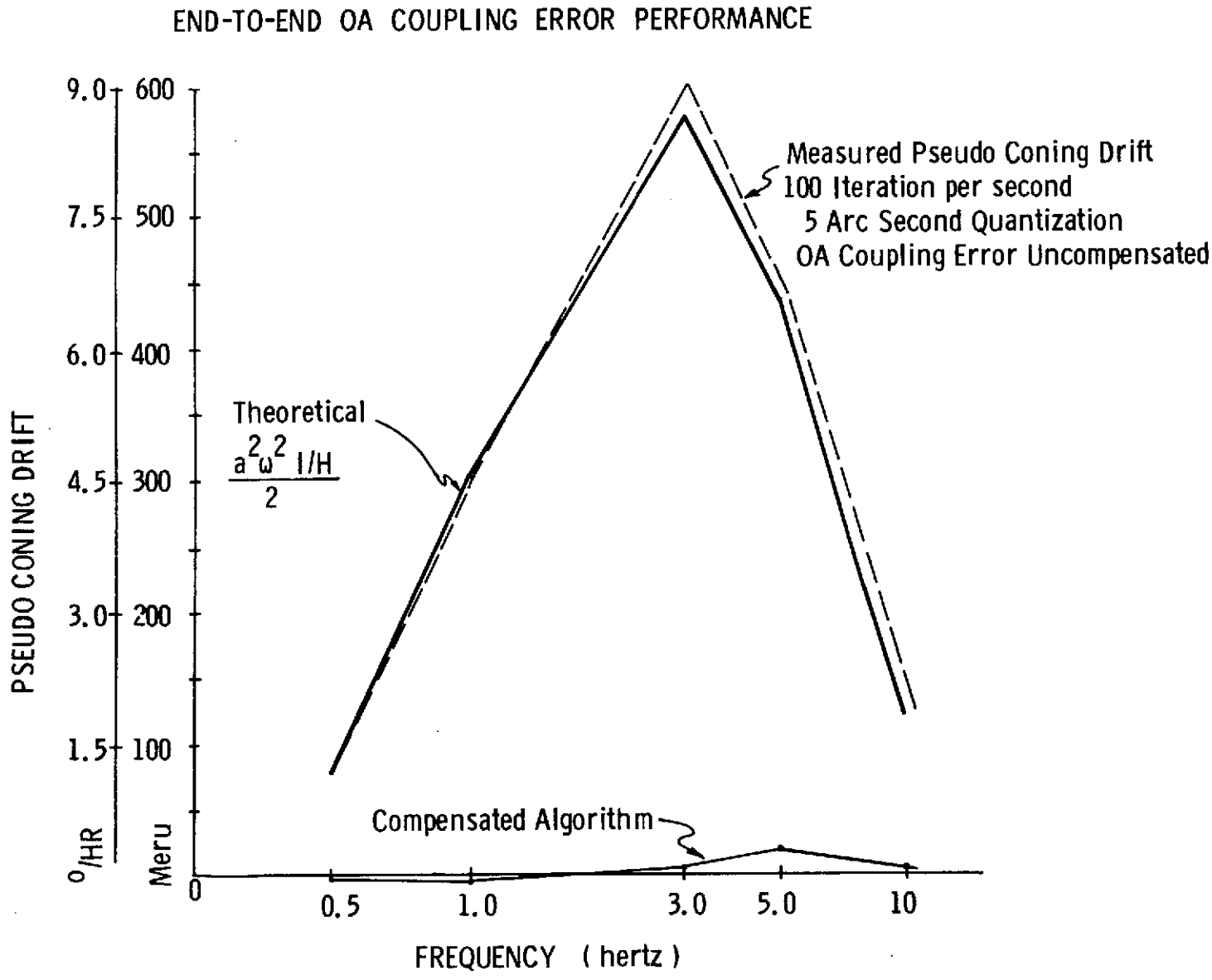

Figure 5.2.10 - END-TO-END OA COUPLING PERFORMANCE

compensated. The compensation scheme used also has bandwidth limitations which are considered next.

Functionally, the compensation technique estimates the OA coupling oscillation and subtracts the estimate from the true oscillation. In a low frequency band this compensation method is effective and no OA coupling error is propagated into the attitude algorithm (Y axis). However, as the oscillatory frequency increases and approaches the compensation iteration rate, the compensation effectiveness degrades. Degradation begins when the oscillatory frequency is one-tenth the iteration rate, verified with 25 and 100 iterations per second algorithms on IBM 360/75 computer simulations.

Figure 5.2.11 shows the simulation results by plotting the OA coupling compensation effectiveness for the 25 and 100 iterations per second algorithms. Observe the low pass bandwidth characteristics with approximately 30% degradation when the forcing frequency is one-tenth the iteration rate.

Now, the evaluation of the OA coupling phenomenon, operating end-to-end through the compensator and attitude algorithms, is possible by considering the combined effects of the OA compensation and the coning bandwidths. Figure 5.2.12 shows the combined effect based on simulation studies with a 25 iteration per second algorithm. Pseudo coning error is expressed in Figure 5.2.12 as the ratio of pseudo coning drift with bandwidth limitations considered to the theoretical pseudo coning drift of an infinite bandwidth algorithm.

Three areas of performance are observed: 1) at low frequencies, the OA coupling error compensation is completely effective and therefore no error is propagated to excite the coning bandwidth. 2) As the frequency increases, the OA coupling compensation loses its effectiveness and excites the attitude algorithm with what appears to be coning. The attitude algorithm's response is to impose a coning drift correction. Thus, the pseudo coning error increases as the input oscillation frequency increases. 3) As the frequency increases further, the coning bandwidth is encountered and the algorithm's capability to correct for a real coning environment degrades. In this region pseudo coning errors flatten out and start to decrease. Hence, OA coupling error propagation is affected by two separate bandwidths: 1) the coning bandwidth, and 2) the OA compensation bandwidth.

Figure 5.2.13 shows the end-to-end OA coupling performance data for three algorithm iteration rates. Pseudo coning error, defined as the ratio of measured pseudo coning drift with compensation to the theoretical pseudo coning drift without compensation, is plotted as a function of frequency.

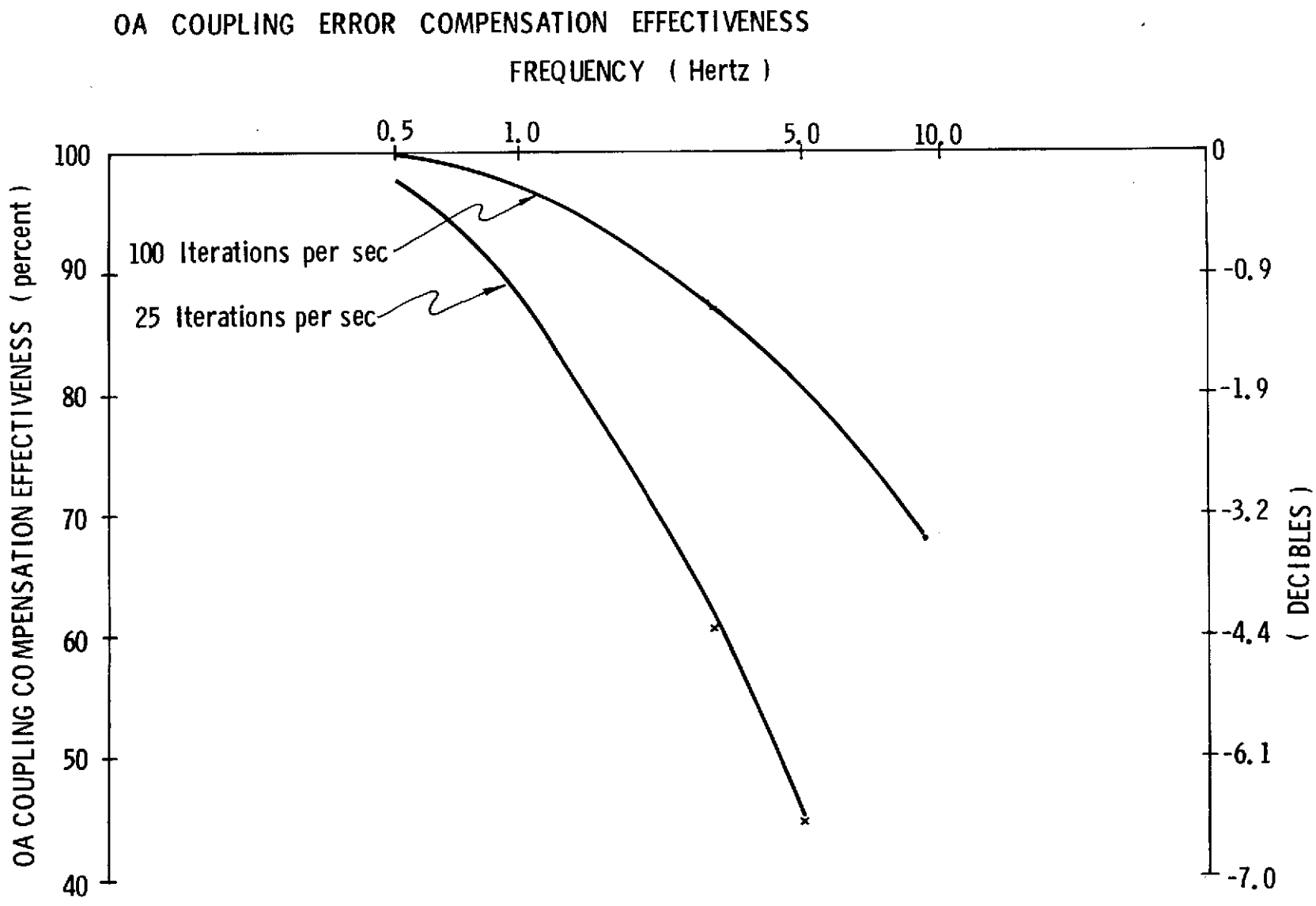

Fig. 5.2.11 OA Coupling Error Compensation Effectiveness.

THEORETICAL END-TO-END OA COUPLING PERFORMANCE

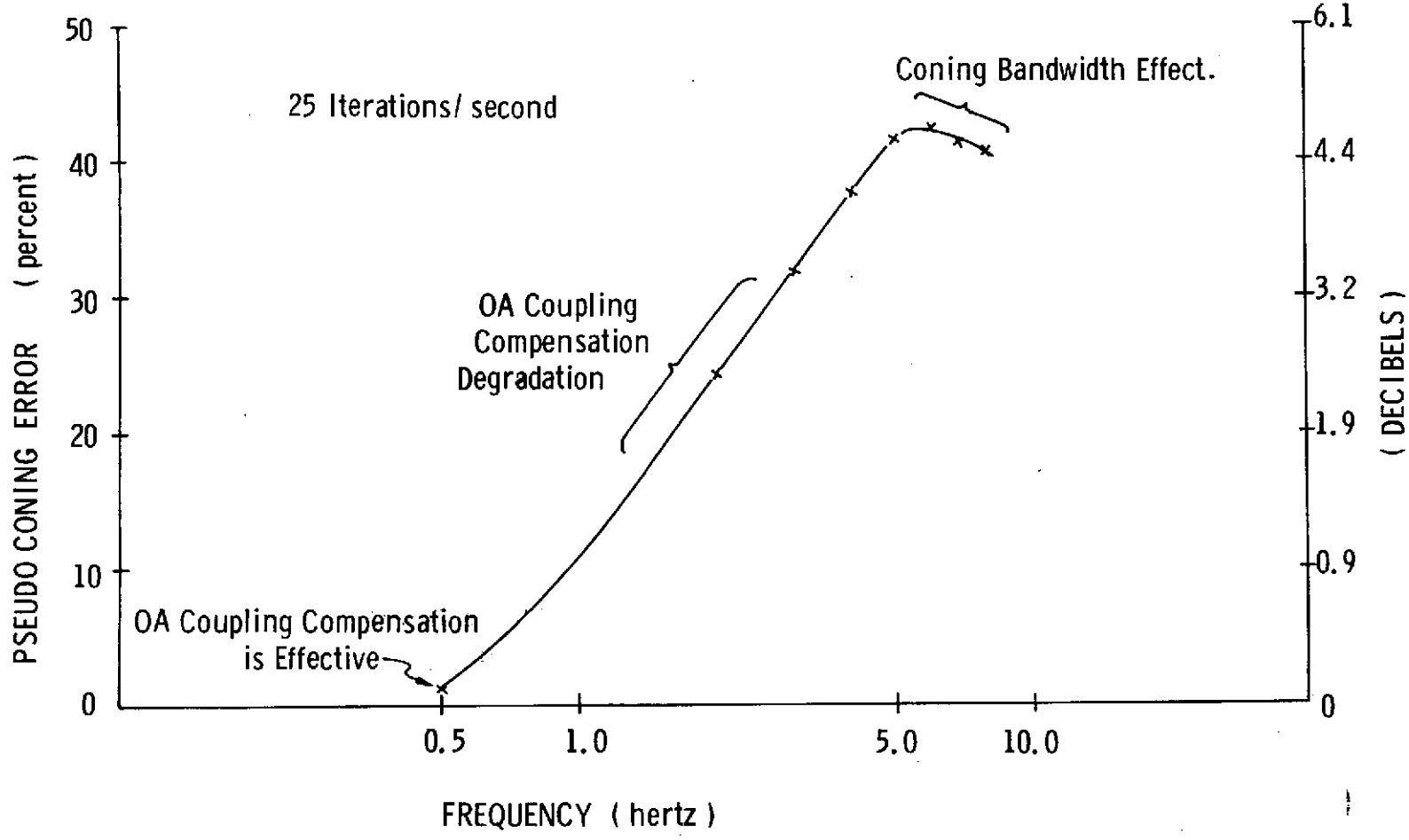

Fig. 5.2.12 Theoretical End-To-End OA Coupling Performance.

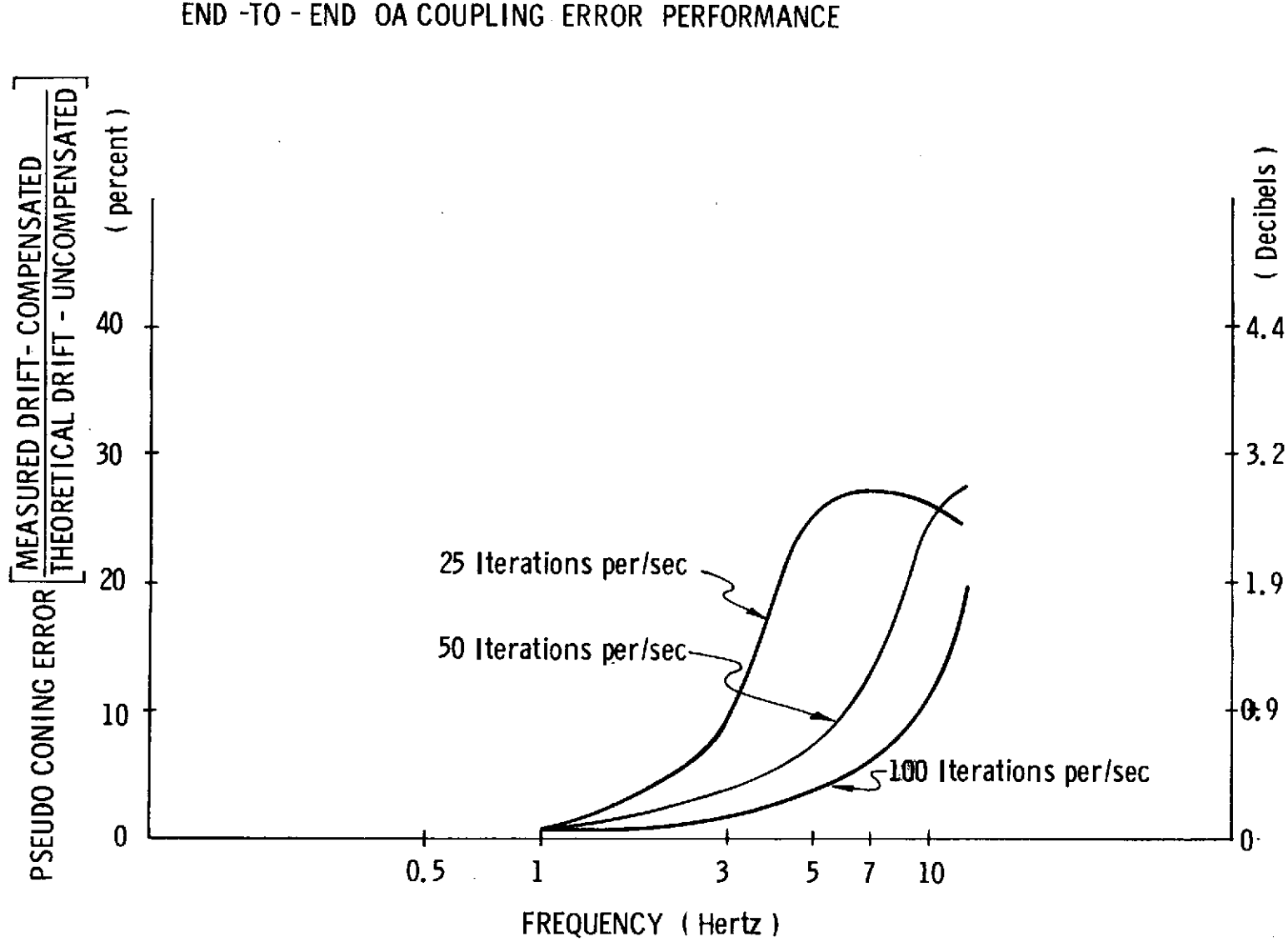

Figure 5.2.13 - OA COUPLING PERFORMANCE

The 25 and 50 iterations per second algorithms match the simulated results given in Figure 5.2.12 . Observe that the 25 iterations per second algorithm begins to degrade at a lower frequency than the 50 iterations per second algorithm. This is the effect of the OA coupling compensation bandwidth. Note also that the 50 iterations per second peak occurs at a higher frequency than the 25 iterations per second algorithm because of its wider coning bandwidth. If a wider test spectrum were possible, the 100 iterations per second algorithm would also illustrate a peaking effect in the 20 to 30 hertz range.

One should recall that in each of these tests the OA coupling compensation routine operated at the same iteration rate as the attitude algorithm. Thus the analysis and the test results show that for optimum suppression of pseudo coning the OA coupling compensation algorithm should operate at a higher iteration rate than the attitude algorithm. For example, referring to Figures 5.2.8 and 5.2.11, one observes that if OA compensation is operated at 100 iterations per second a 30% OA coupling error exists at 10Hz, however, if the algorithm iteration rate is 25 per second the coning correction bandwidth (roll off) is encountered at 5Hz and negligible pseudo coning drift propagates. Hence, as the compensation algorithm loses effectiveness, the coning bandwidth will have already degraded so that the coning environment is not recognized. Clearly, various tradeoffs of algorithm implementation exist, especially in consideration of the wide range of dynamic inputs and error sources which warrant meaningful evaluations with respect to specific test environments.

5.2.3 Anisoinertia and SRA Cross Coupling Compensation

Anisoinertia and SRA cross coupling errors are generated in the multi-axis environment. In the slew environment if rates are applied simultaneously about the Input Axis and Spin Reference Axis an attitude drift error(W_D) is generated as defined by:

$$W_D = \underbrace{\left(\frac{I_{SA} - I_{IA}}{H}\right) W_{IRA}\, W_{SRA}}_{\text{Anisoinertia Error Contribution}} - \underbrace{\left(F_o\right) W_{SRA} - \left(F_m\right) W_{IRA}\, W_{SRA}}_{\text{SRA Cross Coupling Contribution}}$$

Anisoinertia

I_{SA} - float inertia about the Spin Axis.
I_{IA} - float inertia about the Input Axis.
H - wheel angular momentum.

SRA cross coupling

F_o - float hangoff in deadzone of torquing region.

F_m - additional average float hangoff due to input rates about the Input Axis.

SRA cross coupling errors occur from Input Axis misalignment resulting from float hangoffs. Float hangoff is a linear, rate dependent function as illustrated by the calibration curves in Section 3.7.3.c for a 40 arc second quantization gyro loop. From similar curves developed earlier for a 8 arc second gyro loop, the calibrated SRA cross coupling coefficient was determined to be F_o = 10 microradian, and F_m = 4.5×10^{-4} radians per radian/second of Input Axis rate.

Anisoinertia errors occur from simultaneous rates applied to the unequal Spin Axis and Input Axis float inertias. For the low rate capability of the gyro loops at 8 arc second quantization (0.2 radians per second) anisoinertia could not be calibrated directly because of gimbal alignment uncertainties. To circumvent the calibration difficulty, a nominal anisoinertia coefficient is derived from known gyro inertia and angular momentum magnitudes. For gyro MB2 a nominal anisoinertia of 1.2 10^{-4} radians/radian per second was estimated.

A multi-axis slew test was conducted to verify the anisoinertia – SRA cross coupling compensation model described in Equation 5.2.1 and the validity of using a nominal anisoinertia coefficient. Rates of 0.16 radians per second were applied about both the Input Axis and Spin Reference Axis of the X gyro (MB2). At that input, the theoretical drift error is 122 meru (1.83°/Hr). Without anisoinertia and SRA cross coupling errors compensated the measured drift was 138 meru (2.07°/HR). With the error terms compensated the measured drift rate was -3 meru (-.045°/HR).

. Figures 5.2.14 and 5.2.15 show the attitude error propagation for the compensated and uncompensated conditions. These results verify the compensation model and the adequacy of the use of the nominal anisoinertia coefficient for this gyro.

Preliminary evaluation at higher rates (0.5 radians per second) were also conducted, however, with changed compensation parameters because of new gyros and a gyro loop scaling change. At these new conditions, the gyro's (427A) anisoinertia coefficient was estimated to be 1.0×10^{-4} radians/radian per second and the SRA cross coupling coefficients calibrated to be F_o = 20 microradians and F_m = 2.57×10^{-4} radians/radian per second. The initial results were ambiguous and final detailed testing was precluded by the program's termination due to a hardware failure. It is probable that at higher rates, gimbal alignment and compensation uncertainties

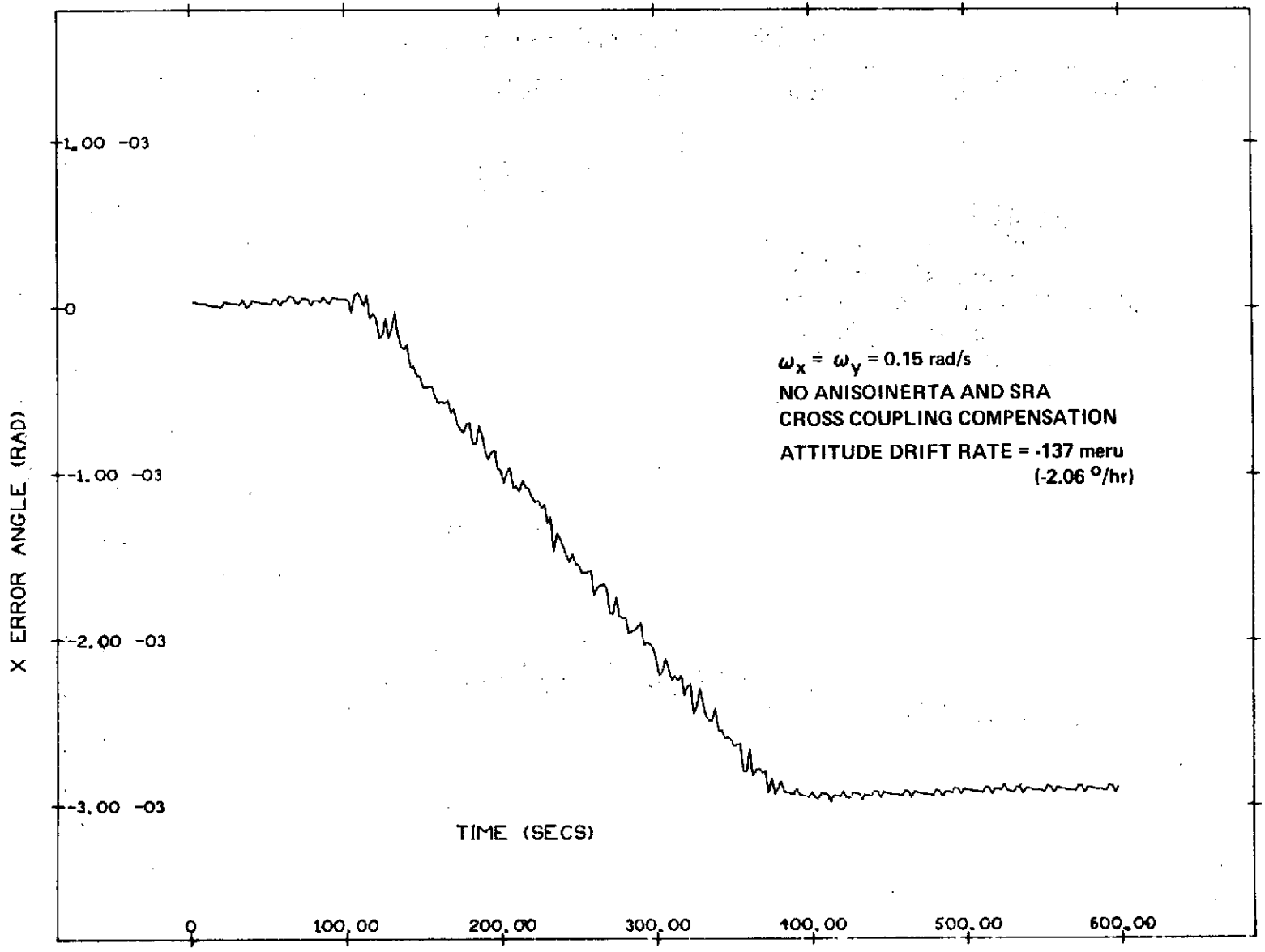

Fig. 5.2.14 Multi-Axis Rotational Environment.

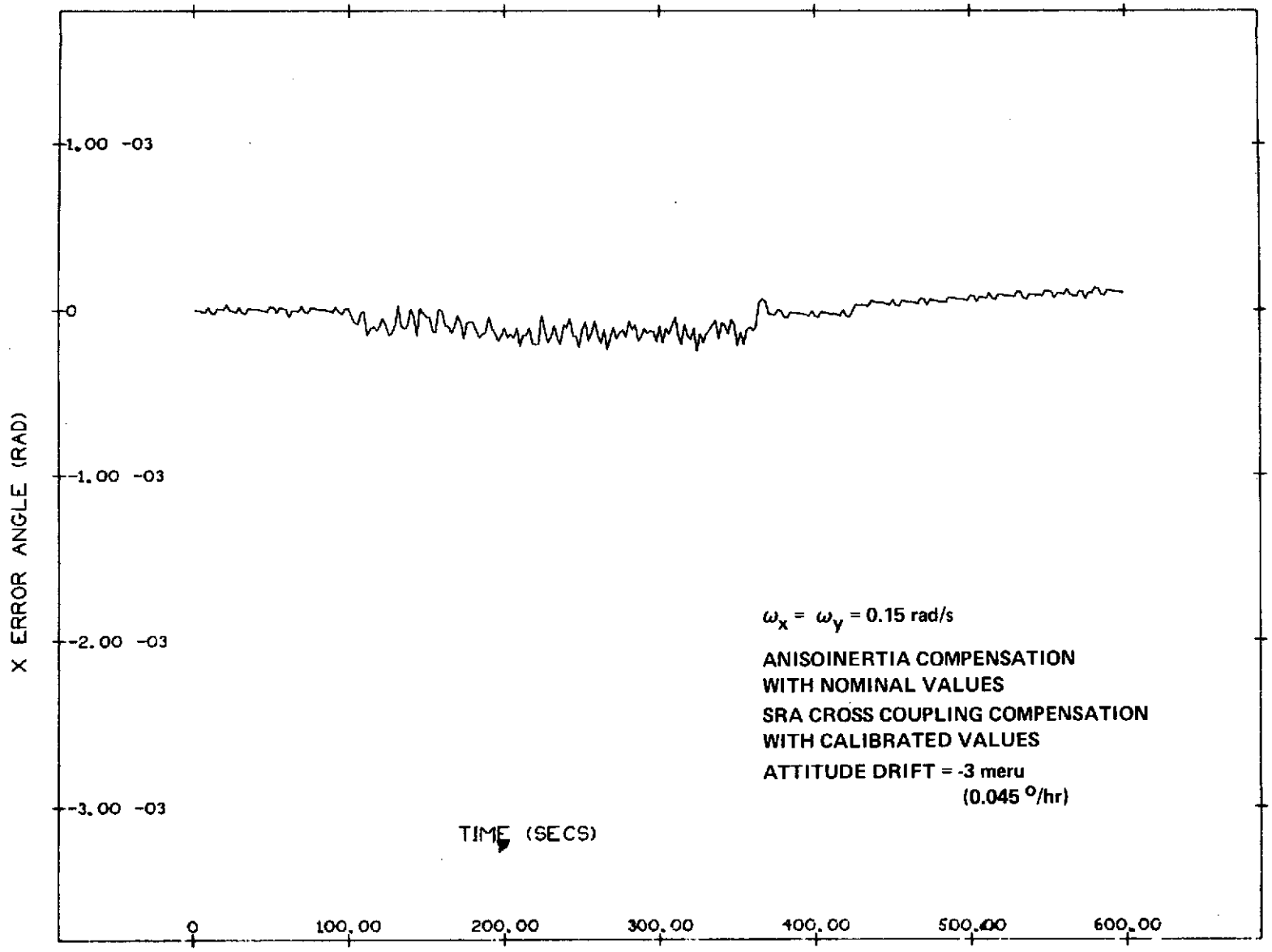

Fig. 5.2.15 Multi-Axis Rotational Environment.

are significant. For example, a ten arc second uncertainty in the gyro's alignment at 0.5 radians per second causes a 332 meru (5^{o}/Hr) error sufficient to mask the evaluation of the anisoinertia compensation performance. Additional evaluation of high rate multi-axes environment error phenomenon is recommended.

Another area of interest is the determination of the sensitivity of system anisoinertia - SRA cross coupling attitude drift to the compensation load. This was done at low rate conditions (0.15 radians per second) by varying the compensation load +20% and -50% from the nominal compensation load. The results are shown in Figure 5.2.16. The linearity relationship shown is valid for the rate condition tested. Since anisoinertia and SRA cross coupling errors are a multi-axis environment phenomenon, the linearity magnitude is a non-linear function which varies as the square of the rate (assuming $W_{IRA} = W_{SRA}$). Hence, a family of sensitivity functions are expected over the full dynamic range. In Figure 5.2.16 the linearity magnitude is 26 meru (0.39^{o}/Hr) per 1×10^{-4} radians/radian per second compensation change. At 0.5 radians per second the expected linearity is 289 meru (4.3^{o}/Hr) per 1×10^{-4} radians/radian per second.

Anisoinertia and SRA cross coupling errors were evaluated in the multi-axes oscillatory environment. The relationship that defines the drift error propagation in the oscillatory environment is expressed as:

$$\text{ATTITUDE DRIFT} = \underbrace{\left(\frac{I_{SRA}(f) - I_{IA}}{H}\right)\frac{ac\omega^2}{2}\cos\phi}_{\text{Anisoinertia Contribution}} \underbrace{- \frac{2}{\pi} F_o a\omega - F_m \frac{ac\omega^2}{2}\cos\phi}_{\text{SRA Cross Coupling Contribution}}$$

where

a, c	are the input excitation peak amplitudes
ϕ	is the phase difference of input excitation
ω	is oscillatory frequency
F_o	is the float hangoff offset (20 μ radians)
$\frac{I_{SA}(f) - I_{IA}}{H}$	is the frequency dependent anisoinertia coefficient (1×10^{-4} sec below the wheel hunt frequency)
F_m	is the SRA cross coupling coefficient (2.57×10^{-4} sec)

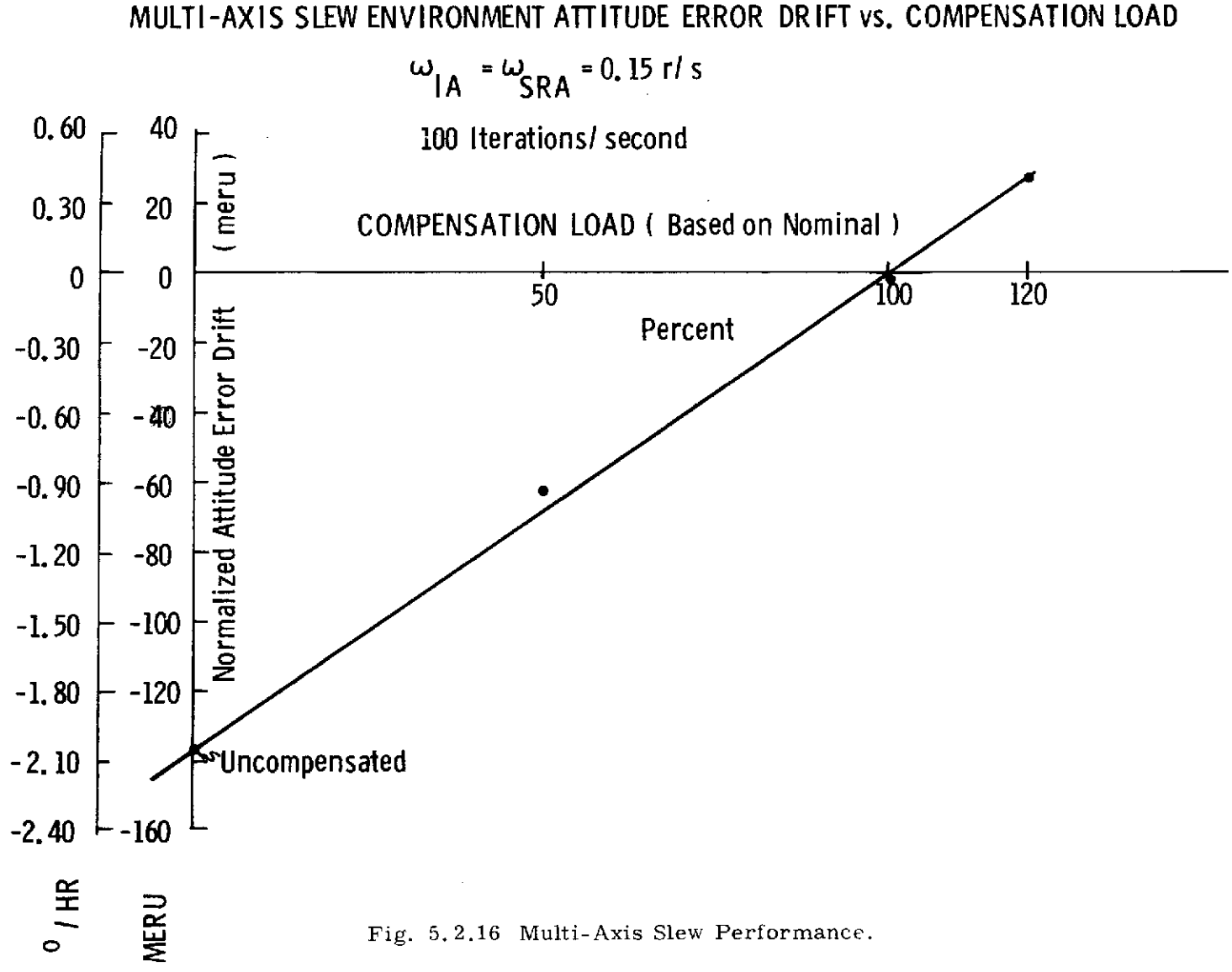

Fig. 5.2.16 Multi-Axis Slew Performance.

The anisoinertia coefficient is now a function of frequency. At the wheel hunt frequency, the wheel rotor element decouples from the input oscillatory motion and thereby shifts the inertia difference (I, SA(f) - IA) from 21 gm-cm^2 at low frequencies to -40 gm-cm^2 above the wheel hunt frequency.

Applying the calibrated parameters and environment magnitudes to the attitude drift equation (Equation 5.2.2), drift magnitudes were computed. These results, are compared to measured data with anisoinertia -SRA cross coupling error uncompensated in Figure 5.2.17.

Clearly, the strapdown system performance exhibits the predicted wheel decoupling phenomenon. The close correlation between measured and theoretical below 5 hertz verifies the error model. Hence, the low frequency compensation model seems adequate. At 5 hertz and above, the measured data differs from theoretical. This difference is related to other uncertainties such as testing (phase and amplitude adjustments) and bandwidth limitations of the algorithms. For example, because of the bandwidth limitations of the OA coupling compensation algorithms, a 20 meru (0.3°/Hr) error is contributed at 5 hertz by OA coupling errors and at 10 hertz, 10 meru (0.15°/HR) is contributed.

The peaking anisoinertia - SRA cross coupling error illustrates the importance of accounting for wheel decoupling effects if environments above the wheel hunt frequency are anticipated. Compensation for this effect may require frequency signature analysis of the gyro data to determine the coefficient to be used for compensation. If only low frequency environments are anticipated then the simpler low frequency compensation model is adequate.

5.2.4 Algorithm Dynamic Uncertainty

5.2.4.a Attitude Uncertainty

Gyro loop quantization affects the level of system attitude uncertainty. This relationship is verified with the comparison of attitude error profile for two quantization mechanizations: 1) the 40 arc second quantization of the gyro torque loop, and 2) the 5 arc second quantization from interpolator information.

Figures 5.2.18 and 5.2.19 illustrate the attitude error propagation for two quantization levels (40 and 5 arc seconds respectively) operating with a 100 iterations per second algorithm.

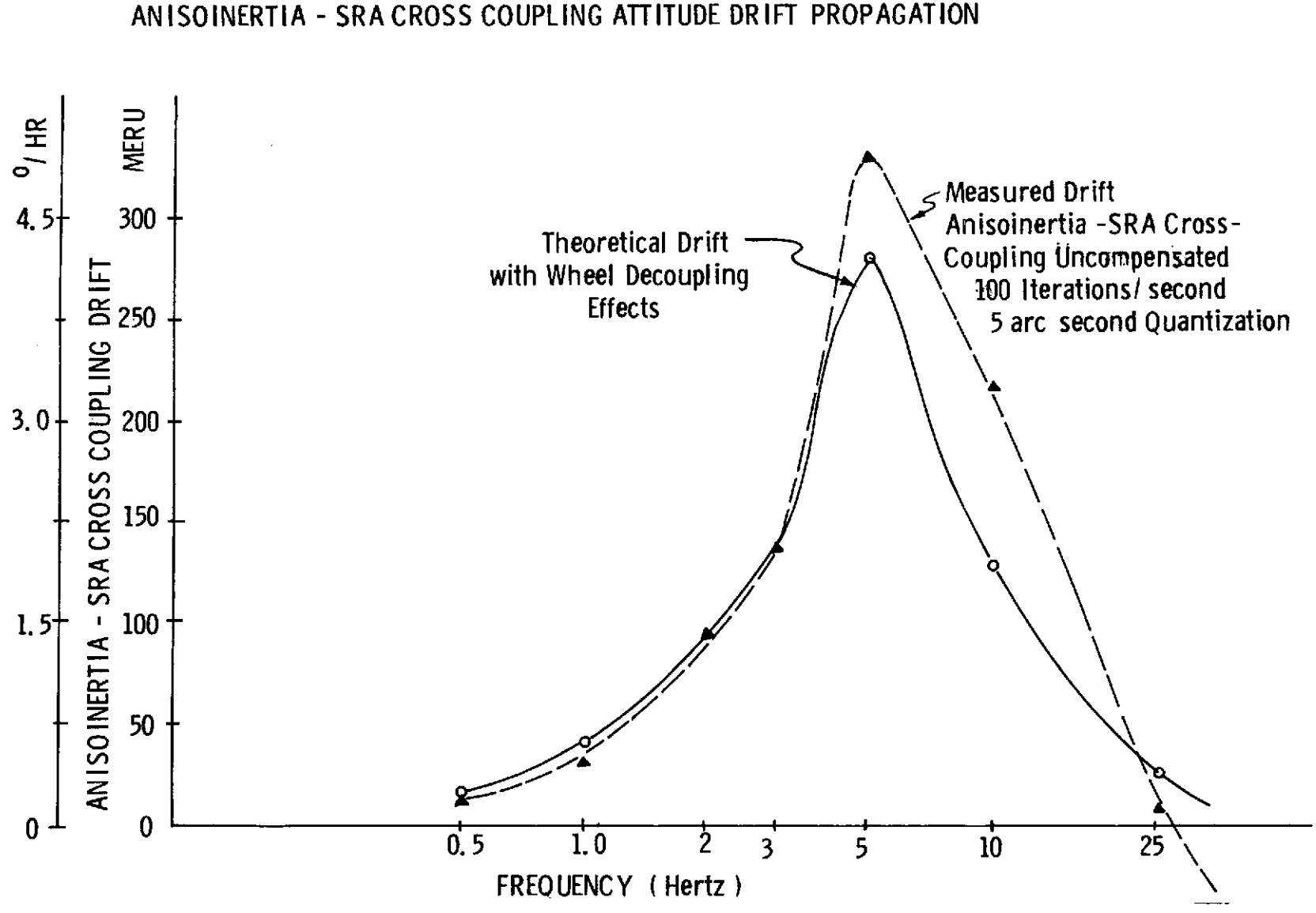

Figure 5.2.17 - MULTI AXIS OSCILLATORY PERFORMANCE

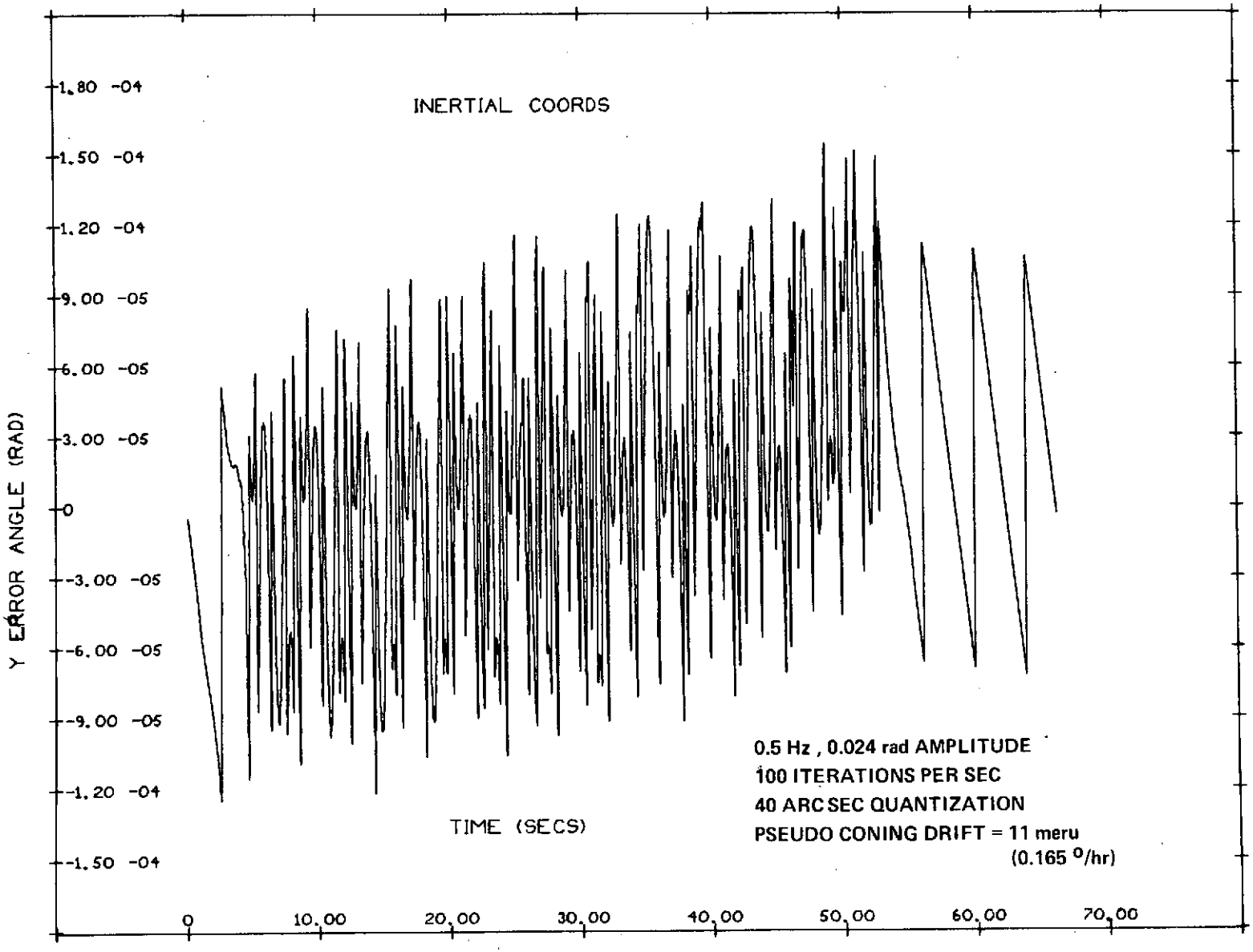

Fig. 5.2.18 Single Axis Oscillatory Environment.

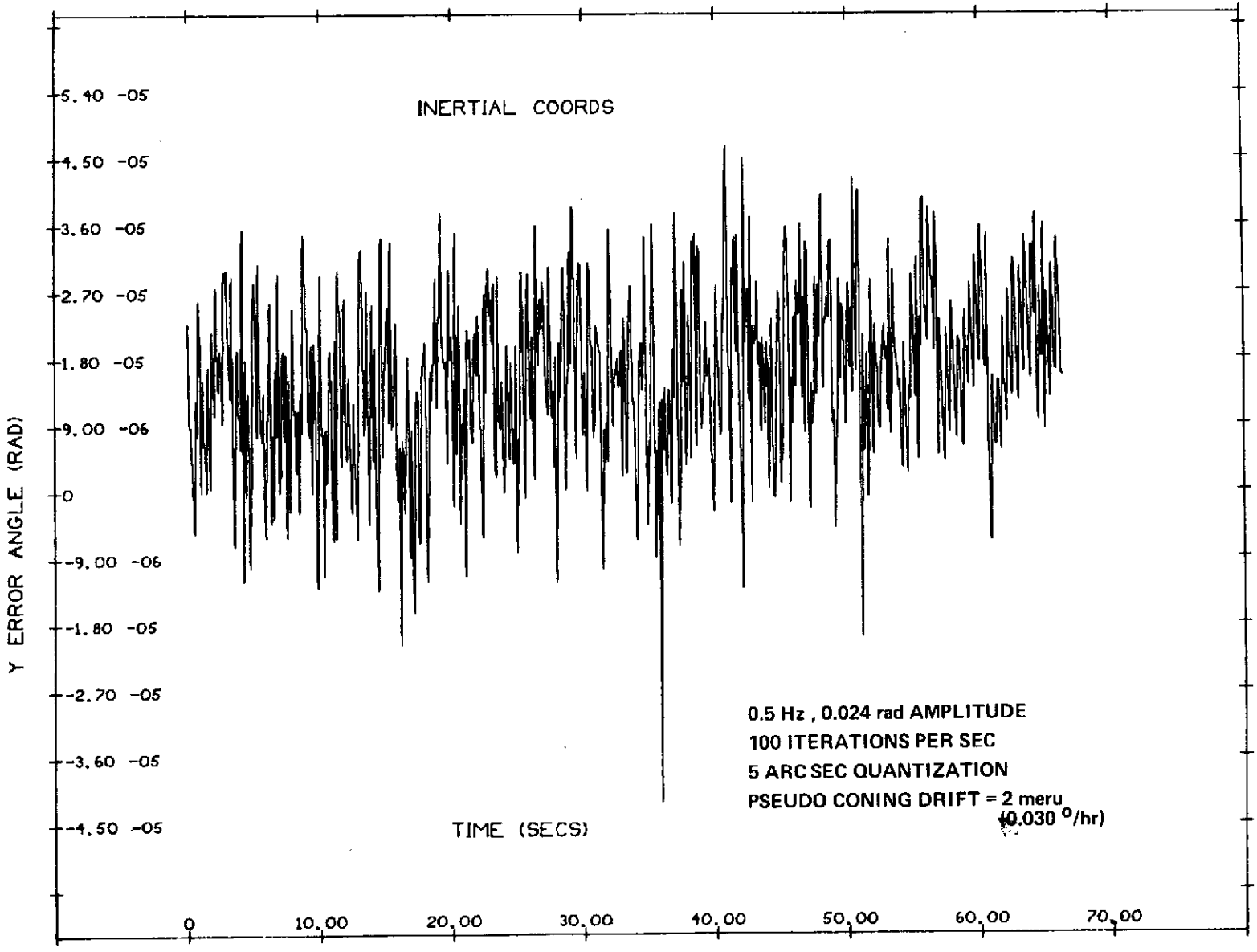

Fig. 5.2.19 Single Axis Oscillatory Environment.

FRAME 002

The test environment is 0.5 hertz with a 0.024 radian peak amplitude. It is interesting to observe that the peak-to-peak attitude uncertainty is 5.5 arc seconds for the 5 arc seconds quantization condition and 37 arc seconds for the 40 arc second quantization level. Thus, a proportional relationship exists between the quantization size and the attitude uncertainty level. This relationship is also observed in test results at 1 and 5 hertz.

5.2.4.b Bandwidth

Quantization level is observed not to effect bandwidth performance. This result was determined with a simulated third order algorithm (without the cross product term) operating in a 1^{o} single axis oscillatory environment. Table 5.2.2 tabulates the pseudo coning error (algorithm drift output with OA coupling errors compensated divided by the theoretical pseudo coning drift) for two quantization levels 2^{-15} and 2^{-20} radians.

TABLE 5.2.2 PSEUDO CONING ERROR

Frequency (hertz)	Theoretical pseudo coning drift for 1^{o} Environment (meru)	Pseudo Coning Error (%)	
		2^{-15} radians (6.3 sec)	2^{-20} radians (0.2 sec)
0.5	41	1.9	0.3
1.0	163	2.0	1.0
2.0	653	3.5	4.0
5.0	4,082	19.0	18.3
10.0	16,327	17.8	17.8
20.0	65,308	22.2	22.2

The high frequency coning errors are unaffected by quantization. Low frequency error differences are the result of attitude information lags introduced by quantization.

System tests to verify the effects of quantization requires the consideration of the relative magnitude of the oscillatory motion with respect to the gyro loop's quantization. Figure 5.2.20 shows this relationship between quantization and the Output Axis (OA) coupling oscillation.

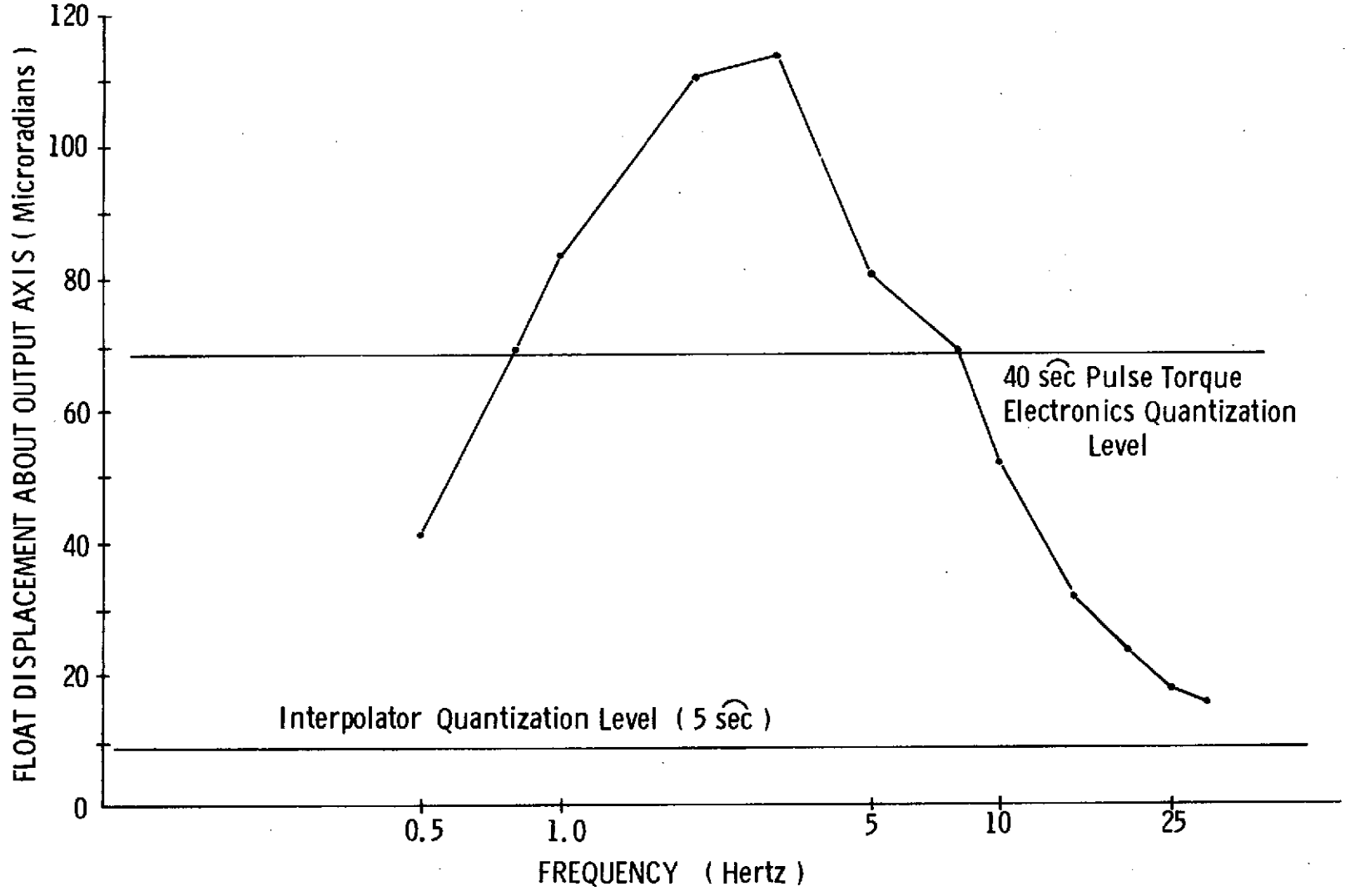

Figure 5.2.20 - OUTPUT AXIS OSCILLATORY DISPLACEMENT

Note at 15 hertz, the float displacement is only four times the 5 arc second quantization level. At this point, the ability of the attitude algorithm to detect magnitude and phase of the system's oscillations is marginal and uncertainties are expected. Therefore, meaningful evaluations at 5 arc second quantizations are restricted to below 15 hertz.

The 40 arc second quantization results are expected to have large uncertainties. Below 0.8 hertz and above 8 hertz, the quantization exceeds the float motion. Hence, in these regions the OA coupling oscillation is not detected and no pseudo drift errors will be generated. Even the region 0.8 to 8.0 hertz, the uncertainty in the pseudo coning drift propagation is likely with the 40 arc second quantization since a sizable amount of the float motion is still masked by the torque threshold and quantization.

Figure 5.2.21 shows the measured pseudo coning drift for the two levels of quantization and a 100 iterations per second algorithm. Observe that with the 40 arc second quantization algorithm since the OA coupling oscillations are suppressed at higher frequencies, a lower pseudo coning error exists. At 0.5 hertz, although the OA coupling oscillation is less than the 40 arc second quantization, a pseudo coning error (22%) was measured. This error propagation, shown in Figure 5.2.19 was a constantly drifting error with a 120 microradian attitude change during the test interval. This drift is still within the pulse torque threshold for the test time and therefore represents system uncertainty.

5.2.5 Pulse Burst Compensation

Pulse burst compensation effectiveness may be verified by observing the pattern of gyro torque pulses for a given test interval. This procedure was followed with the gyro loops compensated for pulse bursting and then without compensation. Significant improvement was observed. Without compensation thirty eight different patterns were observed, 88% of which involved double pulsing. With compensation only four different pulse patterns were observed and none with double pulsing. Hence, the compensation scheme (Reference Section 2.3.1) is effective, by reducing the multiplicity of pulse patterns and the occurrence of pulse burst. Therefore, pulse burst compensation reduces the ambiguities of attitude information.

The verification of the effect of ambiguities on system performance is desired. The test environment selected is the single axis environments (oscillatory and slew) which in retrospect is not adequate for evaluating the pulse burst phenomenon. The oscillatory environment marginally exceeded the threshold rate level that is required for pulse bursting (13% of full-on rate, see Section 4.3.1). Re-test at

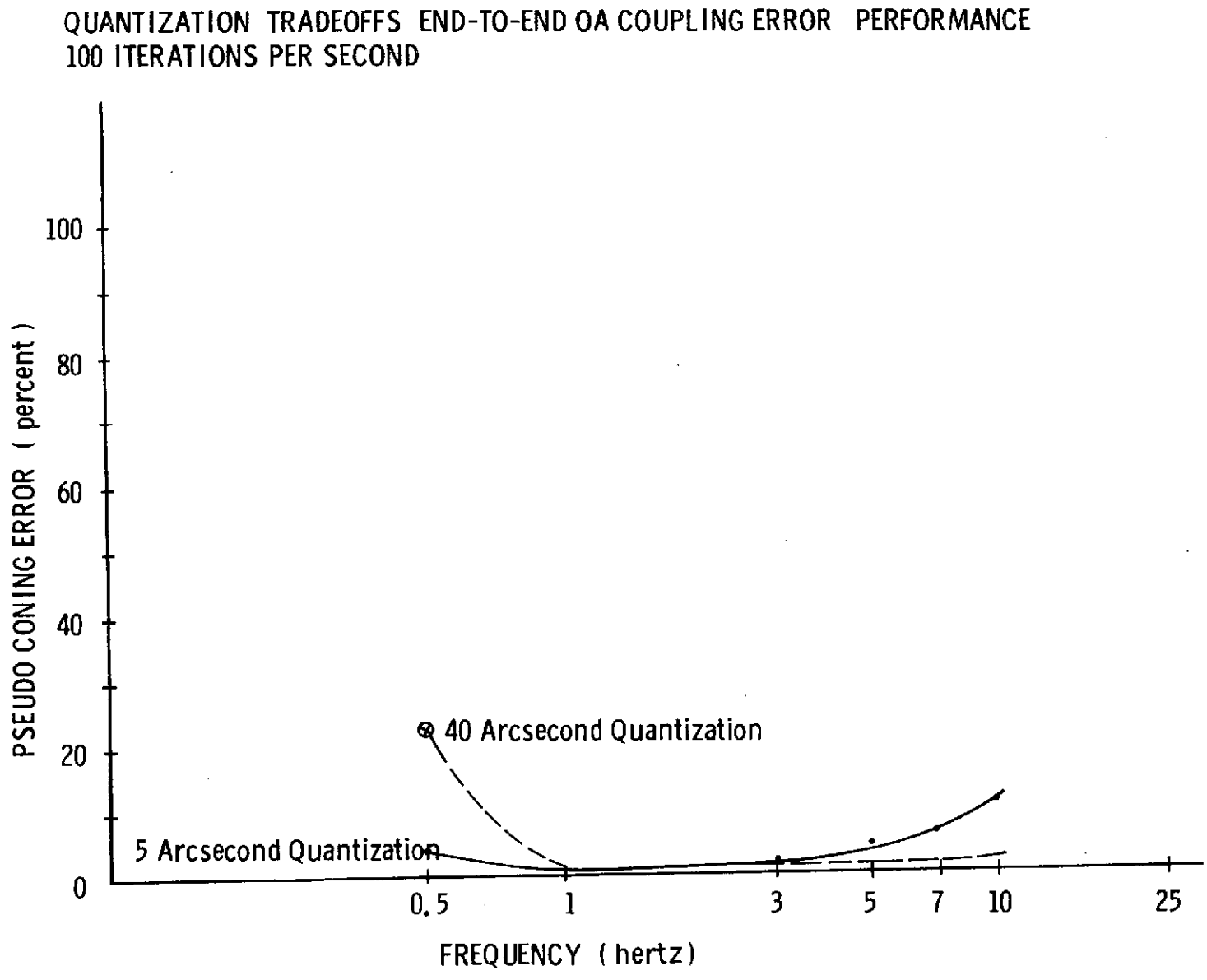

Figure 5.2.21 - QUANTIZATION TRADEOFFS

higher oscillatory magnitudes were planned but were precluded due to termination of testing. In the slew environment the short term instabilities were averaged out by the sampling of attitude data for plotting purpose. Each point plotted is an average of 480 interrogation periods.

A more effective test environment would have been in a multi-axis slew environment with a rate below the pulse burst threshold about one axis and a rate above the threshold about a second axis. Under these conditions, the ability to compensate cross axis errors such as SRA cross coupling would probably have degraded as a result of the pulsing instability.

5.2.6 Scale Factor Linearity Compensation

Scale factor linearity is an error phenomenon that is characteristic of permanent magnet torquer gyroscope/torque-to-balance loop operation. The linearity error is evidenced as a change in the scale factor of the quantized pulse as a function of the input rate (frequency of torquing). For the 18 IRIG and the ternary torque-balance control loop used in this program an essentially linear error curve (scale factor increasing with rate) has been evidenced, (see Figures 3.2.3 and 3.2.4 of Section 3.2.3.b).

The model used for compensation in the system is a linear scale factor function with respect to Input Axis rate. Rate estimates derived from the gyro accumulated torque pulse establish the operating point on the compensation curve.

The evaluation of the linearity model is conducted in the single axis rotational environment. In this environment, the end-to-end performance through the compensation and attitude algorithms is easily evaluated because the attitude error propagated about the slewing axis is essentially the scale factor error (see Figure 5.2.1).

The system sensitivity to scale factor linearity errors was evaluated by rotating the system at eight rates over the full gyro torque loop range. The full strapdown algorithm was excited, and therefore the resultant attitude error drift was scaled to reflect the equivalent scale factor error in parts-per-million (ppm). The evaluation was first conducted without linearity effects compensated. The attitude error (see Figure 5.2.22) depicts the rate dependent scale factor with a 50 ppm spread over the full dynamic range. This is the typical scale factor spread for a resistively tuned 18 IRIG Mod B gyro torquer.

SCALE FACTOR LINEARITY COMPENSATION

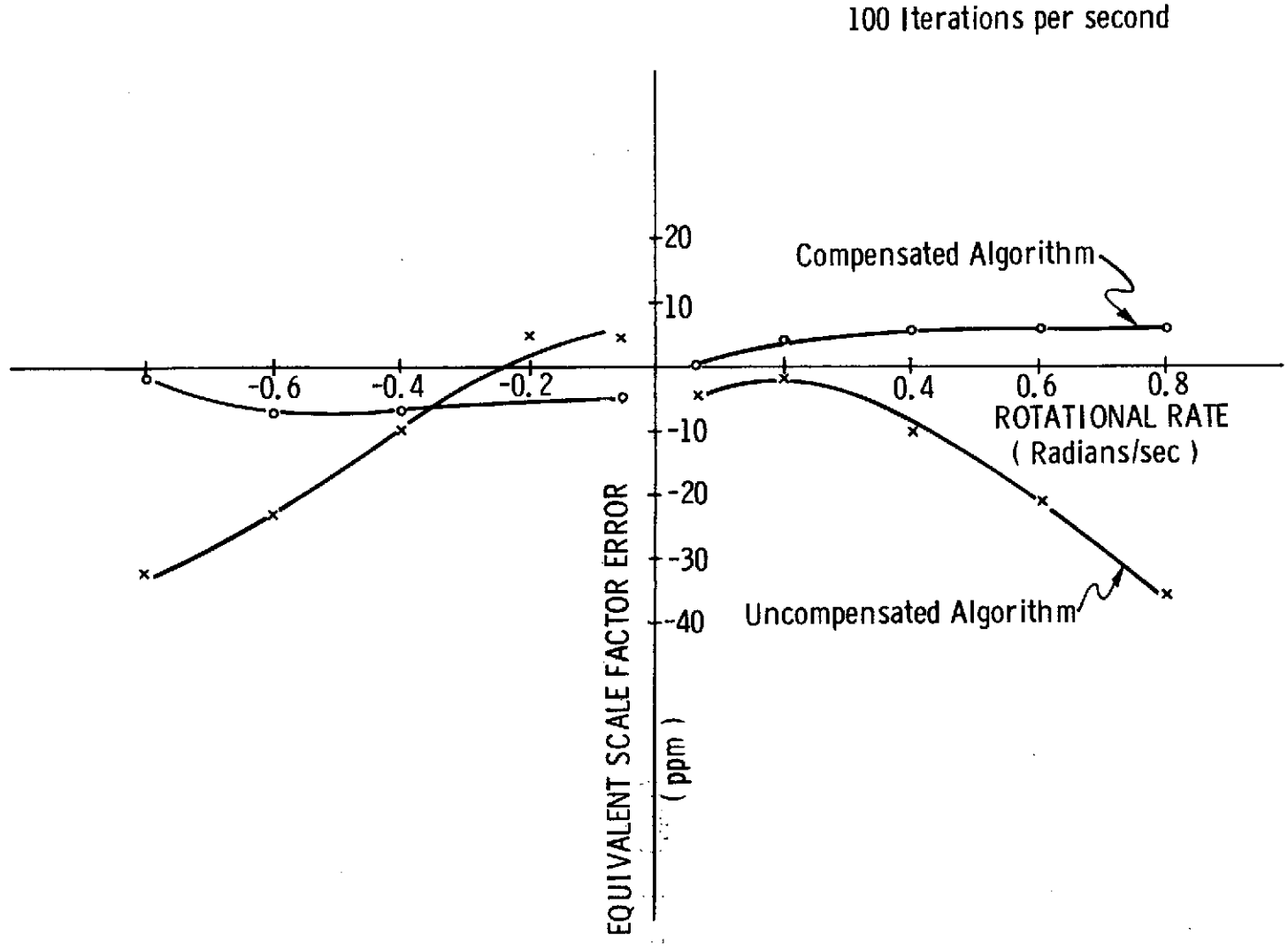

Figure 5.2.22 - SCALE FACTOR LINEARITY COMPENSATION

Compensation was then applied, using a 50 ppm linearity model for positive rates and a 43 ppm linearity model for negative rates. The results in Figure 5.2.22 show that compensation was effective to within 7 ppm spread over the entire test range which is well within the calibration and compensation uncertainties and demonstrates the effectiveness of compensating the scale factor linearity effects.

5.3 LAND NAVIGATION RESULTS

5.3.1 Latitude and Longitude Errors

An inertially stabilized navigator updating at a rate of one per second was implemented for real time processing in the H316 minicomputer. The attitude and velocity algorithms were operated at 100, 50, and 25 iterations per second. Testing of the system was conducted to evaluate performance of the compensated strapdown system in a dynamic environment as processed through the navigation algorithm. The initialization system orientation used during navigation testing is illustrated in Figure 5.3.1 (Z axis is along the polar axis, Y axis is east, and the X axis completes the right handed triad). This orientation was chosen for the simplicity afforded in the software implementation by not requiring a coordinate frame transformation or Coriolis compensation.

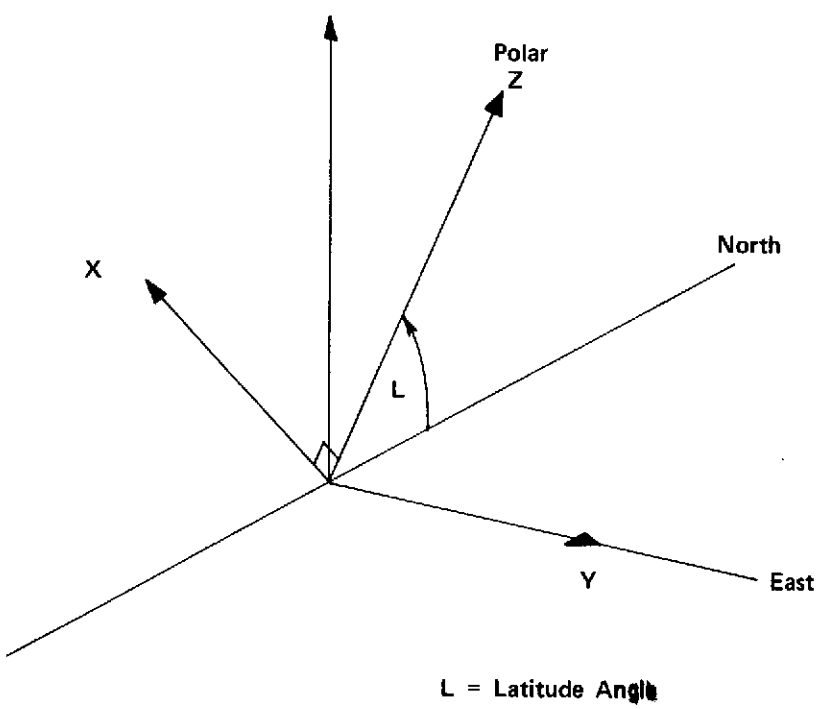

Fig. 5.3.1 Navigation Evaluation Orientation.

In a relatively static environment, a properly operating Schuler tuned inertial navigator[17, 18] operating on the surface of the earth with the system orientation shown in Figure 5.3.1 has performance characteristics that include:

1. a bounded latitude error that has a Schuler oscillation (84 minute period) superimposed on a 24 hour sinusoid. The Schuler oscillation magnitude is primarily a function of the X and Z accelerometer scale factor, bias, and alignment errors. The 24 hour sinusoid magnitude is a function of the Y gyro drift error and system alignment errors.

2. a longitude error that is composed of three components: a Schuler oscillation, a 24 hour sinusoid, and a ramp function. The Schuler oscillation magnitude is a function of the Y accelerometer scale factor, bias, and alignment error, and the 24 hour sinusoid magnitude is a function of the X and Z gyro drift error and system alignment errors. The ramp is a function of the gyro drift error about the polar axis (Z gyro).

Figures 5.3.2 and 5.3.3 shows the latitude and longitude errors respectively for a 93 hour period with the system in the position given in Figure 5.3.1. Note that the latitude error is bounded and has two sinusoid components; the 84 minute and 24 hour oscillation.

Based on sensitivity studies and tests conducted in the SIRU utilization program the Schuler oscillation in Figure 5.3.2 of 0.25 nautical miles is equal to a 35 microradian initialization alignment error about the North Axis (equivalent to 0.035 cm/sec^2 accelerometer bias). The 0.2 nautical mile per hour slope (first three hours) of the 24 hour sinusoid component is equivalent to an East Axis drift of 0.003°/hour. These errors are derived with an earth fixed system, navigating with single position calibration data that was adjusted for the specific navigation orientation. Thus, the bulk of initialization alignment errors were artificially compensated by adjusting the accelerometer bias compensation and the errors observed in the above navigation performance are the residual error after this compensation.

The longitude error in Figure 5.3.3 is a ramping 24 hour sinusoid with Schuler oscillations superimposed. The 0.05 nautical mile Schuler oscillation magnitude translates into East Axis initial alignment error of 7 microradians (equivalent to 0.007 cm/sec^2). The 0.7 nautical mile per hour slope (first three hours) of the 24 hour sinusoid component is equivalent to a North Axis drift of 0.0105°/hour.

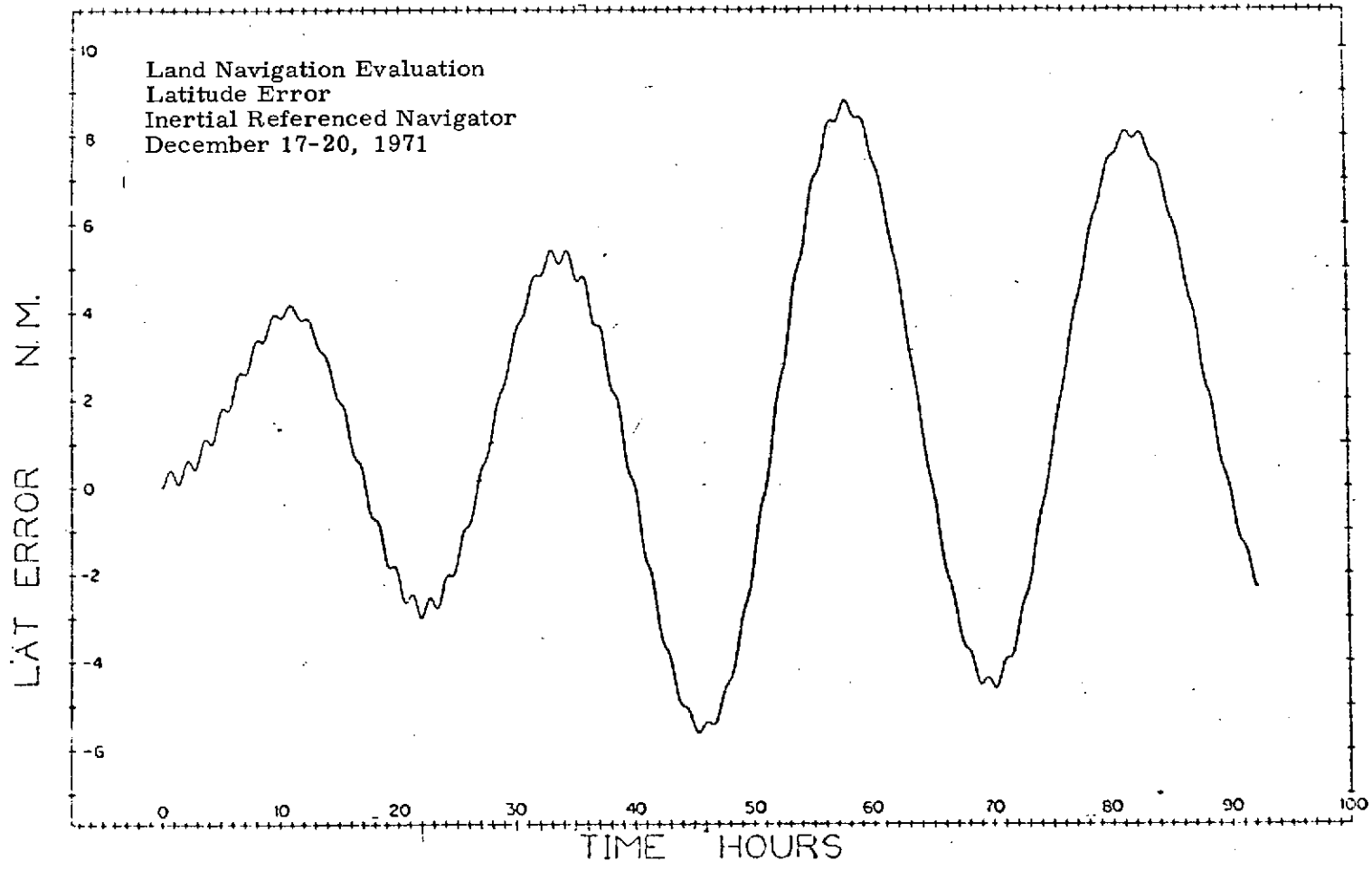

Figure 5.3.2 - Latitude Error in a Stationary Environment

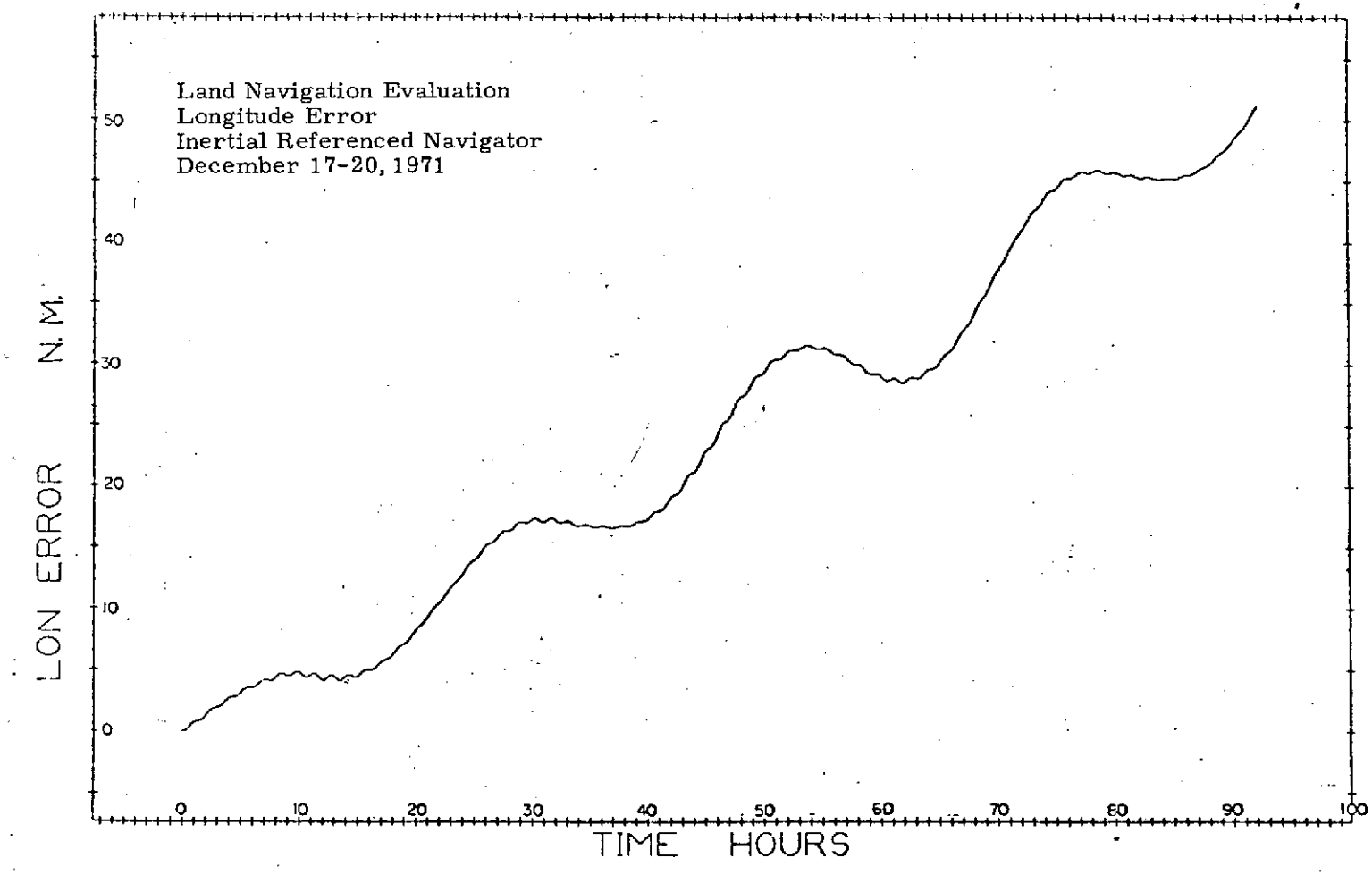

Figure 5.3.3 - Longitude Error in a Stationary Environment

As noted, a single-position-calibration load was used in the navigational testing procedure. This is consistent for land navigation in a real-flight environment. The single-position calibrations load normalizes the orientation sensitivities* of the strapdown package as installed in the gimbal assembly. For example; the drift sensitivities, referred to in Section 5.1, obtained from the multiposition calibration procedure showed a spread between 0.03°/hr–0.45°/hr (1-3 meru) for drifts derived from different position dependent equations (IBD, OBD, and SBD, Appendix P).

The ultimate demonstration of navigational nerformance accuracy is limited using this gimbal test configuration due to the inability to precisely establish the strapdown triad body frame with respect to the initialization inertial attitude. For example, it was estimated that absolute positioning uncertainty, using the gimbal readouts, with respect to an absolute reference is on the order of 50 arc seconds. The uncertainty is inherent in the gimbal non-orthogonalities, the resolver readouts, and the uncertainties in measurement of the strapdown triad with respect to the gimbal axes.

Land navigation testing was also conducted with oscillatory and slew inputs. For the oscillatory inputs the single position load in a first order sense is still satisfactory since the average orientation of the body did not change. With regard to initialization uncertainties, rectification errors may be anticipated that cause the axes perpendicular to the rotational axes to both drift as well as indicate an apparent net acceleration. In general, one would expect performance degradation to be more pronounced in the inertial navigator mechanized in these tests. As opposed to a local-level implementation (in which the two sensing accelerometer axes are level) both the X and Z accelerometers in this inertial orientation see a sizable portion of "g". Another error source introduced that is considered negligible corresponds to the influence of output axis coupling. The X accelerometer has its OA collinear with the oscillatory axis. For the OA coupling input (1 Hz at 0.024 radian) however the effective float motion is below the torquing threshold, less 1 arc second, and negligible OA otuput or PRA cross coupling errros should be introduced.

Slew testing was conducted with constant rate, approximately 50 revolutions at 4°/sec applied about the Y body axis of the strapdown package. As a consequence of this rotation the X and Z axes are tumbled continuously in the "g" field, clearly

---

* Insufficient space existed in the gimbal assembly to allow satisfactory thermal gradient design shielding.

a non-representative environment. Multiple error sources are excited with the inertial orientation reference frame used in this test. As one might expect the single-position-calibration load that was used could not accuratey account for the previously discussed orientation sensitivities, a completely new thermal gradient condition was established in the tumbling mode. The body-inertial frame initialization uncertainty now represents a significant error source that propagates in a manner similar to gyro and accelerometer misalignments but is systematic in nature, i.e., one frame is rotated with respect to the other. Thus, both gyro and accelerometer errors are introduced in a similar manner and tend to be reinforcing. Additional errors are introduced by the rotation about the horizontal Y axis, which also tumbles the X and Z accelerometers. The rotation excites the Y gyro scale factor but the tumbling also introduces accelerometer asymmetry and linearity error sources. Finally, since the navigational algorithm was operating at a one per second iteration rate, velocity sampling errors in tracking the cycling "g" input (approximately a 90 second period) are likely to further degrade navigational performance.

As is obvious, in retrospect, slew testing conducted in this manner was ill-defined. Precise representations of relevant error propagation terms could not be deduced nor could representative strapdown performance capabilities be reflected. Use of a local-vertical navigational mode would have been more consistent with a slew test evaluation. In this case one would have rotated the platform about the vertical axis thereby exciting more realistic error sources while keeping the two sensing accelerometers near null. Recognizing these factors, a subsequent test procedure was defined in which the inertial reference navigator would be initialized so that its axes were in a local vertical orientation as opposed to the polar axis orientation. The inertial navigation mode would still be used, avoiding the necessity for an entire software recoding effort. Local vertical initialization accuracy however would now be consistent with the null bias uncertainties of the two horizontal accelerometers. Rotation about the Z axis of the platform would then primarily reflect gyro scale factor and misalignment error propagation effects. Unfortunately, retest in this orientation was precluded by the gyro failure that was experienced during the retesting phase of the program. To provide a more realistic base-line of strapdown capabilities we have included in this report a slew test conducted at 5° per second on the SIRU strapdown system with the system initialized and operating in a local-vertical mode.

5.3.2 Oscillatory Test Results

Navigation results were accumulated with oscillatory tests at attitude and velocity algorithm iteration rates of 100, 50 and 25 per second.

Tables 5.3.1a and b present the results of the oscillatory tests—1 hertz, 0.024 radians peak to peak, for 1 hour. With the navigation algorithm operating at a rate of one per second, the variation in the velocity iteration rates (100, 50 and 25 per second) becomes a measure of effect of coarseness on the navigation performance. The magnitude of the Schuler oscillation in latitude (Table 5.3.1a) is consistent for all tests indicating an independence from ΔV iteration rate however it is excessively high (equivalent to approximately 0.25 milliradian leveling initialization error). This error is attributed to a misalignment of the XZ plane about the East (Y) axis body frame with respect to the earth centered inertial frame at initialization and is consistent with the estimated absolute positioning capability of the gimbal fixture.

The slopes of the 24 hour sinusoids are tabulated and presented as a general indication of the Y gyro performance. Because of the relatively short test times, accurate slope determination is not feasible. The variation in slope for the three iterations are assessed to be a function of the initial azimuth alignment for each test.

It is interesting to note that with the algorithms operating at 25 iterations per second, the 24 hour slope was better than at 50 and 100 iterations per second. These results do not correlate with the pseudo coning bandwidth studies conducted in Section 5.2.2.b and therefore it is believed that the 25 iterations per second performance reflects an extremely good alignment initialization for that particular test.

5.3.3 Slew Test Results

As noted in the prior discussion, initial slew evaluations in a navigational mode were conducted such that error propagation was significantly influenced by the test initialization uncertainties and the test method, for example tumbling the platform in the "g" field introduced several unrealistic error sources. The test performance degradation was reasonably bounded however, considering the tumbling environment and the number of input revolutions, 50. For example, in the three different 4° per second slew tests, using algorithm iteration rates of 100, 50 and 25 per second respectively, the Schuler oscillation magnitude in longitude corresponded to 1, 1.5 and 2 nautical miles. In latitude the Schuler magnitudes were 1.1, 3 and 4 nautical miles for the same tests. These amplitudes are not inconsistent with the estimated 1/4 milliradian nominal uncertainty in the gimbal chain positioning of the strapdown triad, in that the Schuler amplitude coefficient with respect to the accuracy of leveling initialization is theoretically 7 nautical mile per milliradian. With regard to the 24 hour slope, the longitude error corresponded to approximately

Attitude and Velocity Algorithm Iteration Rate (Iterations/Second)	Schuler Oscillation Peak Magnitude (Nautical Miles)	Equivalent Initial Alignment Uncertainty in the Horizontal Plane (Milliradians)	24 Hour Period Oscillation Slope (Nautical Miles/Hour)	Equivalent Y Axis Gyro Drift (^{o}/Hour)
100	2.1	0.3	~2.0	0.03
50	2.0	0.28	~3.0	0.045
25	1.7	0.25	~0.6	0.009

Table 5.3.1a. Latitude Error (1 Hertz Oscillatory Environment)

Attitude and Velocity Algorithm Iteration Rate (Iterations/Second)	Schuler Oscillation Peak Magnitude (Nautical Miles)	Equivalent Initial Alignment Error (Milliradians)	24 Hour Period Oscillation Slope (Nautical Miles/Hour)	Equivalent X and Z Axis Gyro Drift (^{o}/Hour)
100	0.55	0.08	~1.5	0.022
50	0.6	0.08	~3.0	0.045
25	0.3	0.045	~0.1	0.001

Table 5.3.1b. Longitude Error (1 Hertz Oscillatory Environment)

5 nautical miles per hour in all tests while the latitude 24 hour sinusoid error propagation slope was on the order of 6 nautical miles per hour at 100 and 50 iterations per second. At 25 iterations per second the 18 nautical mile per hour slope in latitude that was observed is considered to represent a significantly larger initialization error (retest was not possible). This conclusion appears to correlate well with the 8 nautical mile Schuler magnitude in latitude (2.3 times the estimated 0.25 mr alignment uncertainty) in the same test. From these results it would appear reasonable to conclude that for the slew environment testing, basic navigational performance is unaffected over the 25 to 100 per second range of iteration rates used for the attitude and velocity algorithms. This conclusion is consistent with theoretically derived drift rates of a third order attitude algorithm (reference Figure 4.3.9) that show for a 4° per second slew the equivalent computational drift is considerably less than 0.00015° per hour (0.01 meru).

The observed 5 nautical mile per hour latitude and longitude 24 hr slopes are surprisingly low when one considers all error sources excited by the constant Y axis rotation. For example, if we assume gyro scale factor error propagation effects only, an equivalent Y system axis drift rate of 0.075°/hr corresponding to approximately 5 ppm scale factor uncertainty would be projected. The more likely occurrence is that multiple errors are being excited and that varying degrees of cancellation exist.

Finally, to provide a more representative base-line of navigational strapdown performance in a slew mode a test made on the SIRU (redundant strapdown system) is presented here. The SIRU facility and software implementation allows a more accurate leveling initialization (gyrocompassing mode with accuracies on the order of 10 seconds of arc). A local-vertical navigator is implemented and the system was constantly rotated for six hours about an axis coincident with the vertical (accelerometers are essentially null sensing) at 5°/sec. The attitude and velocity algorithms iteration rate was 50 per second and the navigational equation operated at a rate of one per second. Although the SIRU dynamic compensation was not as comprehensive* as in SPOT the test results (Figures 5.3.4 and 5.3.5) are indicative of what can be achieved and clearly evidence the reduction in the Schuler magnitude. The latitude (Figure 5.3.4) and longitude Schuler peak position error corresponded to 0.5 nautical mile, equivalent to approximately a 14.5 arc second of alignment initialization uncertainty.

---

* SIRU dynamic compensation does not employ SRA, anisoinertia or scale factor linearity modeling for the gyros and only average scale factor is used for the accelerometers. The SIRU geometry does however, when all six instruments are used, have a measurable level of SRA-Anisoinertia error self-cancelling.

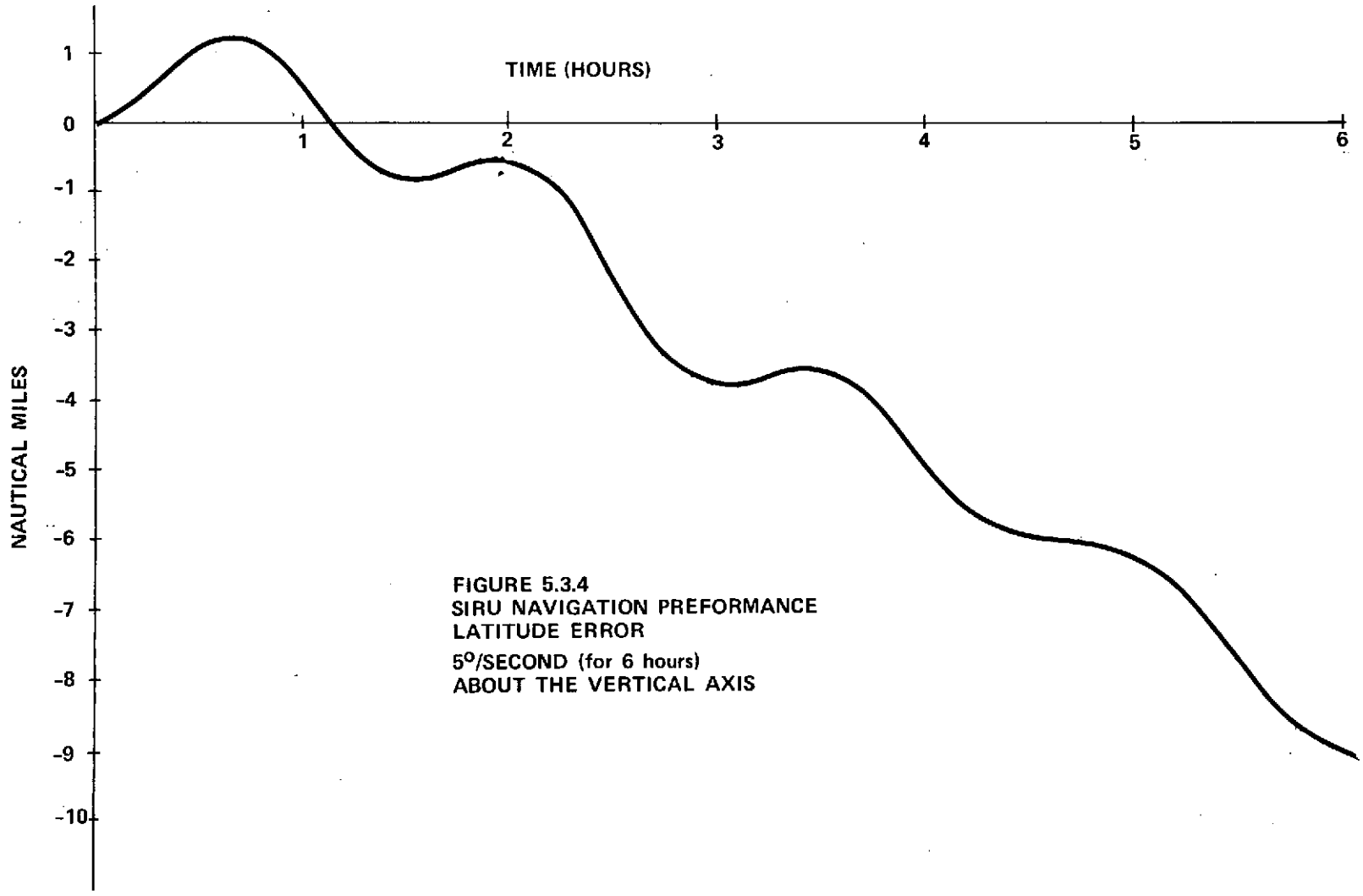

FIGURE 5.3.4
SIRU NAVIGATION PREFORMANCE
LATITUDE ERROR
5°/SECOND (for 6 hours)
ABOUT THE VERTICAL AXIS

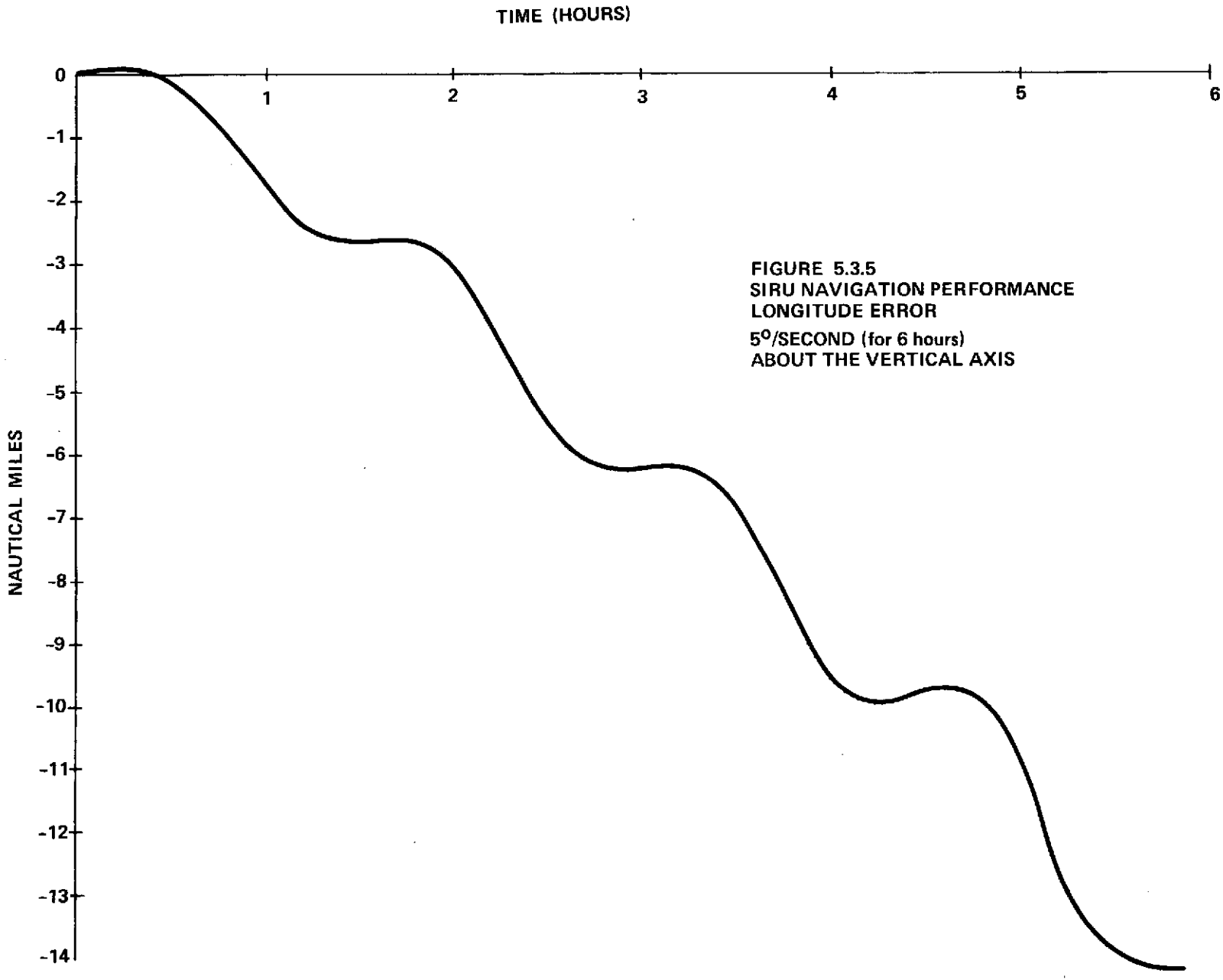

FIGURE 5.3.5
SIRU NAVIGATION PERFORMANCE
LONGITUDE ERROR
5^{o}/SECOND (for 6 hours)
ABOUT THE VERTICAL AXIS

The 24 hour slope for both latitude and longitude is approximately 2 nautical miles per hour. For this SIRU data, the error propagation is more directly representative of the gyro SF and alignment uncertainties. Other probable error sources in the SIRU test at this slew rate although not as dominant arise from the lack of compensation of the SRA and anisoinertia terms. Although they are self-cancelling because of the geometry, the rotation about a single axis does excite these terms due to the non-orthogonality of the SIRU-IA arrangement. Any off-nominal coefficients will therefore result in some second order dynamic error propagation.

5.3.4 Summary

With regard to all of the slew testing one should recognize that a 5^{o} per second constant rotational rate applied for 6 hours is clearly not representative of any realistic environment. The navigational performance that is evidenced therefore in these test results does not directly relate to what might be anticipated in an aircraft mission. The navigational implementation does provide a very sensitive indication of initialization alignment accuracy as well as initial calibration residual errors.

Unfortunately the navigational test evaluations were terminated due to the system hardware failure so that a more comprehensive evaluation using the recommended procedural changes could not be effected. Similarly, a comparative evaluation of performance without the full complement of compensation models was not possible.

In general for the limited testing that was done the modeling appeared to be adequate and performance was consistent with the implementation capabilities. The strong dependence upon accurate initialization was clearly evidenced leading one to conclude that for a strapdown implementation in a land navigation application the local-vertical initialization mode is preferred.

An interesting projection for future evaluations in a navigational mode using the type facility developed under this program is possible. With the incorporation of a linear servo controlled rate drive on the gimbal, an actual flight profile of attitude, angular rate and oscillatory environments could be used to excite the system. One could then accurately assess the applicability of compensation models and system performance in a direct manner with extremely high confidence.

5.4 Multi-Position Accelerometer Evaluations

5.4.1 Introduction

This section discusses the results of multi-position accelerometer testing and the development of higher order accelerometer models. This effort supported a NASA/MSC accelerometer modeling study that used a Delco 653 accelerometer and software support on the Univac 1108 computer. The automatic test capability of the SPOT system proved ideal for the accumulation of multi-position data with little impact to the program's schedule. The analysis of data was accomplished off-line on the IBM 360/75 computer. Two methods were developed to analyze the multi-position accelerometer data: 1) a fourier series analysis, and 2) a least square error analysis.

5.4.2 Fourier Series Analysis

The fourier series analysis fits the data from sixteen different test positions to a fourier series expansion. The accelerometer data is generated by rotating the system through sixteen equidistant increments (22.5^{o}) about a horizontal axis of rotation. The accelerometer whose Pendulous or Output Axis is along the axis of rotation describes an indicated acceleration function $a_{IND}(\theta)$ that is periodic with respect to the system orientation.

The fourier series that fits this periodic data is developed from the Taylor series expansion given as follows:

$$a_{ind} = \frac{A_o}{K_1} = B_o + a_{IA} + K_2 a_{IA}^2 + K_O a_{OA} + K_P a_{PA} + K_{IP} a_{IA}\, a_{PA} + K_{IO} a_{IA}\, a_{OA} + \cdots \qquad (5.4.1)$$

where
- a_{ind} = acceleration input indicated by the accelerometer (g)
- A_0 = accelerometer output indication (output units)
- K_1 = accelerometer scale factor (output units/g)
- a_{IA}, a_{PA}, a_{0A} = acceleration inputs along the input, pendulous, and output axes of the pendulum (g)
- B_0 = accelerometer bias (g)
- K_2 = second order non-linearity coefficient (g/g^2)
- K_0 = output cross-axis coefficient (g/g)
- K_P = pendulous cross-axis coefficient (g/g)
- K_{IP} = input axis - pendulous axis cross-coupling coefficient (g/g^2)
- K_{I0} = input axis - output axis cross-coupling coefficient (g/g^2)

Assume that the system rotation is applied about the Pendulous Reference Axis and that the Input Axis is oriented vertically up in the initial test position. As the system rotates by θ, the acceleration inputs are described as $a_{IA} = g \cos\theta$, $a_{OA} = g \sin\theta$, and $a_{PA} = 0$. The general accelerometer model, under these conditions, simplifies to:

$$a_{ind}(\theta) = B_o + g\cos\theta + K_2 g^2 \cos^2\theta + K_O g \sin + K_{IO} g^2 \sin\theta\cos\theta \quad (5.4.2)$$

This model converts to a fourier series expansion that is truncated at the second harmonic.

Note that for system rotations about the accelerometer Output Axis, the output related cross axis coefficients (K_O, and K_{IO}) are replaced with the Pendulous Axis related coefficients (K_P, and K_{IP}).

A numerical analysis algorithm[19] is used to derive the fourier coefficients from the sixteen equidistant data points.

The fourier series analysis results yields a scale factor and null bias that correlates well with the results from the standard four position accelerometer calibration data. The statistical significance of the cross coupling and cross axis coefficients is marginal. Depending on the accelerometer, the standard deviation of the calibrated coefficient exceeds the mean value. The scale factor non-linearity term is observed to be significant with typical values of $80g/\mu g$ measured. This magnitude of non-linearity causes a 80 ppm scale factor error between a condition of no acceleration and a 1g input.

The large scale factor non-linearity is attributed to the use of one average scale factor in the fourier model. Had two scale factors been used, one for positive acceleration inputs and one for negative acceleration inputs, the non-linearity term is expected to be small.

A decision is therefore required to determine the optimum accelerometer model. In other words, what coefficients are to be included for a model to accurately describe the accelerometer performance? The fourier series analysis revealed that a model comprising the accelerometer scale factor, and the null bias coefficient is an accurate model, but is it the model with the least square error? This question is the impetus of the least square investigation. (Appendix U presents the method of least square evaluation).

5.4.3 Least Square Analysis

The accelerometer model employed in the least square evaluation of the multi-position test data is derived from the general accelerometer model (Equation 5.4.1) and is of the form:

$$a_{ind} = B_o + K_1 \text{ Sin } (\theta - \psi) + K_2 \text{ Sin } (\theta - \psi) + K_{IP} \text{ Sin } (\theta - \psi) \text{ Cos } (\theta - \psi) + K_d \text{ Sin } (\theta - \psi) \quad (5.4.3)$$

where

a_{ind}	=	acceleration input indicated by the accelerometer in pulses per second (pps)
B_0	=	accelerometer bias (pps)
K_1	=	scale factor (pps/g)
K_2	=	second order non-linearity coefficient (pps/g^2)
K_{IP}	=	input axis-pendulous axis cross-coupling coefficient (pps/g^2)
K_d	=	plus and minus scale factor differential (pps/g)
ψ	=	misalignment angle (radians)

The significant difference between the general model (presented in equation 5.4.2) and the computation model (equation 5.4.3) is the omission of the cross axis coefficient (K_0 cos $(\theta-\psi)$ or K_p cos $(\theta-\psi)$) and the addition of the misalignment angle ψ, and the plus and minus scale factor differential term, K_d.

The misalignment angle ψ is included to account for the sum of gimbal and accelerometer misalignments that are relevant for the particular accelerometer and test sequence. With ψ included, however, the least square computation fails to converge. Analysis of the matrix of the partial differentials has shown (See Appendix V) that the partial derivative with respect to the non-linear misalignment angle term is in fact a linear combination of the partial derivatives with respect to the other coefficients and, therefore, is redundant. It can be shown that, if the rectangular matrix A has a redundant row, then the square matrix A^TA is singular and has no inverse. Thus, one of the coefficients in the full general model, is arbitrarily determined. Since the inclusion of the misalignment angle in the model makes more sense than including the Output Axis sensitivity coefficient, the Cos (ψ) term does not appear in the current version of the accelerometer model.

The plus and minus scale factor differential (K_d) recognizes the difference of accelerometer scale factor under conditions of positive and negative acceleration. The average of the plus and minus scale factors is the average scale factor (K_1) expressed by

$$K_1 = \frac{K^+ + K^-}{2}$$

where (5.4.4)

$$K^+ = K_1 + K_d$$

$$K^- = K_1 - K_d$$

This is equivalent, however, to treating the average scale factor as a coefficient of a $\sin(\theta-\psi)$ term and the plus and minus scale factor differential as the coefficient of an $|\sin(\theta-\psi)|$ term. One difficulty encountered here is that such a term is non-linear, and its derivative is undefined for $\sin(\theta-\psi) = 0$. However, there exists no data at this point in any case, and the difficulty is ignored.

5.4.4 Accelerometer Model Evaluation

One objective of the least square analysis is to determine the significance of each term in the accelerometer model. Eight accelerometer models were formed using a basic model that comprises the scale factor, null bias, and misalignment angle and all eight combinations of the three remaining terms. Each model was compared with each other model configuration by computing the sum of the squares (SSR) of the differences between the indicated acceleration and the predicted acceleration using the least square techniques. The SSR is the residual and is expressed in parts per million (ppm) as:

$$\text{ppm} = \sqrt{\frac{\text{SSR}}{\text{TOTAL SQUARE}}} \times 10^6 \qquad (5.4.5)$$

where the "total square" is the sum of the squares of the raw data points. Therefore, the residual in ppm refers to that fraction of the data not explained by the model, and is a figure of merit representing the "goodness of fit" relative to other models.

Fourteen (14) sets of sixteen-position accelerometer data were run against the eight (8) different models. Table 5.4.1 gives the mean, standard deviation, and range of the residuals for each model.

TABLE 5.4.1 SUMMARY OF RESIDUALS (PPM FOR 14 DATA SETS)

		Range			Standard
		Low	High	Mean	Deviation
Model #1	Full Model	7	32	14.0	5.9
Model #2	Without scale factor differential term (K_d)	8	32	17.4	6.7
Model #3	Without scale factor non-linearity (K_2)	8	34	14.8	6.2
Model #4	Without the scale factor differential (K_d) and non-linearity (K_2) terms	28	37	38.0	9.5
Model #5	Without cross coupling coefficient (K_{IP})	12	42	19.1	8.5
Model #6	Without cross coupling coefficient (K_{IP}) and scale factor differential (K_d)	12	42	22.3	7.5
Model #7	Without cross coupling coefficient (K_{IP}) and scale factor non-linearity (K_2)	13	44	19.8	8.7
Model #8	Minimum model with null bias (K_d), scale factor (K_1) and misalignment angle (ψ)	28	63	40.6	9.6

Obviously (from Table 5.4.1), the full computational model provides the "best fit" in terms of yielding the lowest residual. There is very little difference between a model that includes the cross-coupling coefficient (model #4) and model #8 that does not include cross-coupling. This indicates that the cross-coupling coefficient contributes little to the model. The most significant contribution (other than bias and scale factor), appears to be the plus and minus scale factor differential. Compare, for example, the results for models #7 and #8. The other measurable contribution is made by the second order non-linearity factor.

Based on the comparison of residuals, the full model is the best model to implement with respect to the set of models analyzed. The question which remains is: Does improvement in the residual warrant the inclusion in the model of a given coefficient? A corollary question is: What is the best criteria for appropriate model selection?

One technique that may be used to answer this question is to evaluate the probability that the coefficient in question is different from zero. This probability is obtained from the "t" statistic that is computed from the mean value (x) of the coefficient and the standard deviation of the data about the mean(s).

$$t = \frac{\bar{x}\sqrt{n}}{s} \tag{5.4.6}$$

where n is the number of data points.

This statistic is then compared with the normal distribution.

For small samples, it is necessary to use the Student's "t" distribution with n-m degrees of freedom where m is the number of coefficients in the model. The t statistic becomes

$$t = \frac{\bar{x}\sqrt{n-m}}{s} \tag{5.4.7}$$

Student's "t" distribution has a slightly larger dispersion than the normal distribution, but approaches the normal distribution asymptotically as n increases.

Using the full computational model, and data obtained from the Y accelerometer on 29 March 1971, the "t" statistics were computed and are presented in Table 5.4.2.

TABLE 5.4.2 COMPUTED T STATISTICS FOR FULL MODEL

Coefficient	Value	Standard Deviation	t-Statistic
K_b	.065680	.003205	64.8038
K_1	960.392	.004532	670036.
K_2	.036851	.033490	3.47969
K_{IO}	-.009007	.009065	-3.14193
K_d	.032619	.036524	2.82420
$\psi_{x10^{-3}}$	.034193	.004720	22.9105

At the 1% level of significance and for 10 degrees of freedom, the bias, scale factor, and misalignment angle terms, as expected, are highly significant. The scale factor differential, and cross-coupling coefficients are not significant. Thus with a 99% probability, the means of the scale factor differential and cross coupling coefficient are not different from zero. The scale factor non-linearity term marginally passes the significance test. Not all coefficients for all models and data sets have been tested for statistical significance. However, since the least square methods determines the model coefficients in a probabilistic sense, the statistical testing for significance is directly applicable as a criterion of model selection. The levels of significance are chosen as the confidence of model selection warrants.

Another factor that influences model selection is the interaction between terms. The computation program models the plus and minus factor differential as a coefficient of a $|\sin(\theta-\psi)|$ term which is added to or subtracted from the average scale factor to yield the desired plus and minus scale factors. The second-order non-linearity coefficient is modeled as a $\sin^2(\theta-\psi)$ term. Both $\sin^2(\theta-\psi)$ and $|\sin(\theta-\psi)|$ have a positive average value which would interact with the bias term. Such interaction makes it difficult to ascertain whether or not the second-order non-linearity or the plus and minus scale factor differential terms is a statistically significant contributor to the model. The statistical dependence between coefficients is verified by isolating the three coefficients and by performing a cross correlation analysis. The correlation analysis operates on the following expression with dummy variables a and b.

$$B_o + aK_2 + bK_d = \text{CONSTANT VALUE} \qquad (5.4.8)$$

The product moment correlation coefficient computed for 16 data set is 0.963. This high correlation implies that the current accelerometer model is not an optimal one in terms of coefficient independence.

An interesting result derived from the least square analysis is that the significance of computed coefficient is dependent on the input data. Using MIT/CSDL data, little difference was observed in the misalignment angle (ψ) when the data was divided into positive and negative acceleration sets. However, with NASA/MSC furnished data (Delco 653 accelerometer) the difference was significant. This result implies a larger pendulum hangoff in the NASA data than in the MIT/CSDL data.

5.4.5 Sixteen Position Data—Four Position Data Comparison

A second objective of the least square analysis is to compare the estimation of coefficients between a data set from sixteen positions to a data set comprising four of the sixteen positions. The comparison analysis is restricted to the scale factor coefficient (K_1). The first set of four-position test (4PT) data includes the four ordinal points ($\theta = 0^\circ, 90^\circ, 180^\circ$, and 270°) from the sixteen-position test (16PT) data and solves for the bias, plus and minus scale factors, and the misalignment angle in a deterministic sense. Assuming that the 16PT least squares (probabilistic) solution for the accelerometer model coefficients is more "accurate" in some sense than the 4PT solution, it is desirable to compare the results to find out how well the 4PT determines the accelerometer model coefficients. Over the fourteen (14) sets of data points, differences between the computed 4PT and 16PT solutions for scale factor ranged from -1 to +23 parts per million.

While the differences do not seem large, a statistical analysis was made with the following results. The mean difference in scale factors is 6.93 parts per million (ppm) with a standard deviation of 7.52 ppm. The resulting "t"-statistic (3.32) for 13 degrees of freedom indicates that the probability is very low (less than .005) that the scale factors computed by the two methods are the same. This analysis concludes that the 16PT least squares method yields a scale factor coefficient that is more statistically significant than the 4PT solution.

An effort was made to determine the coefficients when four other points (other than the ordinal points) are used in the computation.

For example, an additional four data set was selected from the sixteen position data sets that were rotated 22.5° off the ordinal position ($\theta = 22.5^\circ, 112.5^\circ, 202.5^\circ$, and 292.5°). The 4PT solution was computed for this orientation and for 45° and 67.5° rotations as well. The results are summarized in Table 5.4.3.

TABLE 5.4.3 DIFFERENCE BETWEEN 16PT AND 4PT SOLUTIONS FOR SCALE FACTOR

Rotation from Ordinal	Low	High	Mean(ppm) Difference	Standard Deviation(ppm)	t
0^{o}	- 1	23	6.93	7.52	3.320
22.5^{o}	- 9	16	1.57	6.57	0.350
45.0^{o}	-32	8	-2.79	9.90	1.016
67.5^{o}	- 3	15	1.57	8.39	0.675

It is to be noted that there are no significant differences ("t"-statistics too small) between the 4PT and 16PT solutions in any of the three "off ordinal" positions. The conclusion may be made that the 4PT in the ordinal position is the solution least likely to estimate the accelerometer model scale factor coefficient as determined by the 16PT least squares solution.

A similar comparison between 16PT and 4PT data sets was conducted for null bias and the misalignment angle. The results are not given here. However, the 4PT solution of bias and misalignment angle are generally not good estimators of the corresponding 16PT solution.

An important result, however, is that as the Input Axis approaches 45^{o} with respect to the g-vector, the plus and minus scale factors tend to diverge, yielding obviously poor results. For example, 1090.948 and 829.903 pps/g where the 16PT average scale factor is 946.224 pps/g.

The divergence between plus and minus scale factors is due to the fact that we are trying to compute the slope of the line using two points which are very nearly the same operating point for the accelerometer. For example, the four accelerometer models that express the accelerometer's output for orientations to include 45^{o}, 135^{o}, 225^{o}, and 315^{o} from the horizontal are given as follows:

$$
\begin{aligned}
A_1 &= B_o + K^{+} \sin (45^{o} + \psi) \\
A_2 &= B_o + K^{+} \sin (135^{o} + \psi) \\
A_3 &= B_o + K^{-} \sin (225^{o} + \psi) \\
A_4 &= B_o + K^{-} \sin (315^{o} + \psi)
\end{aligned}
\qquad (5.4.9)
$$

The positive scale factor solution is:

$$K^{+} = \frac{A_1 - A_2}{\sin(45^{\circ} + \psi) - \sin(135^{\circ} + \psi)} = \frac{A_1 - A_2}{\sqrt{2}\sin\psi} \qquad (5.4.10)$$

The differences in both the numerator and denominator are small quantities but with large sensitivities to the computed scale factor. The sensitivity due to this source is obviously smaller in the cases of 22.5° and 67.5° rotations from the ordinal position.

In summary, the 4PT in the ordinal position yields better results for plus and minus scale factors than the 4PT in off ordinal positions. On the other hand, the off ordinal orientations yield better results for the average scale factor.

The compromise 4 position test is the four sets of data that are, rotated 22.5° from the vertical (θ = 22.5°, 157.5°, 202.5°, and 337.5°). If this is a feasible alternative for system testing, it may offer improved results insofar as determining accurately both average scale factor and the plus and minus scale factor.

To correlate the results of the least square evaluation to the fourier series expansion, an analysis was conducted (See Appendix W) that relates the coefficients from the two methods and proves that the two solutions are equivalent if only the low order terms are considered (bias, scale factor and scale factor non-linearity).

Additional evaluations of multi-position accelerometer data are warranted. Least square and "t" statistics techniques provide useful methods to evaluate different models, however, the optimum accelerometer model has not yet been defined. The statistical interaction of the null bias, scale factor differential, and scale factor non-linearity coefficients also illustrates the need for a model with less dependence between terms. Another area of investigation is the evaluation of correlation between the aggregate misalignment term (ψ), and system misalignment errors.

5.5 Program Milestones

This text discusses the achievement of the program milestones that included: the system design, fabrication, integration, and the inertial strapdown performance calibration and evaluation. The chronological sequence of completed program milestones is given in Table 5.5.1 and is illustrated in Figure 5.5.1.

It is observed from the milestone data that four gyro wheel start problems occurred during the course of the program. The 410 series, 18 IRIG Mod B gyro population designated for utilization in this program was known to have a generic wheel start problem from experience with earlier developmental programs. Unfortunately, the gyro population did not withstand the countless power on-off cycles incurred during the system start-up phase where many subsystems were integrated into one facility. Each gyro failure impacted the program schedule approximately one month to harness and calibrate a replacement gyro and to establish a new system baseline upon which strapdown evaluations were based.

The backup gyro population included four similarly designed gyros that were manufactured by the Bendix Corporation. The Bendix gyros, because their hardware actually corresponded to a very early 410 series gyro design release, incurred a similar wheel start problem which exhausted the total planned gyro population prior to the completion of all program objectives. With the concurrence of the NASA technical monitor, the newer designed 420 series gyro was loaned for use in this program. These gyros proved to perform satisfactorily.

It is noteworthy to comment, that the redesigned Mod D gyro uses a beryllium-oxide wheel element which is expected to permanently correct the wheel start problem.

Another factor influencing the milestone performance resulted from the basic program ground rule that the system design was to use hardware and equipment available from earlier programs along with surplus hardware and equipment from the Apollo program to the extent that the only major procured item was the Honeywell H-316 computer. For system supplies and monitoring equipment, this approach was sound.

One system component, the resolver-to-digital encoder (RDE), was of a new design and required a considerable unanticipated developmental effort because of reoccurring noise, transient, and reliability problems. A RDE rebuild effort was necessary to correct these problems. In retrospect, had the design effort occurred

TABLE 5.5.1

SPOT Major Program Milestones

1. August 70	Strapdown inertial system packaging in gimbal completed and ready for test.
2. December 70	Supporting electronics, computer facility and system harnessing completed.
2. January 70	Gyro MB-413 removed from the population (wheel start problem).
3. February 70	Gyro MB-411A removed from the population (wheel start problem).
3. June 71	System integration completed and ready for strapdown evaluations. (Integration effects include: thermal adjustment, pulse torque loop calibration, computer software verification and activation of the automatic test capability. The resolver to digital encoder was completed, however, because of a rebuild effort necessary to correct an operational problem, integration with the system was not completed until October 71.
4. October 71	System end-to-end performance is verified in a stationary environment. Dynamic evaluations started.
4. November 71	Gyro MB-2 removed from the population because of wheel start problem.
5. January 72	Dynamic calibrations completed (Gyro scale factor linearity, anisoinertia, float hang off and centripetal acceleration).
5. March 72	Gyro MB-415 removed from the population because of a wheel start problem.
6. May 72	Program resumed after gyro replacement, gyro torque loop scaling change, establishment of a detailed test

plan and NASA redirection.

7. July 72 — Program evaluation requirements completed.

8. August 72 — Program evaluation to verify earlier test results and to pursue other areas of strapdown investigation. Program terminated because of wheel touchdown failure (MB-4 and 427) from excessive gimbal rates.

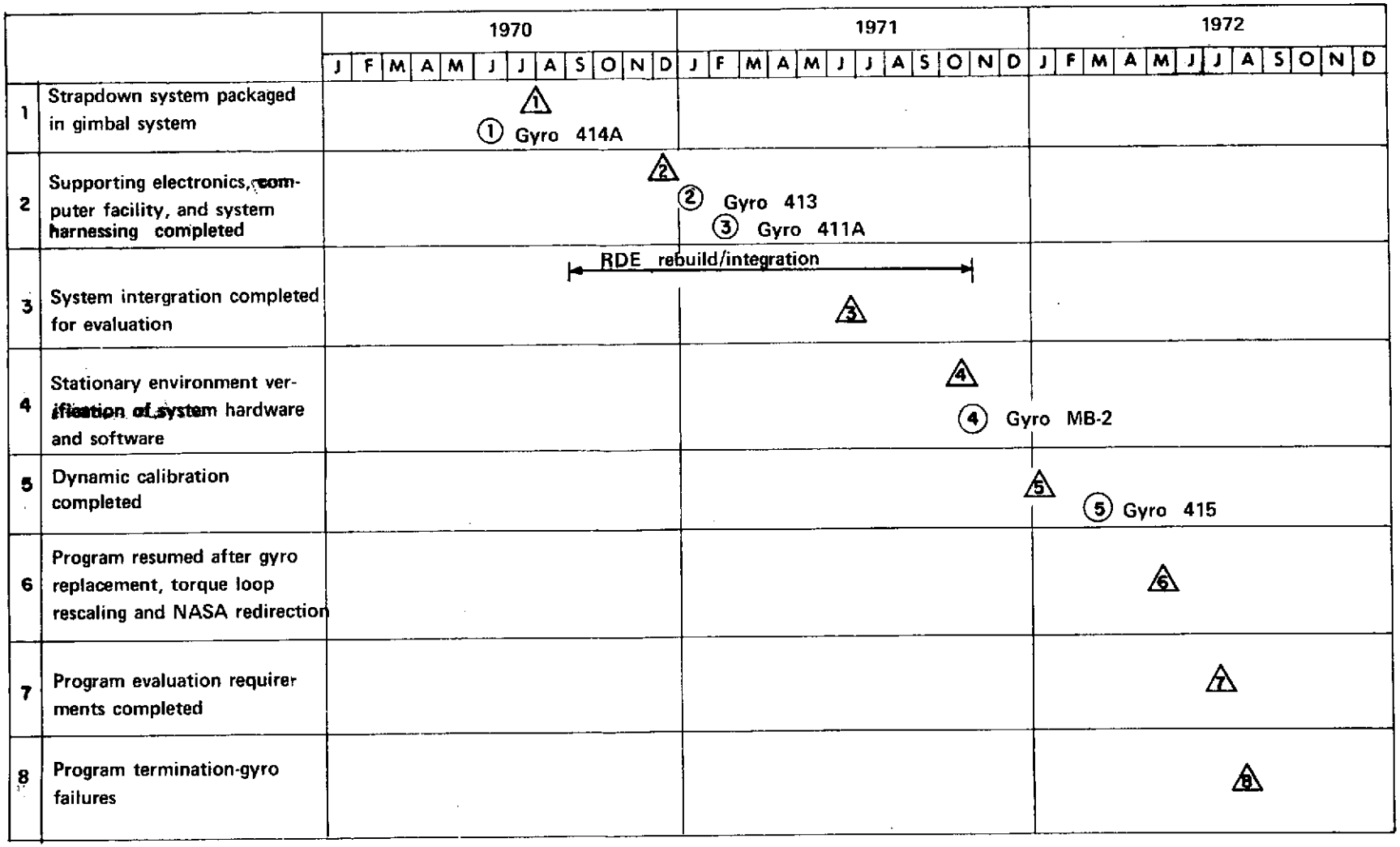

△ Milestone Completed

○ GYRO removal from population (see table 5.5.1)

Fig. 5.5.1 SPOT Program Milestone Chart.

one year later, medium scaled integration logic (MSI) would have permitted reasonably accurate encoders to be purchased as an "off-the-shelf" component and therefore reducing its impact to the program's schedule.

The program was terminated in August 1972 when during verification of earlier test results, two gyros inexplicably failed because of wheel touchdown. Those failures exhausted all available spare gyro resources and because of limited funds, the program's testing was terminated. Those areas of evaluations completed prior to the program's termination included:

1. Gyro scale factor linearity calibration and compensation.
2. SRA cross coupling calibration and compensation in slew (constant rotating) and oscillatory environments.
3. Anisoinertia compensation in slew and oscillatory environments.
4. OA coupling error compensation and pseudo coning error bandwidth studies including the effects of quantization and algorithm iteration rate.
5. Coning bandwidth studies including the effects of quantization and algorithm iteration rate.
6. Centripetal acceleration calibration.
7. Least square accelerometer modeling evaluations.
8. Quantization tradeoff studies.
9. Land navigation performance-tradeoff evaluations with respect to iteration rate.
10. Pulse burst evaluations.
11. Four months of gyro and accelerometer parameter calibration statistics.

Those areas of investigation that remain to be accomplished had the gyro failures not occurred include:

1. Further evaluations of the pulse burst phenomenon by impressing a non-symmetrical multi-axis slew environment (one axis rate above the pulse bursting threshold and the second axis rate below the threshold).
2. Anisoinertia — SRA cross coupling error compensation over the full multi-axis slew environment range (0.1 to 0.8 radians/second).
3. Land navigation evaluations under various conditions of compensation (centripetal acceleration effects compensated and uncompensated, and pulse bursting compensated and uncompensated).
4. Implementation and evaluation of the third order quaternion expansion algorithm.

6.0 Conclusions and Recommendations

A fine grain strapdown evaluation system was mechanized in this program by packaging a three axis inertial system in an Apollo gimbal fixture. The gyros and accelerometers were operated in a strapdown ternary pulse-torque mode. Dynamic environments were imposed on the strapdown system by introducing slew and oscillatory driving functions to the gimbal torque motors. An on-line mini-computer with a comprehensive set of real-time processing algorithms was interfaced with the inertial hardware to enable a fine grain evaluation of the system performance. Performance evaluation was accomplished through the use of extensive data reduction software that derived real-time attitude error profiles. The data reduction was effected on an IBM 360 computer using the recorded output samples (10 times a second) of the on-line mini-computer which included readout of the positioning gimbal fixture.

The evaluation of strapdown performance required the analysis and modeling of all significant error sources such as scale factor linearity, output axis coupling, anisoinertia, SRA cross coupling, static drift, and alignment. Software compensation algorithms were developed based on theoretically derived error models and were subsequently confirmed in the test evaluations. For example, OA coupling compensation was effected by using rate data from a second gyro to estimate the rate change magnitude about a gyro's Output Axis. This relatively simple model suppressed the pseudo coning error by 100 to 1 in the effective operating range determined by bandwidth rolloffs. Other significant compensation results included gyro scale factor linearity error compensation from an uncompensated 50 ppm spread over the full dynamic rate range (0.8 rad/sec) to error magnitudes within 7 ppm. This residual error can be attributed to the fact that the pulse torque electronics were separated from the gyro instruments by the gimbal slip rings and was within the basic SF stability uncertainties. Anisoinertia-SRA cross coupling (using the nominal coefficients) compensation effectiveness was demonstrated by reducing an uncompensated 2.07°/hour (138 meru) error drift to 0.045°/hour (3 meru) for a continuous multiple axis 0.15 radian per second input.

Anisoinertia and SRA cross coupling compensation was also evaluated at higher rates (0.5 radians per second), however, the results were not conclusive because of the large sensitivity to gyro scale factor and alignment uncertainties. Additional evaluations at the high rate multi-axis slew inputs were to be conducted during re-test had the program not terminated because of the gyro failure.

Static error source residuals such as gyro drift proved to be a significant contributor of system performance errors in this test program. The compensation

model used a single set of drift parameters, assuming an insensitivity of drift magnitude to the gimbal position. Because of thermal gradients, wheel compliance*, environmental differences within the gimbal structure, and other second order effects, positional sensitivities did exist such that 0.03°/hour (2 meru) was observed between calibration position drift magnitudes. A fine grain static calibration procedure would be desirable to analyze the source of the positional sensitivity and to derive appropriate models to accommodate for second order effects.

A large inventory of software was amassed to provide system calibration, compensation, attitude maintenance, navigation and analysis capabilities. The strapdown algorithms were implemented at three iteration rates (100, 50 and 25 iterations per second) which permitted the evaluation of various bandwidth tradeoffs. These evaluations verified the theoretical coning bandwidth for a first-order quaternion expansion. For example, the 100 iterations per second algorithm rolloff becomes significant (95% coning compensation effectiveness versus 100%) at 8 hertz. For this program, a third order algorithm was implemented, however, the cross-product term was inadvertently omitted by an initial programming oversight and therefore only a first-order performance in coning was achieved. Had the program not terminated during the re-test phase due to a gyro failure, evaluations with the fully implemented third-order algorithm was planned for the retest phase. It is recommended that the full third-order performance be verified in future evaluations.

Coning errors at low frequencies (0.5 hertz) were observed to increase because of attitude lags introduced by the torque loop quantization. For example, with a 5 arc second quantization the 0.5 hertz coning error is 0.03% and with a 40 arc second quantization it is 0.08%. However, because the error magnitude at this frequency is extremely low, the effects of quantization on coning bandwidth is negligible.

The effective bandwidth of pseudo coning compensation was analyzed and verified to be a combined function of the coning bandwidth and OA compensation bandwidth. The OA compensation bandwidth is determined by the ability of the gyro rate estimator to accurately determine the rate change magnitude of the oscillatory input. Compensation errors are observed to become significant when the oscillatory frequency is one-tenth the compensation algorithm iteration rate. Interestingly, this rolloff occurs at a lower frequency then the basic attitude algorithm when both

* Wheel major compliance has been modeled in the compensation algorithm. However, the minor compliance terms which were not modeled, and they may contribute as a second order effect to the positional sensitivity observed in the data.

are operating at the same iteration rate. Thus when OA compensation ceases to be effective, the attitude algorithm mistakes the OA coupling error with the input oscillatory input as a coning input and then incorrectly compensates for a non-existent coning input. As the oscillatory frequency increases and the attitude algorithm becomes bandwidth limited, the attitude algorithm no longer responds to OA coupling, and pseudo coning errors are not generated. With respect to pseudo coning errors, optimum compensation is therefore achieved when the OA compensation algorithm iteration rate is greater than the attitude algorithm rate. Using such a scheme would extend the OA coupling compensation bandwidth so that when OA coupling errors are generated, they will not be recognized by the attitude algorithms. The optimum implementation would be selected on the basis of the anticipated vehicle's environment.

Gyro loop quantization was observed to proportionally increase the system attitude uncertainty. For example, with a 5 arc second quantization the measured peak to peak attitude uncertainty is 5.5 arc seconds. With 40 arc second quantization the uncertainty level is 37 arc seconds.

Land navigation evaluations were conducted with an inertial referenced navigator operating at one iteration per second and with inertially referenced velocity increments updated at 100, 50, or 25 updates per second. Navigation evaluations were conducted in both slew and oscillatory environments, as well as a 96 hour evaluation during which the system's position was fixed. Classic navigation error profiles (a Schuler oscillation superimposed on a 24 hour sinusoid) were observed in all of the navigation results. The magnitude of the two sinusoid components, being a function of system alignment and residual compensation errors, reflected the salient system error for the environment tested. For example, the slew and oscillatory tests reflected a 50 arc second initialization alignment error in the Schuler oscillation magnitude through a sensitivity factor of 7 nautical miles per milliradian of alignment error. These error magnitudes, unfortunately masked the observance of navigation error propagation from less significant error sources such as centripetal acceleration. Therefore, accurate alignment of the strapdown body frame with respect to an inertial referenced frame is required for future evaluations.

Another factor influencing the resultant navigation data is the choice of environments. The slew environment was imposed by rotating a horizontal east-west axis 50 revolutions at 4^{o}/seconds. Thus, two accelerometers were tumbled through the "g" field and therefore introducing errors attributed to accelerometer scale factor compensation in addition to the initialization alignment error. In retrospect, a better slew environment would have consisted of rotations about a vertical axis such that scale factor errors are not excited.

With regard to the slew testing, however, a 50 revolution rotation is clearly not representative of any realistic environment that might be anticipated in an aircraft mission. An actual flight profile of attitude angular rate and oscillatory inputs is suggested, whereby the applicability of the compensation models and system performance can be assessed in a direct manner with extremely high confidence.

Other recommendations for future strapdown evaluations include:

1. The definitive modeling of accelerometer dynamic error terms such as OA coupling and anisoinertia. These terms were not modeled because the initial dynamic rate range was limited by the gyro torque loops to 0.2 radians per second. At these rates magnitudes, the error magnitudes are not significant. Later with a gyro loop rescaling, the dynamic range was extended to 0.8 radians per second and therefore allowed testing at higher rates which increased the significance of accelerometer OA coupling and anisoinertia.
2. Gyro anisoinertia compensation was accomplished with a constant correction factor based on the low frequency inertia difference between the float's Input Axis and Spin Axis. This compensation model is accurate for environments below the wheel hunt frequency (3 to 5 hertz). However, if environments above the wheel hunt frequency are anticipated then the decoupling of the wheel element from the input oscillation should be accounted for because the inertia about Spin Axis is signficantly reduced. To adequately compensate for the wheel decoupling effect, a more complex model based on the spectral content of the environment sensed data is required.
3. The evaluations conducted in the program centered in the 1 hertz to 10 hertz frequency band. Useful information relating to algorithm bandwidths, quantization and compensation effectiveness were derived from these evaluations. Additional evaluations are required, however, in the frequency range below 1 hertz where the majority of vehicle oscillatory motion is anticipated.
4. The pulse burst phenomenon was evaluated in this program and it was observed that the compensation scheme suggested by Lory is effective. Additional evaluations are required to determine the effects of pulse bursting on attitude error propagation. A suggested environment is a multi-axis rotational excitation where the rate about one axis is below the pulse torquing threshold and the second axis is above the threshold.

In summary, the recommendations for future study and evaluation are listed below:

1. Finer calibration and model techniques to account for second-order gyro error effects and accelerometer dynamic terms.
2. Additional evaluations of higher multi-axis slew rate environments.
3. Development of a frequency dependent gyro anisoinertia compensation model.
4. Additional pulse burst compensation evaluations.
5. Evaluation of a fully implemented third-order quaternion expansion algorithm.
6. Test with OA compensation operating at a higher iteration rate than the attitude algorithm.
7. Land navigation evaluations with greater initialization alignment accuracy and with realistic environments.

References

1. Technical Proposal for the Modification of Contract NAS9-6823, Paragraph 3.2 of Enclosure A.

2. MIT Instrumentation Laboratory Staff, Control, Guidance and Navigation for Advanced Manned Missions, MIT Instrumentation Laboratory Report R-600, Volume IV Inertial Subsystem, September 1968.

3. Lory, C.B., Compensation of Pulse-Rebalanced Inertial Instruments, M.S. Thesis, MIT Department of Aeronautics and Astronautics, Instrumentation Laboratory Report T-495, January 1968.

4. Lory, C., Feldman, J., and Sinkiewicz, J., Dynamic Testing of a Single-Degree-of-Freedom Strapdown Gyroscope, Charles Stark Draper Laboratory Report E-2618, October 1971.

5. Schneider, G.E., Studies on Dynamic Testing of a Single Degree-of-Freedom Integrating Gyroscope used in a Strapped-down Environment, M.S. Thesis, MIT Department of Mechanical Engineering, Instrumentation Laboratory Report T-526, January 1970.

6. Dove, D.W., A Performance Evaluation of a Strapdown Inertial Measurement Unit in the Presence of a Severe Dynamic Environment, M.S. Thesis, MIT Department of Aeronautics and Astronautics, Charles Stark Draper Laboratory Report T-544, January 1971.

7. Charles Stark Draper Laboratory, March 1972 Monthly Progress Report for Contract NAS12-2033, 17 April 1972.

8. Lory, C.B., Float Position of Inertial Instrument having Torque applied in Increments, Charles Stark Draper Laboratory Report E-2622, February 1973.

9. McKern, R., A Study of Transformation Algorithms for use in a Digital Computer, M.S. Thesis, Department of Aeronautics and Astronautics, MIT Instrumentation Laboratory Report, T-493, January 1968.

10. Oehrle, J.B., SIRU Software Description and Program Documentation (Preliminary), Charles Stark Draper Laboratory ISS memorandum #72-82, May 1972.

11. Musoff, H., SIRU Utilization Final Report, Charles Stark Draper Laboratory Report to be published April 1973.

12. Otten, D.D., Body Fixed, Three Axis Reference System Study, Phase 1, Final Report, TRW #4499-6007-R000, May 2, 1966.

13. Wrigley, W., Hollister, W., and Denhard, W., Gyroscopic Theory, Design, and Instrumentation, MIT Press, Cambridge, Mass. 1961.

14. Gilmore, J., McKern, R., and Swanson, D., Real-Time Strapdown-Attitude Package Evaluations, MIT Instrumentation Laboratory Report E-2398, June 1969.

15. Land Navigation Program Final Design Report, TRW Document 0592-6209-T000, May 1968.

16. Redundant Sensor Program Description (ERSA/DDP-124) TRW Document 09665-6013-R000, May 1969.

17. Broxmeyer, C., Inertial Navigation Systems, McGraw-Hill Book Company, New York, 1964.

18. Macomber, G.R., and Fernandez, M., Inertial Guidance Engineering, Prentice-Hall, Englewood Cliffs, New Jersey, 1962.

19. Scarborough, J.B., Numerical Mathematical Analysis, 3rd edition, Oxford University Press, 1955, p. 492.

APPENDIX A

STRAPDOWN TEST FIXTURE PARAMETERS

GIMBAL ALIGNMENT UNCERTAINTY[1]	± 7 arc seconds
GIMBAL POSITIONING ACCURACY[2]	± 50 arc seconds
GIMBAL FREQUENCY RESPONSE	See Figure A-1
GIMBAL ROTATIONAL RATE	Limited to 1 radian per second by gyroscopes

NOTE 1 - Based on 5 arc seconds table uncertainty and 3 arc seconds accelerometer null uncertainty.

NOTE 2 - With respect to an earth fixed frame. The positional accuracy is determined by the gimbal and table alignment errors.

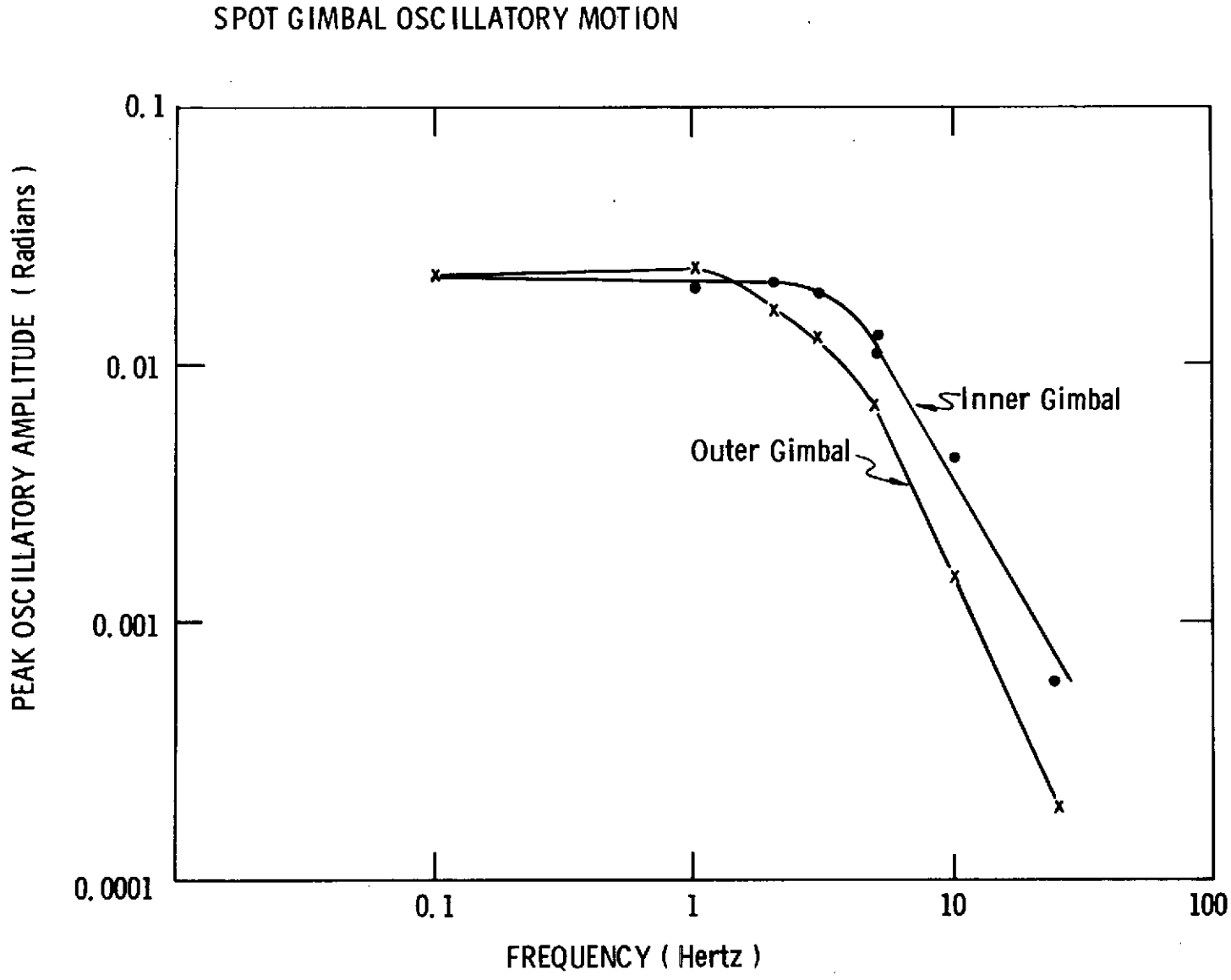

Figure A-1 - GIMBAL OSCILLATORY PERFORMANCE

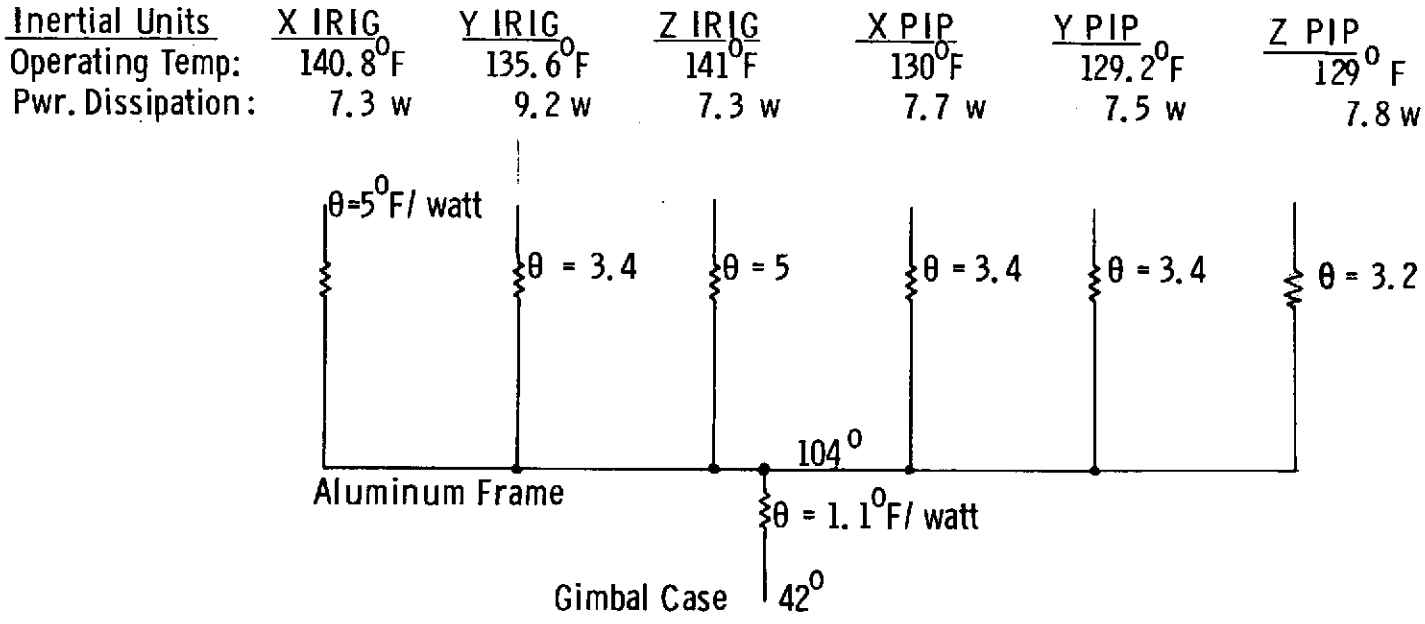

TOTAL POWER DISSIPATION

Gyroscopes	23.8 watts
Accelerometers	23 watts
Temp. Controllers	3 watts
Dart	2 watts
SG Preamplifiers	5 watts
	56.8 watts

Fig. A-2 Spot System Thermal Model.

APPENDIX B

SPOT H316 COMPUTER COMMANDS

Gyroscope, Interpolator and Accelerometer Interface

INA	'1007	Read X Gyro Counter
INA	'1017	Read Y Gyro Counter
INA	'1027	Read Z Gyro Counter
INA	'1047	Read Interpolator
INA	'1107	Read X PIPA Counter
INA	'1117	Read Y PIPA Counter
INA	'1127	Read Z PIPA Counter
OCP	'07	Enable Interrogate to scaler (Interface On)
OCP	'17	Interface Off
OCP	'27	Clear Gyro Counters, Ready FF, and Scaler
OCP	'37	Clear PIPA Counters, Ready FF, and Scaler
OCP	'47	Actual Float Angle Discrete to Interpolator
OCP	'57	Compensated FA Discrete to Interpolator
OCP	'77	Clear Preset Register
OCP	'167	Gate X Interpolator to Transfer Lines
OCP	'267	Gate Y Interpolator to Transfer Lines
OCP	'367	Gate Z Interpolator to Transfer Lines
OTA	'77	Preset Preset Register With C(A)
SMK	'20	Set Interrupt Mask if A12 is Set

SKS	'147	Skip if Ready FF Set
SKS	'157	Skip if Interface not Interrupting
SKS	'167	Skip if Interpolator Inhibited

Resolver/Digital Encoder Interface

INA	'1006	Read RDE Channel 1 High
INA	'1016	Read RDE Channel 2 High
INA	'1026	Read RDE Channel 1 Low
INA	'1036	Read RDE Channel 2 Low
OCP	'06	Set RDE Zero FF
OCP	'16	Reset RDE Zero FF
SKS	'06	Skip if 800 FF Set (SYNC)

Test Sequencer Interface

OCP	'05	Reset Test Sequencer (Start of Test)
OCP	'15	Count Pulse
OTA	'05	Output Data to Test Sequencer
SKS	'05	Skip if Ready (GPC in Fine Mode)

516 - 316 DATA LINE CONTROLLER

OCP

OCP	'60	Enable Receiver
OCP	'160	Search for Sync. (Preceed by OCP '60)
OCP	'1060	Disable Receiver
OCP	'260	Enable Transmitter
OCP	'1260	Disable Transmitter
OCP	'360	Set Data Terminal Ready (Resets Ring Signal, Disconnect Signal)
OCP	'1360	Reset Data Terminal Ready (Disable Receiver before OCP '360 again)

SKS

SKS	'x060	Skip if Receiver Ready is Set
SKS	'160	Skip if Receiver Fault is set { Parity Error / Buffer not emptied on time
SKS	'1260	Skip if Transmitter not Busy
SKS	'260	Skip if Transmitter Ready
SKS	'360	Skip if no Ring Signal
SKS	'1360	Skip if no Disconnect Signal
SKS	'460	Skip if Controller not Interrupting

OTA

OTA	'160	Skip if Receiver Fault is set, Reset it
OTA	'260	Skip and Output from A if Transmitter Ready Set
SMK	'420	Set Mask (Bit 1 of A)

INA

INA	'60	Input and Skip if Receiver Ready is True
INA	'1060	(Reset Receiver Ready)

APPENDIX C

Accelerometer Error Parameters

Accelerometer bias (B_a) is a function of suspension and SG reaction torques acting about the Output Axis to displace the float from its null position.

Cross coupling coefficients (K_{IP} and K_{IO}) are caused by simultaneous linear acceleration along two axes. An acceleration along the Input Axis causes rotation of the pendulum from its null position. A component of pendulosity results from the rotation that is therefore sensitive to acceleration inputs along the Pendulous Axis (K_{IP}). (K_{IO}) is the anisoelastic effect caused by rectified error torques if unequal spring restraints exist along the Input Axis at opposite ends of the float.

Cross Axis coefficients (K_o) are caused by the difference between the center of gravity and center of buoyancy. An acceleration input along the Output Axis causes rotations of the float about the Input Axis. This rotation, within the suspension field, has a small but measureable effect on the accelerometer scale factor and bias.

Output Axis coupling error is related to the float response to velocity changes about the Output Axis. Because of the float inertia, the float motion lags the case motion and additional torque pulses are generated to maintain the float at its null position.

Anisoinertia errors arise from the application of simultaneous angular rates to the inertia difference between the float Pendulous and Input axes.

APPENDIX D

Gyro Drift Parameters

The gyro drift error parameters represent the torques that arise from the non-ideal nature of the gyro.

Acceleration Insensitive Torque (NBD)

The accelerometer insensitive torque (NBD) is a function of torques resulting from flex lead stiffness, and the magnetic restraining torques between the float and case.

Acceleration Sensitive Torque (ADIA and ADSRA, and ADOA)

Acceleration sensitive torques are caused by a non-coincidence of the gyro-float center of gravity (cg) and the center of buoyancy (cb). For example, ADIA is generated by a specific force along the Input Axis operating in conjunction with a cg-cb displacement along the Spin Reference Axis.

ADSRA is generated by a specific force input along the Spin Reference Axis operating in conjunction with a cg-cb displacement along the Input Axis. ADOA is an acceleration sensitive drift inherent to the gyro when specific forces are applied along the Output Axis.

Acceleration Squared Sensitive Drift

Major compliance ($K_{SS} - K_{II}$) is the result of an unbalanced yielding of the wheel structure to simultaneous acceleration input along the Input Axis and Spin Reference Axis. Other compliance terms (K_{IS} and K_{IO}) are not modeled because of their insignificant magnitudes (less than one meru or 0.015°/hr).

APPENDIX E

SPOT GYROSCOPE COMPENSATION EQUATIONS

A. Definition of Terms

GXPC, GYPC, GZPC - The X, Y and Z axis net gyro torque pulses accumulated in one iteration period

IXCC - compensated interpolator information- current update interval

IXCP - compensated interpolator information - previous update interval

GXPS, GXNS - The deviation of the X gyroscope positive and negative scale factors from a nominal scale factor

SSPX, SSNX - X gyroscope positive and negative scale factor linearity slopes respectively

ω_{max} - maximum rate of torque loops, defined by torque pulses per update period

SXSF - X gyro scale factor

GXBX - normal bias drift

ADX, ADY, ADZ - acceleration sensitive drift terms (ADIA, -ADSRA, ADOA for the X gyroscope respectively)

XA2D - major compliance

PXPC, PYPC, PZPC - X, Y and Z accelerometer net torque pulses per iteration time (these pulse count will have been compensated for the accelerometer error magnitudes)

GXIH - I/H coefficient

XOAO, XOAP - correction factor for OA coupling; XOAO calculates for the current update time, XOAP calculates for preceding update time

GMXY - X gyroscope misalignment into the Y reference axis (OA misalignment)

MXYC - compensated misalignment of X gyroscope into the Y reference axis

XFOP, XFON - low rate float offset

XAN - X Gyroscope anisoinertia coefficient

XFOP + (XSOP)GXPC - float hangoff model if GXPC positive

-XFON + (XSON)GXPC - float hangoff model if GXPC negative

IXUC - compensated interpolator information

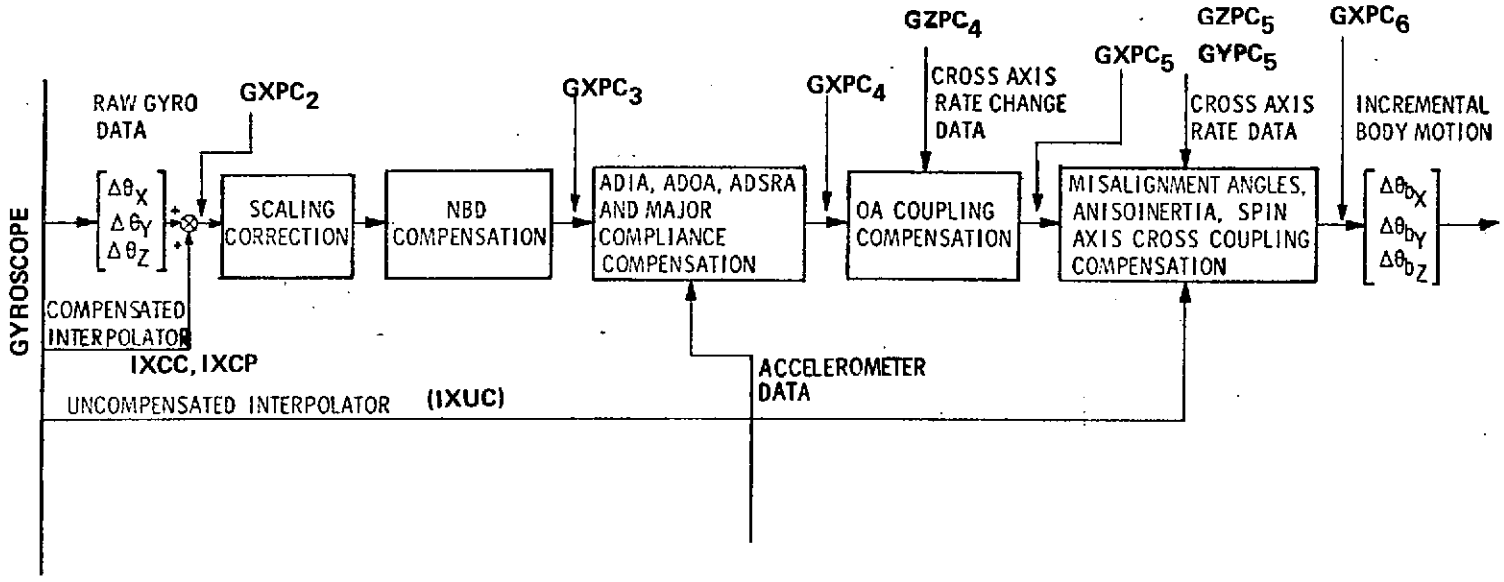

Fig. E-1 Compensation Mechanization (X Axis).

B. Equations

This section explains the gyro compensation algorithm using the X axis gyro as an example. Figure E-1 depicts the compensation steps corresponding to the following discussion.

1. Combination of compensated interpolator information with gyroscope pulse counts

$GXPC_2 = GXPC_1 + IXCC - IXCP$
$IXCP = IXCC$

2. Scale factor determination

$SXSF = (GXPC_2)\,(SSNX/\omega_{MAX}) + GXNS$: If $GXPC_2$ negative
$SXSF = (GXPC_2)\,(SSPX/\omega_{MAX}) + GXPS$: If $GXPC_2$ positive

3. Gyro pulse scaling and normal bias drift compensation

$GXPC_3 = (GXPC_2)\,(SXSF) + GXBD + GXPC_2$

4. Acceleration sensitive drift compensation

$GXPC_4 = GXPC_3 + (ADX)\,(PXPC_4) + (ADY)\,(PYPC_4) + (ADZ)\,(PZPC_4)$
$+ (XA2D)\,(PXPC_4)\,(PYPC_4)$

5. OA coupling compensation

$XOAO = (GXIH)\,(GZPC_4)$
$GXPC_5 = (GXPC_4 + XOAO - XOAP)$
$XOAP = XOAO$

6. SRA cross coupling, anisoinertia, and misalignment compensation

If $GXPC_5$ positive: $MXYC = GMXY + XFOP + (XSOP-XAN)\,GXPC_5$
If $GXPC_5$ negative: $MXYC = GMXY - XFON + (XSOP-XAN)\,GXPC_5$
If $GXPC_5$ zero: $MXYC = GMZY + IXUC$
$GXPC_6 = GXPC_5 + (MXYC)\,(GYPC_5) + (GMXZ)\,(GZPC_5)$

APPENDIX F

SPOT ACCELEROMETER COMPENSATION EQUATIONS

A. Definition of Terms

PXPC, PYPC PZPC - X, Y and Z accelerometer net pulse counts per update time respectively

PXPS, PXNS - X accelerometer positive and negative scale factor deviation from nominal respectively

PXAB - X accelerometer null bias

PMXY, PMXZ - X accelerometer misalignments into the negative Y and Z reference axes (OA misalignment and PRA misalignment respectively)

RXX, RXY, RXZ - X accelerometer position from system center

GXPC, GYPC, GZPC - X, Y and Z gyro net pulse counts respectively

$GYPC_P$ - gyro net pulse count from previous update

B. Equations

This section explains the accelerometer compensation algorithm using the X axis accelerometer as an example. Thus PXPC, is the raw accelerometer pulse count accumulated during an iteration interval.

1. Scale factor and bias compensation

$$PXPC_2 = PXPC_1 + (PXPC_1)\,(PXPS) + PXAB : \text{ If } PXPC_1 \text{ positive}$$

$$PXPC_2 = PCPC_1 + (PXPC_1)\,(PXNS) + PXAB : \text{ If } PXPC_1 \text{ negative}$$

2. Misalignment compensation

$$PXPC_3 = PXPC_2 + (PMXY)\,(PYPC_2) + (PMXZ)\,(PZPC_2)$$

3. Centripetal and tangential acceleration compensation

$$PXPC_4 = PXPC_3 - (RXY)\,(GXPC_6)\,(GYPC_6) - (RXZ)\,(GXPC_6)\,(GZPC_6) + (RXX)\,(GYPC_6)\,(GYPC_6) + (RXX)\,(GZPC_6)\,(GZPC_6) - (RXZ)\,(GYPC_6 - GYPC_{P_6}) + RXY\,(GZPC_6 - (RXZ)\,(GYPC_6 - GYPC_{P_6}) + RXY\,(GZPC_6 - GZPC_{P_6})$$

APPENDIX G

STRAPDOWN ANGULAR RATE INDUCED ACCELERATIONS

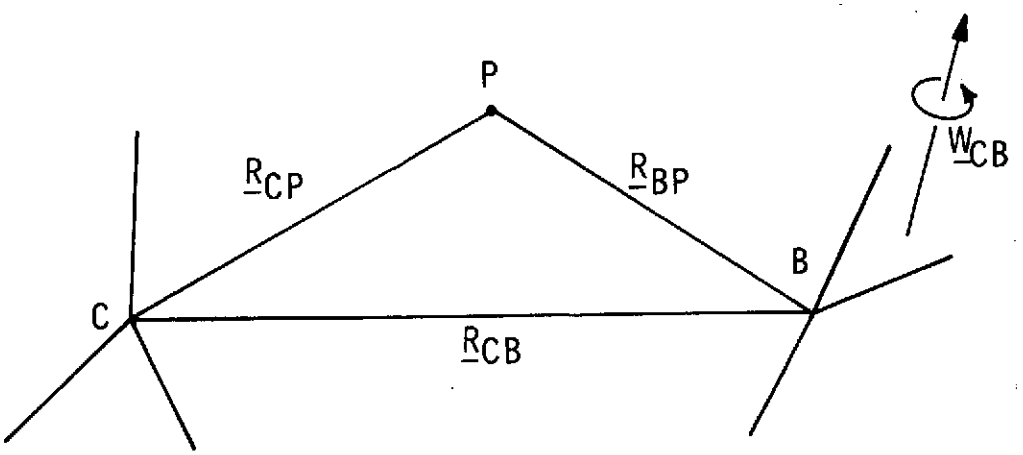

Fig. G-1 Strapdown Angular Rate Induced Accelerations.

From Figure G-1,[13] let P represent an accelerometer mass element and B the chosen body reference point containing an associated body coordinate frame which contains the point (P). Let C be assigned as another point representing the inertial reference of this system which references the motion of the B frame and therefore of P. We are now ready to derive the effect of introducing an angular rate upon the mass element. This angular rate input ($\underline{W}_{CB}$) is measured in the body frame with respect to the inertial reference frame. Notice, in this discussion $R_{\underline{BP}}$ is fixed in the vehicle.

From the Theorem of Coriolis the velocity of P with respect to the C frame will be:

$$P_C \underline{R}_{CP} = P_C \underline{R}_{CB} + P_B \underline{R}_{BP} + \underline{W}_{CB} \times \underline{R}_{BP} \tag{G-1}$$

and the resultant acceleration of P can be derived to be:

$$P_C^2 \underline{R}_{CP} = P_C^2 \underline{R}_{CB} + 2\underline{W}_{CB} \times P_B \underline{R}_{BP} + P_B \underline{W}_{CB} \times \underline{R}_{BP} + \underline{W}_{CB} \times (\underline{W}_{CB} \times \underline{R}_{BP}) \tag{G-2}$$

Notice, in Equation G-2, the coriolis acceleration ($2\underline{W}_{CB} \times P_B \underline{R}_{BP}$) is zero since the mass element is fixed with respect to the body reference point ($P_B \underline{R}_{BP} = 0$). The linear acceleration of the body frame with respect to the reference frame ($P_C{}^2R_{CB}$) is the primary acceleration expected and is not of concern at this time. The remaining terms in Equation G-2 then represent the accelerations induced during rotation by the accelerometer mass elements not being centered at exactly a single point or,

$$\underline{A} = \text{ACCELERATION ERROR} = P_B \underline{W}_{CB} \times \underline{R}_{BP} + \underline{W}_{CB} \times (\underline{W}_{CB} \times \underline{R}_{BP}) \quad \text{(G-3)}$$

In general R_{BP} will contain three dimensions for each accelerometer. The actual error can now be derived for the ith accelerometer in general by resolving Equation G-3 in body computational axis components to obtain:

$$\begin{aligned}
Ae_{ix} &= -(W_Y^2 + W_Z^2)\, R_{iX} + (W_X W_Y - W_Z)\, R_{iY} - (W_X W_Z - W_Y)\, R_{iZ} \\
Ae_{iy} &= -(W_X W_Y - W_Z)\, R_{iX} - (W_X^2 + W_Z^2)\, R_{iY} + (W_Y W_Z - W_X)\, R_{iZ} \\
Ae_{iz} &= -(W_X W_Z - W_Y)\, R_{iX} - (W_Y W_Z - W_X)\, R_{iY} - (W_X^2 + W_Y^2)\, R_{iZ}
\end{aligned} \quad \text{(G-4)}$$

$$\underline{A}\ ei = \begin{bmatrix} (W_Y^2 + W_Z^2) & -(W_X W_Y - W_Z) & (W_X W_Z - W_Y) \\ (W_X W_Y - W_Z) & (W_X^2 + W_Z^2) & -(W_Y W_Z - W_X) \\ (W_X W_Z - W_Y) & (W_Y W_Z - W_X) & (W_X^2 + W_Y^2) \end{bmatrix} \underline{R}_{BP} \quad \text{(G-5)}$$

where, $\underline{R}_{BP}^T = \begin{bmatrix} R_{iX} & R_{iY} & R_{iZ} \end{bmatrix}$ for the ith accelerometer

To determine the actual required compensation for each of the three instruments in SPOT we now recognize,

$$ {}^{1}\underline{1}AX \cdot \underline{A}_{eX} = -X \text{ Accelerometer compensation} $$

$$ {}^{1}\underline{1}AY \cdot \underline{A}_{eY} = -Y \text{ Accelerometer compensation} $$

$$ {}^{1}\underline{1}AZ \cdot \underline{A}_{eZ} = -Z \text{ Accelerometer compensation} \qquad \text{(G-6)} $$

where for the present SPOT system,

$$ {}^{1}\underline{1}AX = \begin{bmatrix} 1 \\ SO_X \\ -SP_X \end{bmatrix} \qquad {}^{1}\underline{1}AV = \begin{bmatrix} -SP_Y \\ 1 \\ SO_Y \end{bmatrix} \qquad {}^{1}\underline{1}AZ = \begin{bmatrix} SP_Z \\ -SO_Z \\ 1 \end{bmatrix} $$

In this discussion no gyro misalignment is assumed for the derivation of the rate information since we can use the input information after scale factor and alignment compensation to derive rate. The accelerometer alignment effects cannot be reduced in this way and are shown so the error effects on compensation can be evaluated.

TABLE H-1

ATTITUDE ERROR PROPAGATION (θ_x, θ_y, AND θ_z) DUE TO GYRO DRIFT AND SYSTEM ALIGNMENT ERRORS

ATTITUDE ERRORS	ATTITUDE ERROR PROPAGATION RESULTING FROM GYRO DRIFT			ATTITUDE ERROR PROPAGATION RESULTING FROM ALIGNMENT	
	RAMP	SINUSOID	CONSTANT	SINUSOID	CONSTANT
θ_x	$\frac{(W_h^2 D_x + W_v W_h D_y)\,t}{W_{ie}^2}$	$-\left[\frac{W_h^2 D_x + W_v W_h D_y}{W_{ie}^3}\right] \sin W_{ie} t$ $\frac{-W_v D_z}{W_{ie}^2} \cos W_{ie} t$ $\frac{+ D_x}{W_{ie}} \sin W_{ie} t$	$\frac{W_v D_z}{W_{ie}^2}$	$\theta_x(0) \cos W_{ie} t$ $+\frac{W_v}{W_{ie}} \theta_z(0) \sin W_{ie} t$ $-\left[\frac{W_h^2 \theta_x(0) + W_v W_h \theta_y(0)}{W_{ie}^2}\right] \cos W_{ie} t$	$\frac{W_h^2 \theta_x(0) + W_v W_h \theta_y(0)}{W_{ie}^2}$
θ_y	$\frac{(W_v W_h D_x + W_v^2 D_y)\,t}{W_{ie}^2}$	$-\left[\frac{W_v^2 D_y + W_v W_h D_x}{W_{ie}^3}\right] \sin W_{ie} t$ $\frac{+W_h D_z}{W_{ie}^2} \cos W_{ie} t$ $\frac{+D_y}{W_{ie}} \sin W_{ie} t$	$\frac{-W_h}{W_{ie}^2} D_z$	$\theta_y(0) \cos W_{ie} t$ $-\frac{W_h \theta_z(0)}{W_{ie}} \sin W_{ie} t$ $-\left[\frac{W_v^2 \theta_y(0) + W_v W_h \theta_x(0)}{W_{ie}^2}\right] \cos W_{ie} t$	$\frac{W_v^2 \theta_y(0) + W_v W_h \theta_x(0)}{W_{ie}^2}$
θ_z	0	$\frac{-(W_h D_y - W_v D_x)}{W_{ie}^2} \cos W_{ie} t$ $\frac{+D_z}{W_{ie}} \sin W_{ie} t$	$\frac{W_h D_y - W_v D_x}{W_{ie}^2}$	$\left[\frac{W_h \theta_y(0) - W_v \theta_x(0)}{W_{ie}}\right] \sin W_{ie} t$ $+\theta_z(0) \cos W_{ie} t$	0

D_x, D_y, D_z Gyro Drift Errors

W_{ie}, W_v, W_h Earth Rate Parameters

$\theta_x(0)$, $\theta_y(0)$, $\theta_z(0)$ Alignment Error

System Orientation: x-North, y-Up, z-West

APPENDIX I

ERROR QUATERNION -BODY REFERENCE FRAME

This section derives the error quaternion in the body frame ($\bar{q}_{eB}$) in terms of a perfect quaternion ($\bar{q}_p$) and a computed quaternion ($\bar{q}_c$) from the attitude algorithm.

The perfect quaternion ($\bar{q}_p$), assumed to be without error, transposes a true velocity vector ($\bar{V}_{Bt}$) in the body frame from the inertial frame.

$$\bar{V}_{Bt} = \bar{q}_p^* \bar{V}_I \bar{q}_p \tag{I-1}$$

The computed quaternion ($\bar{q}_c$) performs the same transformation function as q_p, however, because of compensation, quantization and bandwidth errors the resultant velocity vector ($\bar{V}_{Bc}$) will be in error.

$$\bar{V}_{Bc} = \bar{q}_c^* \bar{V}_I \bar{q}_c \tag{I-2}$$

A quaternion, $\bar{q}_{eb}$, is defined as the transformation quaternion between the true velocity vector ($\bar{V}_{Bt}$) and the algorithm indicated velocity vector ($\bar{V}_{Bc}$)

$$\bar{V}_{Bt} = \bar{q}_{eB} \bar{V}_{Bc} \bar{q}_{eB}^* \tag{I-3}$$

Substituting the inertial frame equivalence for $\bar{V}_{Bt}$ and $\bar{V}_{Bc}$ into the above expression we have

$$\bar{q}_p^* \bar{V}_I \bar{q}_p = \bar{q}_{eB} \bar{q}_c^* \bar{V}_I \bar{q}_c \bar{q}_{eB}^* \tag{I-4}$$

Thus

$$\bar{q}_p^* = \bar{q}_{eB} \bar{q}_c^* \tag{I-5}$$

And

$$\bar{q}_{eB} = \bar{q}_p^* \bar{q}_c \tag{I-6}$$

APPENDIX J

ERROR QUATERNION- INERTIAL REFERENCE FRAME

This section derives the error quaternion in the inertial frame ($\bar{q}_{eI}$) in terms of a perfect quaternion ($\bar{q}_p$) and the computed quaternion ($\bar{q}_c$). The perfect quaternion is without error, therefore $\bar{V}_{It}$ is an arbitrary vector in the inertial frame.

$$\bar{V}_{It} = \bar{q}_p \, \bar{V}_B \, \bar{q}_p^* \tag{J-1}$$

Since $\bar{q}_c$ is an imperfect quaternion with compensation, quantization and bandwidth errors, $\bar{V}_{Ic}$ is an arbitrary vector in the inertial frame indicated by the algorithm

$$\bar{V}_{Ic} = \bar{q}_c \, \bar{V}_B \, \bar{q}_c^* \tag{J-2}$$

The relationship between $\bar{V}_{It}$ and $\bar{V}_{Ic}$ is expressed by a transformation between the two vectors.

$$\bar{V}_{It} = \bar{q}_{eI} \, \bar{V}_{Ic} \, \bar{q}_{eI}^* \tag{J-3}$$

Substituting (J-1) and (J-2) into (J-3) gives

$$\bar{q}_p \, \bar{V}_B \, \bar{q}_p^* = \bar{q}_{eI} \, \bar{q}_c \, \bar{V}_B \, \bar{q}_c^* \, \bar{q}_{eI}^* \tag{J-4}$$

$\bar{q}_p$ is therefore equivalent to $\bar{q}_{eI} \, \bar{q}_c$ and

$$\bar{q}_{eI} = \bar{q}_p \, \bar{q}_c^* \tag{J-5}$$

APPENDIX K

Analysis of Error Quaternions in the Slew Environment

This text analyzes the effects of alignment errors, gyro scale factor errors, and gyro drift in a single axis rotational environment on expected attitude error propagation.

The study computes error quaternions defined in the body ($\bar{q}_{e_B}$) and inertial ($\bar{q}_{e_I}$) reference frames from two quaternions; 1) the perfect ($\bar{q}_p$) and 2) the computed ($\bar{q}_c$) quaternion. The error quaternions are defined below as:

$$\bar{q}_{e_B} = \bar{q}_p * \bar{q}_c \tag{K-1}$$

$$\bar{q}_{e_I} = \bar{q}_p \, \bar{q}_c^* \tag{K-2}$$

Alignment Errors

Figure K-1 is the orthogonal strapdown system with small angle alignment errors (ϵ_x, ϵ_z) about the X and Z axes respectively.

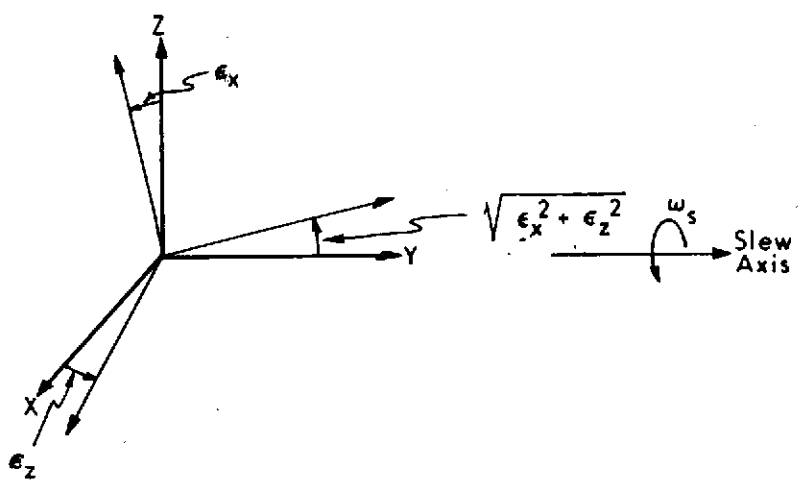

Fig. K-1 Strapdown Body Triad with Misalignment Errors.

Alignment errors such as fixture levelling error and gimbal non-orthogonalities are easily calibrated and will not degrade the system attitude data if programmed into the software. It is the alignment errors that are not calibrated that concerns this analysis. The perfect quaternion ($\bar{q}_p$), a function entirely of the system orientation is unaffected by alignment errors.

Thus:

$$\bar{q}_p = \cos \omega_s t/2 + \bar{j} \sin \omega_s t/2 \qquad \text{(K-3)}$$

The computed quaternion ($\bar{q}_c$) because it is derived from the gyro angular measurements will inherently contain the alignment errors. The computed quaternion is expressed in (K-4) using small angle approximations:

$$\bar{q}_c = \cos \omega_s t/2 + \bar{i}\, \epsilon_z \sin \omega_s t/2 + \bar{j}\,(1 - \sqrt{\epsilon_x^2 + \epsilon_z^2}) \sin \omega_s t/2 - \bar{k}\epsilon_x \sin \omega_s t/2 \qquad \text{(K-4)}$$

Using equations (K-1) and (K-2) error quaternions are formed and expressed as follows:

$$\begin{aligned}\bar{q}_{eB} = 1 &+ \bar{i} \sin \omega_s t/2\,(\epsilon_z \cos \omega_s t/2 + \epsilon_x \sin \omega_s t/2 \\ &- \bar{j}\,(\sqrt{\epsilon_x^2 + \epsilon_z^2} \sin \omega_s t/2 \cos \omega_s t/2) \\ &+ \bar{k} \sin \omega_s t/2\,(\epsilon_x \sin \omega_s t/2 - \epsilon_x \cos \omega_s t/2)\end{aligned} \qquad \text{(K-5)}$$

$$\begin{aligned}\bar{q}_{eI} = 1 &+ \bar{i} \sin \omega_s t/2\,(\epsilon_x \sin \omega_s t/2 - \epsilon_z \cos \omega_s t/2) \\ &+ \bar{j}\,(\sqrt{\epsilon_x^2 + \epsilon_z^2} \sin \omega_s t/2 \cos \omega_s t/2 \\ &+ \bar{k} \sin \omega_s t/2\,(\epsilon_x \cos \omega_s t/2 + \epsilon_z \sin \omega_s t/2)\end{aligned} \qquad \text{(K-6)}$$

Thus, alignment errors propagate attitude errors in both frames of reference that are combinations of sinusoids. The sinusoidal amplitude is of the same magnitude as the alignment error and the frequency is equal to the mechanical rotation frequency.

Gyro Scale Factor Errors

Gyro scale factor errors affect the system attitude accuracy by the quality of angular increment information inputted to the attitude algorithm. If each angular increment is in error, then an accumulation of attitude errors is expected in a constantly rotating environment. This attitude accumulation ($\Delta\omega_e$) is expressed in the computed quaternion as follows:

$$\bar{q}_c = \cos(\omega_s + \Delta\omega e)\, t/2 + \bar{j} \sin(\omega_s + \Delta\omega e)\, t/2 \qquad \text{(K-7)}$$

The perfect quaternion, a function only of the strapdown orientation, is unaffected by scale factor errors.

Using equations (1) and (2), error quaternion are formed and expressed as follows:

$$\bar{q}_{eB} = 1 + \bar{j}\, \Delta\omega e\, t/2 \qquad \text{(K-8)}$$

$$\bar{q}_{eI} = 1 - \bar{j}\, \Delta\omega e\, t/2 \qquad \text{(K-9)}$$

Thus, in both frames of reference, scale factor errors propagate ramping attitude errors with slopes that are proprotional to the scale factor error.

Gyro Drift

The effect of gyro drift is to impress body referenced drift rates about the corresponding axes. For example, X and Z gyro drift errors (ω_{Dx} and ω_{Dz} respectively) impress equivalent attitude drifts as described by the following earth rate compensated quaternion:

$$\bar{q}_D = \cos \omega_T\, t/2 + \bar{i}\frac{\omega_{Dx}}{\omega_T} \sin \omega_T\, t/2 + \bar{k}\frac{\omega_{Dz}}{\omega_T} \sin \omega_T\, t/2 \qquad \text{(K-10)}$$

In a single axis constant rotating environment, the effect of rotation is accounted for by pre-multiplying the above drift quaternion with a quaternion that describes the rotation.

Thus, $\bar{q}_c = \bar{q}_p\, \bar{q}_D$

Where, $\bar{q}_p = \cos \omega_s\, t/2 + \bar{j} \sin \omega_s\, t/2 \qquad \text{(K-11)}$

and

$$\bar{q}_c = \cos \omega_s\, t/2 \cos \omega_T\, t/2 +$$

$$\bar{i}\left(\frac{\omega_{Dx}}{\omega_T} \sin \omega_T\, t/2 \cos \omega_s\, t/2 + \frac{\omega_{Dz}}{\omega_T} \sin \omega_T\, t/2 \sin \omega_s\, t/2\right)$$

$$+\bar{j} \cos \omega_T\, t/2 \sin \omega_s\, t/2 \qquad \text{(K-12)}$$

$$+\bar{k}\left(\frac{\omega_{Dz}}{\omega_T} \cos \omega_s\, t/2 \sin \omega_T\, t/2 - \frac{\omega_{Dx}}{\omega_T} \sin \omega_T\, t/2 \sin \omega_s t/2\right)$$

Using equations (1) and (2), error quaternions can be formed and are expressed as follows:

$$\bar{q}_{eB} = \cos \omega_T \, t/2 \cos \omega_s t + \bar{i} \frac{\omega_{Dx}}{\omega_T} \sin \omega_T t/2 + \bar{k} \frac{\omega_{Dz}}{\omega_T} \sin \omega_T \, t/2 \qquad \text{(K-13)}$$

$$\bar{q}_{eI} = \cos \omega_T \, t/2 \cos \omega_s t - \bar{i} \left(\frac{\omega_{Dx}}{\omega_T} \sin \omega_T \, t/2 \sin \omega_s t + \frac{\omega_{Dx}}{\omega_T} \sin \omega_T \, t/2 \cos \omega_s t \right)$$

$$+ \bar{k} \left(\frac{\omega_{Dx}}{\omega_T} \sin \omega_T \, t/2 \sin \omega_s t - \frac{\omega_{Dx}}{\omega_T} \sin \omega_T \, t/2 \cos \omega_s t \right) \qquad \text{(K-14)}$$

For short test durations the small angle approximations, $\sin \omega_T \, t/2 = \omega_T \, t/2$ is made. Thus gyro drift propagate as constant drift error rates in the body frame and as growing sinusoidals in the inertial frame. As the body frame rotates from the inertial frame the skewed orientation generates the growing sinusoid in the inertial frame.

APPENDIX L

LAND NAVIGATION ALGORITHM AND ANALYSIS SOFTWARE

The inertially stablized land navigation difference equations are described as follows:

1. A velocity vector ($\bar{V}_n$) is computed from the velocity increments ($\Delta\bar{V}_{sn}$) and corrections for the gravitational field ($\Delta\bar{V}_{g_{n-1}}$) and attitude damping ($\bar{D}_{n-1}$).

$$\bar{V}_n = \bar{V}_{n-1} + \Delta\bar{V}g_{n-1} + \Delta\bar{V}_{sn} + \bar{D}_{n-1} \tag{L-1}$$

2. A position vector ($\bar{r}_n$) in the inertial coordinate is determined from the velocity vector.

$$\bar{r}_n = \bar{r}_{n-1} + \frac{\Delta t}{2}(\bar{V}_n + \bar{V}_{n-1}) \tag{L-2}$$

3. A radial unit vector ($\bar{u}_n$) along the position vector ($\bar{r}_n$) is computed from a first order correction (E) for the unnormalized radial vector ($\bar{u}'_n$) along $\bar{r}_n$).

$$\bar{u}'_n = \frac{\bar{r}_n}{R_T}$$

$$E = 1 + \frac{1}{2}(1 - \bar{u}'_n \cdot \bar{u}'_n) \tag{L-3}$$

$$\bar{u}_n = E \cdot \bar{u}'_n$$

where R_T is the geocentric radius.

4. The change in velocity due to the force of gravity ($\Delta\bar{V}_g$) is found from the acceleration vector ($\bar{g}_n$) due to gravity.

$$\bar{g}_n = -G_T \cdot \bar{u}_n$$

$$\Delta\bar{V}g_n = \frac{\Delta t}{2}(3\,\bar{g}_n - \bar{g}_{n-1}) \tag{L-4}$$

where G_T is the acceleration magnitude due to gravity.

5. The velocity correction ($\bar{D}_n$) for attitude damping is determined from the vertical error in $\bar{r}_n$ ($d\bar{r}_n$). Attitude is assumed fixed with the vertical error damped to the altitude defined by R_T. The damping coefficients used include $C_1 = .2$ and $C_2 = -1$.

$$d\bar{r}_n = R_T \cdot \bar{u}_n$$

$$D_n = C_1\, d\bar{r}_n + C_2\, d\bar{r}_{n-1} \qquad \text{(L-5)}$$

The output from the land navigation algorithm is the position vector, $\bar{r}_n$. The data is initially stored in the H316 buffer for later transfer, over the H316-DDP516 data link, to the digistore magnetic tape reader. The magnetic tape serves as the interface to MAC programs that compute and plot the following error parameters:

1. Latitude error in nautical miles is developed from a comparison of the known latitude (42° 15' 56.38") to a computed latitude from the position vector ($\arcsin \frac{\bar{r}_z}{\bar{r}_n \cdot \bar{r}_n}$).

2. Longitude error in nautical miles is developed by comparing the computed rotation in the equatorial plane from the position vector ($\arctan \frac{\bar{r}_y}{\bar{r}_x}$) to a value based on the earth rotation rate and time.

3. Position error in nautical miles is calculated as the root sum of squares of the latitude and longitude errors.

4. North, east, and radial velocity errors are determined from the time differentials of the position vectors components $\bar{r}_x$, $\bar{r}_y$, and $\bar{r}_z$ respectively.

5. Altitude error is found from the difference between the position vector height and the known earth geocentric radius.

APPENDIX M

H316 Diagnostic Software

Program Function

BHSF, BH72	A real time compensation algorithm, implemented to calculate the body referenced acceleration and angular rate vectors from gyro and accelerometer pulse inputs.
ROAHS	A pulse bursting compensation analysis program that outputs the histogram of pulse burst patterns.
RAFO	Measures average float hangoff by averaging 512 successive interpolator samples.
RTHRI	An interpolator diagnostic program that prints twenty successive interpolator states.
SHIS	An interpolator diagnostic program that displays the histogram of interpolator outputs.
RDET2	A RDE analysis program that prints the periodic outputs of both RDE channels. Periodicity is selected with a memory content modification.
TS6TST	A program to test the automatic gimbal positioner function by translating operator inputs into computer commands.
DGPR	Prints the contents of Digistore magnetic tapes.

Remote Terminal Software

Program Function

ALIGN	Computes system misalignment errors from twenty four "accelerometer nulled" positions.
ALIGNCHK	Verifies system misalignment calibration with end to end computations that relate measurement data to computed parameters.
REFAXES	Computes body referenced acceleration and angular rate vectors with a direction cosine matrix.
XGYRO, YGYRO, ZGYRO	Computes the static instrument coefficients using Cramer's solution.
DYNAMIC	An alternative method to compute the dynamic instrument coefficients: scale factor and misalignment angles.
PX, PY, PZ	Computes the anisoinertia coefficients.

SFPPM	Computes the scale factor deviation from a nominal.
PIPA 16	Computes accelerometer parameters by fitting a Fourier series to multiposition data.
LANDNAV	Compute latitude and longitude errors from the position vector.
QUATGEN	Computes quaternion errors based on system attitude data.
REGRESS	Performs a simple linear regression analysis.

APPENDIX N

Gimbal Alignment Error Definition and Calibration

Alignment Term	Definition	Solution/ Calibration* Procedure
ϵ_{TR}	Leveling error of the tilt table in the vertical plane containing the Tilt Axis, Positive when TA is rotated about the south vector.	Optical Alignment technique defined in JDC 00001 (Apollo Documentation)
ϵ_{T_T}	Leveling error of the tilt table in the vertical plane normal to the Tilt Axis.	JDC 0001 or $\phi 6$, $\phi 9$ (Table N-1)
$\epsilon f_{X, Y, \text{ or } Z}$	Cumulative alignment errors between the Table Fixed Axes and the Gimbal Case Fixed Axes using small angle approximations.	ϵ fx JD0011 ϵ fy $\phi 23, \phi 24$ ϵ fz $\theta 2, \theta 5$
ϵ_{OGR}	Outer Gimbal Resolver alignment error defined as the alignment difference between the outer gimbal multi-speed resolver electrical zero and the mechanical zero.	$\phi 6$, $\phi 7$
ϵ_{IGR}	Inner Gimbal Resolver alignment error defined as the alignment difference between the inner gimbal multi-speed resolver electrical zero and the mechanical zero.	$\theta 16$, $\theta 17$
ϵ_{MGR}	Middle Gimbal Resolver alignment error defined as the alignment difference between the middle gimbal multi-speed resolver electrical zero and the mechanical zero.	$\theta 1$, $\theta 2$
ϵ_{MGA}	Middle Gimbal Axis Non-orthogonality error. The rotation of the MGA with respect to the OGA and represented as positive rotation of MGA away from Z_{OG} and Y_{OG}.	$\theta 16$, $\theta 18$
ϵ_{IGA}	Inner Gimbal Non-orthogonality error. The rotation of the IGA with respect to the MGA and represented as positive rotation of IGA away from Y_{MG} and X_{MG}.	$\theta 20$, $\theta 21$
$\epsilon_{11z\ (x)}$	Alignment error between the cube 1 surface 1 normal and the Z reference axis about X_{ref}.	$\theta 10$, $\theta 11$

$\epsilon_{12x\,(z)}$	Alignment error between the cube 1 surface 2 normal and the X reference axis about Z_{ref}.	$\phi 12$, $\phi 13$
$\epsilon_{21x\,(z)}$	Alignment error between the cube 2, surface 1 normal and the X reference axis about Z_{ref}.	$\theta 1$, $\theta 3$
$\epsilon_{22z\,(x)}$	Alignment error between the cube 2, surface 2 normal and the Z reference axis about X_{ref}.	$\phi 6$, $\phi 8$
SO_x, SO_y, SO_z	Alignment rotation of the PIP case fixed triad (IRA, OA, PRA) about the output axis.	SO_x - $\theta 1$, $\theta 5$ SO_y - $\theta 19$, $\theta 21$ SO_z - $\theta 10$, $\theta 15$
α_{B_n}	A fictitious rotation of the n PIPA Case (either about its Output Axis (OA) or its Pendulous Reference Axis (PRA) that is a result of the PIP null bias and will produce a moment due to gravity equal in sign and magnitude to the actual bias moment.	α_{B_x} - $\theta 1$, $\theta 4$ α_{B_y} - $\theta 19$, $\theta 22$ α_{B_z} - $\theta 10$, $\theta 14$

*Each term is determined by the simultaneous solution as applicable from the referenced equations in this column. The referenced equations are listed by these symbols in Table N02. A typical solution example is shown in Table N-2.

TABLE N-2 ALIGNMENT ERROR CALIBRATION POSITIONS AND EQUATIONS

Test Position	Rotary Table Axis	Outer Gimbal Axis	Middle Gimbal Axis	Inner Gimbal Axis	Nulling Accelerometer With Axis Orientation	Alignment Error Equations
1	240°	0°	180°	0°	X PIP (IA-W, PRA-D, OA-S)	$\theta 1 = 240^{\circ} + \epsilon_{TR} - \epsilon_{fz} - \epsilon_{MGR} + SO_x - \alpha_{bx}$
2	60°	180°	180°	180°	X PIP (IA-W, PRA-D, OA-S)	$\theta 2 = 60^{\circ} + \epsilon_{TR} - \epsilon_{fz} + \epsilon_{MGR} + SO_x - \alpha_{bx}$
3*	240°	0°	180°	0°	Cube #2, Surface #1	$\theta 3 = 240^{\circ} + \epsilon_{TR} - \epsilon_{fz} - \epsilon_{MGR} + \epsilon_{21x(z)}$
4	60°	0°	180°	0°	X PIP (IA-E, PRA-U, OA-S)	$\theta 4 = 60^{\circ} + \epsilon_{TR} - \epsilon_{fz} - \epsilon_{MGR} + SO_x + \alpha_{bx}$
5	240°	0°	180°	180°	X PIP (IA-E, PRA-D, OA-N)	$\theta 5 = 240^{\circ} + \epsilon_{TR} - \epsilon_{fz} - \epsilon_{MGR} - SO_x + \alpha_{bx}$
6	240°	0°	180°	0°	Z PIP (IA-N, PRA-U, OA-E)	$\phi 6 = 90^{\circ} - \epsilon_{TT} - \epsilon_{fx} - \epsilon_{OGR} + \epsilon_{IGA} - SO_z - \alpha_{bz}$
7	60°	0°	0°	0°	Z PIP (IA-N, PRA-U, OA-E)	$\phi 7 = 90^{\circ} - \epsilon_{TT} + \epsilon_{fx} + \epsilon_{OGR} + \epsilon_{IGA} - SO_z - \alpha_{bz}$
8*	240°	0°	180°	0°	Cube #2, Surface #2	$\phi 8 = 90^{\circ} - \epsilon_{TT} - \epsilon_{fx} - \epsilon_{OGR} + \epsilon_{IGA} + \epsilon_{22z(x)}$
9	60°	180°	180°	0°	Z PIP (IA-S, PRA-U, OA-W)	$\phi 9 = 90^{\circ} - \epsilon_{TT} + \epsilon_{fx} + \epsilon_{OGR} - \epsilon_{IGA} + SO_z + \alpha_{bz}$
10	240°	0°	180°	270°	Z PIP (IA-W, PRA-U, OA-N)	$\theta 10 = 240^{\circ} + \epsilon_{TR} - \epsilon_{fz} - \epsilon_{MGR} - SO_z - \alpha_{bz}$
11*	240°	0°	180°	270°	Cube #1, Surface #1	$\theta 11 = 240^{\circ} + \epsilon_{TR} - \epsilon_{fz} - \epsilon_{MGR} + \epsilon_{11z(x)}$
12	240°	0°	180°	270°	X PIP (IA-S, PRA-D, OA-E)	$\phi 12 = 90^{\circ} - \epsilon_{TT} - \epsilon_{fx} - \epsilon_{OGR} + \epsilon_{IGA} - SO_x + \alpha_{bx}$
13*	240°	0°	180°	270°	Cube #1, Surface #2	$\phi 13 = 90^{\circ} - \epsilon_{TT} - \epsilon_{fx} - \epsilon_{OGA} + \epsilon_{IGA} - \epsilon_{12x(z)}$
14	240°	0°	0°	270°	Z PIP (IA-E, PRA-D, OA-N)	$\theta 14 = 240^{\circ} + \epsilon_{TR} - \epsilon_{fz} - \epsilon_{MGR} - SO_z + \alpha_{bz}$
15	240°	0°	0°	90°	Z PIP (IA-W, PRA-D, OA-S)	$\theta 15 = 240^{\circ} + \epsilon_{TR} - \epsilon_{fz} - \epsilon_{MGR} + SO_z - \alpha_{bz}$
16	150°	270°	0°	0°	Z PIP (IA-E, PRA-S, OA-D)	$\theta 16 = 150^{\circ} + \epsilon_{TR} - \epsilon_{fz} + \epsilon_{MGA} - \epsilon_{IGR} - SP_z + \alpha_{bz}$
17	150°	270°	180°	0°	Z PIP (IA-E, PRA-N, OA-U)	$\theta 17 = 150^{\circ} + \epsilon_{TR} - \epsilon_{fz} + \epsilon_{MGA} + \epsilon_{IGR} + SP_z + \alpha_{bz}$

TABLE N-2 (cont'd.)

Test Position	Rotary Table Axis	Outer Gimbal Axis	Middle Gimbal Axis	Inner Gimbal Axis	Nulling Accelerometer With Axis Orientation	Alignment Error Equations
18	150°	90°	180°	180°	Z PIP (IA-E, PRA-S, OA-D)	$\theta 18 = 150^{\circ} + \epsilon_{TR} - \epsilon_{fz} - \epsilon_{MGA} - \epsilon_{IGR} - SP_z + \alpha_{bz}$
19	60°	90°	90°	0°	Y PIP (IA-W, PRA-U, OA-N)	$\theta 19 = 60^{\circ} + \epsilon_{TR} - \epsilon_{fz} - \epsilon_{MGA} - \epsilon_{IGA} - SO_y - \alpha_{by}$
20	60°	90°	270°	180°	Y PIP (IA-E, PRA-D, OA-N)	$\theta 20 = 60^{\circ} + \epsilon_{TR} - \epsilon_{fz} - \epsilon_{MGA} + \epsilon_{IGA} - SO_y - \alpha_{by}$
21	60°	90°	90°	180°	Y PIP (IA-W, PRA-D, OA-S)	$\theta 21 = 60^{\circ} + \epsilon_{TR} - \epsilon_{fz} - \epsilon_{MGA} - \epsilon_{IGA} + SO_y - \alpha_{by}$
22	240°	90°	90°	0°	Y PIP (IA-E, PRA-D, OA-E)	$\theta 22 = 240^{\circ} + \epsilon_{TR} - \epsilon_{fz} - \epsilon_{MGA} - \epsilon_{IGA} - SO_y + \alpha_{by}$
23	330°	0°	0°	0°	Z PIP (IA-N, PRA-W, OA-U)	$\phi 23 = 90^{\circ} - \epsilon_{TT} + \epsilon_{fy} + \epsilon_{MGA} - \epsilon_{IGR} - SP_z - \alpha_{bz}$
24	150°	180°	0°	180°	Z PIP (IA-N, PRA-W, OA-U)	$\phi 24 = 90^{\circ} - \epsilon_{TT} - \epsilon_{fy} + \epsilon_{MGA} - \epsilon_{IGR} - SP_z - \alpha_{bz}$

Calibration Examples: $\epsilon_{MGR} = \frac{\theta 2 - \theta 1 + 180^{\circ}}{2}$, $\epsilon_{fx} + \epsilon_{OGR} = \frac{\phi 7 - \phi 6}{2}$

* Test positions $\theta 3$, $\phi 8$, $\theta 11$, and $\phi 13$ calibrate the alignment between the normal vector of the optical cubes and the body referenced axes x and z.

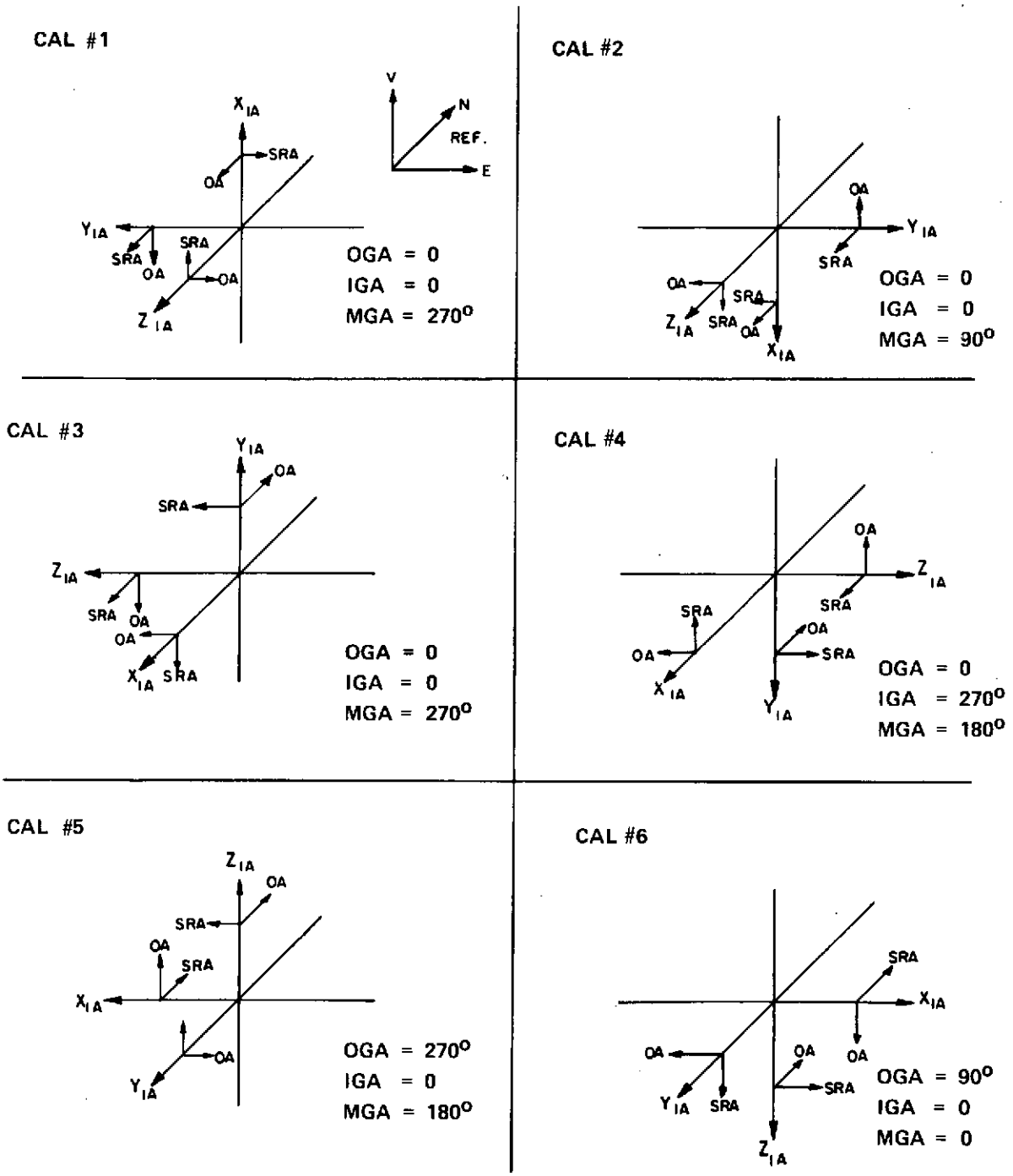

Fig. P-1 Cardinal Calibration Positions- Gyro Orientation.

CAL #1

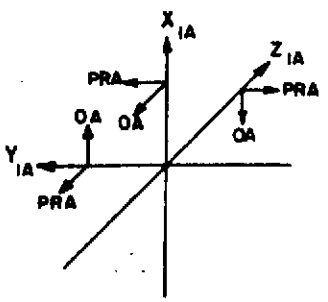

OGA = 0
IGA = 0
MGA = 270°

CAL #2

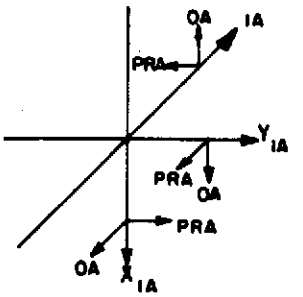

OGA = 0
IGA = 0
MGA = 270°

CAL #3

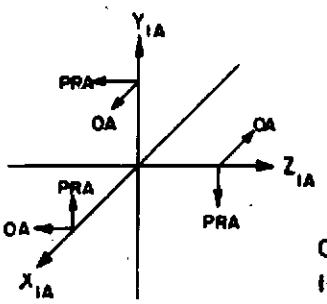

OGA = 0
IGA = 270°
MGA = 0

CAL #4

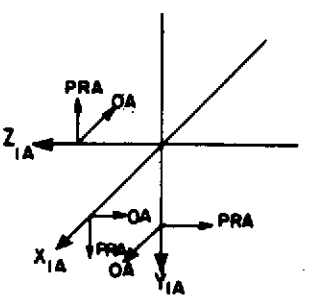

OGA = 0
IGA = 270°
MGA = 180°

CAL #5

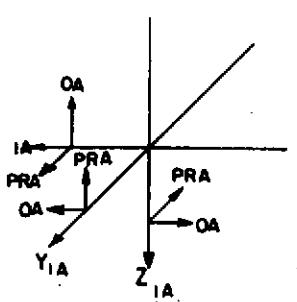

OGA = 270°
IGA = 0
MGA = 180°

CAL #6

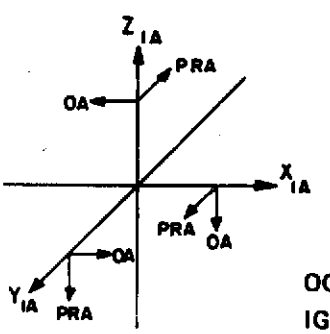

OGA = 90°
IGA = 0
MGA = 0

(U) **Fig. P-2** Cardinal Calibration Positions- Accelerometer (U) Orientation.

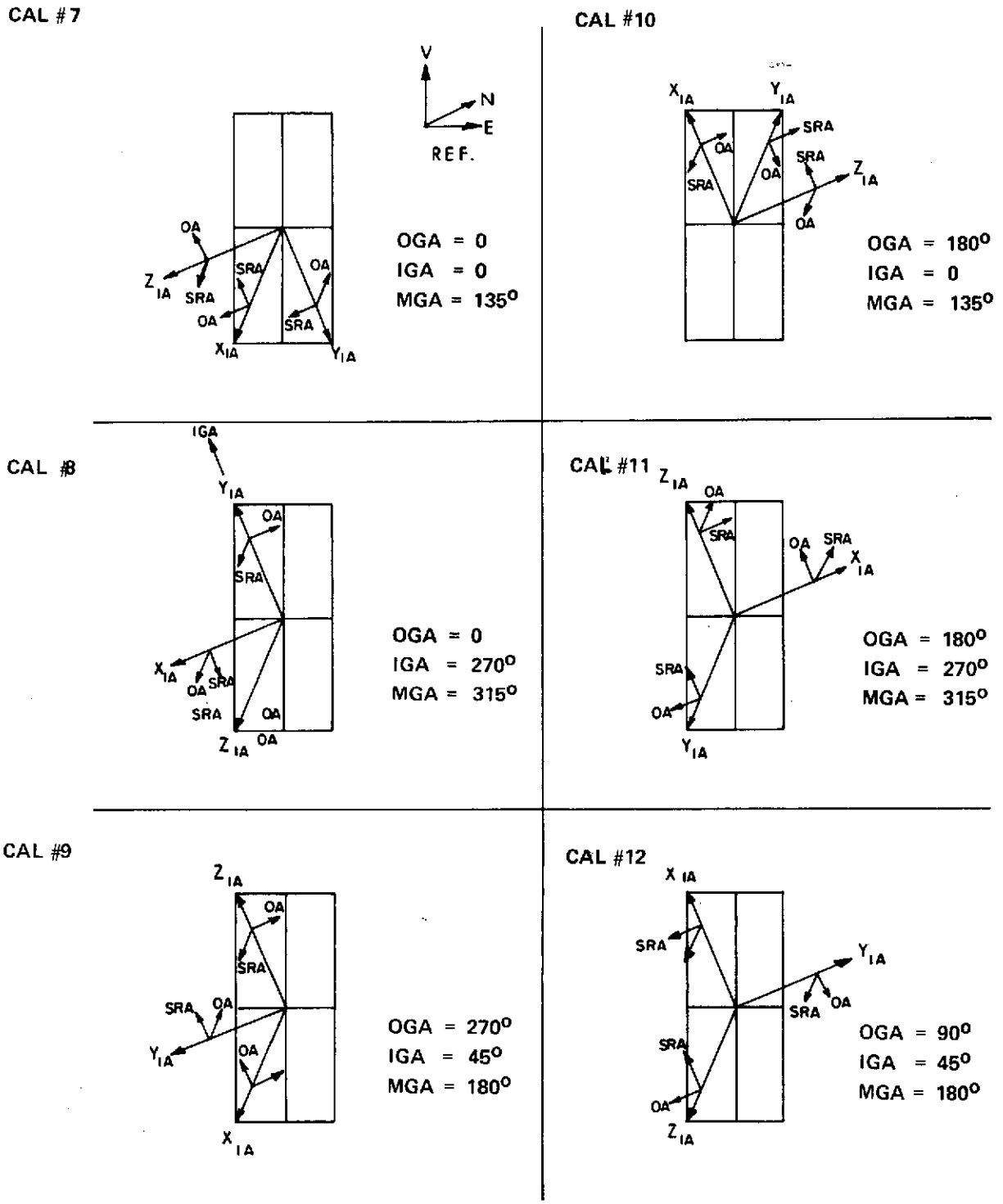

Fig. P-3 Offset Calibration Positions Gyro Orientation.

Appendix P

I. Gyro Calibration Equations

A. Definitions

Wij - Measured Drift Rate of the i^{th} gyro (i = x, y, or z) in the j^{th} test position (j = 1, 2, ... , 12). Each Wij is calculated by scaling the accumulated gyro torque pulses during the calibration interval. Thus, the units of Wij is radians per second.

GOi, GSi - Input axis misalignments of the i^{th} gyro (i = x, y, or z) from its reference axis due to rotation about the Output or Spin Reference Axis respectively.

WIEV, WIEH - vertical and horizontal earth rate components respectively.

ϵ_{jk} - gimbal and test table alignment errors. Definitions are given in Appendix N.

B. Gyro Calibration Equations

Gyro drift parameters (NBD, ADIA, ADSRA, ADOA and major compliance) are solved as a function of measured drift rate, earth rate and gimbal alignment errors. Trigometric identities and small angle approximations have been used.

a) Gyro Normal bias drift about the IA, OA and SRA axes respectively (meru)

$$IBDX = -\frac{WX1+WX2}{2} - WIEH\left[GSX - \epsilon_{IGR}\right]$$

$$OBDX = -\frac{WX5+WX6}{2} - WIEH\left[GOX - \epsilon_{MGR}\right] - WIEV\left[\epsilon_{MGA}\right]$$

$$SBDX = -\frac{WX3+WX4}{2} - WIEH$$

$$IBDY = -\frac{WY3+WY4}{2} + WIEH \left[GSy - \epsilon_{IGA}\right]$$

$$OBDY = -\frac{WY1+WY2}{2} + WIEH \left[GOy - \epsilon_{IGA}\right]$$

$$SBDY = -\frac{WY5+WY6}{2} - WIEH - WIEV \left[\epsilon_{TT} + \epsilon_{fx} + \epsilon_{OGR}\right]$$

$$IBDZ = -\frac{WZ5+WZ6}{2} + WIEH \left[GSZ + \epsilon_{IGA}\right]$$

$$OBDZ = -\frac{WZ3+WZ4}{2} + WIEH \left[GOZ - \epsilon_{IGR}\right]$$

$$SBDZ \quad -\frac{WZ1+WZ2}{2} - WIEH - WIEV \left[\epsilon_{TT} + \epsilon_{fx} + \epsilon_{OGR}\right]$$

b) Acceleration Sensitive Drift along the input axis (meru/g)

$$ADIAX = \frac{WX2-WX1}{2} + WIEV - WIEH \left[\epsilon_{TT} + \epsilon_{fx} + \epsilon_{OGR}\right]$$

$$ADIAY = \frac{WY4-WY3}{2} + WIEV - WIEH \left[\epsilon_{TT} + \epsilon_{fx} + \epsilon_{OGR}\right]$$

$$ADIAZ = \frac{WZ6-WZ5}{2} + WIEV - WIEH \left[\epsilon_{TT} + \epsilon_{fx} + \epsilon_{OGR}\right]$$

c) Acceleration Sensitive Drift along the spin axis (meru/g)

$$ADSRAX = \frac{WX3-WX4}{2} + WIEV \left[\epsilon_{TT} + \epsilon_{fx} + \epsilon_{OGR} + \epsilon_{IGA} - GO_z\right]$$

$$ADSRAY = \frac{WY6-WY5}{2} - WIEV \left[GOY - \epsilon_{IGA}\right]$$

$$ADSRAZ = \frac{WZ2-WZ1}{2} - WIEV \left[GOZ - \epsilon_{IGR}\right]$$

d) Acceleration Sensitive Drift along the output axis (meru/g)

$$ADOAX = \frac{WX6-WX5}{2} + WIEV \left[GSX - \epsilon_{TR} - \epsilon_{fz} + \epsilon_{IGR}\right] + WIEH \left[\epsilon_{fy}\right]$$

$$ADOAY = \frac{WY1-WY2}{2} + WIEV \left[GSY + \epsilon_{TR} - \epsilon_{fz} - \epsilon_{MGR}\right] - WIEH \left[\epsilon_{fy} + \epsilon_{MGA}\right]$$

$$ADOAZ = \frac{WZ3-WZ4}{2} + WIEV \left[GSZ + \epsilon_{TR} - \epsilon_{fz} - \epsilon_{MGR}\right] + WIEH \left[\epsilon_{fy} + \epsilon_{MGA}\right]$$

e) Acceleration Squared Sensitive Drift or Major Compliance (meru/g)

$$A2DX = -WX7 - WX8 - 2IBDX - WIEH\,(\epsilon_{fy}\sqrt{2}) - 2WIEV\,(+\epsilon_{TR} - \epsilon_{fz})\cos\left[45 + GOX - \epsilon_{MGR}\right]$$

$$A2DY = -WY9 - WY10 - 2IBDY + WIEH\,(\epsilon_{fy}\sqrt{2}) + 2WIEV\,(\epsilon_{TR} - \epsilon_{fz})\cos\left[45 + GOY + \epsilon_{MGR}\right]$$

$$A2DZ = -WZ11 - WZ12 - 2IBDZ + WIEH\,(\epsilon_{fy}\sqrt{2}) + 2WIEV\,(\epsilon_{TR} - \epsilon_{fz} - \epsilon_{MGA})\cos$$
$$\left[45 + GOY - (\epsilon_{TT} + \epsilon_{fx} + \epsilon_{OGR} - \epsilon_{MGR} - \epsilon_{IGA})\right]\frac{\sqrt{2}}{2}$$

Appendix P

II. Accelerometer Calibration

A. Definitions

K_{ij} - average accelerometer pulse rate for the i^{th}, accelerometer ($i = x, y,$ or z) in the j^{th} calibration position ($j = 1, 2, \ldots 6$). Each k_{ij} is calculated by averaging the accumulated accelerometer pulses over the calibration interval.

g - gravitational acceleration

ϵ_{ik} - gimbal and test table alignment errors. Definitions are given in Appendix N

B. Accelerometer Calibration Equations

The accelerometer parameters are solved as a function of the measured pulse rates. Trigometric identities and small angle approximations have been used. The average scale factor and the scale factor difference are defined as:

$$SFAi = \frac{SFi^{+} + SFi^{-}}{2}$$

$$\Delta SFi = SFi^{+} - SFi^{-}$$

The isolated PIPA parameters are shown to be:

a) Average Scale Factor, SFAi (cm/sec/pulse)

$$SFAX = \frac{2g}{KX1-KX2}$$

$$SFAY = \frac{2g}{KY3-KY4}$$

$$SFAZ = \frac{2g}{KZ6-KZ5}$$

b) Bias, ABi (cm/sec^2)

$$ABX = 1/2\ SFAX\ (KX5+KX6) + g\ (\epsilon_{MGA})$$

$$= 1/2\ SFAX\ (KX3+KX4) + g(\epsilon_{TT} + \epsilon_{fx} + \epsilon_{OGR})$$

$$ABY = 1/2\ SFAY(KY1+KY2)$$

$$= 1/2\ SFAY\ (KY5+KY6) + g(\epsilon_{TT} + \epsilon_{fx} + \epsilon_{OGR})$$

$$ABZ = 1/2\ SFAZ\ (KZ3+KZ4)$$

$$= 1/2\ SFAZ\ (KZ1+KZ2) - g(\epsilon_{TT} + \epsilon_{fx} + \epsilon_{OGR})$$

c) Scale Factor Difference between ± 1 g positions, ΔSFi (cm/sec/pulse)

$$\Delta SFX = \frac{4ABX - 2SFAX\ (KX1+KX2)}{(KX1-KX2)}$$

$$\Delta SFY = \frac{4ABY - 2SFAY\ (KY3+KY4)}{(KY3-KY4)}$$

$$\Delta SFZ = \frac{4ABZ - 2SFAZ\ (KZ6+KZ5)}{(KZ6-KZ5)}$$

d) Input axis misalignment due to a rotation about the output axis SOi (radians)

$$SOX = \frac{SFAX\ (KX3-KX4)}{2g} + \epsilon_{IGA}$$

$$SOY = +\frac{SFAY\ (KX5-KX6)}{2g} - \epsilon_{IGA}$$

$$SOZ = -\frac{SFAZ\ (KZ3-KZ4)}{2g} + \epsilon_{TR} - \epsilon_{fz}$$

e) Input axis misalignment due to a rotation about the negative pendulum axis, SPi (radians)

$$SPX = \frac{SFAX\ (KX5-KX6)}{2g} + \epsilon_{TR} - \epsilon_{fz} + \epsilon_{IGR}$$

$$SPY = \frac{SFAY\ (KY1-KY2)}{2g} + \epsilon_{TR} - \epsilon_{fz} + \epsilon_{MGR}$$

$$SPZ = -\frac{SFAZ\ (KZ1-KZ2)}{2g} - \epsilon_{IGR}$$

APPENDIX Q

SYSTEM OPERATIONAL LOG

This operational log gives the description of the system event markers given in the calibration curves, Q-1, Q-2, and Q-3.

28 May 71	Controlled system cooldown for planned air conditioner maintenance. All system power shutdown with system in calibration position #1 (X axis up; Y axis west and horizontal; Z axis south and horizontal). System powered up 1 June 71.
16 June 71	Gyro wheels shut off due to voltage transient induced while integrating the interpolator electronics in the system. At time of downmode, the system was rotating about the outer gimbal axis in calibration position #5. Gyro wheels operational 15 minutes after downmode. Accelerometer loops were unaffected.
21 June 71	System powered down in calibration position #1 for system clock repair.
20 July 71	Gyro wheels shut off due to voltage transient* from short in the test sequencer electronics. System orientation at time of downmode included all gimbals at 22.5° (Y axis up, X axis horizontal, Z axis 45° down). Gyro wheels operational approximately 15 minutes after downmode. Accelerometer loops were unaffected.
22 July 71	Gyro wheels shut off due to a voltage transient* while operating system in automatic mode. At time of downmode, all gimbals were oriented to 90° (X axis up, Y axis east and horizontal, Z axis north and horizontal). Time of downmode was approximately 15 minutes. Accelerometer loops were unaffected.
27 July 71	Gyro wheels shut off due to voltage transient* (source unknown). At time of downmode, system was orientated in calibration position #1. Time of downmode was approximately 15 minutes. Accelerometer loops were unaffected.
9 August 71	Gyro wheels shut off due to voltage transient (400 hertz supply fuse blew). At time of failure, system orientation was inner and middle gimbals at 0° and outer gimbal at 338° (X axis east and horizontal, Y and Z axis 22.5° from horizontal). System was cooled to room temperature overnight to start gyro MB-2 (X axis).
22 Sept. 71	System shut down due to accidental turn off of the lamp and relay 28 volt power supply. At time of downmode, system was oriented in calibration position #3 (X axis south and horizontal, Y axis is vertically up and Z axis west and horizontal).

19 November 71	Gyro wheel shut off due to voltage transient* (source unknown). At time of downmode, system was oriented in calibration position #1. System cooled to room temperature in an attempt to start gyro MB-2 (X axis). Gyro MB-2 was removed from system 25 November and replaced with gyro 427A on 7 December 1971.
26 January 72	System shut down due to loss of gimbal coolant (circuit breaker disconnected input 110vac power). Gyro 415 (Z axis) hot temperature alarm tripped to downmode system. At the time of temperature alarm, the system was oriented with IGA, MGA, and OGA set to 0^{o}, 135^{o} and 177^{o} respectively. System cooled to room temperature overnight to start gyro MB4 (Y axis).
10 March 72	System downmoded due to tripped gyro temperature alarm (X axis cold alarm). At time of time of temperature alarm, the system was oriented in calibration position #9 (IGA, MGA, OGA = 270^{o}, 315^{o}, 180^{o}). System was cooled to room temperature to start gyro MB415 (Z axis). Gyro 415 was removed 13 March 72 and replaced with gyro MB 422B on 24 May 1972. In addition to gyro MB415, the DART instrument wheel element failed. No replacement DART instrument was available. During the period 10 March to 24 May the gyro torque loops scaling was increased by a factor of four.

*The system was mechanized with a gyro suspension monitor and interlock circuit which proved to be overly sensitive to system voltage glitches. In the later phases of the program, the circuit function was inhibited because the initial concern for maintenance of suspension and signal generator voltage was outweighed by the repeated non-essential system downmodes experienced.

Appendix Q- Gyro Long Term Drift Profiles.

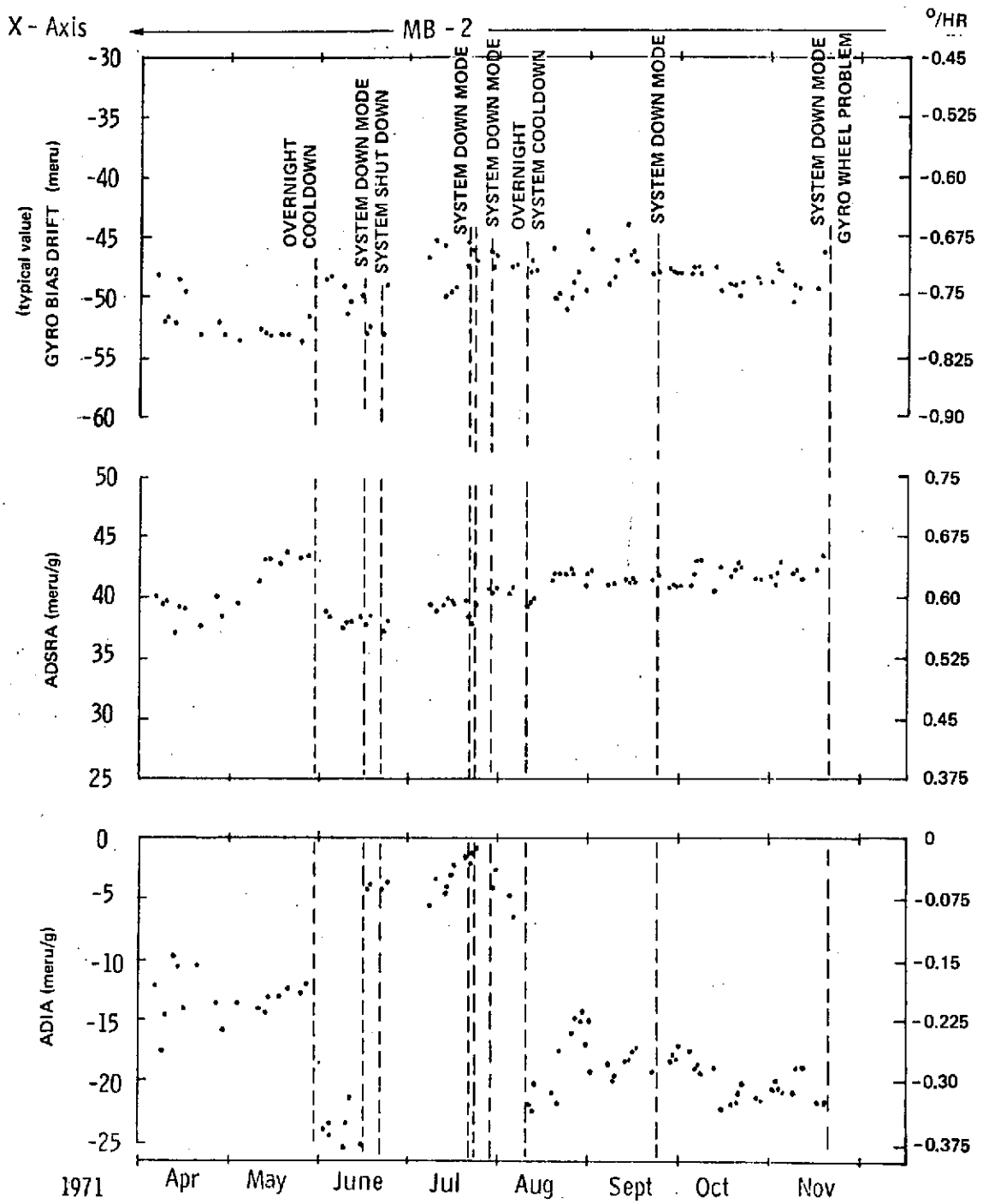

Fig. Q-1 X-Axis Gyro Drift.

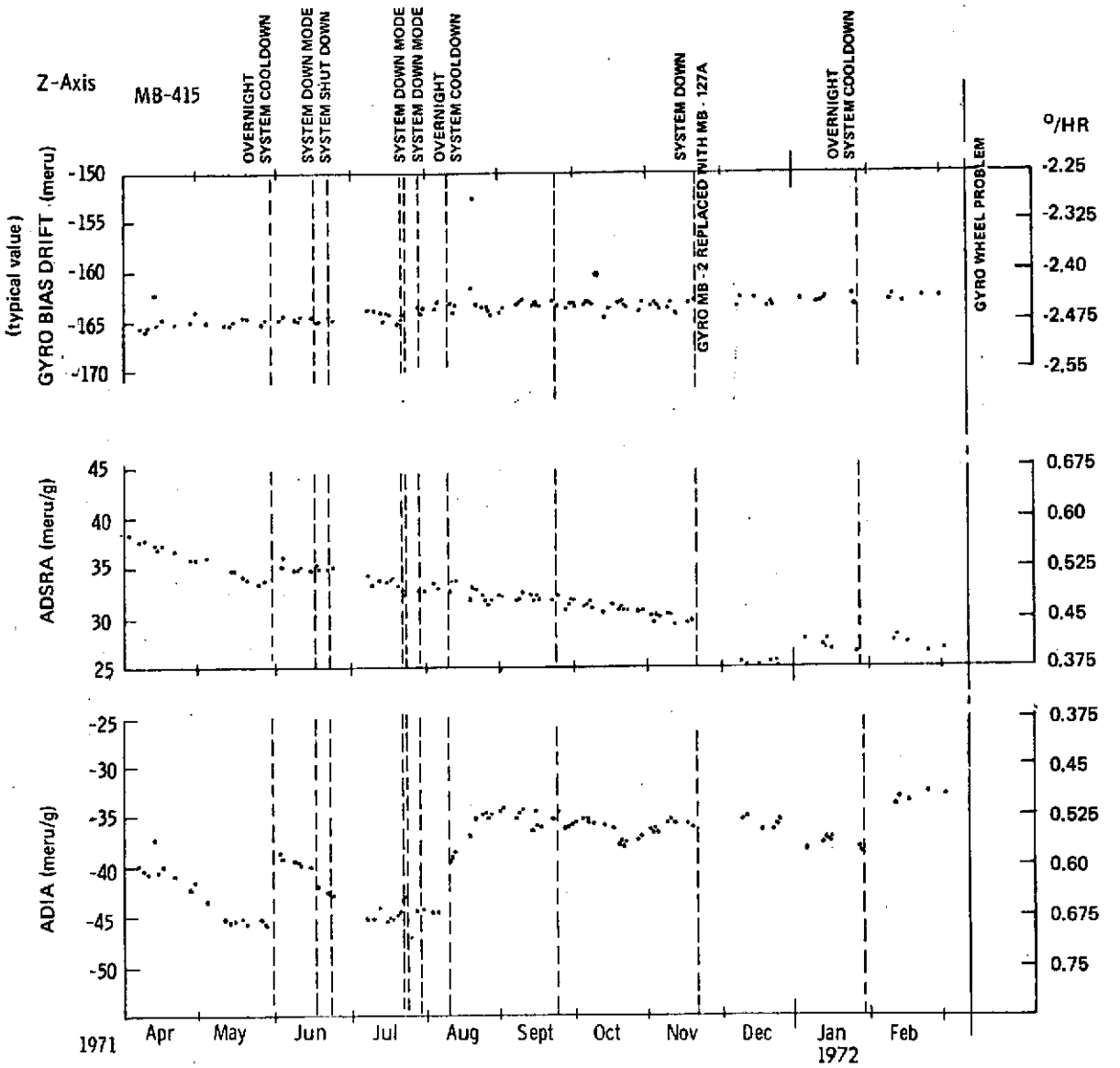

*FIGURE Q-4 Gives Bais Drift On Expanded Scale for October 7.

Fig. Q-3 Z-Axis Gyro Drift.

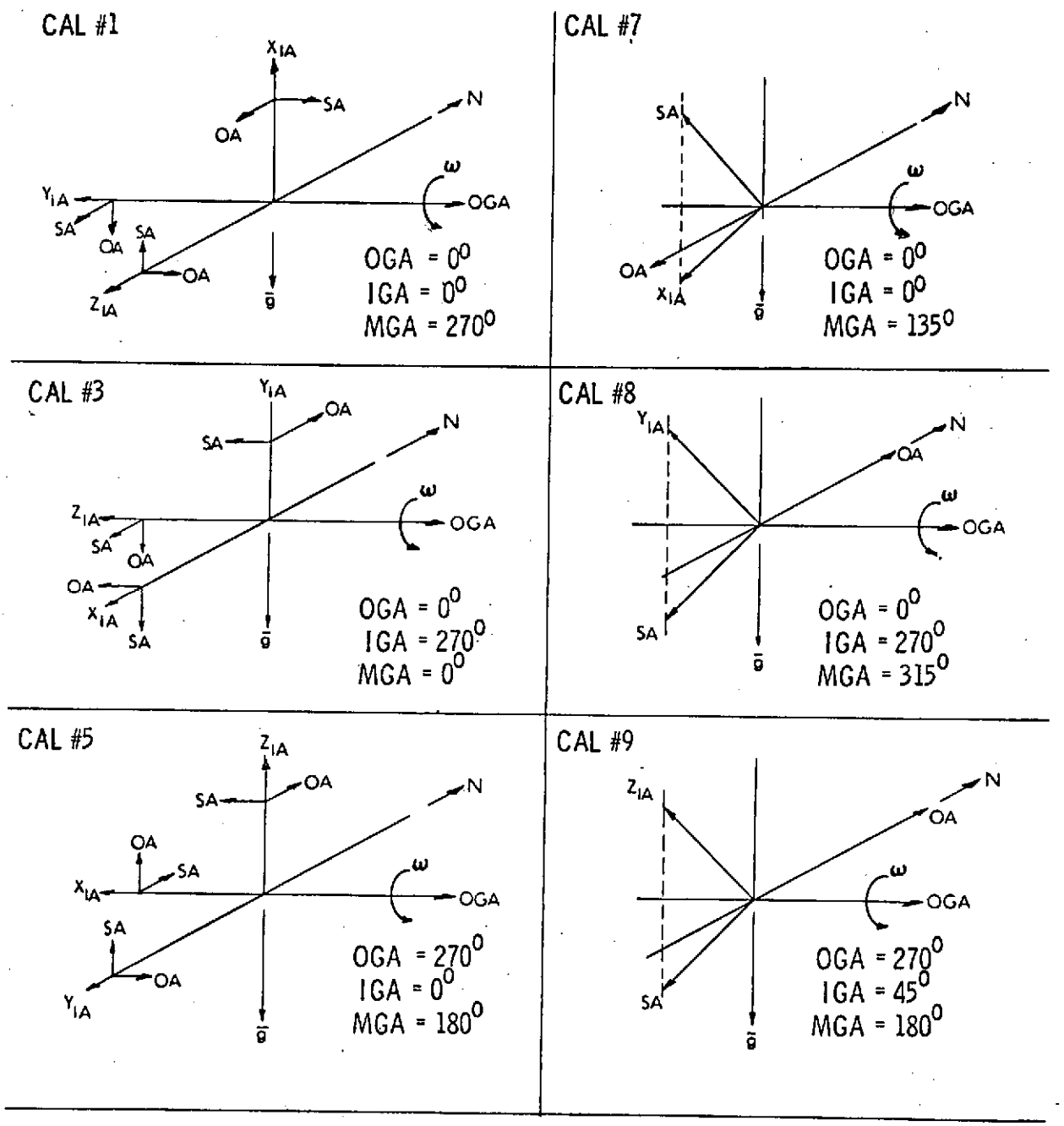

Figure R-1 Calibration Positions - Gyro Orientation.

APPENDIX R

DYNAMIC CALIBRATION EQUATIONS

A. Definitions

POSITIVE OUTER GIMBAL ROTATIONAL RATE

$NGP_{ij}^{\pm}$: Number of positive or negative $(\pm)\Delta\theta$ pulses accumulated for the ith gyro (x, y, or z) in the jth test position for a slew about the positive (P) OGA.

AD_jP_i: Magnitude of the angle driven (radians) about the OGA for a positive slew rate, for the ith gyro in the jth calibration position.

T_jP_i: Time (seconds) to complete total angle displacement AD_jP_i.

NEGATIVE OUTER GIMBAL ROTATIONAL RATE

$NGN_{ij}^{\pm}$: Number of positive or negative $(\pm)\Delta\theta$ pulses accumulated for the ith gyro (x, y, or z) in the jth test position for a negative (N) slew about OGA.

AD_jN_i: Magnitude of the angle driven (radians) about the OGA for a negative (N) slew rate, for the ith gyro in the jth calibration position.

T_jN_i: Time (seconds) to complete total angle displacement AD_jP_i.

FLOAT OFFSET

AF_iR: Average float offset of the ith gyro (i= x, y, or z) defined by the linear relationship:

$$AF_iR = FO_i + (FM_i - FO_i)\,R$$

Where: FO_i is the float offset at zero input angular rate. FM_i is the float offset at an input angular rate of one radian per second. R is the outer gimbal angular rate.

ALIGNMENT ERRORS

EMGA: - the middle gimbal axis non-orthogonality error.

EIGA: - the inner gimbal axis non-orthogonality error.

EIGR: - the inner gimbal resolver misalignment.

EMGR: - the middle gimbal resolver misalignment.

GYRO DRIFT

NBD_i: Normal bias drift of the ith gyro (i= x, y, or z).

B. CALIBRATION EQUATIONS

Scale Factors (radian/$\Delta\theta$)

$$SFGX+ = \frac{+(AD5NX)\ \cos[GSX-EMGA-EIGR]\ \cos[GOX-EMGR+AFXR] - (NBDX)T5NX}{(NGNX5+)}$$

$$SFGX- = \frac{+(AD5PX)\ \cos[GSX-EMGA-EIGR]\ \cos[GOX-EMGR-AFXR] + (NBDX)T5PX}{(NGPX5-)}$$

$$(SFGY+) = \frac{+(AD1NY)\ \cos[GSY-EMGR]\ \cos[GOY+EMGA-EIGA+AFYR] - (NBDY)T1NY}{(NGNY1)}$$

$$(SFGY-) = \frac{+(AD1PY)\ \cos[GSY-EMGR]\ \cos[GOY+EMGA-EIGA-AFYR] + (NBDY)T1PY}{(NGPY1-)}$$

$$(SFGZ+) = \frac{+AD3NZ\ \cos[GSZ-EMGR]\ \cos[GOZ-EIGR+EMGA+AFZR] - (NBDZ)T3NZ}{(NGNZ3+)}$$

$$(SFGZ-) = \frac{+AD3PZ\ \cos[GSZ-EMGR]\ \cos[GOZ-EIGR+EMGA-AFZR] + (NBDZ)T3PZ}{(NGPZ3-)}$$

Gyro Input Axis Misalignment Angles

Output Axis (OA) Misalignments (radians)

$$GOX = \frac{SFGXN[(NGNX1+) - (NGPX1 + (NGPX1-) - (NGNX1-)] - (NBDX)\ (T1PX - T1NX)}{AD1PX + AD1NX} + EMGR$$

$$GOY = \frac{SFGYN[(NGPY3+) - (NGNY3+) - (NGPY3-) + (NGNY3-)] + (NBDY)\ (T3PY - T3NY)}{AD3PY + AD3NY} - EMGR$$

$$GOZ = \frac{SFGZN[(NGPZ5+) - (NGNZ5+) - (NGPZ5-) + (NGNZ5-)] + (NBDZ)\ (T5PZ - T5NZ)}{AD5PZ + AD5NZ} + EMGA + EIGR$$

Gyro Input Axis Misalignment Angles (Cont'd.)

Spin Ref. Axis (SRA) Misalignments (radians)

$$GSX = \frac{SFGXN\,[(NGPX3+)-(NGNX3+)+(NGPX3-)-(NGNX3-)] - NBDX(T3PX-T3NX)}{AD3PX + AD3NX} - EMGA + EIGR$$

$$GSY = \frac{SFGYN\,[(NGPY5+)-(NGNY5+)-(NGPY5-)+(NGNY5-)] + NBDY(T5PY-T5NY)}{AD5PY + AD5NY} + EMGR$$

$$GSZ = \frac{SFGZN\,[(NGPZ1+)-(NGNZ1+)-(NGPZ1-)+(NGNZ1-)] + NBDZ(T3PZ-T3NZ)}{AD1PZ + AD1NZ} - EIGA + EMGA$$

Anisoinertia (seconds - time)

$$PX+ = 2\left[\frac{-(NGPX7-)\,(SFGX-)+AD7PX\,\sin\left[\frac{\pi}{4} - GOX+EMGR+FO_X+\frac{\sqrt{2}}{2}(FM_X-FO_X)\,R\right]\,\cos\left[GSX-(EIGR)-\frac{\sqrt{2}}{2}EMGA\right]+(NBDX)T7PX}{\frac{(AD7PX)^2}{T7PX}\,\sin 2\left[\frac{\pi}{4}-GOX+EMGR+\frac{\sqrt{2}}{2}(AFXR)\right]}\right]$$

$$PX- = 2\left[\frac{+(NGNX7+)\,(SFGX+)-AD7NX\,\sin\left[\frac{\pi}{4}-GOX+EMGR-FO_X-\frac{\sqrt{2}}{2}(FM_X-FO_X)\,R\right]\,\cos\left[GSX-(EIGR)-\frac{\sqrt{2}}{2}EMGA\right]+(NBDX)T7NX}{\frac{(AD7NX)^2}{T7NX}\,\sin 2\left[\frac{\pi}{4}-GOX+EMGR-\frac{\sqrt{2}}{2}(AFXR)\right]}\right]$$

$$PY+ = 2\left[\frac{-(NGPY8-)\,(SFGY-)+AD8PY\,\sin\left[\frac{\pi}{4}-GOY-EMGR+FO_Y+\frac{\sqrt{2}}{2}(FM_Y-FO_Y)\,R\right]\,\cos\left[GSY+\frac{\sqrt{2}}{2}(+EMGA)-EIGA\right]+(NBDY)T8PY}{\frac{(AD8PY)^2}{T8PY}\,\sin 2\left[\frac{\pi}{4}-GOY-EMGR+\left(\frac{\sqrt{2}}{2}\right)AFYR\right]}\right]$$

$$PY- = 2\left[\frac{(NGNY8+)\,(SFGY+)-AD8NY\,\sin\left[\frac{\pi}{4}-GOY-EMGR-FO_Y-\frac{\sqrt{2}}{2}(FM_Y-FO_Y)\,R\right]\,\cos\left[GSY+\left(\frac{\sqrt{2}}{2}\right)EMGA-EIGA\right]+(NBDY)T8NY}{\frac{(AD8NY)^2}{T8NY}\,\sin 2\left[\frac{\pi}{4}-GOY-EMGR-\left(\frac{\sqrt{2}}{2}\right)AFYR\right]}\right]$$

Anisoinertia (Cont'd.)

$$PZ+ = 2\left[\frac{-(NGPZ9-)\,(SFGZ-)+AD9PZ\,\sin\left[\frac{\pi}{4}GOZ+EMGA+EIGR+FO_Z+\frac{\sqrt{2}}{2}(FM_Z-FO_Z)R\right]\cos\left[GSZ+\left(\frac{\sqrt{2}}{2}\right)(EIGA+EMGR)\right]+(NBDZ)T9PZ}{\frac{(AD9PZ)^2}{T9NZ}\sin 2\left[\frac{\pi}{4}-GOZ-EMGA+EIGR+\frac{\sqrt{2}}{2}(AFZR)\right]}\right]$$

$$PZ- = 2\left[\frac{(NGNZ9+)\,(SFGZ-)-AD9NZ\,\sin\left[\frac{\pi}{4}-GOZ+EMGA+EIGR-FO_Z-\frac{\sqrt{2}}{2}(FM_Z-FO_Z)R\right]\cos\left[GSZ+\left(\frac{\sqrt{2}}{2}\right)(EIGA+EMGR)\right]+(NBDZ)T9NZ}{\frac{(AD9NZ)^2}{T9NZ}\sin 2\left[\frac{\pi}{4}-GOZ-EMGA+EIGR-\frac{\sqrt{2}}{2}(AFZR)\right]}\right]$$

Appendix S

Anisoinertia Sensitivity Analysis

This section establishes the sensitivity of the anisoinertia coefficient to gyro scale factor errors, pulse count variations, and alignment errors. Figure S-1 establishes that, negative rotations about the outer gimbal axis generates positive X gryoscope torque pulses that are described by the expression:

$$\frac{(SF_x^+)\,(\Delta\theta^+)}{T} = \omega_{IA} + NBD + 1/2(\omega_{IA})\,(\omega_{SRA})\,(K_a^+) \quad \text{(S-1)}$$

where

SF_x^+ = positive scale factor (radians/pulse)

$\Delta\theta^+$ = positive torque pulse (pulses)

T = test time interval (second)

NBD = Drift (radians/second)

ω_{IA} = Input axis rate (radians/second)

ω_{SRA} = Spin reference axis rate (radians/second)

K_a^+ = anisoinertia coefficient (radians/radians per second)

The input and spin reference axis rates (ω_{IA}, ω_{SRA}) can be defined with an axis offest (θ) and alignment error (ϵ).

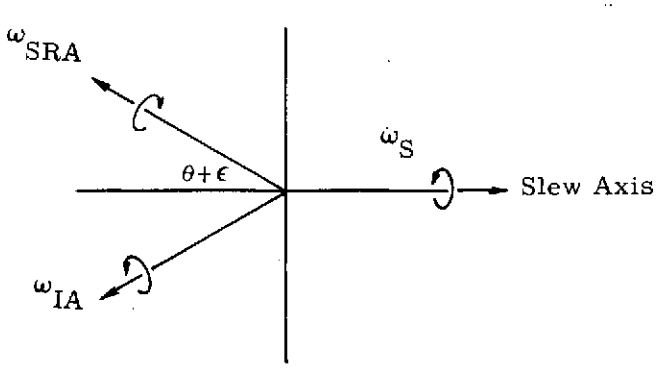

Figure S-1: Anisoinertia Calibration Position with Alignment Uncertainties

$$\omega_{IA} = \omega_S \sin(\theta+\epsilon)$$
$$\omega_{SRA} = \omega_S \cos(\theta+\epsilon) \qquad \text{(S-2)}$$

Anisoinertia is explicitly solved by substituting the input and spin axis rates into equation (S-1).

$$K_a^+ = \frac{2(SF_x^+)(\Delta\theta^+) - (NBD)(T)}{(T)(\omega_S^2)\sin(\theta+\epsilon)\cos(\theta+\epsilon)} - \frac{2}{\omega_S \cos(\theta+\epsilon)} \qquad \text{(S-3)}$$

Sensitivity functions are determined with partial differentiations of anisoinertia with respect to each independent parameter.

The sensitivity to scale factor is determined by

$$\frac{\partial K_a^+}{\partial SF_x^+} \qquad \frac{2\Delta\theta^+}{(T)\omega_S^2 \sin(\theta+\epsilon)\cos(\theta+\epsilon)} \qquad \text{(S-4)}$$

Note that, the total angular displacement ($T\omega_S$) is proportional to the total pulses accumulated ($\Delta\theta^+$). Therefore, the scale factor sensitivity is simplified, and found inversely affected only by the slew rate:

$$\frac{\partial K_a^+}{\partial SF_x^+} = \frac{2K}{\omega_S \sin(\theta+\epsilon)\cos(\theta+\epsilon)} \text{ where } \quad K = \frac{\Delta\theta^+}{T\omega_S} \qquad \text{(S-5)}$$

The sensitivity expression is bounded by $0 > \theta > \pi/2$, and is found to be a minimum when $\theta = 45^\circ$. At $\theta = 45^\circ$ the sensitivity value is $\frac{4\Delta\theta^+}{T\omega_S^2}$.

Thus, the anisoinertia sensitivity to scale factor decreases with increasing rotational rates.

For a 40 arc seconds per pulse loop quantization, and a 4 revolution test duration, the scale factor sensitivity is 0.079×10^{-4} sec/PPM at 0.5 radians per second and 0.158×10^{-4} sec/PPM at 0.25 radians per second. Hence, the error per ppm scale factor error in terms of the anisoinertia coefficient is 8% at 0.5 radians per second and 16% at 0.25 radians per second.

The sensitivity of anisoinertia to the total pulse count is determined as:

$$\frac{\partial K_a^+}{\partial \Delta\theta^+} = \frac{2SF_x^+}{(T\omega_S)(\omega_S)\sin(\theta+\epsilon)\cos(\theta+\epsilon)} \qquad \text{(S-6)}$$

The pulse count sensitivity is inversely affected by slew rate and total angular displacement. Thus a multi-revolution test would diminish the effect due to pulse count uncertainties. The sensitivity to pulse counts is a minimum value of $\frac{4SF_x^+}{T\omega_S^2}$ when $\theta = 45^o$.

For a 40 arc seconds per pulse loop quantization, and a 4 revolution test duration, the pulse count sensitivity is 0.61×10^{-4} sec/pulse at 0.5 radians per second and $1.22\ 10^{-4}$ sec/pulse at 0.25 radians per second. The best solution to reduce the error sensitivity is to increase the number of revolutions per test and to increase the speed. Hence, at 1 radian per second and at ten revolutions, the error is 0.061×10^{-4} sec/pulse or 6%.

The sensitivity of anisoinertia to alignment errors is determined to be:

$$\frac{\partial K_a^+}{\partial \epsilon} = \frac{2K_1 \cos 2(\theta+\epsilon)}{\sin^2 2(\theta+\epsilon)} + \frac{K_2 \sin(\theta+\epsilon)}{\cos^2(\theta+\epsilon)} \qquad \text{(S-7)}$$

where

$$K_1 = \frac{4(SF_x^+)(\Delta\theta_x^+) - NBD(T)}{T\omega_S^2}, \text{ and } K_2 = \frac{2}{\omega_S}$$

At $\theta = 45^o$, the first term reduces to zero and the sensitivity expression simplifies to:

$$\left.\frac{\partial K_a^+}{\partial \epsilon}\right|_{\theta=45^o} = \frac{\sqrt{2}}{\omega_S} \qquad \text{(S-8)}$$

Thus, the anisoinertia sensitivity to alignment errors decreases with increasing rotational rates. Note that the sensitivity function is bounded by $0 > \theta > \pi/2$ with singular points at $\theta = 0$ and $\pi/2$.

For a 40 arc seconds per pulse loop quantization, and a 4 revolution test duration the alignment sensitivity is 0.136×10^{-4} sec. per arc second at 0.5 radians per second and 0.27×10^{-4} sec. per arc second at 0.25 radians per second. These error magnitudes represent approximately 14% at 0.5 radians per second and 27% at 0.25 radians per second.

APPENDIX U

Method of Least Squares

Introduction

This appendix is a brief presentation of the method of least squares as applied to both a linear and non-linear model.

Linear Model

The linear model relates a known sequence of observations $y_1, \ldots, y_n$ to a set of parameters $b_1, \ldots b_q$ (to be determined) through a known nxq matrix $(\bar{\bar{A}})$ so that

$$\bar{y} = \bar{\bar{A}}\bar{b} \tag{U-1}$$

The solution $\bar{b}$ is determined by minimizing the following quadratic risk function.

$$R(\bar{b}) = (\bar{y} - \bar{\bar{A}}\bar{b})^T (\bar{y} - \bar{\bar{A}}\bar{b}) \tag{U-2}$$

The resulting least squares estimate is given by:

$$\hat{\bar{b}} = (\bar{\bar{A}}^T\bar{\bar{A}})^{-1}\bar{\bar{A}}^T\bar{y} \tag{U-3}$$

where $\bar{\bar{A}}^T\bar{\bar{A}}$ is assumed to be non-singular.

Non-Linear Model

The least squares estimate for a non-linear model is obtained by first linearizing the model using the first two terms of the Taylor series expansion (Gauss-Newton method). The non-linear model is represented by

$$\bar{y} = \bar{w}(\bar{b}) = \begin{bmatrix} w(\bar{b}) \\ \cdot \\ \cdot \\ \cdot \\ \bar{w}_n(\bar{b}) \end{bmatrix} \tag{U-4}$$

$\bar{w}(\bar{b})$ is expanded into a Taylor series as follows

$$\bar{w}(\bar{b}) = \bar{w}(\bar{b}_o) + \bar{J}(\bar{b}_o)(\bar{b} - \bar{b}_o) \tag{U-5}$$

$$\bar{J}(\bar{b}_o) = \left[\begin{array}{ccc} \frac{\partial w_1}{\partial b_1} & \frac{\partial w_1}{\partial b_2} \cdots & \frac{\partial w_1}{\partial b_q} \\ \frac{\partial w_2}{\partial b_1} & \frac{\partial w_2}{\partial b_2} \cdots & \frac{\partial w_2}{\partial b_q} \\ \vdots & \vdots & \vdots \\ \frac{\partial w_n}{\partial b_1} & \frac{\partial w_n}{\partial b_2} \cdots & \frac{\partial w_n}{\partial b_q} \end{array}\right]_{\bar{b} = \bar{b}_o} \tag{U-6}$$

where $\bar{b}_o$ is the known nominal value of parameter vector $\bar{b}_o$.

Substituting (U-4) into (U-5) yields

$$\bar{y} = \bar{w}(\bar{b}_o) = \bar{J}(\bar{b}_o)\ (\bar{b} - \bar{b}_o) \tag{U-7}$$

For a solution by iteration, (U-7) becomes

$$\bar{y} - \bar{w}(\hat{\bar{b}}_{n-1}) = \bar{J}(\hat{\bar{b}}_{n-1})\ (\bar{b}_n - \hat{\bar{b}}_{n-1}) \tag{U-8}$$

By definition:

$$\bar{\Delta}y = \bar{y} - \bar{w}(\hat{\bar{b}}_{n-1}),\ \Delta\bar{b} = \bar{b}_n - \hat{\bar{b}}_{n-1}) \tag{U-9}$$

Substituting (U-9) into (U-8) yields

$$\Delta\bar{y} = \bar{J}\,(\hat{\bar{b}}_{n-1})\,\Delta\bar{b} \tag{U-10}$$

Equation (U-10) has the same form as (U-1), hence

$$\Delta\hat{\bar{b}} = \left(\bar{J}^T\,(\hat{\bar{b}}_{n-1})\ \bar{J}\,(\hat{\bar{b}}_{n-1})\right)^{-1}\ \bar{J}^T\,(\hat{\bar{b}}_{n-1})\,\Delta\bar{y} \tag{U-11}$$

or

$$\hat{\bar{b}}_n = \hat{\bar{b}}_{n-1} + \left(\bar{J}^T\,(\hat{\bar{b}}_{n-1})\ \bar{J}\,(\hat{\bar{b}}_{n-1})\right)^{-1}\ \bar{J}^T\,(\hat{\bar{b}}_{n-1})\,\Delta\bar{y} \tag{U-12}$$

The iteration continues until $\Delta\hat{\bar{b}}$ reaches a small predetermined value.

APPENDIX V

Mathematical Analysis of the Model

This appendix shows the detailed mathematical analysis of an early model which led to the removal of the Cos $(\theta - \psi)$ term from the model.

C.1 Singularity in the Matrix

The early model had the form

$$\begin{aligned} a_{ind} = y = K_b + K_1 \text{ Sin } (\theta - \psi) + K_2 \text{ Sin}^2 (\theta - \psi) \\ + K_{IO} \text{ Sin } (\theta - \psi) \text{ Cos } (\theta - \psi) \\ + K_O \text{ Cos } (\theta - \psi) \end{aligned} \qquad (V\text{-}1)$$

In order to solve for the model coefficients in a least square sense, we first obtain the matrix of partial derivatives of the form

$$A = \left[a_{ij}\right] = \left[\frac{\partial y_i}{\partial K_j}\right] \qquad (V\text{-}2)$$

where i = 0, 1, ... 15 ranges over the data points and K_j is the j^{th} coefficient. The partial derivatives have the same form for all i

$$\begin{aligned} \frac{\partial y}{\partial K_b} &= 1 \\ \frac{\partial y}{\partial K_1} &= \text{Sin } (\theta - \psi) \\ \frac{\partial y}{\partial K_2} &= \text{Sin}^2 (\theta - \psi) \\ \frac{\partial y}{\partial K_{IO}} &= \text{Sin } (\theta - \psi) \text{ Cos } (\theta - \psi) \\ \frac{\partial y}{\partial K_O} &= \text{Cos } (\theta - \psi) \end{aligned} \qquad (V\text{-}3)$$

$$\begin{aligned} \frac{\partial y}{\partial \psi} = -K_1 \text{ Cos } (\theta - \psi) - 2K_2 \text{ Sin } (\theta - \psi) \text{ Cos } (\theta - \psi) \\ -K_{IO} (1 - 2 \text{ Sin}^2 (\theta - \psi) \\ +K_O \text{ Sin } (\theta - \psi) \end{aligned}$$

Note, however, that the partial derivative with respect to the misalignment angle ψ is a linear combination of the remaining partials

$$\frac{\partial y}{\partial \psi} = -K_{IO}\frac{\partial y}{\partial K_b} + K_O\frac{\partial y}{\partial K_1} + 2K_{IO}\frac{\partial y}{\partial K_2} \qquad \text{(V-4)}$$

$$-2K_2\frac{\partial y}{\partial K_{IO}} - K_1\frac{\partial y}{\partial K_O}$$

Now, this is true for all i; therefore, the column of partial derivatives with respect to ψ is redundant. However, one can not yet speak of singularities in the matrix since only square matrices may have inverses in any case. It happens, however, that the matrix we seek to invert for the least square method is A^TA, which is square. It will not be shown here, but it is true that if A has a redundant column (or row) then A^TA is singular and has no inverse. Therefore, the model as stated in Equation (V-1) cannot be used in the least square method.

C.2 Ambiguity in the Model

The same result can be obtained if Equation (V-1) is expanded using the small angle approximation (ignoring ψ^2 terms), thus

$$\begin{aligned} y = {} & K_b + K_1\left[\text{Sin }\theta - \psi\text{ Cos }\theta\right] \\ & + K_2\left[\text{Sin}^2\theta - 2\psi\text{ Sin}\theta\text{ Cos}\theta\right] \\ & + K_{IO}\left[\text{Sin}\theta\text{ Cos}\theta + \psi - 2\psi\text{ Sin}^2\theta\right] \\ & + K_O\left[\text{Cos}\theta + \psi\text{ Sin}\theta\right] \end{aligned} \qquad \text{(V-5)}$$

collecting like terms we have

$$\begin{aligned} y = {} & \left[K_b + \psi K_{IO}\right] \\ & + \left[K_1 + \psi K_O\right]\text{Sin}\theta \\ & + \left[K_2 - 2\psi K_{IO}\right]\text{Sin}^2\theta \\ & + \left[K_{IO} - 2\psi K_2\right]\text{Sin}\theta\text{ Cos}\theta \\ & + \left[K_O - \psi K_1\right]\text{Cos}\theta \end{aligned} \qquad \text{(V-6)}$$

We now form a new set of model coefficients

$$K_b' = K_b + \psi K_{IO}$$

$$K_1' = K_1 + \psi K_O$$

$$K_2' = K_2 - 2\psi K_{IO} \qquad \text{(V-7)}$$

$$K_{IO}' = K_{IO} - 2\psi K_2$$

$$K_O' = K_O - \psi K_1$$

$$\psi' = O$$

The last equation, a null equation, is of use leaving five equations and six unknowns. Therefore, one of the unknown coefficients is completely arbitrary. In practice, the model either does not converge in fifteen iterations or converges at some arbitrary misalignment angle.

APPENDIX W

Least Square and Fourier Series Analysis Equivalence

This section proves the equivalence between a simple least square accelerometer model that comprises bias, scale factor, the misalignment angle, and the scale factor nonlinearity term to a fourier series expansion truncated at the second harmonic.

A simple least square model is given as follows:

$$y = B_o + K_1 \text{ Sin } (\theta - \psi) + K_2 \sin^2 (\theta - \psi)$$

where

- y is the accelerometer output
- B_o is the null bias
- K_1 is the scale factor
- K_2 is the scale factor non-linearity term
- ψ is the misalignment angle

Expanding the above equation and simplifying yields the truncated fourier expansion:

$$y = B_o \underbrace{- \frac{K_2 (1 + \psi^2)}{2}}_{\text{DC Components}} + \underbrace{K_1 \text{ Sin } \theta - \psi K_1 \text{ Cos } \theta}_{\text{First Harmonics}} \underbrace{- \psi K_2 \text{ Sin} 2\theta - \frac{K_2 (1 - \psi^2)}{2} \text{Cos} 2\theta}_{\text{Second Harmonics}}$$

Thus, the truncated fourier series model is a least square solution consisting of three parameters.